TECHNISCHE UNIVERSITÄT WIEN
Vienna University of Technology

Diese Dissertation haben begutachtet:

Prof. Dr. K. Held   Prof. Dr. E. Tosatti

DISSERTATION

Electronic correlations at the nanoscale

ausgeführt zum Zwecke der Erlangung des akademischen Grades eines
Doktors der Naturwissenschaften unter der Leitung von

Prof. Dr. Karsten Held
Prof. Dr. Giorgio Sangiovanni (betreuender Assistent)
Priv. Doz. Dr. Alessandro Toschi (betreuender Assistent)

E 138 - Institut für Festkörperphysik
eingereicht an der Technischen Universität Wien
Fakultät für Physik

von

M. Sc. Angelo Valli

Matrikelnummer: 0928991
Baumgasse 58, 1030 Wien

Wien, am 7. Mai 2013

Contents

Deutsche Kurzfassung

Das Thema der vorliegenden Arbeit wird das Problem der elektronischen Korrelationen in nanoskopischen Systemen. Elektronische Korrelationen sind wichtig für das Verständnis der Physik der Übergangsmetalle und der Seltenen Erden, die durch teilweise besetzte, stärker lokalisiert d- oder f-Orbitale charakterisiert sind. Elektronische Korrelationen können auch in niedrig-dimensionalen Systemen mit ausgedehnten Orbitalen eine wichtige Rolle spielen.
Im **Kapitel 1** führen wir die experimentellen und theoretischen *fingerprints* der elektronischen Korrelationen in einigen relevanten nanoskopischen Systemen ein.

Obwohl der allgemeine Festkörper-Hamilton-Operator bekannt ist, stellt die theoretische Behandlung von *Vielteilchen-Systemen* eine der großen Herausforderungen für die moderne theoretische Festkörperphysik dar. Im **Kapitel 2** führen wir die *state-of-the-art* theoretische Methode für die Modellierung korrelierter Elektronsystemen ein. Hinsichtlich dessen, stellte die Dynamische Molekularfeldtheorie (DMFT) einen Durchbruch für die numerische Lösung des Gitter-Modelle von korrelierte Fermionen z.B. des Hubbard Modells dar. Außerdem erlaubt die Kombination von DMFT mit *ab-initio* Dichte Funktional Methoden theoretische Vorhersagen und quantitative Vergleiche mit Experimenten.
Niedrig-dimensionale nanoskopische Systemen erfordern aufgrund nicht-lokaler Korrelations-Effekte andere Näherungen, d.h. Enweiterungen der DMFT wie die Dynamische Vertex Approximation (DΓA). Deshalb haben wir ein neuartiges Schema auf der Grundlage von DMFT und DΓA eingeführt, um komplizierte, korrelierte Nanostrukturen zu behandeln.

In den anderen Kapiteln dieser Arbeit präsentieren wir die Anwendung der nano-DMFT und nano-DΓA Methoden auf physikalisch interessante Systeme. In **Kapitel 3** betrachten wir zuerst Modelle für quasi-1-dimensionale organische Moleküle. Hier können wir die Näherungen mit der exakten numerischen Lösung vergleichen. Wir zeigen, dass sowohl lokale als auch nicht-lokale elektronische Korrelationen die elektronische Struktur und Transporteigenschaften dieser Systeme stark beeinflussen, und stellen qualitative Kriterien für die Zuverlässigkeit der nano-DMFT/DΓA Methoden auf. Die Ergebnisse, die wir erhalten haben, motivieren weitere Untersuchungen sowie die Entwicklung weiterer numerischer Methoden.

Danach analysieren wir kompliziertere nanoskopische Strukturen: in **Kapitel 4** simulieren wir einen mechanisch kontrollierten Bruchkontakt und zeigen, dass durch die elektronischen

Korrelationen ein lokaler Metall-Isolator-Übergang auftritt. Das Phänomen kann in der elektrische Leitfähigkeit und möglicherweise auch in Experimenten beobachtet werden. Die Untersuchung unter verschiedenen Bedingungen legt nahe, dass dies eine allgemeine Eigenschaft von Nanokontakten sein könnte.

Schlussendlich, betrachten wir in **Kapitel 5** die Effekte der Kornzerkleinerung im halbdotierten Manganat $La_{0.5}Ca_{0.5}MnO_3$. Die Destabilisierung der Ladungs-Orbital Ordnung in nanoskopische Manganaten ist experimentell etabliert, doch die Interpretation der experimentellen Messdaten ist aufgrund von unreinen oder nicht stöchiometrischen Proben umstritten.
Wir analysieren das Problem mittels der Kombination von *ab-initio* und DMFT Methoden (DFT+DMFT). Einerseits berücksichtigt DFT die realistischen Kristallstrukturen des Systems, anderseits bindet DMFT starke elektronische Korrelationen in Manganaten ein. Mit diese Vorgangsweise können somit sowohl ‘‘bulk’’ Manganate als auch nanoskopische Manganate auf Basis ein und der selben Methode beschrieben werden. Auf diese Weise zeigen wir, dass die Änderungen der Kristallstruktur für das Phänomen der Instabilität des Landungs-Orbital Ordnung verantwortlich gemacht werden kann.

Introduction

> *The principles of physics do not speak against the possibility of maneuvering things atom by atom.*
>
> Richard Feynman, *There's Plenty of Room at the Bottom (1959)*

Those inspiring words were pronounced in a memorable lecture [1], way before modern physics and chemistry managed to explore and manipulate the matter on a length scale comparable with the one of its fundamental constituent, i.e., the individual atoms.
Despite Feynman's prophetic claim, the world had to wait almost twenty years to attend the birth of the expression *nanotechnology*, due to Norio Taniguchi (1974), or the spelling of the letters ''IBM'' obtained by Eigler & Schweizer arranging individual Xe atoms on a surface with a *scanning tunneling microscope*. While the latter deed had a significant mediatic impact, worth even an article on the New York Times [2], for many years to follow the prefix *nano* became part the collective imagination mostly as *science fiction*, rather than being associated to an emerging technology. In this respect, one may think e.g., of the *nanoprobes* of the *Borgs* in the Star Trek series, used to assimilate other living beings, or of the hypothetical *gray goo* end of the world scenario, suggested by Drexler in his book *Engines of Creation: The Coming Era of Nanotechnology* [3], involving self-replicating molecular nanotechnology out of control consuming all matter on earth in their reproduction process.

While the world may not be aware of it, nanotechnology is indeed way closer to reality than to imagination, and many devices which exploit quantum-mechanical effects are already massively present in everyday life. Since the 1970s the *semiconductor memory* became competitive in the computer market, replacing the *magnetic-core memory*[1] which previously was the predominant technology. The novel data storage devices are implemented on semiconductor (usually Si-based) integrated circuits, whose size recently dropped to a few nanometers. The possibility of engineering devices at lower length scales improves both their portability and efficiency. Contemporary forefront research aims to develop revolutionary methods to build, e.g., high-density Ni-nanowire arrays for magnetic data recording or high-energy density storage devices for batteries and renewable energy sources technologies.

[1] Curiosiously, the nomenclature of the bothersome system error *core dump*, so well known to programmers, derive from those devices.

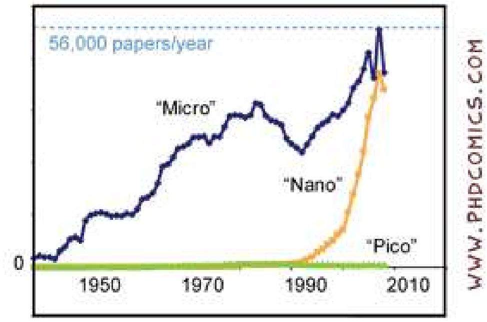

The boost that *nano* science experienced within the scientific community eventually lead to filling the gap with previous existing technologies. Those considerations are, e.g, supported by the data extracted from the ISI Web of Science and shown aside, referring to the number of papers published per year with the corresponding *buzzword* in the title, normalized by the number of journal in print each year. While the plot reproduced here was originally published in an ironic context [4], its intrinsic scientific validity is nevertheless *not* under discussion, and represents a proof that the current frontier of research is evidently the nano scale. The research is not limited to physics and chemistry, but rapidly spread also to biology and medicine: within the current technology, flexible and to some extent tunable nanoparticles with a size comparable with the one of human cells can be engineered. These seem to have the potential to become an important tool for emerging diagnosis and therapy techniques.

Despite the amazing skill developed in the manipulation of matter, the theoretical understanding of the related phenomena is far from being satisfactory. While material properties may often be experimentally controlled without having a deep theoretical understanding of the underlying microscopic mechanism, only the latter may indicate the path toward further progresses. The field of strongly correlated electronic systems, due to its complexity, offers an interesting combination: the lack of a complete understanding and an apparently unlimited range of fascinating physical phenomena with a prospective for technological applications. In particular, the presence of several competing energy scales and their intrinsic tunability, make nanoscopic systems particularly predisposed to both experimental and theoretical investigation of electronic correlations. In this respect, the absence of a crystal environment evidently represents a significant simplifications with respect to solids, so that a general understanding of correlation-driven phenomena can be achieved already in the framework of relatively simple models. However, as soon as the complexity of the systems under consideration increases, simple models are not sufficient anymore to capture and explain the relevant physics, and numerical simulations with the available computational tools become unfeasible if many degrees of freedom are involved. The aim of this work is, hence, to fill this gap. To this end, we employ advanced many-body techniques, embedding them into a flexible scheme, explicitly developed in order to deal with complex nanostructures.

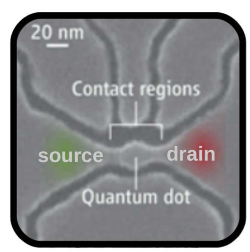

This thesis is organized as follows: **chapter 1** provides for a general introduction to the physics of nanoscopic systems, both from the experimental and the theoretical point of view. The aim of discussing a few relevant experiments is two-fold: it allows us to define the systems we are interested in, but also allows to identify the fingerprint of many-body effect. The latter play a important role in determining electronic and transport properties, and may dramatically enhance the tendency of the system to changes, and give rise to huge responses

which are possibly exploited for technological applications, i.e., in the realization or the improvement of solid state devices.
In this respect, we discuss the interplay between the relevant energy scales, and we discuss different parameter regimes within the theoretical framework of impurity models: even these simple models entail complex many-body effects which lead to fascinating physical phenomena. The last part of this chapter is devoted to the discussion of quantum transport in nanoscopic systems. Transport spectroscopy probably represents one of the most valuable source of information to probe the excitation spectra and electronic properties of confined systems, and often represents the contact between theory and experiments. We derive the electrical conductance both in the Landauer-Büttiker formalism, within scattering theory, and in the Kubo linear response theory, comparing the results and discussing their limit of validity.

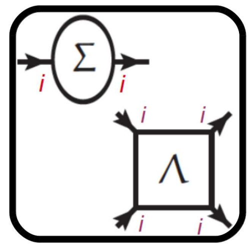

Essentially, **chapter 2** consists of three parts, devoted to a review of many-body techniques for strongly correlated electronic systems.
The first part introduces the dynamical mean-field theory (DMFT) and its combination with *ab-initio* density functional theory (DFT). While the latter contributed to the important steps toward the understanding of electronic correlations both in model systems and realistic materials, an important line of research also concerns the improvement of the available methodology.
In the second part we briefly review the main available extension of DMFT, aiming at including non-local spatial correlations beyond mean-field. These are expected to be relevant in systems where electrons are confined in narrow or low-dimensional regions. In particular, we discuss in details one diagrammatic extension of DMFT, the dynamical vertex approximation (DΓA) and introduce the relevant two-particle and parquet formalism for the vertex functions.
The third part focuses on a recent extension of the latter theory that we developed in order to deal with nanoscopic systems, and includes a critical comparison with alternative/complementary schemes proposed in the literature.

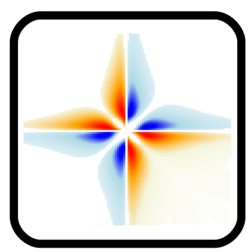

As any other approximation in their early stage of development, the nanoscopic extension of DMFT and DΓA need to be tested on reference systems: the aim of **chapter 3** is, hence, to explore both its potential and its limitations. Suitable candidates to this end, are models of quasi one-dimensional π-conjugated organic molecules, mainly for the following reasons: (i) π-conjugated systems, e.g., the benzene molecule, are of concrete interest to research, and a clear understanding of their electronic transport properties is still lacking; (ii) those systems can be described considering only a few relevant degrees of freedom, resulting in a (numerically) *exactly* solvable model, which provides an important benchmark.
In order to test the approximations employed, we aimed to keep all possible sources of systematic errors under control, as much as possible. In this ideal conditions electronic and transport properties can be analyzed and compared to the exact benchmark within both the DMFT and DΓA approximation schemes. A preliminary analysis within the nano-DMFT approximation,

which is numerically less demanding, allows us to test the reliability of the method in a wide range of parameters. With other sources of uncertainty removed, a possible failure of the nano-DMFT approximation would indicate a prominent role of non-local spatial correlations, to be analyzed within the technically more involved nano-DΓA.

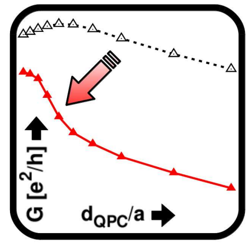

In order to explore the potentiality of the nanoscopic extension of DMFT, in **chapter 4** we employ it to model quantum junctions. In experiments, chemically stable and atomically-sharp contacts can be realized by means of the mechanically controlled break-junction technique. Here, a piezoelectric device allows a precise control over the size of the tunneling gap bridging the contacts. Exploiting the spatially-resolved information obtained within nano-DMFT, we are able to correlate the relaxation of the electronic structure of the system to its (non-local) transport properties. Assuming the crystal structure not to rearrange in the process, we show that, as the contacts are pulled apart and the tunneling barrier increases, electronic correlations induce a local metal-to-insulator transition (or rather a crossover) involving the atoms at the sharp edge of the junction. The fact that the phenomenon is present in different realizations of the junction supports the hypothesis of it being a generic feature. Its possible observation in the experiments is not yet clear, but could have an impact on transport spectroscopy data analysis.

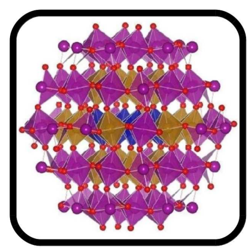

Finally, in **chapter 5** we discuss the effect of size reduction on the half-doped manganite $La_{0.5}Ca_{0.5}MnO_3$. Recent experiments reported the destabilization, upon size reduction, of the complex charge-orbital (CO) and antiferromagnetic ordering, which is realized in the bulk. Some experiments suggested the structural changes of the lattice parameters to be responsible for the phenomenon, while previous analysis reported no crystal deformation of the lattice parameters with respect to the bulk. However, the interpretation of the experimental data is controverse due to the difficulties connected to the experimental synthesis of the nanoscopic clusters, e.g., impure phases, grain boundaries, and non-stoichiometry.

We analyze the phenomenon theoretically, combining DFT in its generalized gradient approximation (GGA) and DMFT: while DMFT provides for the strong electronic correlations responsible for the complex electronic structure, DFT(GGA) realistically takes into account the changes of the lattice parameters (and the corresponding crystal field) in a defect-free and stoichiometric cluster. This avoids the experimental issues regarding the quality of the sample. Moreover, the analysis of bulk and nanocluster manganites on equal footing allows for a direct comparison of the results: the emerging theoretical picture is remarkably in qualitative agreement with the experimental scenario, establishing the link between the changes of the lattice structure and the electronic properties of the ground state.

Chapter 1

Down to the nanoscale: State-of-the-Art

In this chapter, we give a brief introduction to the State-of-the-Art in nanoscopic physics, without pretending to be exhaustive. Specifically, we begin reviewing selected experiments, in order to show the fingerprints of many-body effects in electronically confined systems. As for the theory, a qualitative understanding of the experimental observation can be achieved in the framework of standard impurity models, whose discussion allows us to introduce the reader to the complex interplay between quantum fluctuations and electronic correlations. Eventually, at the end of this chapter, we discuss challenges and open questions which, together with the lack of a comprehensive, reliable theory to describe transport through strongly correlated nanostructures, have motivated the methodological development presented in the rest of this work.

At the nanoscale, the quantum mechanical nature of electrons becomes evident, and the physics of matter is dominated by quantum effects. Moreover, when electrons are spatially confined into low-dimensional structures, electronic correlations are naturally enhanced, determining the occurrence of a variety of unexpected physical phenomena.

While the 1970s witnessed the birth of novel ideas related to the concept of nanotechnology, the effective rise of nanotechnology may be traced back to the 1980s, due to the technological and experimental advances that led eventually to the invention of the *scanning tunneling microscope* (STM) [5, 6, 7], which allowed in practice what scientists have been yearning for: the possibility to manipulate matter at the atomic scale. As we shall see, nanotechnology established itself as a promising and interdisciplinary field of science, ranging from (in)organic chemistry to biology, and material science. The impressive development of experimental techniques in controlling the composition of the matter raised interest in functionalizing materials. Material properties can be tuned by changing their chemical composition, and novel compounds can be made, e.g., by heterostructuring, in order to either enhance peculiar properties of the individual components, or even generating unexpected electronic phases. This has obviously a huge impact on technological applications, but also makes the field very attractive from the point of view of basic research. In nanoscopic devices as well as in self-assembly molecular structures, basic quantum phenomena can be investigated devoided from many of the complications arising in bulk materials. In particular, the main focus is on understanding electronic transport mechanism, which, e.g., is fundamental in order to extract information by means of transport spectroscopy, but also play a key role in biological and chemical processes, like pain and brain signals transmission. Moreover, the possibility to easily tune the properties of nanoscopic systems also suggests to employ engineered nano particles and *quantum dots* for medical applications, including cancer diagnostics [8, 9].

1.1 Experimental overview

The available literature concerning the experimental investigation of nanoscopic systems is certainly huge, but a comprehensive survey of the most important contributions in this field is certainly out of the scope of the present work. Hence, in the following we shall instead provide a brief introduction to the systems of interest and give and idea of their wide range of applicability. Furthermore, the discussion of selected *milestone* experiment allows to identify the fingerprint of electronic correlations, and qualitatively understand the underlying physical phenomena, but also raise the attention of the difficulties to achieve an unambiguous interpretation of the experimental data, proided by complementary techniques, without the support of a comprehensive theory.

1.1.1 Confined systems: properties & applications

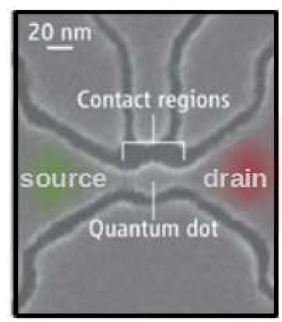

Modern techniques of lithography made it possible to confine electrons to a length scale at which charge (and energy) quantization are observable. Perhaps, in this respect, the most widely known system is the so-called **quantum dot** (QD). The name was coined by Reed *et al.* [10] in order to describe a system, in which electrons are confined into a zero-dimensional structure, *a dot*, realized at the interface of a GaAs/Al$_x$Ga$_{1-x}$As semiconductor heterostructure.
A scanning electron micrograph of a graphene-based single-electron transistor is shown in the figure aside, adapted after Ref. [16]. The spectrum of a QD is quantized, resembling that of an isolated atom (and it is hence often referred to as *artificial atom*), but with a typical level spacing $\Delta\epsilon$ between μeV and meV, depending on the size of the QD. Under this condition, the physics of the system is dominated by quantum effects. Moreover, at the typical system size at which quantum confinement occurs (a region of diameter $d \sim 100$ nm) the mutual Coulomb interaction between electrons is of the order of meV, and the effect of electronic correlations can hence be experimentally observed.

Whereas natural atoms are usually studied with optical spectroscopy, due to the typical size of the level spacing $\Delta\epsilon$ in QDs, an early experimental evidence of **quantum confinement** was obtained by electronic transport measurements, where a quasi-bound QD is contacted to metallic electrodes, which play the role of charge reservoirs [10]. If the energy scale set by the temperature $k_BT \ll \Delta\epsilon$, with k_B being the Boltzmann constant, only a few levels close to the Fermi energy contribute to transport. Under this conditions, a series of plateau in the current characteristic $I(V_{\text{SD}})$ is observed as a function of the voltage V_{SD} applied between the source and drain electrodes (also often referred to as bias voltage, and denoted V_b). The presence of the plateaus, indicates charge and energy quantization inside the QD: the current raises, flowing through the confined structure, when an energy level of the dot falls in the bias energy window $eV_{\text{SD}} = \mu_S - \mu_D$, where $\mu_{S,D}$ is the chemical potential of the source and drain reservoir, respectively, wile -$|e|$ denotes the bare electron charge.

Applications of optical & transport properties of confined systems. For instance, electronically confined systems are characterized by interesting optical properties. It is well-known that the *optical band gap*, i.e., the energy threshold to create an *exciton* (bound electron-hole pair) via the absorption of a photon, is controlled by the size of the QD [11, 12]. The radiation-induced excitation of electrons confined to the valence band and the radiative electron-hole recombination process, due to relaxation of the electron returning to the ground state, lead to the emission of light. The *color* of the emitted light (i.e., the wavelength of the photon) is hence determined by the size of the band gap. In CdSe nanocrystals, it has been experimentally shown that the color of the emission can be varied by changing the size of the nanocrystal [13], allowing a controlled **electrolumiescence**. This is exploited, e.g., in fluorescent dye applications. The tunability of the QD optical band gap has also been addressed as an important characteristic feature for the realization of next generation QD-based **solar cells**, with the possibility to cover a large portion of the solar emission spectrum. Recently it was shown that it is possible to modify the electronic and photophysical properties of QDs by doping optically active transition metal ions, as, e.g., Mn^{2+}, providing a strategy to achieve an efficiency boost (estimated up to 5%) [14]. Those applications mentioned above are just few of the possible, but already give an idea of how the intrinsic tunability of nanoscopic systems can be exploited in many field of research and technology.

Indeed, while a confined structure bridging source and drain reservoirs (being them physical electrodes or the layers of an semiconductor heterostructure separated by a confided electron gas) constitutes what is generally referred to as a *two-terminal* device, interesting physical phenomena are observed if the confined structure is also capacitively coupled to a gate electrode, giving room to several other applications. In fact, the gate voltage V_G can be used to (rigidly) shift the position of the energy levels of the QD with respect to the Fermi energy of the electrodes. In such a setup, the system was shown to behave as a **single electron transistor** (SET): see, e.g., Refs. [15, 16] for interesting studies of graphene-based SETs, or Ref. [17] for a review. Unlike conventional transistors, where the charge changes continuously with V_G, in a SET the (low-bias) differential conductance $G = dI/dV_{\text{SD}}$ as a function of V_G displays a periodic structure of peaks, due to charge quantization, arising each time another level of the QD is drawn by the gate voltage below the Fermi level (or within the bias window, at finite V_{SD}). The possibility of controlling electronic transport through the confined structure represents an important achievement in the context of solid-state devices (SSDs) in which a SET can act as a *switcher* between to configurations: 0 or 1, corresponding to the cases of zero and finite current flowing through the device, respectively. In contrast to the theoretical picture, however, Si-based SETs still suffer from problems that arise from material deficiency, leading e.g., to leakage current that may disrupt the device [18], and the practical implementation of such SSD is far from being trivial.

Experimental evidence for strong electronic correlations. The fascinating periodic structure in the gate voltage dependence of the differential conductance is theoretically understood to be a direct (i.e., experimentally observable) consequence of strong electronic correlations: In the range of V_G between two consecutive conductance peaks, the system is said to be in a *Coulomb blockade* regime, and the conductance is zero due to the sizable Coulomb repulsion experienced by the confined electrons, which prevents charge fluctuations within the QD. The conductance peaks, hence, corresponds to configuration in which charge fluctuation requires no energy cost and the current can flow within the confined structure.
Interestingly, one realizes that sweeping the gate voltage allows to observe electronic correlation effects far beyond the Coulomb blockade. At low-enough temperature (i.e, below an energy scale set by the details of the system, e.g., typically of a few Kelvin in semiconductor QDs) the conductance may be sensibly enhanced in regions where tunneling process are prohibited at

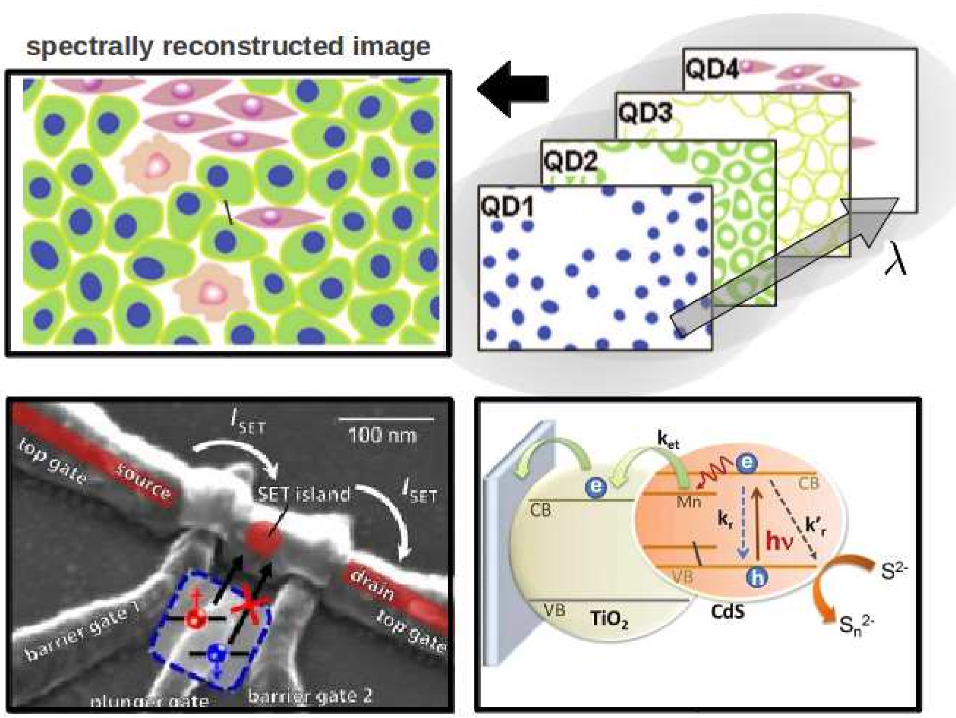

Figure 1.1: Applications of QDs. Upper panel: schematic spectral reconstruction of a tissue specimen RGB image via disentanglement of emission spectra at different wavelengths exploiting the QD electroluminescence. Lower panels: spin-dependent transport in Si-based SET (left); schematic representation of electron transfer from Mn-doped CdS/CdSe semiconductor into TiO_2 nanoparticles, and electron-hole recombination in a QD synthesized solar cell (right). Adapted after Refs. [9, 14, 19].

higher temperature due to the Coulomb blockade. This is understood to be a manifestation of the **Kondo effect** [20, 21]. Originally, this phenomenon was associated to scattering properties of magnetic impurities in metal hosts, leading to logarithmic increase of the resistivity at low-temperatures, unlike non-magnetic impurities, resulting in a finite and temperature independent contribution. The nature of the resistivity behavior (referred to as *the Kondo problem*) is determined by an effective exchange coupling between the impurity magnetic moment and the spin degrees of freedom of the conduction electrons of the metallic host. Interestingly, due to the different condition in which transport takes place in QDs with respect to metals, the same physical processes lead in electronically confined systems to an enhancement of the conductivity. In the following we consider the latter issue from an experimental point of view, while a more detailed discussion of its theoretical interpretation is postponed to the following section.

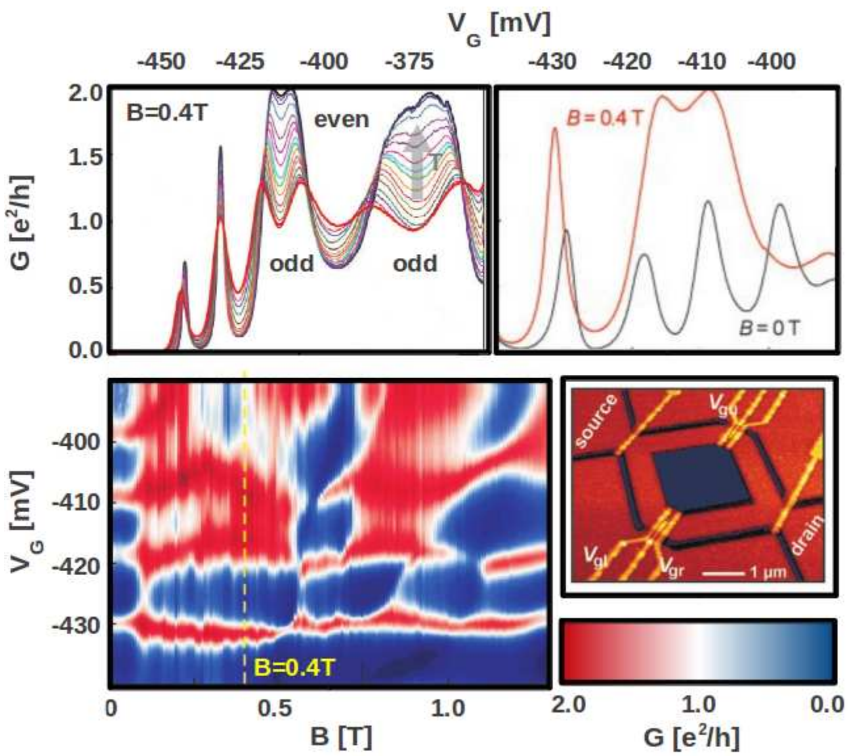

Figure 1.2: Coulomb blokade and Kondo effect in a semiconductor QD. Upper panels: conductance G as a function of V_G (denoted as V_{gl} in the experiment). Left panel shows the temperature dependence between between $T = 15$ mK and $T = 900$ mK in the presence of a magnetic field $B = 0.4$ T. When the number of electrons n in the dot is even, G decreased with T due to the Coulomb blockade (Kondo valley), while for odd occupation one observes the Kondo effect with G approaching the unitary limit $G = 2e^2/h$ (e.g., the evolution lowering T in highlighted by the gray arrow). Right panel: the comparison of two selected traces taken with and without magnetic field show that the latter allows the Kondo effect to fully develop. Lower panel: color plot of G as a function on B and V_G at $T == 15$ mK. Red and blue correspond to high and low conductance, respectively. At zero-field, due valence fluctuations the QD has no well defined magnetic moment, and a peak structure typical of the Coulomb blockade regime is observed. Adapted after Ref. [26].

Semiconductor QDs were indeed theoretically predicted [22, 23] and experimentally shown [24, 25] to exhibit Kondo effect. Of particular relevance is the experiment performed by van der Wiel *et al.* [26] on a QD in the presence of a magnetic field, which allowed the fist observation of the Kondo effect in the *unitary limit*, i.e., when G reaches the conductance quantum $G_0 = 2e^2/h \approx 77.5\ \mu$S (being h the Planck's constant). Some representative experimental results are shown in Fig. 1.3 and briefly discussed in the following. In the Coulomb blockade regime, the low-conductance regions (also known as Kondo valleys) are characterized by a fixed occupation of the QD, and each conductance peak separates valleys differing by a unit of charge. As the temperature is lowered, the valleys associated to an evn occupation in the dot become deeper, and the conductance features sharpen, as expected. On the other hand, in the valleys associated to an odd occupation, the conductance raises due to the Kondo effect. While in the ideal case the Kondo effect is expected already at $B = 0$, in the experiment the conductance enhancement in the odd Kondo valleys was only of about 20% [26], while at $B \sim 0.1$ T an change of transport regime is observed, and the conductance reaches eventually the unitary limit $G = G_0$ above at a $B = 0.4$ T field, as shown in the lower panel of Fig. 1.3 by a gate voltage versus magnetic field map. Among the possible explanations to the experimental data are related to the presence iof a ground state more complicated than a $S = 1/2$ spin singlet, due to, e.g., the presence of a spontaneous spin polarization, suppressed by the magnetic field. or the accidental degeneracy of spin singlet and triplet state.

1.1.2 Quantum junctions

Besides electronically confined systems, such as QDs, another vast research field, concerned with **quantum junctions** (QJs) developed between the 1980s and the 1990s, which could be realized by means of STM and mechanically controlled break junctions (MCBJ) techniques. As the understanding of transport mechanisms in those systems is relevant in the context of this work, let us briefly describe their experimental realization, while quantum transport will be discussed from a theoretical point of view in a following section.

The development of the **mechanically controlled break junction** (MCBJ) technique allowed the fabrication of extremely stable atomic-sized contacts. Although more than one contact variation exists, depending on the details of the fabrication, the working principle is the same in all cases. A MCBJ can be made, e.g., in the following way: a suspended metallic bridge (made of Au, but also Cu or other metals are suitable) in fixed on a flexible substrate covered with a electrically isolating material (e.g., polyimide). The system can be bent with a piezo-controlled mechanism, consisting of a pushing rod and two counter-supports, causing the elongation of the metallic electrodes until an adjustable tunneling nano-gap of $\Delta d \sim 100\ \mu$m is formed. Another possibility to open a nano-gap between electrodes is based on electromigration, where the displacement of metallic ions is due to a large momentum transfer by electrons at large current densities. More details about the fabrication of MCBJ can be found, e.g., in Ref. [44] and references therein.

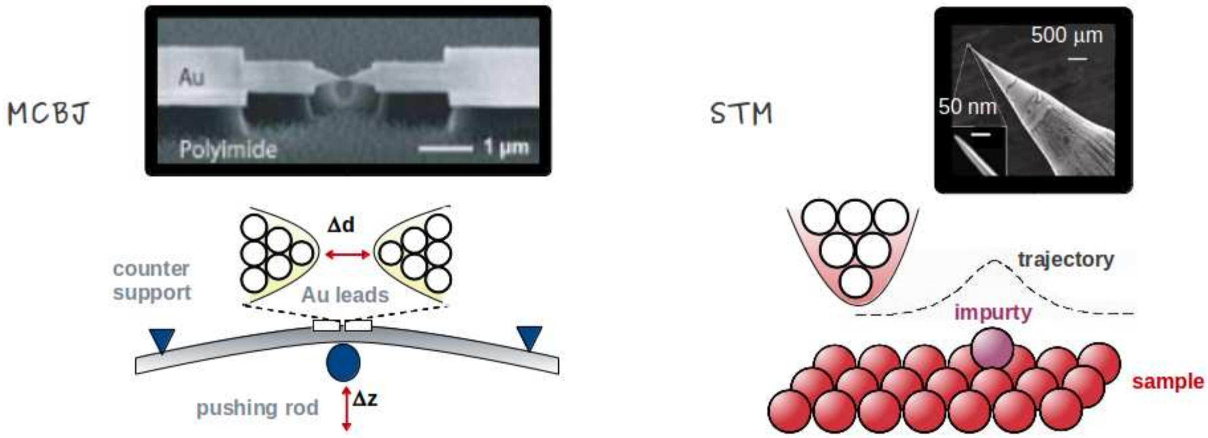

Figure 1.3: Left panel: a MCBJ made breaking an Au constriction in order to form atomic-sized contacts. Right panel: a STM infers the real-space image of the sample. Adapted after Refs. [27, 28].

On the other hand, as already mentioned, the **scanning tunneling microscope** (STM) is one of the most versatile tools for the realization and manipulation of atomic contacts (for a review see, e.g., Ref. [229]). In the usual setup consists in an atomically sharp electrode held at a fixed distance from a *sample*: the measurement of the tunneling current between the junction allows to infer the real-space image of the sample with μmetric precision, assuming an exponential dependence of the tunneling current with the size of the (vacuum) tunneling gap. A variety of samples can be investigated, ranging from metallic surfaces to more complex objects, like a single-walled CNT [230]. Another possibility is to indent the STM tip in the surface and carefully withdrawn so that atoms from the surface are adsorbed on the tip until a stable atomic contact is formed.

Those techniques could be used to obtain metallic nanoscopic wires (*nano-wires*) [29]: contrary to QDs, in (quasi) one-dimensional wires the level spacing $\Delta\epsilon$ is not the dominating energy scale, so that the system is characterized by almost a continuous spectrum and possesses many correlated degrees of freedom. In this respect, theoretical predictions suggest charge-spin separation and *all* the system's excitations to be of *collective* nature (plasmons) below a typical energy scale $k_{\mathrm{B}}T_{\mathrm{L}}$: those systems are usually addressed as Luttinger liquids (LL) [32], although a clear fingerprint of LL physics was experimentally not observed yet [33].
In this situation, the conductance of nano-wires can hardly be changed by a gate voltage, and often a linear $I(V_{\mathrm{SD}})$ characteristics is displayed, which makes nanostructures less functional for electronic applications. However, besides being not particularly ‘‘flexible’’ systems in many respects, in the state-of-the-art of nanoscopic electronic transport, **quantum junctions** (QJs) play a fundamental role, as they result in atomically sharp contacts with an adjustable tunneling gap. Indeed, strong evidences from conductance quantization have been reported, both at low [30] and room temperature, [31] as a proof of the experimental realization of single atomic

junctions. Moreover, molecules can be adsorbed into the gap, forming stable tunneling contacts of systems of the dimension of a few nanometers, which is out of the range of conventional lithography. The possibility of obtaining molecular junctions immediately raised quite a lot of interest for many reasons. Charge transport through a complex molecular system is certainly a many-body effect, and correlation-driven phenomena are hence to be expected. Moreover, due to their complexity, molecules possess also internal degrees of freedom which can be susceptible to mechanical stress, electric field, and local environment (chemical reactions), thus intrinsically providing a much higher degree of tunability with respect to the nano-wires themselves. For instance, an interesting property has been recently reported by Venkataraman *et al.* [34], where it was shown that the conductance of a molecular chain can be changed by varying the twisting angle between the chemical bonds within the chain: this supports the hypothesis that the conformation of the molecule bridging the electrodes is relevant and strongly influence the transport properties of the junction, and at the same time represents a way to tune the current, provided the possibility to mechanically control the molecule twisting.

Puzzles in quantum molecular junctions. A pioneering experiment in the history of molecular nanotechnology was performed by Reed *et al.* [35] and represents the first attempt to fabricate a single-molecule junction ever reported. In the experimental setup, **benzene-**$1,4$**-dithiol** ($1,4$-BDT) molecules self-assembled onto a gold MCBJ form a stable junction, in which the molecule bridges the Au electrodes. For the sake of completeness, we remind that $1,n$-BDT (chemical formula $C_6H_4(SH)_2$) is an organic compound, which is obtained from benzene (C_6H_6) by the chemical substitution of the H bound to C occupying in the ring position 1 and n, with a S-based functional group: thiol (SH). In the experiment, the current characteristics $I(V_{\mathrm{SD}})$ and the differential conductance $G = dI/dV_{\mathrm{SD}}$ were measured at room temperature as a function of an external bias voltage V_{SD}. Reproducible evidence for a charge gap at $V_{\mathrm{SD}} = 0$ and steps in the conductance G as a function of V_{SD}, reminiscent of Coulomb staircase in QDs, were observed. Although the results suggested charge and energy quantization to be responsible of the observed behavior, at that time the question was not fully solved due to the impossibility to accurately probe the charge states by means of an additional gate electrode, which only recently have been successfully integrated into MCBJs via electromigration [36] or electrostatic gating [37] techniques.

Besides the importance of the findings reported, this experiment is regarded as a crucial step in the field of molecular nanotechnology, as it triggered the realization of many other similar experiments [38, 39]. However, the results reported by different groups, obtained by the analysis of conductance histograms, were puzzling, because the values of the measured conductance were scattered across several orders of magnitudes: e.g., the conductance $G \sim 0.011\ G_0$ in STM measurements [38] is much lower than $G < 10^{-4}\ G_0$ reported in a MCBJ settings [35]. This sheds shadows on the reproducibility of the results. Obviously, this is also related with the impossibility of directly controlling the chemical processes behind the formation of a stable junction, and also intrinsically dependent on the measurement technique. In this respect, some configuration-dependent signals can be eliminated by a statistical analysis of several repeated

measurements, which are often summarized in *conductance histograms* [40, 41], and some features are clearly reproducible, like, e.g., the last plateau in Au (configuration: [Xe] $4f^{14}5d^{10}6s^1$) Al ([Ne] $3s^2 3p^1$) or Pb ([Xe] $4f^{14}5d^{10}6s^2 6p^2$) contacts,
connected with the material-dependent orbital structure as well as with conductance quantization [42, 43, 44]. However, quoting Ref. [44], it is clear that *''statistical methods are not the panacea and the interpretation of the conductance histograms is not always straightforward''*. Indeed there are cases, including the above mentioned measurements in $1,4$-DBT, in which the origin of the discrepancies between the reported results is still not clear.
Recently, it has been reported by Kiguchi *et al.* [45] that a highly conducting molecular junction can be achieved by *direct* binding a π-conjugated molecule (benzene) on Pt electrodes, which also pointed out that the conductance strongly depends on the properties of the chemical bond between the molecule and the electrodes. Hence, the properties of the *anchoring groups*, e.g., thiol in the case of BDT, eventually determine the conductivity and the stability of the junction. While one may still have the freedom to choose between few different anchoring groups, the conductance also strongly depends on the relative *position* within the molecule of the anchoring groups atoms, e.g., the value of n in $1,n$-BDT, so that systems with different bonding configuration will also display completely different conducting properties. In this respect, see also, e.g., Ref. [44] for a deeper reading.

The experiments mentioned above demonstrate the important **role of conjugation** in organic π-electron systems: in particular , the presence of alternating single and double C-bonds results in the formation of π orbitals delocalized within the whole molecule, hence making those systems particularly suitable for charge transport. Indeed, π-conjugated molecules are still considered the prototype systems for molecular junctions, both from an experimental and a theoretical point of view. These will hence have a pivotal role also in the rest of this work. Definitively, molecular nanotechnology ha the potentiality to become an alternative (or at least complementary) to traditional Si-based SSDs, employing molecules or nano-clusters of atoms as its fundamental blocks for (bio)technological applications: if Si represents the history, and in many cases still also the present, of nanotechnological devices, can then C represent the future instead?

1.2 Understanding the role of electronic correlations

As mentioned in the previous section, the investigation of nanoscopic systems is strongly related to charge (or spin) transport. Electronic transport at the nanoscale is a many-body phenomenon, and while a deeper understanding of the transport mechanisms is *per se* interesting, it also provide valuable information that can be extracted performing transport spectroscopy. Measuring the differential conductance as a function of the bias voltage $V_{\rm SD}$ between the source and the drain electrodes, and of the gate voltage V_G, allows to detect discrete charge states and to identify complex excitations, e.g., involving spin or vibrational degrees of freedom. In order to understand how tunneling spectroscopy works, it is useful to briefly discuss the transport mechanisms in nanoscopic devices.

1.2.1 Interplay between competing energy scales

Finite-size systems share many similarities with electronically confined systems, and in many cases are believed to behave essentially as QDs. In fact, Coulomb blockade, Kondo physics and even more exotic phases have been observed in many nanoscopic systems, including molecular junctions [46, 47, 48, 49, 50, 51], individual [52, 53, 54] or cluster [55, 56] of *adatoms* on surfaces, and carbon nanotubes (CNTs) [57], just to mention a few. This allows theoretical investigation of complex nano-systems to be performed in the framework of well-established models.
Nevertheless, for molecular scale quantum dots, the excitation spectra may be quite complex due to the presence of several competing energy scales: the level spacing of the discrete spectrum $\Delta\epsilon$ or the hopping amplitude in spatially extended systems, the charging energy U due to the Coulomb interaction between electrons, the reservoir-dot hybridization Γ, and the temperature T. Without interactions, quantum fluctuations are well understood. However, correlation effects and their interplay with the other *bare* energy scales cause the emergence of *novel effective* energy scales, and lead to a variety of transport regimes and interesting physical phenomena. This is indeed the case of the Kondo effect, associated to the Kondo scale $k_{\rm B}T_{\rm K}$, and of its intrinsic non-perturbative nature, originating from the spin and charge fluctuations involving the confined and delocalized degrees of freedom, mixing due to the reservoir-dot coupling.

At cryogenic temperatures, i.e., $k_BT \ll \Delta\epsilon, U$, the discrete spectrum of the system can be resolved, and depending on the value of Γ with respect to these parameters, one can define different transport regimes. In this respect, see also Fig 1.4 and Ref. [58] for a deeper reading.
In this situation, a theoretical understanding of the experimental observation discussed in the previous section, can be achieved considering the constant interaction model [59]. Here, the QD is described as a set of single-particle levels ϵ_λ by the following Hamiltonian

$$\mathcal{H}_{\mathcal{QD}} = \sum_{\lambda\sigma}(\epsilon_\lambda + eV_G)n_{\lambda\sigma} + \frac{U}{2}n(n-1), \tag{1.1}$$

where $n_{\lambda\sigma}$ is the occupancy of the spin σ state of the level labeled by the (set of) quantum number(s) λ, and $-|e|n = -|e|\sum_{\lambda\sigma} n_{\lambda\sigma}$ denotes the total charge in the QD, controlled by the gate voltage V_G. The charging energy of the QD is defined in terms of the capacitance C of the whole system (i.e., including the source, drain, and gate electrodes) as $U = e^2/C$, while the potential energy depends on the number of electron pairs and does *not* affect the energy levels of the single-particle spectrum. The QD is connected via hybridization processes, associated to a tunneling barrier Γ to a source and a drain reservoirs [1] with chemical potentials μ_S and μ_D, respectively, so that the bias voltage is defined by $V_{\text{SD}} = \mu_S - \mu_D$.

In the **weak-hybridization regime** ($k_BT < \Gamma \ll \Delta\epsilon, U$) the Coulomb Blockade is lifted by resonant tunneling processes, occurring whenever a single-particle state lies within (a range k_BT of) the bias voltage window. This can be achieved both varying the bias voltage itself or the gate voltage V_G. Spanning the gate voltage and measuring the (zero bias) conductance results in a series of sharp peaks, occurring each time two states of the QD with n and $n+1$ electrons become degenerate, allowing charge fluctuation with no energy cost and a current to flow through the QD. This phenomenon is also known as *Coulomb oscillations*. The peaks, whose height represents a substantial fraction of the unitary conductance $G_0 = 2e^2/h$, follows a periodic pattern: the current through the QD reise only at the degeneracy point, when charge fluctuations are allowed, i.e., being $E(n)$ the energy as of the Hamiltonian $\mathcal{H}$ for the n electron system, if any of the following condition is fulfilled

$$0 \stackrel{!}{=} \begin{cases} E(n+1) - E(n) = \epsilon_{n+1} + eV_G^+ + Un, \\ E(n) - E(n-1) = \epsilon_n \quad + eV_G^- + U(n-1), \end{cases} \tag{1.2}$$

defining the values of the gate voltage $V_G^\pm$ at which the peak is observed. Hence, the separation between consecutive peaks

$$|e|(V_G^+ - V_G^-) = \overbrace{\epsilon_{n+1} - \epsilon_n}^{\Delta\epsilon} + U, \tag{1.3}$$

is controlled by U. Therefore one can conclude that the Coulomb blockade is a direct manifestation of the Coulomb interaction between confined electrons. Considering, e.g., a harmonic confining potential for the QD, one can theoretically understand the periodicity of the separation and experimentally show [11] that the states identified by tunneling spectroscopy follow an atom-like *Aufbau* principle of sequential energy level occupation, defining a *periodic table* for QDs [60].

The map of the differential conductance as a function of the bias voltage V_{SD} and the gate voltage V_G displays the typical diamond structure, which is often referred to as *stability diagram*. A schematic representation of the stability diagram is shown in Fig. 1.4 and reads as following. Within each *diamond* (dark regions) the occupation of the QD is fixed, and there is no conductance. The *instability lines* separating the dark and light regions of the diagram correspond to the particular values of the bias and gate voltage at which resonant tunneling sets in. The slope of the instability carries quantitative information about the capacitance of the source,

[1] Here, for the sake of simplicity, we assume that electrons can tunnel back and fourth between the QD and the reservoirs, while a more detailed discussion of the tunneling Hamiltonian, connecting the confined system and the reservoirs, will be discussed in details in the following sections.

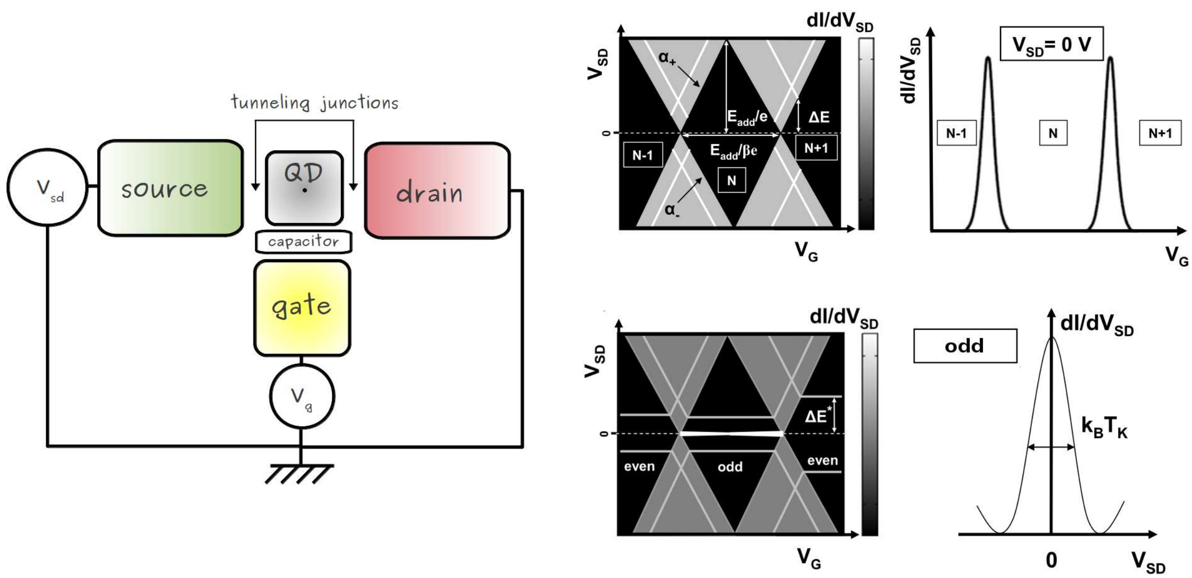

Figure 1.4: Left panel: schematic representation of a QD three-terminal junction. Right panels: electron transport through a weakly-hybridized junction; the gate voltage probes three different charge states in the Coulomb blockade (upper right panels) and Kondo (lower right panels) regimes. Schematic representation on the map of the differential conductance dI/dV_{SD} versus the bias voltage V_{SD} and the gate voltage V_G (stability diagram, see text for details) and conductance profile along selected lines of the stability diagram. Adapted after Ref. [58].

drain, and gate electrodes, while the width of the diamonds is controlled by the addition energy, which is defined in Eq. (1.3) as: $E_{\text{add}} := \Delta\epsilon + U$, and β quantifying the maximum shift of a QD level which can be induced by the gate [58]. As the hybridization Γ is enhanced, higher order processes with respect to the resonant tunneling become important. We can distinguish between a strong- and intermediate-hybridization regime. In the **strong-hybridization regime** ($\Gamma \gg \Delta\epsilon, U, k_B T$) the charge distribution inside the dot becomes continuous, the charge quantization is lost together with any sign of Coulomb blockade, and coherent tunneling dominates transport.

The **intermediate-hybridization regime** is way more interesting, as the interplay between the interaction and the hybridization is non-perturbative. While, to some extent, it is still possible to observe *Coulomb diamonds*, high-order processes yields a finite current also in regions where resonant tunneling is prohibited by the Coulomb blockade. Among those are included elastic and inelastic *cotunneling*, as well as spin-flip processes.

In the *elastic cotunneling* processes, the occupation of the dot is raised (or lowered) by a unity involving the temporary occupation of a forbidden virtual state without violating the energy conservation thanks to the Heisenberg's uncertainty principle. On the contrary, *inelastic cotunneling* processes leave the QD in an excited state with energy ΔE^* with respect to the one of the initial state, and occur at $eV_{\text{SD}} = \Delta E^*$, according to the energy conservation law. In the stability diagram, those processes correspond to (white) lines running parallel to the diamond shaped regions. Moreover, whenever the QD occupation is odd the system is in a magnetic state (e.g., $S = 1/2$), and while charge fluctuations are blocked, the QD still posses a spin degree of freedom. Hence, *spin-flip* processes entail an antiferromagnetic superexchange between the spin of the QD and the reservoirs spin degrees of freedom. At low enough temperature, this gives rise to a (Kondo) resonance at the Fermi energy in the density of states (DOS) of the QD [25, 26]. The Kondo resonance is associated with the quenching of the local moment, and connects two consecutive degeneracy points through the odd occupation sector, while it does not occur if the QD is initially in a non-magnetic state.

The Kondo physics as well as other many-body effect driven by strong electronic correlations are, obviously, not an exclusive of nanoscopic systems. However, the enhancement of the Coulomb interaction due to the quantum confinement, and the tunability of manufactured nanoscale devices, set up the ideal conditions for both theoretical and experimental investigation of the interplay of the Coulomb interaction with the hybridization between localized electrons and delocalized degrees of freedom. Hence, in the next section we introduce a model which is important in a two-fold prospective: on one hand, it allows to study the interplay between the relevant energy scale: the temperature, the (local) Coulomb interaction, and the hybridization with the reservoirs, while on the other it represents the tool to take into account electronic correlations also in lattice systems within the dynamical mean-field theory (and its extensions).

1.2.2 The Anderson impurity model

Already since the 1940s, Mott and Peierls advanced the hypothesis that the electron localization tendency due to a strong enough Coulomb repulsion could drive a metal-to-insulator transition (MIT) [61, 62]. Some years later, Friedel proposed that tunneling of electrons between the localized levels of a magnetic atoms and a Fermi sea could give rise to a resonance in the electronic spectrum [63]. Both effects, which are at the basis of the Kondo effect, are taken into account in the Anderson impurity model (AIM), originally introduced by Anderson in 1963 in order to theoretically explain the mechanism determining the formation of local moments in system of diluted magnetic impurities in a metallic host [64]. The motivation for it was an unpredictable behavior of, e.g., the dilution of Fe impurities dissolved in Nb_{1-x}-Mo_x alloy giving rise (above a threshold concentration) to a typical Curie-Weiss dependence of the magnetic susceptibility $\chi_m \sim 1/T$, which is the hallmark for the existence of a magnetic state. On the other hand, the Fe impurities resulted in a Pauli (i.e., temperature independent) susceptibility in Ti, V or Nb hosts [65].

Beside providing a solution of the puzzle it was originally introduced for, the Anderson model, together with the renormalization theory, gave an important contribution to the understanding of the nature of the Kondo physics as a consequence of quantum many-body effects. Furthermore, the AIM plays a crucial role in the analysis of electronic correlations in strongly correlated systems, especially in the context of one of the most successful many-body methods available so far: the dynamical mean-field theory (to be discussed in details in Sec. 2.1).

The Hamiltonian of the AIM reads

$$\mathcal{H}_{\mathcal{AIM}} = \overbrace{\sum_{k\sigma} \epsilon_{k\sigma} n_{k\sigma} + \sum_{k\sigma} V_k (c^\dagger_{k\sigma} d_\sigma + \text{h.}c.)}^{\mathcal{H}_{\text{hyb}}} + \underbrace{\epsilon_d n_d + U n_{d\uparrow} n_{d\downarrow}}_{\mathcal{H}_{atomic}}, \tag{1.4}$$

where $d^\dagger_\sigma$ (d_σ) creates (annihilates) an impurity electron with energy ϵ_d, while the Coulomb interaction on the narrow impurity state is taken into account by an on-site repulsion U. Those contributions constitute the atomic (i.e., local) part of the impurity model Hamiltonian. The operator $c^\dagger_{k\sigma}$ ($c_{k\sigma}$) instead, creates (annihilates) a conduction electron with spin σ, momentum k, and energy $\epsilon_{k\sigma} = E_{k\sigma} - \mu$, setting the zero of energy at the chemical potential μ. When immersed in a metallic host, the impurity electrons can tunnel into the conduction band and vice versa. Those tunneling processes are described by the hybridization terms, which mixes the localized impurity state $|d\rangle$ and the delocalized states of the conduction band $|k\rangle$. The quantum mechanical amplitude of those processes is given (to a first approximation) by the matrix elements of the ionic potential

$$V(k) \approx \langle k|V_{\text{ion}}|d\rangle. \tag{1.5}$$

In order to understand the interplay between the local interaction on the impurity and the hybridization with the conduction band of the host, following Ref. [66], we analyze the AIM: in the atomic limit, describing the formation of a well-defined magnetic moment in an isolated impurity due to the local interaction, and in the non-interacting limits, in which a non-interacting DOS develops a resonance due to the hybridization with a localized impurity.

The atomic limit. As anticipated, the Kondo resonance is generated from the hybridization of a localized spin degree of freedom with the conduction electrons. Hence, the necessary condition for the Kondo effect to take place is the existence of a magnetic state in the impurity. The formation of a magnetic moment can be easily understood considering the *atomic limit* of the AIM, described by

$$\mathcal{H}_{atomic} = \epsilon_d n_d + U n_{d\uparrow} n_{d\downarrow}, \tag{1.6}$$

While one may note similarities with Hamiltonian (1.1) introduced for the description of the QD, in contrast, Hamiltonian 1.6 describes a single impurity level $|d\rangle$ with energy ϵ_d, with an on-site Coulomb repulsion U depending on the filling of $|d\rangle$. Hence, in the atomic limit there are only **four quantum states** available, namely the *empty state* $|d^0\rangle$ and the *doubly occupied state* $|d^2\rangle$, with energy $E(d^0) = 0$ and $E(d^2) = 2\epsilon_d + U$ respectively, which are non-magnetic, and the *Kramer's magnetic doublet* $|d^1\sigma\rangle$, for a single occupation with spin $\sigma = \uparrow, \downarrow$ and energy $E(d^1) = \epsilon_d$, as summarized below:

empty state:	$\lvert d^0\rangle$	$E(d^0) = 0$	non magnetic
doubly occupied state:	$\lvert d^2\rangle$	$E(d^2) = 2\epsilon_d + U$	
Kramer's doublet:	$\lvert d^1 \uparrow\rangle, \lvert d^1 \downarrow\rangle$	$E(d^1) = \epsilon_d$	magnetic

In order to derive the condition under which a magnetic moment is well defined, one considers the cost of charge fluctuations corresponding to the addition or the removal of an electron from the magnetic (ground) state $|d^1\sigma\rangle$, and impose it to be positive. Considering the **removal** process yields

$$|d^1\rangle \rightarrow |d^0\rangle \;:\; \Delta E = E(d^0) - E(d^1) = -\epsilon_d > 0, \tag{1.7}$$

while the **addition** one yields instead

$$|d^1\rangle \rightarrow |d^2\rangle \;:\; \Delta E = E(d^2) - E(d^1) = \epsilon_d + U > 0. \tag{1.8}$$

Neglecting thermal fluctuations, i.e., $k_{\mathrm{B}}T \ll |\epsilon_d|, U$, the combination of the previous relations (1.7) and (1.8) leads to the condition

$$|\epsilon_d + U/2| < U/2, \tag{1.9}$$

under which a magnetic moment is well defined. If condition (1.9) is fulfilled, the ground state of the system has only one electron sitting on the impurity, otherwise, depending on the relative value of ϵ_d and U, the system is in a non-magnetic state with either none or two electrons sitting on the impurity. The previous consideration can be summarized in the phase diagram of the atomic limit of the AIM shown in the left panel of Fig. 1.5 (where we restricted ourselves to the case of repulsive interaction $U > 0$).

The non-interacting limit: virtual bound-states. It is also interesting to understand the interplay between a non-interacting localized state with energy ϵ_d and a Fermi sea of delocalized electrons, which is described by the following Hamiltonian

$$\mathcal{H}_{resonance} = \sum_{k\sigma} \epsilon_{k\sigma} n_{k\sigma} + \sum_{k\sigma} V_k (c^{\dagger}_{k\sigma} d_{\sigma} + \mathrm{h}.c.) + \epsilon_d n_d. \tag{1.10}$$

Here, the effect of the hybridization processes is to broaden the localized impurity state $|d\rangle$, and to give rise to a resonance (or a *virtual bound-state*) of width Δ, given by the Fermi's golden rule

$$\Delta = \pi \sum_k |V(k)|^2 \delta(\epsilon_k - \epsilon_d), \tag{1.11}$$

which corresponds to an average of the conduction band DOS $\rho(\epsilon) = \sum_k \delta(\epsilon_k - \epsilon)$ at energy ϵ_d, weighted with the (modulus square of the) hybridization amplitude.
The previous expression can be derived considering the scattering process of the (non-interacting) localized level by the conduction electrons. In terms of Feynman diagrams, the bare propagators for the impurity and the conduction electrons can be represented (in Fourier space) as follows

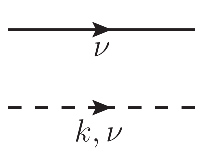

$$\begin{aligned} G^0(\nu) &= \frac{1}{\nu - \epsilon_d}. \\ G^0(k,\nu) &= \frac{1}{\nu - \epsilon_k}, \end{aligned} \tag{1.12}$$

In this formalism, the hybridization process can be represented as an off-diagonal scattering that allows impurity and conduction electron to transform one into each other

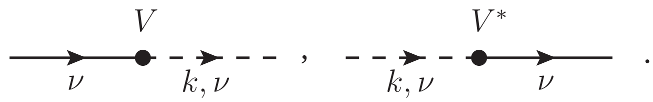

(1.13)

The process of an electron to hop from the impurity state into the conduction band and back to the impurity can be associated to an effective scattering potential for the localized electrons

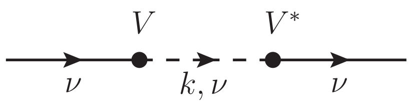

$$= \frac{|V(k)|^2}{\nu - \epsilon_k}, \tag{1.14}$$

where the frequency dependence implies the scattering potential to be retarded in time. This reflects the fact that impurity electrons are allowed to spend a lapse of time in the conduction band before tunneling back to the impurity. Multiple scattering processes off this potential result logically in a *dressed* propagator of the impurity electrons

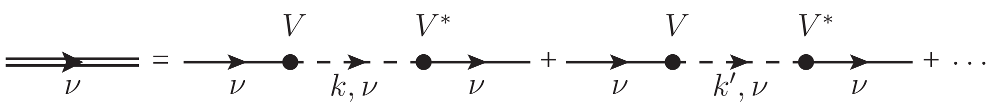

(1.15)

and the exact resummation of the infinite series of scattering diagrams yields the Dyson equation for the impurity propagator

$$G_d(\nu) = \frac{1}{\nu - \epsilon_d - \Sigma(\nu)}, \tag{1.16}$$

where the *purely local* self-energy is given by the summation over the independent momenta of the intermediate (virtual) states

$$\Sigma(\nu) = \sum_k \frac{|V(k)|^2}{\nu - \epsilon_k}. \tag{1.17}$$

For the sake of simplicity, in the following we shall ignore any momentum dependence of the hybridization amplitude, i.e., $V(k) = V^*(k) = V$, so that an analytical expression for the self-energy can be derived. Substituting the discrete sum over the momentum with an energy integral over the conduction band DOS yields

$$\Sigma(\nu) = \int d\epsilon\, \rho(\epsilon) \frac{V^2}{\nu - \epsilon} = \int d\epsilon\, \frac{1}{\pi} \frac{\Delta(\epsilon)}{\nu - \epsilon}, \tag{1.18}$$

where we have defined the *hybridization function* $\Delta(\epsilon) = \pi\rho(\epsilon)V^2$. In the complex frequency plane, the self-energy $\Sigma(\nu)$ has a branch cut along the real axis, with a discontinuity in its imaginary part

$$\mathrm{Im}\Sigma(\nu) = \int d\epsilon\, \frac{1}{\pi}\, \Delta(\epsilon)\, \overbrace{\mathrm{Im}\frac{1}{\nu - \epsilon \pm \imath 0^+}}^{\mp\imath\pi\delta(\nu-\epsilon)} = \mp\Delta(\nu), \tag{1.19}$$

where the $\pm$ signs correspond, to the usual definition of the advanced and retarded self-energy, respectively [67] . If we consider the case of a featureless conduction band, characterized by flat DOS symmetric with respect to the Fermi energy ϵ_F, i.e., $\rho(\epsilon) = 1/2D$, where D is the half-bandwidth, then

$$\Sigma(\nu) = \frac{\Delta}{\pi}\int_{-D}^{D} d\epsilon\, \frac{1}{\nu \pm \imath 0^+ - \epsilon} = \frac{\Delta}{\pi}\ln\left|\frac{\nu + D}{\nu - D}\right| \mp \imath\Delta\Theta(D - |\nu|), \tag{1.20}$$

where $\Theta(\cdot)$ is the Heaviside step function. The imaginary part of the self-energy determines the branch cut, which can be non-zero only in an region of the complex plane where also the hybridization function is non-zero, while the real part, becomes negligible in the broad band limit, i.e., $\mathrm{Re}\Sigma(\nu) = O(\nu/D)$. Considering the constant contribution of the real part of the self-energy as a chemical potential shift, and absorbing it in the definition of the energy of the impurity level: $\epsilon_d \to \epsilon_d - \mu$, the impurity propagator can be written as

$$G_d(\nu) = \frac{1}{\nu - \epsilon_d - \imath\Delta}, \tag{1.21}$$

yielding the spectral function

$$A_d(\nu) = -\frac{1}{\pi}\mathrm{Im}G_d^r(\nu) = \frac{1}{\pi}\frac{\Delta}{(\nu - \epsilon_d)^2 + \Delta^2}. \tag{1.22}$$

The latter corresponds to a virtual bound-state with a Lorentzian profile around ϵ_d and characterized by a finite lifetime given by $\tau_{\text{vbs}} = \hbar/\Delta$, where $\hbar$ is the reduced Plank's constant. The latter result can be extended to any hybridization function, provided it is slowly varying over the width of the resonance.

Mean-field solution. So far we have understood the role of the Coulomb interaction and of the hybridization when considered separately, analyzing two limiting cases of the AIM. However, to understand their interplay is way more challenging. According to Landau's Fermi Liquid (FL) theory, the excitation spectrum of a metal can be adiabatically connected to the one of a non-interacting Fermi gas. This leads to an apparent inconsistency: from the adiabatic point of view, the ground state of the AIM has a FL nature, while, in the atomic limit, where the interaction U much larger than the hybridization, one would expect the formation of a magnetic moment. Therefore there must be a crossover scale, separating the FL and the local moment phases. In this respect, it was shown by Anderson, within the framework of a Hartree mean-field approach [64], that the system will develop a local magnetic moment provided the Coulomb interaction is larger than a critical value $U > U_c = \pi\Delta$. Though being an over-simplified description of the magnetic moment, the mean-field solution provides a qualitative understanding of the phenomenon, that can be briefly sketched in the following. In the Hartree mean-field approximation, one can decompose the interaction term as

$$U\langle n_{d\uparrow}n_{d\downarrow}\rangle \to U\langle n_{d\uparrow}\rangle n_{d\downarrow} + Un_{d\uparrow}\langle n_{d\downarrow}\rangle + o(\delta n_d^2), \tag{1.23}$$

which physically corresponds to neglect spatial fluctuations. Under this condition, the interaction only produces a spin-dependent shift of the impurity level

$$\epsilon_{d\sigma} = \epsilon_d + U\langle n_{d-\sigma}\rangle. \tag{1.24}$$

According to the Friedel's sum rule [63], the number of localized electrons trapped inside the resonance, at $k_B T \ll \Delta$, is connected to the **scattering phase shift** $\eta_{d\sigma}$ by the relation

$$\langle n_{d\sigma} \rangle = \int_{-\infty}^{0} d\epsilon \rho_{d\sigma}(\epsilon) = \frac{1}{\pi}\eta_{d\sigma} = \frac{1}{\pi}\cot^{-1}\left(\frac{\epsilon_d + U\langle n_{d-\sigma}\rangle}{\Delta}\right), \tag{1.25}$$

yielding a relation that couples the average occupation of opposite spin polarization. In order to proceed, it is convenient to rewrite it in terms of the occupation $n_d = \sum_\sigma \langle n_{d\sigma}\rangle$ and the magnetization $m_d = \langle n_{d\uparrow}\rangle - \langle n_{d\downarrow}\rangle$ yielding the mean-field equations

$$n_d = \frac{1}{\pi}\sum_{\sigma=\pm 1} \cot^{-1}\left(\frac{2\epsilon_d + U(n_d - \sigma m_d)}{2\Delta}\right), \tag{1.26a}$$

$$m_d = \frac{1}{\pi}\sum_{\sigma=\pm 1} \sigma \cot^{-1}\left(\frac{2\epsilon_d + U(n_d - \sigma m_d)}{2\Delta}\right). \tag{1.26b}$$

Hence, the critical value of the interaction U_c is obtained performing the limit $m_d \to 0^+$ in Eq. (1.26a), resulting in the self-consistent condition

$$\frac{\pi n_d}{2} = \cot\left(\frac{\epsilon_d + U_c n_d}{\Delta}\right). \tag{1.27}$$

Linearizing Eq. (1.26b) with respect to m_d yields

$$1 = \frac{U_c}{\pi\Delta}\sin^2\left(\frac{\pi n_d}{2}\right), \tag{1.28}$$

so that at half-filling ($n_d = 1$), it simplifies to

$$1 = \frac{U_c}{\pi\Delta}. \tag{1.29}$$

Below the critical value of the Coulomb interaction U_c the mean-field equations (1.26) are consistent only for $\langle n_{d\uparrow}\rangle = \langle n_{d\downarrow}\rangle$, and the system is a FL with a Lorentzian DOS, described by Eq. (1.22). Above U_c the equations admit two more solutions, corresponding to a finite value of the magnetization m_d. For the latter solutions, the DOS shows two Lorentzian peaks, separated by a magnetization gap $\Delta_m = 2Um_d$

$$A_d(\nu) = -\frac{1}{\pi}\sum_\sigma \frac{\Delta}{(\nu - \epsilon_d - \sigma U m_d)^2 + \Delta^2}, \tag{1.30}$$

leading to the mean-field phase diagram of the AIM, shown in the right panel of Fig. 1.5. While in the atomic limit a local magnetic moment develops at any finite value of the interaction U, provided the condition (1.9) is fulfilled, in the mean-field solution it happens only above a critical value of the interaction, determined by the microscopic details of the hybridization between the impurity and the host conduction electrons.

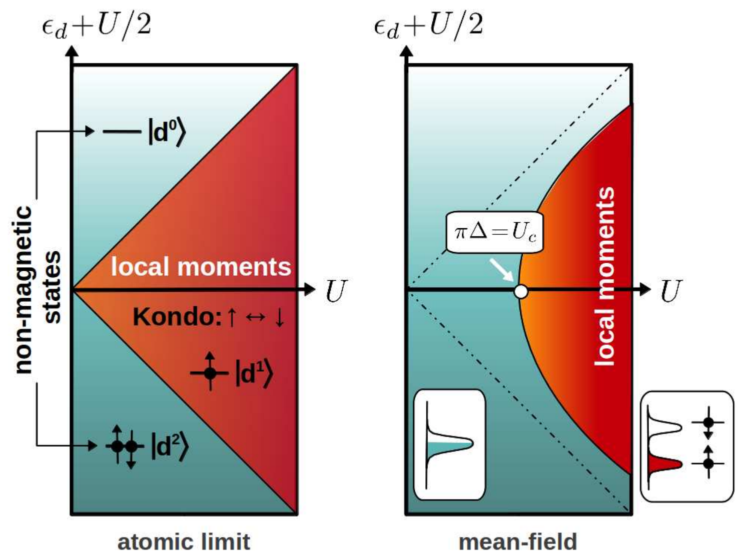

Figure 1.5: Phase diagram of the AIM in the atomic limit (left panel) and within the mean-field approximation (right). In the atomic limit the single particle states are well defined, and a local magnetic moment is formed provided the condition (1.9) is fulfilled. On the other hand, the interplay between the interaction and the hybridization sets $U_c = \pi\Delta$ as a threshold for the formation of the local moment, associated to a finite magnetization gap. Adapted after Ref. [66].

Relation with the Kondo model. The mean-field solution of the AIM provides a qualitative understanding of the behavior of magnetic impurities within a metallic alloy. It provides a clear example for the generation of a new effective energy scale from the bare ones. In fact, the condition for the formation of a local magnetic moment originates from the interplay between the local Coulomb interaction and the impurity-host hybridization. As both the ionic potential, determining the hybridization amplitude V, as defined by relation (1.5), and the strength of the Coulomb repulsion can vary substantially within different atomic species, the critical condition for the formation of a magnetic moment is not always fulfilled. However, within the mean-field description, the formation of the magnetic moment is associated to a spontaneous symmetry breaking, and to a finite magnetization. While this may be a reasonable description for an ensemble of magnetic atoms, which develop effective long range ferromagnetic correlations, if magnetic impurities are diluted in a metallic host, magnetic correlations between the impurities are expected to be negligible (if this condition is not met *a priori*, the single impurity Anderson model cannot provide a reasonable description of the system, see also Sec. 1.2.3).

The scattering of the conduction electrons off a single magnetic impurity leads to a completely different physics: the Kondo effect, which is a non-perturbative, many-body effect associated to a characteristic energy scale $k_\mathrm{B}T_\mathrm{K}$. As already mentioned, the earliest experimental observation that motivated research interest in this direction, and eventualy the discovery of the Kondo effect, was related to an **anomalous resistivity**, increasing logarithmically at low temperature, in the presence of magnetic impurities dilute in a metallic host.

In the temperature dependence of the resistivity in a metal, one can identify several contribution with different origins, leading to the following behavior

$$\rho(T) = \rho_0 \Big[1 + \alpha \log\Big(\frac{T}{T_{\mathrm{K}}}\Big) + \dots\Big] + \gamma T^2 + \lambda T^5. \tag{1.31}$$

The constant contribution ρ_0 is the one due to electron scattering off (non-magnetic) defects, vacancies, or impurities, which prevents the resistivity to vanish even in the $T = 0$ limit. The temperature dependent contributions, on the other hand, are determined by electron-electron (i.e., like in the Fermi liquid theory $\propto T^2$), or by electron-phonon ($\propto T^5$) scattering processes. The anomalous contribution, which can be shown to depend on an universal function of T/T_{K}, is instead given by scattering processes due to magnetic impurities, as discussed in the following. The relative magnitude of the prefactors is, obviously, material dependent.

In the AIM (1.4) one can identify a low-energy subspace d^1 and a high-energy subspace, containing valence fluctuation involving the d^0 and d^2 states. The hybridization term is an off-diagonal term that mixes the subspaces, allowing charge fluctuations. As was shown by Schrieffer and Wolf [68], the Anderson Hamiltonian can be reduced to a block diagonal form through a canonical transformation, requiring all first order terms in V to be vanishing. This is equivalent to a renormalization approach, where the high-energy degrees of freedom, corresponding to the valence fluctuations, are traced out of the Hilbert space, leading to the formation of a new effective energy scale, which is a function of the bare Coulomb interaction and the hybridization.

While a detailed derivation is beyond the scope of this work, it is interesting to discuss the physical implications of the Schrieffer-Wolf transformation, resulting in a low-energy Hamiltonian[2] which reads

$$\mathcal{H}_{\mathrm{Kondo}} = \sum_{k\sigma} \epsilon_k c^\dagger_{k\sigma} c_{k\sigma} + \sum_{k\sigma k'\sigma'} J_{k,k'}\, c^\dagger_{k\sigma} \boldsymbol{\tau}_{\sigma\sigma'} c_{k'\sigma'} \cdot \boldsymbol{S}_d, \tag{1.32}$$

where $\boldsymbol{\tau} = (\tau_x, \tau_y, \tau_z)$ are the Pauli matrices. The model associated to Hamiltonian (1.32) is commonly referred to as the Kondo model, and describes the dynamics of the local magnetic moment $\boldsymbol{S}_d$, provided by the unpaired spin of the impurity (as its occupancy in the low-energy model is constrained to be $n_d = 1$) coupled to the spin density of the conduction electrons via an **exchange interaction**

$$J_{k,k'} = V_k\, V^*_{k'} \Big[\frac{1}{\epsilon_d + U} - \frac{1}{\epsilon_d}\Big]. \tag{1.33}$$

Note that the interaction parameter is quadratic in the hybridization and involves the excitation energies ϵ_d and $\epsilon_d + U$ of the $|d^0\rangle$ and $|d^2\rangle$ valence states of the AIM in the atomic limit.

Within this model one can compute the resistivity due to scattering processes involving the impurity and the conduction electrons within perturbation theory, that we briefly discuss below. We restrict ourselves, for the sake of simplicity, to the case $S_d = 1/2$ (i.e., two-fold degeneracy) and assuming J to be a constant. The lowest order involves processes in which, e.g., a

[2]apart from a residual one-particle scattering potential that has not been explicitly considered here.

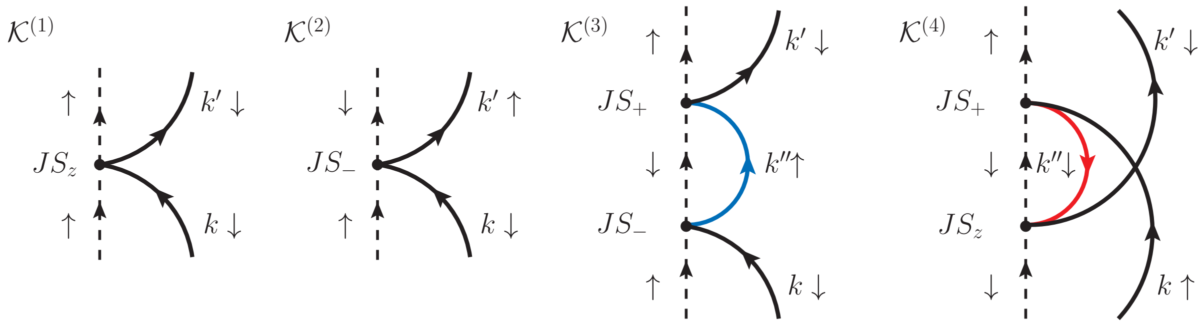

Figure 1.6: Representative Feynman diagram $\mathcal{K}^i$ corresponding to lowest order $(i = 1, 2)$ and higher order $(i = 3, 4)$ scattering processes between the impurity and the conduction electron in the Kondo model. The scattering amplitudes $J^{(1)}$ (1.34) and $J^{(2)}$ (1.35) considered in the text correspond to the above diagrams labeled $\mathcal{K}^1$ and $\mathcal{K}^3$, respectively. The blue (red) fermionic line describes the propagation of the virtual conduction electron (hole) involved in the spin-flip process. Finally, each interaction vertex in the above processes can be elegantly expressed in terms of the corresponding z-component (S_z), *rising* (S_+) and *lowering* (S_-) operators of the impurity spin.

conduction electron in the initial state $|k \downarrow\rangle$ scattering off an impurity with $S_d^z = \uparrow$ to the final state $|k' \downarrow\rangle$, whose diagrammatic representation is shown in Fig. 1.6 (diagram $\mathcal{K}^{(1)}$). Under the above assumptions, the scattering amplitude for such a process reads

$$J^{(1)} := J(k \downarrow, \uparrow \rightarrow k' \downarrow, \uparrow) = J. \tag{1.34}$$

The evaluation of all the topologically distinct lowest order diagrams, taking the trace over the conduction electron spin as well as on the impurity state, leads, however, to a temperature *independent* contribution to the resistivity. Hence, Kondo [20] considered a higher order correction, including processes involving a *spin-flip* of the impurity in a virtual state, whose diagrammatic representation is shown in Fig. 1.6 (diagram $\mathcal{K}^{(3)}$), associated to the scattering amplitude

$$J^{(2)} := \sum_{k''} J(k \downarrow, \uparrow \rightarrow k'' \uparrow, \downarrow) J(k'' \uparrow, \downarrow \rightarrow k' \downarrow, \uparrow) \frac{1 - f(\epsilon_{k''})}{\nu - \epsilon_{k''}}. \tag{1.35}$$

In expression (1.35), the factor $1 - f(\epsilon_q)$ takes into account the probability of the virtual state involved in the spin-flip process to be unoccupied. Below we show that it leads to a temperature-dependent scattering rate and eventually to the anomalous resistivity. However, a rigorous derivation, would require the evaluation of all topologically distinct diagrams associated to the process, involving the Matsubara sum of the Green's function of the virtual state $G(\nu, \epsilon_{k''})$. Replacing the sum over the virtual momentum k'' in the scattering amplitude (1.35) with an energy integral using the DOS $\rho(\epsilon_k'')$ we obtain, at low temperatures

$$J^{(2)} = J^2 \int d\epsilon_{k''} \frac{1 - f(\epsilon_{k''})}{\nu - \epsilon_{k''}} \rho(\epsilon_{k''}) \approx J^2 \rho \int_{\epsilon_F}^{D} d\epsilon_{k''} \frac{1}{\nu - \epsilon_{k''}}, \tag{1.36}$$

where we assumed $\rho(\epsilon_k'')$ to be a constant, symmetric, and characterized by a half-bandwidth D.

Evaluating the integral eventually yields

$$J^{(2)} = J^2 \rho \log\left|\frac{\nu - \epsilon_F}{\nu - D}\right|. \tag{1.37}$$

The scattering rate, is proportional to the square of the total scattering amplitude

$$\frac{1}{\tau_{\text{imp}}} \propto |J^{(1)} + J^{(2)}|^2 = J^2 + 2J^3\rho \log\left|\frac{\nu - \epsilon_F}{\nu - D}\right| + \mathcal{O}\big(J^4\big). \tag{1.38}$$

As only the electrons within a window $k_{\mathrm{B}}T$ around the Fermi surface will contribute to the resistivity, we have $|\nu - \epsilon_F| \approx k_{\mathrm{B}}T$, eventually yielding

$$\rho_{\text{imp}} = \rho_0 \left[1 + 2J\rho \log\left|\frac{k_{\mathrm{B}}T}{D - \epsilon_F}\right|\right], \tag{1.39}$$

where the prefactor $\rho_0 \propto J^2$. The sign of the exchange interaction determines the low-temperature behavior of the resistivity: if $J > 0$ the interaction favor the parallel alignment of the local magnetic moment to the spin density of the conduction electrons (ferromagnetic exchange), while if $J < 0$ if favors an antiparallel alignment (antiferromagnetic exchange). Only in the latter case, the scattering processes involving a *spin-flip* determine the anomalous contribution to the resistivity, providing an explanation for the resistance minimum. Similar corrections also arise in other experimentally accessible quantities, as the *magnetic susceptibility* and the *specific heat*.

However, the effective temperature-dependent exchange coupling $J_{\text{eff}}(T)$ *diverges as* $T \rightarrow 0$, and the limit of validity of the above results, as expected within a perturbative approach, is set by the condition

$$2J\rho \log\left|\frac{k_{\mathrm{B}}T}{D - \epsilon_F}\right| \sim 1, \tag{1.40}$$

implying higher order diagrams to become non-negligible, and corresponding to an energy scale given by

$$k_{\mathrm{B}}T_{\mathrm{K}} \sim (D - \epsilon_F)\, \mathrm{e}^{-1/2|J|\rho}, \tag{1.41}$$

which defines the **Kondo temperature**. Extending Kondo's calculations to obtain a satisfactory solution below T_{K}, became known as the *Kondo problem*. Among the most important contributions in this direction we recall the works of Abrikosov & Suhl [69, 70], and Nozières [71]. Further understanding of the Kondo problem was provided by Anderson's *poor man's scaling* [72], which allowed to show that the local moment of the impurity is *screened* by the conduction electrons, as their spin degrees of freedom become entangled. The resulting state is non-magnetic and for $T \rightarrow 0$ the system displays a Pauli temperature independent susceptibility. Eventually, the non-perturbative **renormalization group** approach proposed by Wilson [108] to confirmed this picture. Within the Kondo model, the enhanced contribution to the resistivity, magnetic susceptibility an the specific heat, stem from a narrow quasi-particle peak which develops below T_{K}: the resonance is known as the **Abrikosov-Suhl resonance**, but is often referred to as the **Kondo resonance**.

Interestingly, this lead to a completely different physics in QDs, where electrons can only tunnel through a narrow region due to the confining potential. Here, instead of increasing the resistivity, the presence of a Kondo resonance determines an *enhancement* of the conductance, allowing electrons to overcome the Coulomb blockade.

1.2.3 Beyond impurity models: challenges & open questions

As we have seen so far, the interplay between strong electronic correlations and hybridization in the AIM is qualitatively well-understood, and a (numerical) solution of the AIM is reliably accessible (in this respect see also Sec. 2.1). Hence, when the system is expected to behave as QD, i.e., is dominated by charge and energy quantization effects and only few-orbitals contribute to determine the low-energy physics, a reliable theoretical description and a satisfying agreement with experiments is possible. Whether this condition is fulfilled or not strongly depends on the relevant energy scales in the system under investigation. However, it seems to be the case in several cases of interest, e.g., as shown in the recent results reported in Refs. [74, 75, 76, 57], just to mention a few.

We have also seen that, beside semiconductor (mostly Si-based) SSDs, modern technologies also allow to grow, synthesize, and manipulate high-quality nanoscopic systems, ranging from nano particles to nano-wires and cluster, but also to trap few or individual molecules within quantum junctions. As the complexity of experimentally available systems increases, so does also their potential. In particular, the complex interplay between electronic correlations and internal degrees of freedom of the nanostructure is responsible for a variety of physical phenomena, which are interesting from the basic research point of view, and appealing for technological applications. Among those, are non-linear current-voltage characteristics, and electronic transitions to be triggered by means of weak external perturbation, e.g., mechanical stress, and electric or magnetic field.

The knowledge of the microscopic mechanism underlying correlation-driven phenomena may allow to improve the efficiency of existing devices, and possibly the discovery of novel physics. However, the present theoretical understanding, beyond the framework of the few relatively well-known models, of those properties is far from being satisfactory, and a comprehensive, and unified theory of strongly correlated nanoscopic structure is still lacking. In this respect, the challenges are mainly due to the many orbitals involved and with long-range fluctuations (of importance in critical phenomena). An interesting example in this context is represented by the Ruderman-Kittel-Kasuya-Yosida (RKKY) interaction [77, 78, 79], which is a non-local *indirect* magnetic echange correlating localized impurities. As for the Kondo temperature T_{K}, the typical scale associated to the RKKY exchange T_{RKKY}, is generated by the interplay between the bare local Coulomb interaction in the narrow impurity orbital, and the non-local hybridization processes between the impurity electrons and the delocalized conduction electrons. In the limit of low impurity concentration in the metallic host (dilute impurities) the impurity-impurity correlation is weak; otherwise the RKKY and the Kondo physics would compete in the intermediate-coupling regime, making the description of the system incredibly complex, but also incredibly fascinating.

1.3 Quantum transport

As we have seen, transport spectroscopy is a valuable experimental tool to investigate electronic structures, and excitation spectra of nanoscopic systems. Hence, one of the most important (and challenging) issues is the theoretical understanding of electronic transport through a nanoscopic conductor (be it a QD, a molecule or a cluster of atoms) bridging metallic electrodes. In this regime the typical Fermi wavelength λ_{F} is comparable to the size of the nanoscopic conductor $\mathcal{L}$, both being much smaller than the electronic coherence length l_ϕ, so that electronic transport is completely dominated by quantum effects. Moreover, both the atomic and the electronic structure of the conductor strongly influences the transport properties, which, on the other hand, also means that valuable information about the system can be inferred from electronic transport measurements. Early studies of quantum transport by Landauer [80] and later on by Büttiker [81] proposed a novel view of electronic conductance through a nanoscopic structure in terms of transmission. In former times in fact, the electrical conduction was treated within a semi-classical picture, electrons accelerated according to the Bloch's theorem by an external applied electric field, and equilibrium was restored due to momentum relaxation induced by (incoherent) scattering processes off impurities or lattice phonons. A purely quantum mechanical description of conductivity was proposed by Kubo, yet energy and particle conservation did not allow for dissipation effects beyond polarizability (linear response).

In the following the Landauer-Büttiker single-particle approach to conductance [80, 81] will be discussed within scattering theory. In the limit of infinitesimal bias voltage applied to the system, Landauer-Büttiker formula can also be derived within linear response theory in a Green's function formalism. Generalizations to interacting systems will also be discussed in this framework.

1.3.1 Landauer-Büttiker formalism

In the Landauer-Büttiker formalism, the nanoscopic conductor is regarded as a quantum mechanical scatterer of the electrons incoming from the leads and transport results from a diffusion process of charge carries due to a chemical potential (and therefore carrier concentration) gradient. Electrons are assumed to scatter only elastically inside the nanostructure, discarding inelastic processes due to, e.g. electron-phonon or electron-electron interactions. The above relations between the important length scales can be summarized as follows

$$a_0 \ll \lambda_{\mathrm{F}} \lesssim l_0 < \mathcal{L} < l_\phi \lesssim l_{\mathrm{in}}, \tag{1.42}$$

where a_0 is the Bohr radius, l_0 is the elastic mean-free path and l_{in} is the length scale related to the typical inelastic relaxation processes. Thus electronic transport, within Landauer-Büttiker formalism, emerge as a quantum mechanically coherent process and can be described in terms of non-interacting quasi-particles elastically scattered by the nanostructure.

The above condition defines the so-called **ballistic transport** regime. For the sake of completeness, we briefly discuss the other possible transport regimes, depending on the mutual relations of the characteristic lengths. In presence of multiple scattering events, i.e. $l_{\text{in}} < \mathcal{L}$, the transport is **diffusive**, and it is characterized by a reduced conductance with respect of the elastic one. Moreover in presence of multiple *coherent* scattering events inside the nanostructere, which means that $l_{\text{in}} \ll l_\phi \ll \mathcal{L}$ one can have electronic **localization** due to quantum interference at low temperatures which determines an increased resistivity. The classical **incoherent** regime and the standard relation for an ohmic resistor is finally recovered when $\mathcal{L} \gg l_{in}, l_\phi$.

Following Ref. [82], we consider a nanoscopic system divided, for convenience, into three regions: a central nanoscopic scattering region (S) connected via metallic leads to two reservoirs, to the left (L) and to the right (R), as schematically represented in Fig. 1.7.

In the ballistic regime ($\mathcal{L} \ll l_\phi, l_{\text{in}}$) the electron propagation within the sample is quantum mechanically coherent, i.e. electrons can be described by a wave packet with a definite phase. On the other hand, when transmitted to the reservoirs, one can safely assume the electrons to be thermalized at the temperature T and the chemical potential $\mu_{\text{L,R}}$ of the leads, and therefore described by the corresponding Fermi-Dirac distribution function. We will consider the electrons in the leads to propagate freely along the z direction, and to be confined in the transverse plane with respect to the propagation direction, giving rise to a quantized spectrum, whose energy eigenstates are labeled by the (set of) quantum number(s) n. Hence, the wavefunction of an electron propagating through the nanostructure can be written as a plane wave in the z-direction $\mathrm{e}^{\imath k_n z}$ modulated by a transverse wave-function $\Phi_n(x, y)$, as

$$\psi_{n;k_n}(x, y, z) = \Phi_n(x, y)\mathrm{e}^{\imath k_n z}, \tag{1.43}$$

where n labels an eigenmode of the L or R lead, so that k_n denotes the wavevector associated to the n-th eigenmode at a given energy E (see also Fig. 1.7). In the case of a real material, the wave function is modulated by the underlying lattice potential, according to the Bloch's

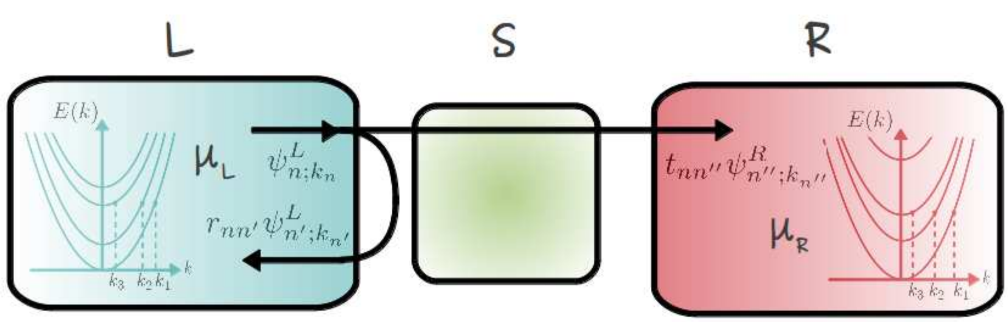

Figure 1.7: Schematic representation of electronic transport through a nanoscopic device: macroscopic charge reservoir are bridged by metallic leads (L and R) contacted to a scattering region (S). The electrons in the leads are thermalized at chemical potential μ_L and μ_R, respectively. The wavefunction $\psi^{\text{L}}_{n;k_n}$ incoming from L and characterized by wavevector k of eigenmode n, at energy $E(k)$, is partially reflected to a generic eigenmode of L (with probability $r^2_{nn'}(E)$) and partially transmitted to a generic eigenmode of R (with probability $t^2_{nn''}(E)$) through the scattering region S.

theorem, and the transverse eigenmodes correspond to the energy bands of the leads.

The **Landauer-Büttiker formula** expresses the conductance as the sum of the transmission probabilities $\mathcal{T}_n$ in all possible transmission *channels*

$$G = 2\frac{e^2}{h}\sum_n \mathcal{T}_n. \tag{1.44}$$

This suggests a **conductance quantization** with a conductance quantum $G_0 = 2e^2/h$, where the channels are identified with the quantized eigenmodes of the leads. In this respect, it can be shown, e.g., as in Ref. [83], that to each transverse mode there is an associated potential barrier in the propagation direction due to the kinetic energy bound in the transverse motion. Therefore only a finite number of modes with a barrier less than the Fermi energy E_F will contribute to the conductance. Since in general the transmission probability can assume any value between 0 and 1, conductance quantization will be observed only in particular geometries where the reflection is negligible, e.g., in the case of a quantum point contact (QPC). Conductance quantization has been experimentally reported [30, 84], and triggered theoretical speculation [85], providing strong evidences in support of the Landauer-Büttiker result.

In order to derive the Landauer-Büttiker formula (1.44), we define the current density associated with the propagating mode n as

$$j_n(k) = ev_n(k) = e\frac{1}{\hbar}\frac{\partial E_n}{\partial k}(k), \tag{1.45}$$

where the group velocity $v_n(k)$ of mode n, is given, within the Peierls approximation [86], by the derivative of the dispersion relation $E_n(k)$ of the electron in the lead. According to the previous assumptions, the incoming wave can only be scattered, via elastic processes, into states with the *same* energy E. Thus a wave with energy E incoming from the lead L will give rise to a coherent superposition of the form

$$\psi^{\mathrm{L}}_{n;k_n} + \sum_{n'\in\mathrm{L}} r_{nn'}(E)\psi^{\mathrm{L}}_{n';k_{n'}} + \sum_{n''\in\mathrm{R}} t_{nn''}(E)\psi^{\mathrm{R}}_{n'';k_{n''}}, \tag{1.46}$$

where $r_{nn'}(E)$ is the probability amplitude for an electron on mode n and energy E to be reflected into mode n' in the lead L, while $t_{nn''}(E)$ is the probability amplitude for the same mode to be transmitted into mode n'' in the lead R. The probability of an electron in mode n of the lead L, to be transmitted to *any* mode of the lead R through the scattering region S is, hence, given by $\sum_{n''}|t_{nn''}(E)|^2$, giving rise to a total current density

$$j^{\mathrm{L}}_n(k) = \sum_{n''\in\mathrm{R}} |t_{nn''}(E)|^2 j_{n''}(k_{n''}), \tag{1.47}$$

assuming the currents to be independent. The current flowing from the lead L to R is eventually obtained summing the current density $j^{\mathrm{L}}_n(k)$ over all possible modes of the left lead, up to the chemical potential μ_{L}, as

$$I^{\mathrm{L}} = \sum_{n\in\mathrm{L}}\int_{E_n(k)<\mu_{\mathrm{L}}} dk\; j^{\mathrm{L}}_n(k) = \sum_{n\in\mathrm{L}}\sum_{n''\in\mathrm{R}}\int_{-\infty}^{\mu_{\mathrm{L}}} dE\; \rho^{\mathrm{R}}_{n''}(E)|t_{nn''}(E)|^2 j_{n''}(k_{n''}), \tag{1.48}$$

in which the integral over the wavevector k is converted into an integral over the energy by means of the DOS $\rho^{R}_{n''}(E)$ projected onto the generic mode n'' of the lead R. As we are assuming a one-dimensional transport, the DOS of the leads is given by $\rho(E) = \frac{1}{2\pi}(dk/dE)$ and cancels exactly with the group velocity in the definition of the current density, so that

$$I^{\mathrm{L}} = \frac{e}{h} \sum_{n \in \mathrm{L}} \sum_{n'' \in R} \int_{-\infty}^{\mu_{\mathrm{L}}} dE \, |t_{nn''}(E)|^2 = \frac{e}{h} \sum_{n \in \mathrm{L}} \int_{-\infty}^{\mu_{\mathrm{L}}} dE \, \mathcal{T}^{\mathrm{L}}_{n}(E), \tag{1.49}$$

where

$$\mathcal{T}^{\mathrm{L}}_{n}(E) = \sum_{n'' \in \mathrm{R}} |t_{nn''}(E)|^2 \tag{1.50}$$

is the **transmission coefficient per conduction channel**. In a completely analogous way the electrons in the modes of the lead R up to the corresponding chemical potential μ_R give rise to a current flowing to the lead L

$$I^{\mathrm{R}} = \frac{e}{h} \sum_{n'' \in R} \int_{-\infty}^{\mu_{\mathrm{R}}} dE \, \mathcal{T}^{\mathrm{R}}_{n''}(E). \tag{1.51}$$

Here the transmission coefficient

$$\mathcal{T}^{\mathrm{R}}_{n''}(E) = \sum_{n \in \mathrm{L}} |t_{n''n}(E)|^2 \tag{1.52}$$

is analogously defined in terms of the probability amplitude for an electron with energy E to be transmitted from mode n'' in the lead R to mode n in the lead L. Due to time-reversal symmetry, $t_{nn''}(E)$ and $t_{n''n}(E)$ can differ only by a phase factor, so that the **transmission probability** $\mathcal{T}(E)$ is the same for the current generated from electrons injected into the L or R lead

$$\mathcal{T}(E) := \sum_{n \in \mathrm{L}} \mathcal{T}^{\mathrm{L}}_{n}(E) = \sum_{n \in \mathrm{L}} \sum_{n'' \in \mathrm{R}} |t_{nn''}(E)|^2 = \sum_{n'' \in \mathrm{R}} \sum_{n \in \mathrm{L}} |t_{n''n}(E)|^2 = \sum_{n'' \in \mathrm{R}} \mathcal{T}^{\mathrm{R}}_{n''}(E). \tag{1.53}$$

Moreover, denoting with N_{L} is the number of channels in the lead L, due to the conservation of the probability current the **reflection probability** for the electrons injected from the L reservoirs at some energy E is given by

$$R(E) = N_{\mathrm{L}} - \sum_{n \in \mathrm{L}} \mathcal{T}^{\mathrm{L}}_{n}(E) = N_{\mathrm{L}} - \sum_{n \in \mathrm{L}} \mathcal{T}^{\mathrm{R}}_{n}(E), \tag{1.54}$$

where the last equality follows from Eq. (1.53). Therefore the contribution to the current of the electrons incoming from the L reservoir cancels out with the one of the *backscattered* electrons and the transmitted electrons incoming from the right reservoir. The same happens in the lead R as well. This means that the net current at some energy E flowing through the device is zero when electrons are injected from both reservoirs at that energy.

Hence, in order to have current flowing through the nanostructure, one has to apply a bias voltage is, so that, e.g. $\mu_{\mathrm{L}} = \mu_{\mathrm{R}} + eV < \mu_{\mathrm{R}}$, and only electrons with energy larger than μ_{R} will effectively contribute to transport, yielding a net current

$$I(V) = \frac{e}{h} \sum_{n \in \mathrm{L}} \int_{\mu_{\mathrm{R}}}^{\mu_{\mathrm{L}}} dE \, \mathcal{T}_{n}(E), \tag{1.55}$$

and the corresponding conductance, calculated taking the derivative of the current with respect of the bias voltage

$$G(V) = \frac{\partial I}{\partial V} = \frac{e^2}{h} \sum_{n \in \mathrm{L}} \mathcal{T}_n(eV). \tag{1.56}$$

At low bias $|eV_{\mathrm{SD}}| = |\mu_{\mathrm{L}} - \mu_{\mathrm{R}}| \ll \mu$, with μ being the equilibrium chemical potential, and at low temperatures one can assume $\mathcal{T}_n$ to be energy independent, so that one can expand around $E \approx \mu$, yielding

$$I(V) = \frac{e^2}{h} V \sum_{n \in \mathrm{L}} \mathcal{T}_n(\mu) \quad \xrightarrow{\text{hence}} \quad G(V) = \frac{e^2}{h} \sum_{n \in \mathrm{L}} \mathcal{T}_n(\mu). \tag{1.57}$$

In this notation the spin degree of freedom is contained in the mode index n, but for spin-degenerate systems the transmission probability is the same for both spin channels yielding an additional factor 2, yielding the Landauer-Büttiker formula (1.44) with the conductance quantum $G_0 = 2e/h$ as a prefactor. As the transmission coefficient is an hermitian matrix, the sum over all possible channels is often expressed in terms of a trace

$$\sum_n \mathcal{T}_n = \sum_n \Big(\sum_m t^*_{nm} t_{mn} \Big) = \sum_n (\hat{t}^\dagger \hat{t})_{nn} \tag{1.58}$$

so that the expression for the conductance reduces to

$$G = 2 \frac{e^2}{h} \mathrm{tr}(\hat{t}^\dagger \hat{t}), \tag{1.59}$$

The knowledge of the transmission coefficient (or equivalently, of the transmission matrix) is therefore of fundamental importance as it allows to compute the electrical conductance and the (I/V) characteristics of a nanoscopic conductor.

Where does the resistance come from? If the inelastic relaxation length ℓ_{in} is much larger than the size $\mathcal{L}$ of the scattering region, there is no mechanism for energy dissipation, and one would expect the conductance to be infinite. Instead, the presence of boundaries determines the existence of eigenmodes. The number of eigenmodes that can be activated at energy E is given by $M(E) = \sum_n \Theta(E - E_n)$, and each of them is occupied according to the Fermi distribution function $f(\epsilon_n)$. The resistance cn be separated into two parts as

$$G^{-1} = \frac{h}{2e^2 MT} = \frac{h}{2e^2 M} + \frac{h}{2e^2 M} \frac{1-T}{T}, \tag{1.60}$$

where in the last equality the former is the *contact resistance*, generated by the transitions to the leads, and the latter represents the residual *scatterer resistance*, generated by scattering processes within the $\mathcal{S}$ region. It follows that a *quantum resistance* $R_0 := h/e^2$ is associated to each mode, setting an upper bound to the conductance, corresponding to the case of negligible backscattering, i.e., $1 - T = 0$.

Interestingly, the resistance can be obtained also directly from the Heisenberg uncertainly principle: $\Delta E \Delta t = (e^2/C)RC > h$, where ΔE induced by charge fluctuations is given by the charging energy e^2/C and Δt is given by the RC-time (i.e., the time required to charge or discharge a capacitor C through a resistor R). It follows that $R > R_0$, i.e., the resistance must be larger than the quantum resistance in order to reduce the uncertainty on energy (well defined charge state in the system).

1.3.2 Extended interacting systems: Linear Response conductance

The merit of Landauer was to introduce a completely new point of view, describing charge transport in terms of transmission. However, as already mentioned, in the *non*-ideal case the Landauer-Büttiker assumption, that the transmission is reduced only due to *elastic* backscattering from the barrier, breaks down for an interacting system at finite temperature.
Extension to the case of an interacting region has been carried out by Meir & Wingreen [87] within the Keldysh formalism [88]. The Meir-Wingreen formula does not imply any approximation, provided the knowledge of the *exact* Green's function of the interacting region. While this i not a trivial requirement in the general case of an extended interacting region, in some special cases, e.g., for the AIM, the Green's function can be obtained, and due to vanishing vertex corrections, the conductance can be expressed in terms of the one-particle spectral function of the interacting region [87], as also discussion at the end of this section.
Following Oguri [89], we derive within the Kubo formalism the expression of the equilibrium (finite temperature) linear conductance for an extended interacting system, as well as the corresponding vertex corrections. In this respect, we conveniently divide the system into three regions: a scattering region (S) bridging a left (L) and a right (R) non-interacting leads, as shown in Fig. 1.8. The scattering region consists of N sites coupled via an interaction $U_{j_1 j_2; j_3 j_4}$,

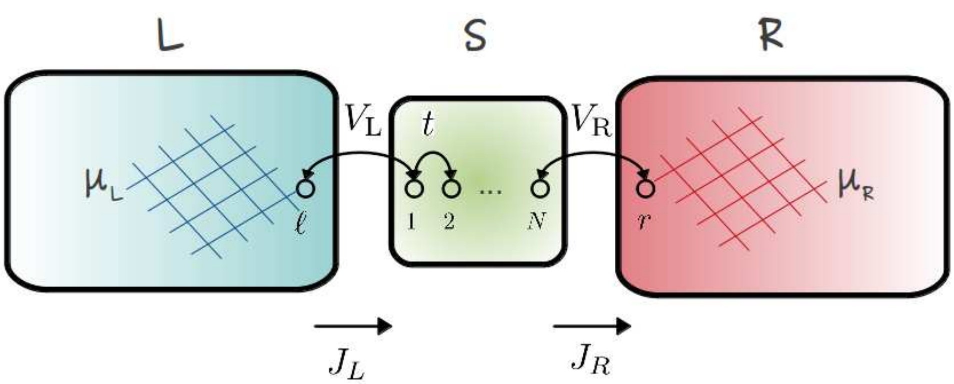

Figure 1.8: Schematic representation of electronic transport through a naoscopic device: an interacting scattering region (S) bridging non-interacting leads (L and R). The sites belonging to the scattering region are labeled $i = 1...N$, and are connected by hopping channels t_{ij}. Sites 1 and N are also connected via hybridization channels $V_{\mathrm{L,R}}$ to the interface sites ℓ and r, belonging to the L and R lead, respectively. The arrow above the current $J_{\mathrm{L,R}}$ indicates the direction of a positive current.

while the leads are assumed to be infinitely extended and characterized by a continuum spectrum. The Hamiltonian of the system reads

$$\mathcal{H} = \mathcal{H}_{\mathrm{S}} + \mathcal{H}_{\mathrm{L}} + \mathcal{H}_{\mathrm{R}} + \mathcal{H}_{\mathrm{hyb}}, \tag{1.61}$$

where the scattering region is described within a tight-binding lattice in the presence of an electron-electron interaction

$$\mathcal{H}_{\mathrm{S}} = \sum_{i,j\in \mathrm{S}} \sum_{\sigma} t_{ij} c^{\dagger}_{i\sigma} c_{j\sigma} - \mu \sum_{i\in \mathrm{S}} \sum_{\sigma} n_{i\sigma} + \frac{1}{2} \sum_{\{j\}\in \mathrm{S}} \sum_{\sigma\sigma'} U_{j_1 j_2; j_3 j_4} c^{\dagger}_{j_4\sigma} c^{\dagger}_{j_3\sigma'} c_{j_2\sigma'} c_{j_1\sigma}, \tag{1.62}$$

and it is connected to the tight-binding representation of the L and R non-interacting leads

$$\begin{aligned} \mathcal{H}_{\mathrm{L}} &= \sum_{i,j\in \mathrm{L}} \sum_{\sigma} t^{\mathrm{L}}_{ij} c^{\dagger}_{i\sigma} c_{j\sigma} - \mu_L \sum_{i\in \mathrm{L}} \sum_{\sigma} n_{i\sigma}, \\ \mathcal{H}_{\mathrm{R}} &= \sum_{i,j\in \mathrm{R}} \sum_{\sigma} t^{\mathrm{R}}_{ij} c^{\dagger}_{i\sigma} c_{j\sigma} - \mu_R \sum_{i\in \mathrm{R}} \sum_{\sigma} n_{i\sigma}, \end{aligned} \tag{1.63}$$

via the following hybridization term

$$\mathcal{H}_{\mathrm{hyb}} = -\sum_{\sigma} V_{\mathrm{L}} (c^{\dagger}_{1\sigma} c_{\ell\sigma} + c^{\dagger}_{\ell\sigma} c_{1\sigma}) - \sum_{\sigma} V_{\mathrm{R}} (c^{\dagger}_{r\sigma} c_{N\sigma} + c^{\dagger}_{N\sigma} c_{r\sigma}). \tag{1.64}$$

Here $c^{\dagger}_{i\sigma}$ ($c_{i\sigma}$) creates (annihilates) an electron on site i and spin σ, and $n_{i\sigma} = c^{\dagger}_{i\sigma} c_{i\sigma}$. The sites within each region are connected via hopping channels t_{ij} or $t^{\mathrm{L};R}_{ij}$ corresponding to the parameters of the tight-binding representation of the S, L, and R regions; however, in order to obtain the results presented below, no assumption is needed on the actual tight-binding parameters. The mixing between those regions is provided by the hybridization amplitudes $V_{\mathrm{L,R}}$ connecting the interface sites of the L and R leads (labeled ℓ and r, respectively) with the interface sites in the scattering region (labeled $i = 1, N$); the remaining sites of the scattering region $i = 2, \ldots, N-1$ do not hybridize. We denote with μ_L, μ_R and μ the chemical potential of the L and R leads, and of the scattering region, respectively. The interaction $U_{j_1 j_2; j_3 j_4}$ could in principle be a general interaction fulfilling time reversal symmetry [89], and in particular the derivation holds in the case of the local Hubbard interaction.

The **conductance** is defined within linear response theory by means of the Kubo formula [90] an obtained from the linear contribution of the imaginary part of the current-current retarded correlation function as

$$G = e^2 \lim_{\Omega\to 0} \frac{K^r_{\alpha\alpha'}(\Omega) - K^r_{\alpha\alpha'}(0)}{\imath\Omega}, \tag{1.65}$$

which can be calculated performing the *analytic continuation* of the finite temperature current-current correlation function

$$K^r_{\alpha\alpha'}(\Omega) = K_{\alpha\alpha'}(\imath\Omega_l)\Big|_{\imath\Omega_l \to \Omega + \imath 0^+}. \tag{1.66}$$

The **current-current correlation function** is defined as

$$K_{\alpha\alpha'}(\imath\Omega) = \int_0^\beta d\tau \, \Big\langle T_\tau J_\alpha(\tau) J_{\alpha'}(0) \Big\rangle \mathrm{e}^{\imath\Omega\tau}, \tag{1.67}$$

where T_τ denotes the ordered product in the imaginary time representation: $\imath t = \tau \in [0, \beta)$, with $\beta^{-1} = k_B T$ being the inverse temperature, and $\Omega_l = (2l)\pi/\beta$, $l \in \mathbb{Z}$ the (bosonic) Matsubara frequency. The current density operator J_α, with $\alpha =$ L,R, of the current flowing in and out of the scattering region reads

$$J_L = \imath \sum_\sigma V_{\mathrm{L}}(c^\dagger_{1\sigma} c_{\ell\sigma} - c^\dagger_{\ell\sigma} c_{1\sigma}), \tag{1.68a}$$

$$J_R = \imath \sum_\sigma V_{\mathrm{R}}(c^\dagger_{r\sigma} c_{N\sigma} - c^\dagger_{N\sigma} c_{r\sigma}). \tag{1.68b}$$

and the density in the scattering region $\rho_{\mathrm{S}} = \sum_{\{j\}\in \mathrm{S}} \sum_\sigma c^\dagger_{j\sigma} c_{j\sigma}$, satisfies the continuity equation

$$\frac{\partial \rho_{\mathrm{S}}}{\partial t} + J_{\mathrm{L}} - J_{\mathrm{R}} = 0, \tag{1.69}$$

implying that the current (and therefore the conductance) does not depend on the position, i.e., it does not depend on α and α'. The correlation function can be conventionally separated into two terms, represented diagrammatically in Fig 1.9, as

$$K_{\alpha\alpha'}(\imath\Omega_l) = K^{\text{bubble}}_{\alpha\alpha'}(\imath\Omega_l) + K^{\text{vertex}}_{\alpha\alpha'}(\imath\Omega_l), \tag{1.70}$$

where the *bubble* contribution $K^{\text{bubble}}_{\alpha\alpha'}(\imath\Omega_l)$ and the *vertex corrections* $K^{\text{vertex}}_{\alpha\alpha'}(\imath\Omega_l)$, take into account the independent propagation of a particle-hole pair, and multiple scattering events between the propagating particles, respectively. The latter are enclosed in the two-particle vertex

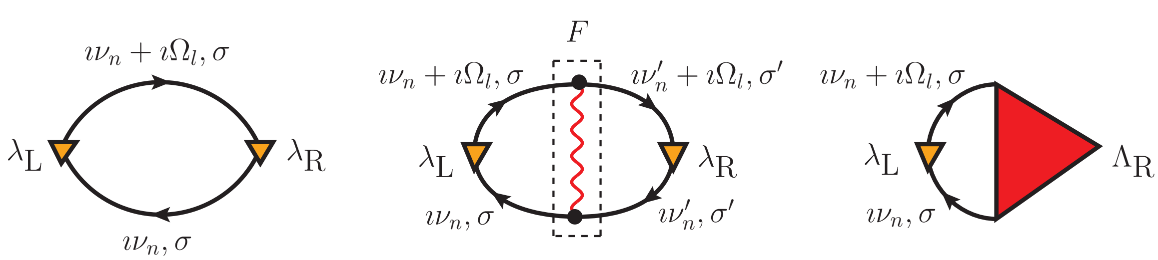

Figure 1.9: Feynmann diagrams for the electical conductance. Left panel: particle-hole bubble $K^{\text{bubble}}_{\text{RL}}$, describing the independent propagation of a particle-hole pair; the bubble contribution of the current-current correlation function is associated to the bare current vertex $\lambda_{\text{L,R}}$. Middle panel: scattering process (wiggled line) contributing to the vertex corrections $K^{\text{vertex}}_{\text{RL}}$; the complete resummation of all possible scattering events, denoted by the dashed line, is taken into account by the full two-particle vertex F. Right panel: vertex corrections $K^{\text{vertex}}_{\text{RL}}$ expressed in terms of the renormalized three-point current vertex Λ_R.

$F_{12;34}(\imath\nu_n, \imath\nu'_n, \imath\Omega_l)$, which depends on the bosonic Matsubara frequency Ω_l as well as on two fermionic Matsubara frequencies $\nu_n^{(\prime)} = (2n^{(\prime)} + 1)\pi/\beta$, $n^{(\prime)} \in \mathbb{Z}$. In the case $\alpha = \mathrm{R}$ and $\alpha' = \mathrm{L}$, the two contributions of the correlation function read

$$\begin{aligned} K_{\mathrm{RL}}^{\mathrm{bubble}}(\imath\Omega_l) = &- (\imath V_{\mathrm{R}})(\imath V_{\mathrm{L}})\frac{1}{\beta}\sum_n\sum_\sigma \\ &\times \big[G_{N1\sigma}(\imath\nu_n + \imath\Omega_l)G_{\ell r\sigma}(\imath\nu_n) - G_{N\ell\sigma}(\imath\nu_n + \imath\Omega_l)G_{1r\sigma}(\imath\nu_n) \\ &- G_{r1\sigma}(\imath\nu_n + \imath\Omega_l)G_{\ell N\sigma}(\imath\nu_n) + G_{r\ell\sigma}(\imath\nu_n + \imath\Omega_l)G_{1N\sigma}(\imath\nu_n)\big] \end{aligned} \tag{1.71a}$$

$$\begin{aligned} K_{\mathrm{RL}}^{\mathrm{vertex}}(\imath\Omega_l) = &- (\imath V_{\mathrm{R}})(\imath V_{\mathrm{L}})\frac{1}{\beta^2}\sum_{nn'}\sum_{\sigma\sigma'}\sum_{\{j\}\in \mathrm{S}} \\ &\times \big[G_{j_1 1\sigma}(\imath\nu_n + \imath\Omega_l)G_{\ell j_4\sigma}(\imath\nu_n) - G_{j_1\ell\sigma}(\imath\nu_n + \imath\Omega_l)G_{1j_4\sigma}(\imath\nu_n)\big] \\ &\times \; F^{\sigma\sigma'}_{j_1j_2;j_3j_4}(\imath\nu_n, \imath\nu'_n, \imath\Omega_l) \\ &\times \big[G_{Nj_2\,\sigma'}(\imath\nu'_n + \imath\Omega_l)G_{j_3r\sigma'}(\imath\nu'_n) - G_{rj_3\sigma'}(\imath\nu'_n + \imath\Omega_l)G_{j_4N\sigma'}(\imath\nu'_n)\big], \end{aligned} \tag{1.71b}$$

which can be obtained from the correlation function (1.67) and of the current density operator (1.68) introducing the proper definition of the (non-local) generalized susceptibility; for the sake of completeness, a detailed derivation of the above expression is provided in Appendix A. The following relation are fulfilled by the one-particle Green's function (for each spin polarization) involving the interface sites of the leads and any site of the scattering region, $j \in \mathrm{S}$:

$$\begin{aligned} G_{\ell(j\neq\ell)}(\imath\nu_n) &= -g_{\mathrm{L}}(\imath\nu_n)\, V_{\mathrm{L}}\, G_{1j}(\imath\nu_n), \\ G_{(j\neq r)r}(\imath\nu_n) &= -G_{jN}(\imath\nu_n)\, V_{\mathrm{R}}\, g_{\mathrm{R}}(\imath\nu_n), \end{aligned} \tag{1.72}$$

where g_{L} (g_{R}) is the local Green's function of the non-interacting isolated leads L (R) at the interface site ℓ (r). Using the latter, the correlation function can be straightforwardly rewritten in terms of the bare and renormalized vertex as

$$K_{\mathrm{RL}}(\imath\Omega_l) = \frac{1}{\beta}\sum_\sigma\sum_n\sum_{j_1,j_4\in \mathrm{S}} \lambda_{\mathrm{L}}(\imath\nu_n, \imath\nu_n{+}\imath\Omega_l)G_{1j_4\sigma}(\imath\nu_n)\Lambda_{\mathrm{R};j_4j_1}(\imath\nu_n, \imath\nu_n{+}\imath\Omega_l)G_{j_11\sigma}(\imath\nu_n{+}\imath\Omega_l), \tag{1.73}$$

where the bare vertex, associated to the L or R lead, is defined as

$$\lambda_{\mathrm{L}}(\imath\nu_n, \imath\nu_n + \imath\Omega_l) = -\imath V_{\mathrm{L}}^2[g_{\mathrm{L}}(\imath\nu_n + \imath\Omega_l) - g_{\mathrm{L}}(\imath\nu_n)], \tag{1.74a}$$

$$\lambda_{\mathrm{R}}(\imath\nu_n, \imath\nu_n + \imath\Omega_l) = \quad \imath V_{\mathrm{R}}^2[g_{\mathrm{R}}(\imath\nu_n + \imath\Omega_l) - g_{\mathrm{R}}(\imath\nu_n)], \tag{1.74b}$$

and the renormalized (three-point) vertex is defined as

$$\Lambda_{\mathrm{R}}(\imath\nu_n, \imath\nu_n + \imath\Omega_l) = \lambda_{\mathrm{R}}(\imath\nu_n, \imath\nu_n + \imath\Omega_l)\delta_{j_1N}\delta_{Nj_4} + P_{\mathrm{R};j_4j_1}(\imath\nu_n, \imath\nu_n + \imath\Omega_l), \tag{1.75}$$

where the vertex corrections are enclosed in the auxiliary quantity

$$\begin{aligned} P_{\mathrm{R};j_4j_1}(\imath\nu_n, \imath\nu_n + \imath\Omega_l) = &\frac{1}{\beta}\sum_{n'}\sum_{\sigma'}\sum_{j_2,j_3\in \mathrm{S}} \\ &\times F^{\sigma\sigma'}_{j_1j_2;j_3j_4}(\imath\nu_n, \imath\nu'_n, \imath\Omega_l)G_{j_3N\sigma'}(\imath\nu'_n)\lambda_{\mathrm{R}}(\imath\nu_n, \imath\nu'_n + \imath\Omega_l)G_{Nj_2\sigma'}(\imath\nu'_n + \imath\Omega_l). \end{aligned} \tag{1.76}$$

The conductance can be obtained by performing the **analytic continuation** $\imath\nu_n \to \epsilon + \imath 0^+$, and $\imath\Omega_l \to \Omega + \imath 0^+$ of the correlation function (1.73), and the limit (1.65) for $\Omega \to 0$, as anticipated previously in this section (Appendix A provides for details on the derivation). If we restrict, for the sake of simplicity, to the paramagnetic case, the linear conductance eventually reads

$$G = 2\frac{e^2}{h}\int_{-\infty}^{\infty} d\epsilon\, \Big(-\frac{\partial f(\epsilon)}{\partial \epsilon}\Big)\mathcal{T}(\epsilon), \tag{1.77}$$

where the (spin-independent) transmission coefficient[3] encloses the information about the details of the system. Neglecting vertex corrections, the transmission coefficient can be recast as

$$\mathcal{T}(\epsilon) = \Gamma_{\mathrm{L}}(\epsilon)G^a_{1N}(\epsilon)\Gamma_{\mathrm{R}}(\epsilon)G^r_{N1}(\epsilon), \tag{1.78}$$

where $G^{a,r}(\epsilon)$ are the advanced and retarded one-particle Green's function of the scattering region, respectively, and the **scattering amplitude**, which is obtained from the bare current vertex, depends on the leads through the hybridization amplitude and the local DOS as

$$\Gamma_\alpha(\epsilon) = 2\pi V_\alpha^2 \rho_\alpha(\epsilon). \tag{1.79}$$

In order to take the vertex corrections into account, one need to consider the analytic properties of the full vertex [89, 91]. The corresponding analytic continuation (Appendix A provides for details on the derivation) yields the transmission coefficient

$$\mathcal{T}(\epsilon) = \sum_{j_1,j_4\in S} \Gamma_{\mathrm{L}}(\epsilon)G^a_{1j_4}(\epsilon)\Gamma_{\mathrm{R};j_4j_1}(\epsilon,\epsilon)G^r_{j_11}(\epsilon), \tag{1.80}$$

where the renormalized scattering amplitude reads

$$\Gamma_{\mathrm{R};j_4j_1}(\epsilon) = 2\pi\rho_{\mathrm{R}}(\epsilon)V_{\mathrm{R}}^2\delta_{j_1N}\delta_{Nj_4} + P_{\mathrm{R};j_4j_1}(\epsilon,\epsilon), \tag{1.81}$$

and $P^{[2]}_{\mathrm{R};j_4j_1}(\epsilon,\epsilon)$ has a complicated expression in terms of $F(\epsilon,\epsilon,0)$. Note that neglecting vertex corrections would correspond to set (arbitrarily) this term to zero, so that the sum over the indexes of the scattering region $\sum_{j_1,j_4\in S}$ in Eq. (1.80) is saturated by the corresponding Kronecker symbol $\delta_{j_1N}\delta_{Nj_4}$, yielding the result (1.78) of the bubble transmission coefficient.

Finally, we note that the transmission coefficient (including vertex corrections) can be elegantly recast in terms of a trace

$$\mathcal{T}(\epsilon) = \mathrm{tr}[\Gamma_{\mathrm{L}}(\epsilon)G^a(\epsilon)\Gamma_{\mathrm{R}}(\epsilon)G^r(\epsilon)], \tag{1.82}$$

where both the scattering amplitudes and the Green's functions are matrices in the Hilbert space of the scattering region.

[3]The formula for the conductance is easily generalized to the spin-polarized case restoring the sum over the spin polarizations and considering a spin-dependent transmission coefficient.

Concluding this section, some questions naturally arise, related to the applicability of the discussed formalisms, i.e., Landauer-Büttiker and linear response theory, as well as to the relation between the corresponding conductance. In order to establish the consistency of both methods, it is interesting to compare the transmission coefficient (1.82) obtained within linear response to the one derived within scattering theory, as well as to other results in the literature.
Noteworthy, with the following definition

$$t(\epsilon) = \Gamma_{\mathrm{L}}^{1/2}(\epsilon) G^r(\epsilon) \Gamma_{\mathrm{R}}^{1/2}, \tag{1.83}$$

and considering that, in the limit $T \to 0$, the derivative of the Fermi function is pinned at the Fermi energy, the result (1.77) of the Kubo formula reduces to the low-bias Landauer-Büttiker formula (1.59) for the conductance.
Due to the nature of the Kubo formalism, the above conductance is expected to provide reliable results only if the system displays a linear $I(V_{\mathrm{SD}})$ characteristics. The latter requirement is generally fulfilled only in the low-bias regime, and evidently represents a limitation to the applicability of the method in many interesting cases, as technological applications usually rely on (or benefit from) the presence of non-linear characteristics and unexpected physical phenomena. On the other hand, while the Landauer-Büttiker formula is not limited to that regime, it is not of help in the practical evaluation of the transmission coefficient, and does not hold in the presence of inelastic scattering.

We note that, the transmission coefficient (1.82) is formally equivalent to the results obtained (out-of-equilibrium) by Caroli et al. [92] as well as by Meir & Wingreen [87], when considering their low-bias limit. However, while in the former case, the transmission function was obtained under the assumption that the system is non-interacting, in the latter, as well as within the present formalism, the transmission coefficient is defined in terms of the full interacting Green's function of the scattering region, and the conductance also takes into account inelastic processes due to, e.g., electron-electron interaction and scattering off impurities or phonons.
In particular, in the case in which the interacting region collapses onto an AIM, and under the condition for the scattering amplitude $\Gamma_{\mathrm{L}}(\epsilon) = \lambda \Gamma_{\mathrm{R}}(\epsilon)$ (λ being a scalar factor), the transmission coefficient can be recast in terms of the spectral function of the AIM as

$$\mathcal{T}(\epsilon) = \frac{\Gamma_{\mathrm{L}}\Gamma_{\mathrm{R}}}{\Gamma_{\mathrm{L}} + \Gamma_{\mathrm{R}}} \Big(-\frac{1}{\pi} \mathrm{Im} G^r(\epsilon) \Big), \tag{1.84}$$

and the vertex corrections vanish [87].

On the other hand, vertex corrections are in general expected to be relevant for a quantitative description transport properties of low-dimensional systems: e.g., for an Hubbard chain, already within perturbation theory, it has been shown that in the high-temperature regime vertex correction are important and result in quantitative modification to transport properties of the system [89]. However, the knowledge of the two-particle vertex beyond perturbation theory [158] is *not* a trivial requirement, as will be discussed in detail in the following chapter, and represents a huge challenge for contemporary theoretical condensed matter physics. As a consequence, the effect of vertex corrections is poorly investigated in the literature.

Chapter 2

Dynamical mean field theory and beyond

In this chapter we will provide a self-contained overview of some methods used to take many-body effects into account. Dynamical mean-field theory (DMFT) established itself as the standard tool for dealing with strongly correlated systems, mostly because of its predictive power when employed in combination with first principle calculations for real materials. However, the purely local picture of DMFT is not sufficient to reliably describe the properties of correlated systems when non-local spatial fluctuation becomes relevant, as in the case of, but not limited to, low-dimensional or electronically confined systems. In this prospective, we also briefly review the main extensions of DMFT, which aim at including also spatial electronic correlations beyond mean-field. We focus in particular on the dynamical vertex approximation (DΓA), and on the related recently introduced nanoscopic version (nano-DΓA), which represents the main topic of this work and was developed in order to study local and non-local correlation effects at the nanoscale.

In the previous chapter we learned that correlation effects can lead to unexpected and spectacular physical phenomena and phases in many-electron systems. However, since the very beginning, back to the 1960s, the theoretical investigation of strongly correlated material had to face difficulties arising from the intrinsic non-perturbative nature of problems, where competing energy scales are comparable to each other. In a lattice, the main competing energy scales are the kinetic energy that tends to delocalize electrons into Bloch's waves, and the electrons mutual Coulomb repulsion, with the opposite tendency to localize the charges. The essence of this problem is usually addressed theoretically in the framework of the Hubbard model [95], which is described by the following Hamiltonian

$$\mathcal{H} = -t \sum_{\langle ij \rangle} \sum_{\sigma} c^{\dagger}_{i\sigma} c_{j\sigma} + U \sum_{i} c^{\dagger}_{i\uparrow} c_{i\uparrow} c^{\dagger}_{i\downarrow} c_{i\downarrow}, \tag{2.1}$$

where $c^{\dagger}_{i\sigma}$ ($c_{j\sigma}$) are the creation (annihilation) operators of an electron at site i with spin σ, associated to the maximally localized Wannier functions, typically used to describe narrow (typically d or f) orbitals. The electrons can move through the lattice via hopping processes between nearest neighbor (NN) sites $\langle ij \rangle$, described by the hopping amplitude t. The Coulomb repulsion, on the other hand, is approximated by its major contribution, i.e., a purely local repulsion term U. This is often considered a reasonable approximation for localized d or f orbital, as the non-local matrix elements of the Coulomb potential decay rapidly with distance. Despite its apparent simplicity, this Hamiltonian represents a real challenge, and no analytic solution of the Hubbard model in two or three dimensions is known. In fact, the interplay between kinetic energy and Hubbard repulsion is crucial in determining the properties of the ground state, giving rise to a complex and rich phase diagram.

2.1 Dynamical mean-field theory

A huge development in the understanding of strongly correlated physics described by the Hubbard model was triggered by the work of Metzner and Vollhardt [96], showing that a proper scaling of the hopping term in the limit of infinite dimensions $d = \infty$ (or equivalently infinite coordination number z) leads to non-trivial (local) correlations among electrons. From the point of view of practical implementations, the breakthrough was, however, the works of Georges and Kotliar [97, 98], and Müller Hartmann [**?**], who developed a novel quantum-like mean-field approach for the Hubbard model that becomes exact in $d = \infty$ limit previously analyzed by Metzner and Vollhardt. The idea to map the lattice problem in $d \to \infty$ onto an Anderson Impurity Model (AIM, see Sec. 1.2.2) where an impurity site in embedded into an effective bath determined by a self-consistent condition. The impurity model is still a quantum many-body problem, but it is characterized, evidently, by a purely local dynamics. As a consequence, all spatial fluctuations beyond MF are neglected, while local quantum fluctuations are fully taken into account, as it is reflected by the name of the method, known as dynamical mean-field theory (DMFT).

In the following we discuss the generic aspects of the theory, introducing the limit of infinite dimension, and provide a schematic derivation of the DMFT equations.

Proper scaling in the limit of $d = \infty$. The main issue here is to understand how the two terms of Hamiltonian (2.1) scale with d (or z). The local interaction U is related to the potential energy per site, therefore

$$\sum_i U_i \left\langle c^\dagger_{i\uparrow} c_{i\uparrow} c^\dagger_{i\downarrow} c_{i\downarrow} \right\rangle \xrightarrow{z\to\infty} \text{constant}, \tag{2.2}$$

i.e., the thermal expectation value of the potential energy stays finite in the limit of infinite dimensions, neither vanishing nor diverging. If only NN (isotropic) hopping processes are taken into account, the kinetic energy per site consists, instead, of z equivalent terms, and it would diverge in the limit $z \to \infty$ unless it is properly rescaled. The following consideration is of help in understanding how to define proper scaling: t represents a quantum mechanical amplitude for electrons to move between NN sites, and hence $|t|^2$ has the meaning of a hopping probability. In order to be physically consistent, the probability of hopping to any of the z equivalent neighbors of site i has to be of $\mathcal{O}(1)$, implying that the probability of hopping into a

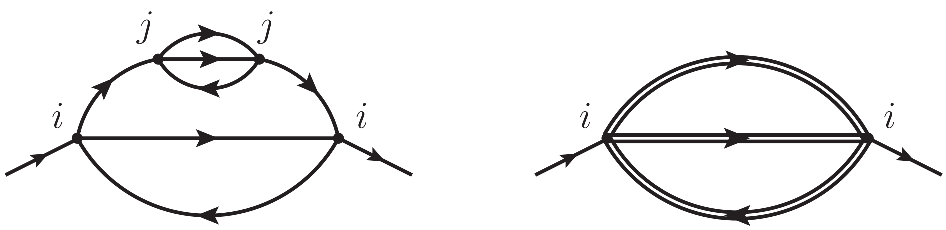

Figure 2.1: A second-order irreducible diagram for the self-energy of the Hubbard model (denoting with a dot ''•'' the local interaction). Due to the scaling of the bare fermionic propagator (single line), the non-local contribution (i.e. $i \neq j$) of this diagram vanishes in the limit $d \to \infty$, and only local contributions with $i = j$ survive. The non-skeleton diagram on the left-hand side is contained in the fully local diagram on the right-hand side obtained using the dressed fermionic propagator (double line).

given neighbor scales like $1/z$, hence $t \sim 1/\sqrt{z}$. As a consequence of this, the bare propagator, or Green's function [90], between NN sites i and j, $G^0_{ij}(\tau) = -\langle T_\tau c_i(\tau) c^\dagger_j(0)\rangle$ scales also as $1/\sqrt{z}$. This way the kinetic term per site will stay finite, i.e,

$$-t \sum_{\langle ij\rangle} \sum_\sigma \left\langle c^\dagger_{i\sigma} c_{j\sigma} \right\rangle \stackrel{z\to\infty}{\longrightarrow} \text{constant}, \tag{2.3}$$

since the z factor stemming for the equivalent contribution for each NN j is canceled by the $1/\sqrt{z}$ scaling factors of $t_{ij} = t$ and $\langle c^\dagger_{i\sigma} c_{j\sigma}\rangle$. The latter is directly connected to the Green's function G^0_{ij} by means of the fermionic algebra. This is the only non-trivial scaling in infinite dimension, which preserves the competition between kinetic energy and Coulomb interaction also in $d \to \infty$: in fact, this is the only scaling which yields a finite (non-interacting) DOS for the lattice. These scaling prescriptions are directly reflected in the corresponding self-energy Σ. This can be shown most comfortably in terms of Feynman diagrams. Let us consider, e.g., the (one-particle irreducible) Feynman diagram of Fig. 2.1, where sites i and j are connected by three independent Green's functions. The contribution to this diagram scales as $(1/z)^3$ if $i \neq j$, hence it becomes irrelevant in the limit $z \to \infty$. If the self-energy is expressed in terms of the dressed propagator G_{ij}, in order to avoid double counting of diagrams one has to consider only *skeleton* diagrams. These do not contain any part connected to the rest of the diagram by less than three Green's functions. As a consequence of the scaling, it can be shown that all skeleton diagrams become local in $d = \infty$, yielding, therefore, a purely local self-energy

$$\Sigma_{ij}(\nu) \stackrel{z\to\infty}{\longrightarrow} \delta_{ij}\Sigma(\nu). \tag{2.4}$$

Note that this represents a huge simplification for the description of correlation effects in the lattice model, and the main achievement by Metzner and Vollhardt [96].

Mapping onto the AIM. As already mentioned, the results achieved by Metzner and Vollhardt with the scaling in infinite dimension, opened the way for the development of the novel theoretical method of DMFT. The idea of Georges and Kotliar [97, 98] was that the lattice problem in infinite dimension can be mapped exactly onto an AIM coupled to a self-consistent bath of conduction electrons, described by the Hamiltonian

$$\mathcal{H}_{\mathcal{AIM}} = \sum_{k\sigma} \epsilon_{\mathbf{k}\sigma} a^{\dagger}_{k\sigma} a_{k\sigma} + \sum_{k\sigma} V_k (a^{\dagger}_{k\sigma} c_{\sigma} + \mathrm{h.}c.) + U n_{\uparrow} n_{\downarrow}, \tag{2.5}$$

where $c^{\dagger}_{\sigma}$ (c_{σ}) are the creation (annihilation) operator of an impurity electron, and $n_{\sigma} = c^{\dagger}_{\sigma} c_{\sigma}$ is the corresponding electronic density at the impurity site. Here $a^{\dagger}_{k\sigma}$ ($a_{k\sigma}$) are the creation (annihilation) operators of a conduction electron with spin σ, momentum k, and energy $\epsilon_{k\sigma}$, and V_k describes the hybridization between the impurity and the conduction band.
The condition that makes the mapping possible is that all the local skeleton diagrams of the AIM have the same topology of the ones of the Hubbard model in infinite dimension. This means that the AIM would yield the same self-energy of the lattice model in $d = \infty$, provided that the dressed propagators appearing in the diagrammatic expansion of the self-energy are also the same.

In this framework, it is convenient to reformulate the problem (2.5) in an imaginary-time integral representation in terms of Grassmann variables [100], where all fermionic degrees of freedom are traced out, except for the local ones, i.e., those of the impurity site, yielding the effective action

$$S^{\mathrm{eff}} = \int_0^{\beta} d\tau \int_0^{\beta} d\tau' \sum_{\sigma} c^{\dagger}_{\sigma}(\tau) \mathcal{G}_0^{-1}(\tau - \tau') c_{\sigma}(\tau') + U \int_0^{\beta} d\tau \; n_{\uparrow}(\tau) n_{\downarrow}(\tau). \tag{2.6}$$

As already discussed, the AIM describes the local dynamics of an interacting impurity in a non-interacting background. The bare propagator of the AIM, $\mathcal{G}_0^{-1}(\tau - \tau')$, plays the same role of the Weiss field in the classical mean-field theory: it is an effective field coupled to the impurity, containing all non-local information of the underlying lattice, described as a reservoir of non-interacting electrons. The main difference with the classical Weiss field relies in its time dependence, which accounts for the local dynamics of the system. From the physical point of view, this means taking into account local *quantum fluctuations*, i.e., the transitions between different configurations of the impurity site ($|0\rangle$, $|\uparrow\rangle$, $|\downarrow\rangle$, or $|\uparrow\downarrow\rangle$), via hopping processes from/to the bath in which electrons leave the impurity and come back on a time scale $\tau \sim 1/\omega$.

From the practical point of view, instead, the main advantage of the mapping is that several well established methods to solve the AIM are known, and it is possible to exploit them to compute local quantities from the effective action (2.6), such as the impurity Green's function

$$G_{\sigma}(\tau - \tau') = -\frac{1}{\mathcal{Z}} \prod_{\sigma'} \int \mathcal{D}c_{\sigma'} \mathcal{D}c^{\dagger}_{\sigma'} \left(c_{\sigma}(\tau) c^{\dagger}_{\sigma}(\tau') \, \mathrm{e}^{-S\{c, c^{\dagger}, \mathcal{G}_0^{-1}\}} \right), \tag{2.7}$$

where the partition function is defined as

$$\mathcal{Z} = \prod_{\sigma'} \int \mathcal{D}c_{\sigma'} \mathcal{D}c^{\dagger}_{\sigma'} \left(\mathrm{e}^{-S\{c, c^{\dagger}, \mathcal{G}_0^{-1}\}} \right), \tag{2.8}$$

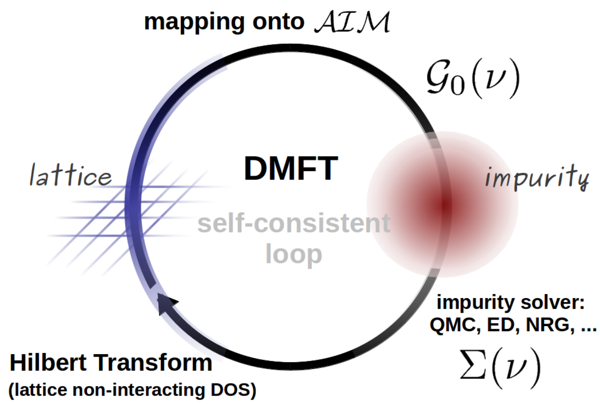

Figure 2.2: Flowchart of DMFT. The lattice problem (l.h.s. of the flowchart) is mapped onto an auxiliary Anderson model, consisting in an impurity embedded in a self-consistent bath (r.h.s.), defining a dynamical Weiss field $\mathcal{G}_0(\nu)$. The impurity model is solved numerically, yielding a local self-energy $\Sigma(\nu)$. The local quantities on the impurity are related to the ones of the lattice (defined by the corresponding DOS) via a self-consistent condition. The DMFT scheme further iterates the lattice and the impurity models until convergence is reached.

and the functional integral is performed over the Grassmann variable associated to the fermionic creation and annihilation operators. However, the solution of Eq. (2.7) and (2.8) does not provide complete information, since the specific choice of the AIM which yields the same self-energy of the lattice problem is a priori not known. Therefore, one needs to establish a relation connecting the interacting Green's function generated from the effective action of the AIM with the local one of the lattice model. Specifically, all the information about the lattice will be encoded in the corresponding DOS

$$D(\epsilon) = \sum_k \delta(\epsilon - \epsilon_k), \qquad \epsilon_k = \sum_{ij} t_{ij} \mathrm{e}^{\imath k (R_i - R_j)}. \tag{2.9}$$

The explicit relation is provided by the self-consistency condition

$$\mathcal{G}_0^{-1}(\nu) = \nu + \mu + G(\nu)^{-1} + R\big[G(\nu)\big], \tag{2.10}$$

where $G(\nu)$ is the Fourier transform (FT) of the impurity interacting Green's function (2.7) in frequency space,[1] and $R\big[G(\nu)\big]$ denotes the reciprocal function of the Hilbert transform of the lattice DOS

$$\tilde{D}(\zeta) = \int_{-\infty}^{\infty} d\epsilon \, \frac{D(\epsilon)}{\zeta - \epsilon}, \tag{2.11}$$

[1] The imaginary time is related to the Matsubara frequency via the FT $\tau \to \imath\nu$; while the physical quantities on the real axis are obtained performing the analytical continuation $\imath\nu \to \nu + \imath 0^+$ (see, e.g., Ref. [90]). While here we keep a generic notation, one has to be aware that, if the Green's function is known only numerically on the imaginary time/frequency axis, its analytic continuation is not trivial [101].

which corresponds, in fact, to the local Green's function of the lattice if $\zeta = \nu + \mu - \Sigma(\nu)$, see below. Condition (2.10) establishes the relation needed to obtain a closed set of equations, which can be solved self-consistently (see also Fig. 2.2) according to the following scheme:

- the local Green's function of the lattice problem is computed via the Hilbert transform with an initial guess for the self-energy $\Sigma(\nu)$ (e.g. $\Sigma(\nu)\equiv 0$)

$$G_{\rm loc}(\nu) = \int_{-\infty}^{\infty} d\epsilon \, \frac{D(\epsilon)}{\nu + \mu - \Sigma(\nu) - \epsilon}; \tag{2.12}$$

- the auxiliary impurity problem is defined by $\mathcal{G}_0^{-1}(\nu) = G_{loc}^{-1}(\nu) + \Sigma(\nu)$;
- the corresponding impurity Green's function is calculated solving the AIM

$$G_{\rm imp}(\tau - \tau') = -\frac{1}{\mathcal{Z}} \int \mathcal{D}c \, \mathcal{D}c^\dagger \left(c\,(\tau) c^\dagger(\tau') \, \mathrm{e}^{-S\{c,c^\dagger,\mathcal{G}_0^{-1}\}} \right); \tag{2.13}$$

- the Dyson equation yields a new self-energy $\Sigma(\nu) = \mathcal{G}_0^{-1}(\nu) - G_{imp}^{-1}(\nu)$;
- $\Sigma(\nu)$ enters Eq. (2.12) again and defines a new local Green's function etc. till convergence.

The usual guess sets the self-energy to zero, which corresponds to identify the Weiss field with the local bare Green's function of the lattice problem, but depending on the physical system and on the set of parameter considered, different guess may be more appropriate and shorten the self-consistency cycle. For the sake of simplicity, above and in the following we restrict ourselves to the paramagnetic case, where the Green's function is spin-degenerate. However, the DMFT self-consistency can be generalized to deal with phases with broken symmetry, e.g., in presence of long range (anti)ferromagnetic ordering or superconductivity, as discussed in the review of Ref. [98].

Impurity solvers: evaluate the local one-particle irreducible self-energy. It is important to recall that, contrary to the static mean-field theory the AIM is still a quantum many-body problem. Its (numerical) solution, though being much simpler than the one of the full lattice problem, is nevertheless challenging, and still represents the computational bottleneck of the DMFT scheme. However, several well established solvers are available for the solution of the impurity model, including: iterated perturbation theory [102], numerically exact Quantum Monte Carlo (QMC) [103, 104, 105, 93], exact diagonalization (ED) [106, 107]), numerical renormalization group (NRG) [108], and diargrammatic resummation like the non-crossing approximation and its extensions [109, 110, 111].

In the following we focus on the evaluation of the irreducible self-energy in the impurity solvers used for the calculations presented in this work.

• **Exact Diagonalization:** the AIM is solved performing a direct diagonalization of the Hamiltonian (2.5), where the (continous) bath is parametrized by an effective discrete bath consisting of few orbitals n_s, described by a set of Anderson parameters ϵ_k and V_k, $k=1,\ldots,n_s$. The procedure suffers from severe limitation due an exponential growing Hilbert space. Nevertheless, ED can provide accurate results for the single band case (especially for integrated quantities). The Green's function of the discretized AIM is evaluated from the corresponding Lehmann representation [67]

$$G(\nu) = \frac{1}{\mathcal{Z}} \sum_{m,n} \frac{|\langle n|c|m\rangle|^2}{\nu + \epsilon_n - \epsilon_m} \left(\mathrm{e}^{-\beta\epsilon_n} + \mathrm{e}^{-\beta\epsilon_m} \right) \tag{2.14}$$

where the sum extends over all exact many-body eigenstates $|n\rangle$, with eigenenergies ϵ_n. The knowledge of the impurity Green's function allows one to access the irreducible self-energy by means of the Dyson equation

$$\Sigma(\nu) = \mathcal{G}_0^{-1}(\nu) - G^{-1}(\nu), \tag{2.15}$$

as well as other physical quantities of the impurity model like, e.g., the impurity spectral function $A(\nu) = -\frac{1}{\pi}G(\nu)$, or the double occupation $\langle d\rangle = \langle n_\uparrow n_\downarrow\rangle = (\beta U)^{-1}\sum_\nu \Sigma(\nu)G(\nu)$. The data obtained by means of ED are obviously not affected by statistical noise: this results in a proper high-energy asymptotic behavior of the physical quantities. On the other hand, the corresponding spectral functions display a typical peaky structure, as a consequence of the discretization of the bath.

• **Quantum Monte Carlo:** available on the ‘‘market’’ are several algorithm in this category, sharing some features, but also characterized by important differences. For the QMC algorithm there is no need for a discretization of the effective bath, as the solver deals with the effective action functional integral representation in imaginary time, built by the Anderson Hamiltonian. Moreover, due to its potential to treat multi-orbital Hamiltonians, it is more suitable than ED, e.g., for realistic calculations. Below we briefly discuss the main features of the Hirsch-Fye Quantum Monte Carlo (HF-QMC) [103], which we have employed in the context of this work.

In the HF implementation, the time domain $[0,\beta)$ is discretized into L equally spaced *time-slices* $\Delta\tau = \beta/L$ (Trotter decomposition). One therefore performs, for each time-slice i, a discrete Hubbard-Stratonovich transformation on the interaction term, which is decoupled introducing a set of auxiliary (classical) fields, i.e. Ising fields. For a fixed configuration of the auxiliary fields $\{s_i\}$, the problem is reduced to non-interacting fermion model in a time-dependent magnetic field $h(\tau_i) = s_i$, which can be solved exactly by a Gaussian integral. The configuration are updated by Markov processes consisting of spin flips, and the sum over all configurations is evaluated with Monte Carlo. The quantum mechanical problem is therefore reduced to a matrix problem, i.e., the Green's function -as well as other physical quantities- can be evaluated from the determinant of a 2^L dimensional matrix in the auxiliary fields' space. It is therefore clear, that the computational effort grows substantially with L, i.e., the number of time slices used in the discretization process.

Again, the knowledge of the Green's function allows one to compute the irreducible self-energy by means of the Dyson equation, which is, in τ, a complicated convolution integral

$$G(\tau) = G_0(\tau) + \int_0^\beta d\tau' \int_0^\beta d\tau''\, G(\tau')\Sigma(\tau''-\tau')G(\tau-\tau''). \tag{2.16}$$

Therefore, it is preferable to perform a FT to the frequency space already at this level, where the equation assumes the simple form (2.15). The instability problems associated with the FT (from τ to $\imath\nu$) in the HF are well known, and originate from the limited number of time slices available in the calculations. Some techniques, involving high-frequency expansions of the Green's function and semi-analytic FT, have been developed in order to decrease systematic errors (see, e.g., Ref. [112] as well as Appendix B and references therein).

The limitation of the HF-QMC are related to the discretization of the time domain, which introduces a Trotter error of order $(\Delta\tau)^2$, and that the computational effort scales as T^{-3}, with the additional issues that at strong coupling and low temperatures the numerical results may become unstable, the complexity even increases in the presence of more involved interactions, e.g., in multi-orbital models. Those limitations motivated the development of modern continuous-time Quantum Monte Carlo (CT-QMC) methods, which are free of the Trotter decomposition error. Among the several approaches reported in the literature, we mention the weak coupling [104] and the (strong-coupling) hybridization expansion [105] versions. However, it was recently shown that a state-of-the-art implementation of HF-QMC (with extrapolation of discretization $\Delta\tau \to 0$ is competitive with CT-QMC [113], A detailed description of CT-QMC methods, and its comparison with HF-QMC is, however, beyond the scope of this section and remand to- Ref. [93] for a review.

Success and limitations of DMFT. One of the main achievement of DMFT was the non-parturbative description of the physics behind the correlation-driven Mott-Hubbard metal-to-insulator transition (MIT) in infinite dimension [114, 98]. The MIT is characterized by the transfer of spectral weight from a coherent quasi-particle (QP) peak to the incoherent lower (LHB) and upper (UHB) Hubbard bands. Within DMFT it was shown that in the intermediate coupling regime the system retains *both* QP feature and Hubbard bands, with the formation of a typical three-peak structure. The QP peak shrinks and it is suppressed as the interaction is increased and eventually disappears at a critical value of U. The success of DMFT in describing the MIT lies certainly in its intrinsic non-perturbative nature, which represents a huge advance over previously available techniques, and allows to explore the whole range of coupling strenght. No doubt that the venue of DMFT marked indeed the beginning of a new era for the theoretical investigation of strongly correlated electronic systems.

The wide range of applicability of DMFT may be surprising, considering that in the real world one deals with finite (e.g., $d=3$ or $d=2$) dimensional systems. However, the coordination number z is already quite large for several three-dimensional lattices: $z=6$ for a cubic lattice, $z=8$ for a body-centered cubic lattice, or even $z=12$ for a face-centered cubic lattice. The controlled limit of DMFT, which becomes exact as $z \to \infty$, ensures the internal consistency of the method and establish $1/z$ as a control parameter. Therefore DMFT can be considered not only as a purely mathematical construction for describing the *fermionology* in $d = \infty$, but also as a useful approximation to many realistic finite-dimensional systems.

At the same time, despite of providing a good qualitative description of the Mott MIT in three-dimensional systems, DMFT still remains a mean-field approximation in space, as it completely neglects spatial fluctuations. Therefore a **failure of the purely local picture** of DMFT is to be expected, as soon as non-local spatial correlations among the electronic degrees of freedom become predominant. In order to understand the limitations of DMFT, and the way how to improve the description of strongly correlated systems beyond mean-field, it is interesting to analyze the physical situations which favor the presence of significant non-local correlations.

In **low dimensional**, e.g., $d = 1$, $d = 2$, or layered $d = 3$ systems, the lattice coordination number becomes low: e.g., $z = 4$ for a square or Kagomé [94] lattice, $z = 3$ for a triangular lattice, or even $z = 2$ for a unidimensional chain. In this case the dynamics of electrons is obviously strongly influenced by the actual configuration of the neighboring sites, rather than from the average on the whole lattice. Therefore, in this situation a mean-field description is generally a poor approximation.

Also **confinement effects** are closely related to the dimensionality of the systems. As already discussed in Sec. 1.1), at the nanoscale electrons can be confined, e.g., in low-dimensional interfaces of semiconductors (quantum dots) or propagate into narrow structures whose size is comparable with the electrons' Fermi wavelength λ_F. As a consequence local as well as non-local correlation effects may arise even in materials which do not exhibit evidences for strong correlations in the bulk.

Finally, it is well known, from the theory of **critical phenomena** [115], that close to a second-order phase transition (e.g., from the paramagnetic to the ferromagnetic phase in spin systems) specific collective (critical fluctuations) dominate the low-energy physics of the system and that their spatial coherence extends on a length scale ξ, usually known under the name of correlation length. As it is immediately visible from the Orstein-Zernike [116] formula for the propagator of the critical fluctuations

$$\chi(q) \sim \frac{1}{\xi^{-2} + q^2}. \tag{2.17}$$

the correlation length ξ^{-2} plays the role of an effective mass, providing an infrared (IR) cutoff to the correlation function $\chi(q)$ and exponentially dumping the fluctuation on a scale ξ. At the critical temperature T_c, the correlation length ξ diverges, resulting in a thermodynamic instability and leading to critical phenomena, which cannot be described (at least for dimensions $d < 4$) within a mean-field theory in space.

In this sense, also **inhomogeneity** or **disorder effects**, as e.g., those responsible for the Anderson localization [117], are washed away from the averaging of the spatial fluctuation in mean-field.

2.2 Merging many-body with ab-initio methods

So far we have discussed how to take into account electronic correlations in the context of model Hamiltonians, as in the case of the Hubbard model. However, the original intent of the Hubbard Hamiltonian is the description of the relevant physics of the solid state, i.e., a system of mutually interacting (valence) electrons in a background potential generated by a periodic lattice of ions. In the Born-Oppenheimer approximation [118], where the electronic and the lattice degrees of freedom have been decoupled, and neglecting relativistic correction[2], the solid state Hamiltonian reads

$$\mathcal{H} = \sum_{\sigma} \int d^3r \; \psi^{\dagger}(\mathbf{r},\sigma)\Big[-\frac{\hbar^2\Delta}{2m} - \sum_i \frac{e^2}{4\pi\varepsilon_0}\frac{Z_i}{|\mathbf{r}-\mathbf{R}_i|}\Big]\psi\;(\mathbf{r},\sigma)$$
$$+\frac{1}{2}\sum_{\sigma\sigma'}\int d^3r \int d^3r' \; \psi^{\dagger}(\mathbf{r},\sigma)\psi^{\dagger}(\mathbf{r}',\sigma')\frac{e^2}{4\pi\varepsilon_0}\frac{1}{|\mathbf{r}-\mathbf{r}'|}\psi\;(\mathbf{r}',\sigma')\psi(\mathbf{r},\sigma), \qquad (2.18)$$

where $\psi^{\dagger}(\mathbf{r},\sigma)(\psi\;(\mathbf{r},\sigma))$ are the creation (annihilation) field operators of an electron with charge $-e$, spin σ, and mass m at the position $\mathbf{r}$, while $\Delta \equiv \partial^2/\partial^2\mathbf{r}$ is the Laplace operator. The coordinate $\mathbf{R}_i$ denotes the position of an ion i with charge $Z_i e$. Finally, $\hbar$ and ε_0 are the reduced Plank constant and the vacuum dielectric permittivity.

The presence of the Coulomb electron-electron interaction correlates the propagation of the electrons (see Fig. 2.3) and makes of the lattice Hamiltonian (2.18) a full quantum many-body problem, impossible to be solved exactly for a realistically large number of electrons. One has, therefore, to develop approximations. One possibility is to consider many-body model Hamiltonians, as already discussed, which provided useful insight toward the qualitative understanding

[2] e.g., the spin-orbit coupling, which would be important in f-electron systems.

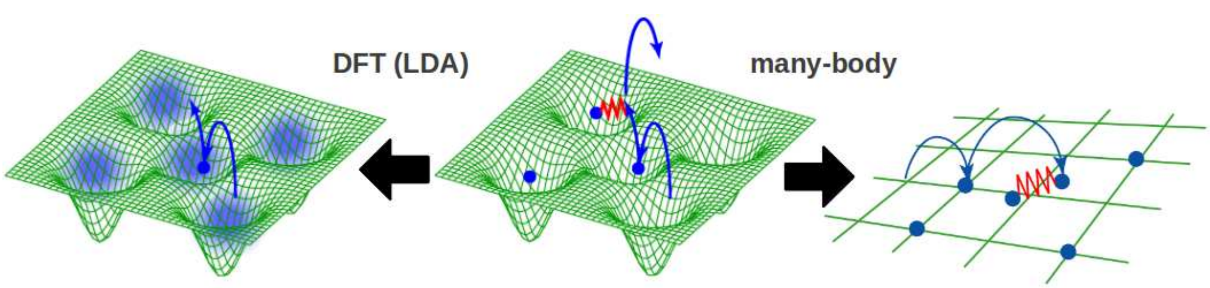

Figure 2.3: Two possible ways of approaching the solid state Hamiltonian (2.18). Within DFT, one considers the effective problem of an electron propagating in a underlying time-averaged potential obtained as a functional of the electron density: this allows one to deal with a realistic bandstructure and compute electronic properties of materials, but neglects strong electronic correlations. Within many-body approaches, including DMFT, one relies on an essential model Hamiltonian (e.g., as in the Hubbard model) which, although being a drastic approximation of the original Hamiltonian, is believed to take into account the relevant physics for a qualitative understanding of strongly correlated electronic systems. Adapted after Ref. [119].

of the role of electronic correlations. The results of these calculations, however, do not provide a quantitative description of realistic compounds and are based on parameters that have to be, e.g., extracted from a fit of experimental data. The other possibility is to employ *drastic approximations* to Hamiltonian (2.18) in order to deal with it directly. In this framework developed the **Density Functional Theory** (DFT) [120] which, combined with the **Local Density approximation** (LDA) or other DFT approximations, revealed itself to be unexpectedly successful to compute the bandstructure and electronic properties of many materials. In the following we briefly review the basic concept of the DFT(LDA). In particular, we discuss the reasons why it fails to describe strongly correlated materials, and we illustrate how it can be combined with many-body approaches in order to overcome this limitation.

2.2.1 Density Functional Theory

The DFT is based on the Hohenberg-Kohn theorem [120]. The latter states that the ground state energy is a functional of the electron density $E[\rho(\mathbf{r})]$ which is minimized by the ground state density $\rho(\mathbf{r})=\rho_0(\mathbf{r})$. This functional can be constructed [122] as

$$E[\rho] = \min\Big[\langle\phi|\mathcal{H}|\phi\rangle\Big|\langle\phi|\sum_{i=1}^{N}\delta(\mathbf{r}-\mathbf{r}_i)|\phi\rangle = \rho(\mathbf{r})\Big], \tag{2.19}$$

where $\phi = \phi(\mathbf{r}_1, \sigma_1, \ldots, \mathbf{r}_N, \sigma_N)$ is the full many-body wave function for a fixed number of electrons N; and its minimization yields the ground state energy $E_0 = \min_\rho E[\rho]$.
As far as only ground state properties are concerned, this implies the existence of an effective potential $V^{\text{eff}}[\rho(\mathbf{r})]$ that includes all many-body effects into a (solvable) one-particle Schrödinger equation. However, being such a potential unknown, in general one would still need to compute the expectation value of the Hamiltonian on a complicated set of many-body wave functions.

A possible way out solution is to separate the energy functional as

$$E[\rho] = E_{\text{kin.}}[\rho] + E_{\text{ion}}[\rho] + E_{\text{hartree}}[\rho] + E_{\text{xc}}[\rho], \tag{2.20}$$

where $E_{\text{ion}}[\rho] = \int d^3r\ V_{\text{ion}}(\mathbf{r})\rho(\mathbf{r})$ is the energy of the electrons in the external potential generated by the ionic lattice, and $E_{\text{hartree}}[\rho] = \frac{1}{2}\int d^3r \int d^3r'\ \rho(\mathbf{r})V_{\text{ee}}(\mathbf{r}-\mathbf{r}')\rho(\mathbf{r}')$ is the Hartree (mean-field) contribution of the Coulomb interaction. This way, all the complexity due to many-body effects is hidden into the exchange correlation term $E_{\text{xc}}[\rho]$, which remains the only unknown term of the energy functional[3] and needs to be approximated.

In order to avoid the practical difficulty of expressing the kinetic energy $E_{\text{kin.}}[\rho]$ through $\rho(\mathbf{r})$, due to the presence of the Laplace operator, Kohn and Sham [124] introduced a set of single particle auxiliary wave functions φ_i, yielding the same density of the system under consideration

$$\rho(\mathbf{r}) = \sum_{i=1}^{N}|\varphi_i(\mathbf{r})|^2. \tag{2.21}$$

[3]Remarkably, one can show [123] that the functional $E[\rho] - E_{\text{ion}}[\rho]$ is material independent. Hence, if one would know the exact DFT functional for a given material, one could calculate all materials by simply adding $E_{\text{ion}}[\rho]$.

Hence, one can perform the minimization of the energy functional in terms of these auxiliary wave functions as

$$\delta\Big\{E[\rho] - \sum_{1=1}^{N}\big[\epsilon_i \int d^3r\, |\varphi_i(\mathbf{r})|^2 - 1\big]\Big\}/\delta\varphi_i = 0, \tag{2.22}$$

where the Lagrange multipliers ϵ_i guarantee the normalization of the auxiliary wave functions. The above variational scheme yields the well-known Kohn-Sham (KS) equations

$$\Big[-\frac{\hbar^2}{2m_e}\Delta + V_{\text{ion}}(\mathbf{r}) + \int d^3r'\, V_{\text{ee}}(\mathbf{r}-\mathbf{r}')\rho(\mathbf{r}') + \frac{\delta E_{\text{xc}}[\rho]}{\delta\rho(\mathbf{r})}\Big]\varphi_i(\mathbf{r}) = \epsilon_i\varphi_i(\mathbf{r}), \tag{2.23}$$

which reduce the original interacting problem to a set of Schrödinger equations in a time-averaged potential generated by all other electrons (see also illustration in Fig. 2.3)

$$V^{\text{eff}}(\mathbf{r}) = V_{\text{ion}}(\mathbf{r}) + \int d^3r'\, V_{\text{ee}}(\mathbf{r}-\mathbf{r}')\rho(\mathbf{r}') + \frac{\delta E_{\text{xc}}[\rho]}{\delta\rho(\mathbf{r})}. \tag{2.24}$$

Note that the auxiliary wave function, solution of the KS equations, are introduced for the only purpose of minimizing the density energy functional, and have, hence, no physical meaning. Moreover, the kinetic energy term in (2.23), i.e.:

$$E_{\text{kin.}[\rho]} = -\sum_{i=1}^{N}\langle\varphi_i|\frac{\hbar^2}{2m_e}\Delta|\varphi_i\rangle, \tag{2.25}$$

corresponds to the kinetic energy of *independent* particles, while the one of the correlated system also includes many-body effects (e.g., in the form of a mass renormalization). The latter can be, nevertheless, absorbed into $E_{\text{xc}}[\rho]$, so that the many-body complexity is formally included in the exchange energy functional.
The KS equations (2.23) can be solved self-consistently according to the following scheme:

- an initial guess for the electron density is made;
- the effective density functional effective potential is determined by

$$V^{\text{eff}}(\mathbf{r}) = V_{\text{ion}}(\mathbf{r}) + \int d^3r'\, V_{\text{ee}}(\mathbf{r}-\mathbf{r}')\rho(\mathbf{r}') + \frac{\delta E_{\text{xc}}[\rho]}{\delta\rho(\mathbf{r})}. \tag{2.24}$$

- the KS equations (2.23) are solved, yielding the auxiliary wave functions φ_i and the Lagrange multipliers ϵ_i;
- the density is updated, by means of equation (2.21);
- the whole process is iterated till convergence;

Obviously, in order to build the KS effective potential (2.24), one has to make an approximation for the unknown exchange energy functional $E_{\text{xc}}[\rho]$. In this respect, several schemes have been proposed, however, the choice of a given approximating functional able to reproduce material-specific properties is often still a matter of debate in the DFT community. Among the possible approximations, perhaps the most widely employed is LDA, where $E_{\text{xc}}[\rho]$ is replaced with a functional of the local density only:

$$E_{\text{xc}}[\rho] \approx \int d^3r\, \epsilon_{\text{xc}}^{\text{LDA}}(\rho(\mathbf{r})). \tag{2.26}$$

In order to ease numerical calculations, the LDA exchange correlation functional $\epsilon_{\text{xc}}^{\text{LDA}}$ can be a parametrized analytic function. It can be obtained by, e.g., the solution of the homogeneous electron gas (HEG, or jellium) model, defined by a constant potential $V_{\text{ion}} = \text{const.}$, yielding a constant electronic density $\rho(\mathbf{r}) = \rho_0$. Evidently, such an approximation is reasonable for materials characterized by a slowly varying electron density, or equivalently, with small density gradients.[4] Hence, it may be suitable for materials with s- or p-orbital valence electrons, while it is no longer justified in strongly correlated transition-metal and rare-earth compounds, characterized by open shells of narrow d- and f-orbitals.

Adopting the LDA for the exchange energy functional is equivalent to place the *ab-initio* Hamiltonian (2.18) with the following effective one-particle (LDA) Hamiltonian

$$\mathcal{H}_{\text{LDA}} = \sum_{\sigma} \int d^3r\, \psi^{\dagger}(\mathbf{r},\sigma)\Big[-\frac{\hbar^2}{2m_e}\Delta + V^{\text{LDA}}(\mathbf{r})\Big]\psi(\mathbf{r},\sigma). \tag{2.27}$$

where the effective LDA potential is defined as

$$V^{\text{LDA}}(\mathbf{r}) = V_{\text{ion}}(\mathbf{r}) + \int d^3r'\, V_{\text{ee}}(\mathbf{r}-\mathbf{r}')\rho(\mathbf{r}') + \frac{\partial E_{\text{xc}}^{\text{LDA}}(\rho(\mathbf{r}))}{\partial \rho(\mathbf{r})}. \tag{2.28}$$

One can, hence, solve the KS equation (2.23) with the LDA exchange correlation energy functional (2.26), expanding the many-body wave functions in a suitable basis. However, with the idea of performing LDA+DMFT calculations (see below), one needs also to define a set of localized orbitals; possible choices are plane waves projected onto Wannier orbitals [126], or Muffin Tin Orbitals (MTO), either in the linear (LMTO) [127] or the Nth-order (NMTO) [128] version.

As already mentioned, LDA has revealed indeed quite successful and established itself as *the* method for the realistic material calculation. However, it fails in describing the bandstructure of correlated materials, the major reason being the presence of localized states, which strongly modify the electronic density distribution with respect to the one of a weakly correlated HEG. In other words, the LDA prescription (2.26) for the exchange energy functional leads to an effective one-particle approach, where the effect of other electrons is treated within a static (time-averaged) mean-field.

[4] More sophisticated exchange energy functionals, beyond the LDA one, can be obtained, e.g., within the Generalized Gradient Approximation (GGA) (see, e.g., Ref. [125] and references therein) or by means of hybrid functionals.

2.2.2 LDA+DMFT

Both the *ab-initio* and the model Hamiltonian paths have been extensively followed by modern solid-state theorists, and despite being very different in spirit, those approaches result nevertheless complementary. More recently, important advances came along from the ‘‘marriage’’ of the two schools, giving ‘‘birth’’ to a joint approach, where many-body techniques are merged into first principles schemes, able to make quantitative predictions for strongly correlated materials.

Obviously, the full LDA basis would be impossible to handle by means of an impurity solver (see also Sec. 2.1), and its delocalized nature will be also not appropriate to define an Hubbard-like interaction as in Eq. (2.1). Thus, in order to perform LDA+DMFT calculations, we need to trace out of the full LDA Hamiltonian the subspaces which are irrelevant for the description of the physical processes we are interested in. More precisely, the effective low-energy Hamiltonian is projected onto a basis of localized orbital, where we define the (local) interaction Hamiltonian

$$\psi^\dagger(\mathbf{r},\sigma) = \sum_{i\ell} \varphi^*_{i\ell}(\mathbf{r}) c^\dagger_{i\ell\sigma}, \tag{2.29}$$

where $c^\dagger_{i\ell\sigma}$ denotes the creation operator of an electron on site i and orbital ℓ, associated to the wave function $\varphi^*_{i\ell}(\mathbf{r})$. Hence, the LDA Hamiltonian **downfolded/projected** onto a suitable local basis, takes the tight-binding form

$$\mathcal{H}^*_{\mathrm{LDA}} = \sum_\sigma \sum_{ij} \sum_{\ell m} t_{ij\ell m} c^\dagger_{i\ell\sigma} c_{jm\sigma}, \tag{2.30}$$

where the hopping matrix elements are defined through the effective LDA potential (2.28) as

$$t_{ij\ell m} = \int d^3r \; \varphi^*_{i\ell\sigma}(\mathbf{r}) \Big[-\frac{\hbar^2}{2m_e}\Delta + V^{\mathrm{LDA}}(\mathbf{r}) \Big] \varphi_{jm\sigma}(\mathbf{r}). \tag{2.31}$$

One has, however, to keep in mind that the identification of the minimal basis set that takes into account the relevant physics is a delicate issue and strongly material dependent. In the most fortunate cases the correlated manifold is well separated from the others, and the process is relatively straightforward. On the other hand, there are cases in which the hybridization between, e.g. the d bands of the transition metal and the sp bands of the surrounding ligands is not negligible and the latter bands play an active role in the physical processes.

A generic form of the effective Hamiltonian for LDA+DMFT reads, hence

$$\mathcal{H} = \mathcal{H}^*_{\mathrm{LDA}} + \sum_i \sum_{\ell\ell' mm' \in L_U} \sum_{\sigma\sigma'} U_{i\ell m\ell' m'} c^\dagger_{i\ell\sigma} c^\dagger_{im\sigma'} c_{im'\sigma'} c_{i\ell'\sigma}, - \sum_i \sum_{\ell\in L_U} \sum_\sigma \Delta\epsilon \, n_{i\ell\sigma}, \tag{2.32}$$

where the interaction is only taken onto account in the subspace L_U of the correlated orbitals. This means that $U_{i\ell m\ell' m'}$ are effective parameters describing the local interaction, screened by the electrons residing in the orbitals projected out, typically estimated with the constrained LDA (cLDA) method. The task of determining the interaction parameters *ab-initio* is a prominent issue, and represents an active field of forefront research. However, the actual derivation of the

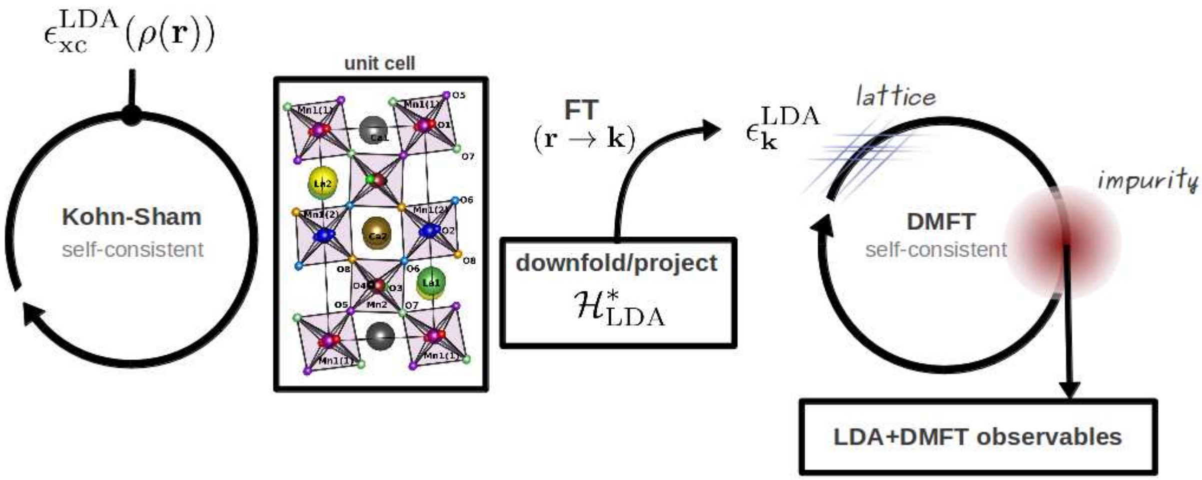

Figure 2.4: Flowchart for the LDA+DMFT scheme. The LDA approximation for the exchange energy functional allows the (numerical) self-consistent solution of the KS equations, yielding the LDA one-particle eigenstates of the while unit cell (in the box the sample case of $La_{0.5}Ca_{0.5}MnO_3$ is shown). A downfolding or a Wannier projection procedure provides the input for the DMFT self-consistency.

interaction parameters is beyond the scope of this work, and for a detailed discussion of the problem we remand, e.g., to Ref. [121] and references therein.
It is also important to consider that LDA already takes into account rudimentarily part of the interaction effects, such as the static Hartree contribution of the Coulomb interaction. This leads to the additional well-known *double counting* problem when using an LDA input to perform DMFT. In order to mitigate this problem, one needs to introduce a correction $\Delta\epsilon$ to each of the on-site energies of the orbitals in the correlated subspace, taking into account the contributions of the interaction already included in LDA: $\epsilon^{\rm LDA}_{i\ell m\sigma} \to \epsilon^{\rm LDA}_{i\ell m\sigma} - \delta_{\ell m}\Delta\epsilon$, for $\ell, m \in L_U$. A physically sensible and consistent way to do this is unknown, at least in the framework of LDA+DMFT, yet for the most well-known prescription we refer, e.g., to Refs. [129, 130].

In practice an LDA+DMFT calculation is implemented as follows (see also Fig. 2.4). In the case of solids, where the real-space translational symmetry is granted by the periodic structure of the underlying ionic lattice, one can calculate the LDA bandstructrure by means of a FT of the hopping matrix on a coarse-grained Brillouin zone

$$\epsilon^{\rm LDA}_{\ell m}(\mathbf{k}) = \frac{1}{L}\sum_{ij} t_{ij\ell m} \mathrm{e}^{-\imath \mathbf{k}(\mathbf{R}_i - \mathbf{R}_j)}, \tag{2.33}$$

where L denotes the number of lattice positions R_i of the atoms in the unit cell. The LDA bandstructure $\epsilon^{\rm LDA}_{\ell m}(\mathbf{k})$ represents the *ab-initio* input of the LDA+DMFT calculations. The local Green's function of the corresponding lattice model is defined as

$$G_{\rm loc}(\nu) = \sum_{\mathbf{k}} \frac{1}{\nu - \epsilon^{\rm LDA}_{\ell m}(\mathbf{k}) - \Sigma(\nu)}. \tag{2.34}$$

Hence, the corresponding auxiliary local impurity problem, defined analogously to Eq. (2.13), can be solved self-consistently within the DMFT scheme described in the previous section. This way, one is able to include local correlation effects *on top* of LDA. Most of the calculations are performed in this spirit, albeit depending on the change of occupation in the different orbitals, a fully self-consistent LDA+DMFT calculation may also be needed.

2.3 Including correlations beyond DMFT

The Hubbard interaction represents obviously a drastic approximation to the Coulomb repulsion: it retains only its local contribution under the assumption that the strength of the (screened) interaction falls with distance fast enough that non-local interaction on the typical lattice distance are essentially negligible. However, even assuming this assumption to be correct, leading to an effective interaction purely local in space, non-local spatial correlations may still arise. Those spatial correlations, when non negligible, have profound consequences on the physics and need to be taken into account, beyond the mean-field picture of DMFT, in order to quantitatively describe the properties of the system. An instructive example concerns the Néel temperature T_{N} associated to the paramagnetic to antiferromagnetic (AF) transition in the lattice model: for the Hubbard model in $d=2$, DMFT predicts a finite T_{N} while it should instead be exactly zero, according to the theorem of Mermin & Wagner for second order phase transitions [131]. Such intrinsic limitations of DMFT motivated to include non-local correlations beyond mean-field into account. In fact, many possible extensions of DMFT, which recover DMFT in some well-defined limit, were proposed. In the following we briefly review the main ones, in order to provide an overview on the theories of electronic correlations beyond (dynamical) mean-field.

Chronologically, one of the first extensions to DMFT was the $1/d$ expansion [132], which was meant to be the natural analytic extension of DMFT. It is based on the idea of making a resummation of all skeleton diagrams with inter-site distance not greater than n: for $n=0$ DMFT is recovered, while at higher inter-site distance n would give the leading corrections to DMFT to order $1/d^n$. However, though formally elegant, the method revealed itself to be of scarce practical use: in fact, when non-local correlations become really relevant, retaining only the leading terms in a $1/d$ expansion does not provide any longer a reasonable approximation. Moreover, in some parameter region, the method can develop non-analyticities originated from the violation of the causality principle.

The forthcoming extensions to DMFT, whose application has been more successful than the $1/d$ expansion, can mainly be grouped into **cluster** [134] and **diagrammatic extensions**.
To the former branch belongs the cellular-DMFT [133] and the dynamical cluster approximation (DCA) [135, 136]. The main idea of the cluster extensions is to approximate the spatial correlations of the infinite lattice with those of a finite-size cluster. Therefore, both methods map the original lattice problem *not* onto a single-site AIM, but onto a cluster of lattice sites embedded into a self-consistent bath, with the main difference that the cluster is built in real

(cellular-DMFT) or in momentum space (DCA). In both cases, DMFT is recovered in the limit in which the cluster collapses to a site. Those theories allows one to naturally take into account *short-range* correlations within the cluster size exactly, while treating correlations at longer length scales within mean-field. To include short range non-local correlations is certainly important, as they, e.g., suppress the Neél temperature T_{N} with respect to the DMFT predictions, and to restore the k-dependence of the self-energy allows one to describe phases characterized by a non-local order parameter, such as spin density waves (SDW) or d-wave superconductivity [137]. Cluster extensions were indeed quite successful and are still probably the most well established extension to DMFT. Among the most important achievements we recall investigation of the phase diagram, and in particular the pseudogap phase of the two-dimensional Hubbard model [134, 138, 139], and of the interplay between electronic correlation and structural (Peierls) distortions in VO_2 [140, 142, 141].

However, cluster theories are numerically much more demanding than DMFT, as the size of the Hilbert space of the effective impurity model, defined on a cluster of lattice sites, is much larger compared to the one of the single impurity Anderson model. This obviously impose limitations to the maximal cluster size (especially in the three dimensional case) and the intrinsic finiteness of the cluster prevents one to treat long-range correlations, almost certainly of importance in critical regions. In order to access information on the thermodynamical system, one usually needs to make extrapolations as a function of the cluster size. However such a procedure is delicate and its accuracy can depend both on the system, on the cluster geometry, and on the physical quantity considered. At the same time, for each fixed cluter size (no matter how large), cluster theories will always find a mean-field critical behavior (i.e., critical exponents) close to the phase transition, and may still lead (as well as DMFT does) to unphysical phase transition prohibited by the theorem of Mermin & Wagner [131]. Perhaps, in this context it is worth to notice that though being both self-consistent and Φ-derivable in the sense of Baym and Kadanoff [143, 144], DMFT, as well as its cluster extensions are not conserving, as all of them violate local momentum conservation, and are therefore likely to violate some set of Ward identities [134, 136].

Those drawbacks became the main motivation to develop **complementary extensions** to DMFT, where the approximations are introduced at the diagrammatic level. The main approximations in this spirit are the dynamical vertex approximation (DΓA) [145, 146, 147] and the dual fermion (DF) [149] approach. The basic idea of those methods is very similar, as they aim to introduce non-local correlations at all length scales performing an approximation at the level of two-particle quantities.

In the case of the DF approach, the approximation is done in a dual fermion space, defined via an Hubbard-Stratonovich transformation performed on the hopping term of Hamiltonian (2.1), or to be more precise, on the difference between the hopping term and the dynamic Weiss field. The transformation yields an effective local problem in the dual fermion space to be perturbatively expanded around its non-interacting limit, which corresponds, in the original space, to DMFT. The theory is conserving in the sense of Baym and Kadanoff (though this was proven only for the dual space [149, 150]), and the coefficients of the Taylor expansion are the dual n-particle Green's functions, e.g., for $n=2$ the coefficient corresponds to the dual two-particle reducible vertex functions F. This series is claimed to be rapidly converging, and the method allows one to compute the susceptibilities in the Hubbard model [151], although this has been recently questioned in Ref. [152]. Retaining the lowest order in the effective dual interaction F is not enough and, for example, in order to reproduce the pseudogap formation one needs to build a ladder solution of the Bethe-Salpeter equation [150]. Recently the DF method has also been combined with DCA [153] in the framework of the so-called multiscale approach [154].

In the case of DΓA instead, the diagrammatic approximation is directly applied to the space of the physical fermions. It consists in requiring the locality of the two-particle fully irreducible vertex Λ (often called also $\Gamma_{\mathrm{i}rr}$, from which stems the name of the method), in order to include non-local fluctuations in the one-particle irreducible self-energy. Among the achievement of DΓA in the context of bulk systems, we recall the study of the spectral properties of the Hubbard model at half-filling both in $d=3$ and $d=2$ [145, 147]. Noteworthy, in the latter case, a proper treating of non-local spatial correlations beyond mean-field are shown to restore a zero Néel temperature, as well as to determine the formation of a pseudogap state at intermediate T, providing significant qualitative and quantitative improvement with respect of DMFT. Moreover, within DΓA it is also possible to address critical properties close to a second order phase transition, as it was done, e.g., for the critical exponents of the $d=3$ Hubbard model [168].

Since DΓA represents the starting point, we have chosen for dealing with correlated nanostructures, it is worth to discuss this approximation in more details.

2.3.1 Dynamical Vertex Approximation

In order to understand the diagrammatics of DΓA, it is useful to recall, and make a comparison with the diagrammatics of DMFT. From the diagrammatic point of view, DMFT corresponds to all the topologically distinct, purely local, one-particle irreducible skeleton diagrams for the self-energy. The approximation is justified in high dimasions by the scaling of the Green's function in the limit $d\to\infty$, in which all non-local contribution becomes irrelevant, and DMFT is exact (see Sec. 2.1).

A systematical generalization of DMFT can indeed be obtained by requiring the locality of the n-particle irreducible vertex, allowing, in turn, all irreducible vertices of lower orders n–1, n–2, ... to be non-local [145, 147]. At $n=1$ the one-particle irreducible vertex corresponds to the self-energy, so that DMFT is recovered, while the limit $n\to\infty$ corresponds to consider all diagrams, and therefore to the exact solution of the Hubbard model, which is, however, unknown. In this framework, the DΓA corresponds to require the locality of the $n=2$-particle fully irreducible vertex allowing the self-energy to be non-local (see Fig. 2.5). Indeed, once the two-particle fully irreducible local vertex has been determined, it allows one to compute the two-particle full vertex function $F^{\nu\nu'\omega}_{kk'q\uparrow\downarrow}$, which enters the exact equation of motion (also

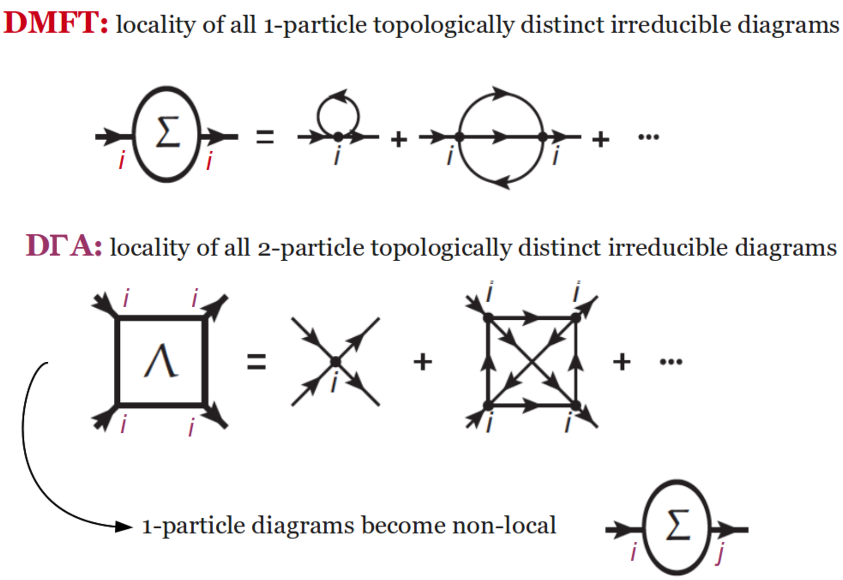

Figure 2.5: DMFT and DΓA from the diagrammatic point of view. DMFT corresponds to all local one-particle irreducible diagrams for the self-energy, while DΓA assumes the locality of the two-particle fully irreducible vertex in order to include non-local contribution in the self-energy. Adapted after Ref. [155].

known as Dyson-Schwinger equation) for the self-energy

$$\Sigma_k(\nu) = U\frac{n}{2} - UT^2 \sum_{\nu'\omega} \sum_{kq} F^{\nu\nu'\omega}_{kk'q\,\uparrow\downarrow} G_{k'+q}(\nu'+\omega) G_{k'}(\nu') G_{k+q}(\nu+\omega). \tag{2.35}$$

This way, the information of non-local spatial correlations beyond mean-field can be included non-parturbatively in the self-energy, and into valuable two-particle quantities, e.g., the susceptibilities.

The justification of the approximation employed in DΓA is the following. The fully irreducible diagrams are by definition the most compact ones i.e., they cannot build any kind of ladder (see Sec. 2.3.2 below): those diagrams are hence the closest one to the bare interaction in the case of the Hubbard model, where the interaction U is purely local in space. It is therefore reasonable to expect only a weak momentum dependence of the two-particle fully irreducible vertex also in finite dimensions, making the assumption behind DΓA particularly plausible. Indeed, numerical evidence supporting the reliability of this argument was recently reported [156] within DCA in the two-dimensional Hubbard model at non-integer density.[5] While this would not hold any longer in presence of *non-local interactions*, e.g., the full Coulomb potential $V(\mathbf{r}) \sim 1/\mathbf{r}$, long-range interaction terms may still be taken into account within the mean-field approximation, or within further extensions of the diagrammatic methods, such as the recently proposed *ab-initio* DΓA [157] or Dual Boson [148] methods.

[5]It was rather a sporadic investigation, concerning with the structure of the pairing interaction in a case relevant for the superconducting instability in the cuprates.

The main task is, hence, to compute the two-particle fully irreducible local vertex Λ non-perturbatively at all orders. This is more conveniently done at the level of the single-site AIM, exploiting the self-consistency relation between the impurity Green's function and the local Green's function of the original lattice. In this respect, the flowchart of DΓA is conceptually similar to the one of the DMFT, as in both methods the lattice problem is mapped onto an AIM. In DΓA however, one is required to fully compute local two-particle quantities out of the AIM, thus enhancing the workload associated to the solution of the impurity problem. Nevertheless, this workload is still lower than the one required by, e.g., DCA for large cluster sizes, which is an essential property for the future development of the method [157].

2.3.2 Diagrammatics & Parquet formalism

The main part of the following discussion and the derivation of the parquet formalism is published in the APS Journal ''Physical Review B'': PRB **86**, 125114 (2012) [158].

In order to understand the essence of DΓA we need to define some fundamental quantities and to get familiar with the diagrammatic formalism of the two-particle vertex functions. This is most conveniently done in the context of the AIM, which is used to evaluate two-particle local vertex functions in DMFT and its extensions. However, a formal and extended derivation of the diagrammatic relation presented below in beyond the scope of this work, and for this purpose we refer instead to Ref. [158], where state-of-the-art of the knowledge about two-particle local vertex functions has been revised and completed in a unified formalism.

General definitions. The starting point of the following analysis is the Hamiltonian of the AIM (2.5), which we recall here for the sake of clarity in a notation consistent with the notation adopted in Ref. [158]

$$\mathcal{H}_{\mathcal{AIM}} = \sum_{k\sigma} \epsilon_{\mathbf{k}\sigma} a^{\dagger}_{k\sigma} a_{k\sigma} + \sum_{k\sigma} V_k (a^{\dagger}_{k\sigma} c_{\sigma} + \mathrm{h.}c.) + U n_{\uparrow} n_{\downarrow}, \tag{2.36}$$

where $c^{\dagger}_{\sigma}$ (c_{σ}) are the creation (annihilation) operator of an impurity electron, and $n_{\sigma} = c^{\dagger}_{\sigma} c_{\sigma}$ is the corresponding electronic density at the impurity site. Here $a^{\dagger}_{k\sigma}$ ($a_{k\sigma}$) are the creation (annihilation) operators of a conduction electron with spin σ, momentum k, and energy $\epsilon_{k\sigma}$, and V_k describes the hybridization between the impurity and the conduction band.

Besides the one-particle Green's function, at the two-particle level one usually defines the **generalized susceptibility**, as a combination of one- and two-particle Green's functions

$$\chi_{\sigma_1\sigma_2\sigma_3\sigma_4}(\tau_1, \tau_2, \tau_3, \tau_4) := G_{\sigma_1\sigma_2\sigma_3\sigma_4}(\tau_1, \tau_2, \tau_3, \tau_4) - G_{\sigma_1\sigma_2}(\tau_1, \tau_2) G_{\sigma_3\sigma_4}(\tau_3, \tau_4), \tag{2.37}$$

which represents the fundamental two-particle local quantity needed to be computed on the impurity level. The notation can be substantially simplified taking into account the symmetries of the system. Due to the time-translational invariance of (2.36) and exploiting the properties of the Matsubara representation for the Green's functions, one can restrict the imaginary time τ domain to $[0,\beta)$ and set $\tau_4=0$, yielding

$$\chi_{\sigma_1\sigma_2\sigma_3\sigma_4}(\tau_1,\tau_2,\tau_3,0)=G_{\sigma_1\sigma_2\sigma_3\sigma_4}(\tau_1,\tau_2,\tau_3,0)-G_{\sigma_1\sigma_2}(\tau_1,\tau_2)G_{\sigma_3\sigma_4}(\tau_3,0). \tag{2.38}$$

Moreover, in the $SU(2)$ symmetric case considered here, due to the conservation of spin, among the $2^4=16$ combination of $\sigma_1\ldots\sigma_4$, only 3×2 are actually independent: i) $\sigma_1=\sigma_2=\sigma_3=\sigma_4$, ii) $(\sigma_1=\sigma_2)\neq(\sigma_3=\sigma_4)$, and iii) $(\sigma_1=\sigma_4)\neq(\sigma_2=\sigma_3)$, with $\sigma_1=\uparrow,\downarrow$ in each case. This suggests the following definitions, which cover all the possible combination mentioned above.

$$\chi_{\sigma\sigma'}(\tau_1,\tau_2,\tau_3)=\chi_{\sigma\sigma\sigma'\sigma'}(\tau_1,\tau_2,\tau_3), \tag{2.39a}$$

$$\chi_{\overline{\sigma\sigma'}}(\tau_1,\tau_2,\tau_3)=\chi_{\sigma\sigma'\sigma'\sigma}(\tau_1,\tau_2,\tau_3). \tag{2.39b}$$

Furthermore one can show that the two previous definitions of the susceptibility are related by the crossing symmetry [158, 159, 160] and that, in the Fourier space, e.g, the definition (2.39a) can be obtained by the one of (2.39b) by means of a mere frequency shift (cf. also the Appendixes of Ref. [158]). In light of the previous considerations, for the rest of this work, we will here restrict ourselves to the susceptibility (2.39a) keeping in mind that all relations derived for this will apply, without any restriction, to (2.39b) as well.

A clearer interpretation of the susceptibility in terms of Feynman diagrams, is obtained in Fourier frequency space, where the susceptibility can be defined equivalently in both the **particle-hole** (ph) and **particle-particle** (pp) **notation**, as

$$\begin{aligned}\chi^{\nu\nu'\omega}_{ph,\sigma\sigma'} &:= \chi\big(\underbrace{\nu\sigma,(\nu+\omega)\sigma}_{\text{outgoing electrons}};\underbrace{\nu'\sigma',(\nu'+\omega)\sigma'}_{\text{incoming electrons}}\big)=\\ &=\int_0^\beta d\tau_1 d\tau_2 d\tau_3\,\chi_{\sigma\sigma'}(\tau_1,\tau_2,\tau_3)\mathrm{e}^{-i\nu\tau_1}\mathrm{e}^{i(\nu+\omega)\tau_2}\mathrm{e}^{-i(\nu'+\omega)\tau_3},\end{aligned} \tag{2.40a}$$

$$\begin{aligned}\chi^{\nu\nu'\omega}_{pp,\sigma\sigma'} &:= \chi\big(\underbrace{\nu\sigma,(\omega-\nu)\sigma'}_{\text{outgoing electrons}};\underbrace{(\omega-\nu')\sigma,\nu'\sigma'}_{\text{incoming electrons}}\big)=\\ &=\int_0^\beta d\tau_1 d\tau_2 d\tau_3\,\chi_{\sigma\sigma'}(\tau_1,\tau_2,\tau_3)\mathrm{e}^{-i\nu\tau_1}\mathrm{e}^{i(\omega-\nu')\tau_2}\mathrm{e}^{-i(\omega-\nu)\tau_3},\end{aligned} \tag{2.40b}$$

where we adopt the notation $\nu\equiv\nu_n^{(\prime)}=(2n^{(\prime)}+1)\pi/\beta$, $n^{(\prime)}\in\mathbb{Z}$, and $\omega\equiv\omega_l=(2l)\pi/\beta$, $l\in\mathbb{Z}$, for the fermionic and bosonic Matsubara frequencies, respectively.

The choice of the frequency convention for the susceptibilities (2.40a) and (2.40b) has a clear physical motivation: they describe an electron-hole (ph channel) and an electron-electron (pp channel) scattering process of total energy ω, respectively. It is worth to stress that the ph and pp notations defined above are introduced just for convenience in the definition of two-particle quantities in the pp channel, and that the corresponding susceptibilities are not independent, as can be obtained from each other by means of a frequency shift, i.e., both scattering processes are included in the definition (2.39a) of the two-particle Green's function. However, the equivalence of the notation may also be exploited in the numerical implementation of DΓA, lowering the workload associated to the evaluation of the generalized susceptibility. In this section we can restrict ourselves to one of the two expression in Eq. (2.40), e.g., to the ph channel, keeping in mind that all relations derived for χ_{ph} will apply, without any restriction, to χ_{pp} in the pp notation as well [158].

The scattering process defined above includes all possible interactions between the two incoming particles, and can be separated into a term describing the independent propagation of the two particles, and the vertex corrections (see Fig. 2.6)

$$\chi_{\sigma\sigma'}^{\nu\nu'\omega} = -\beta G_\sigma(\nu)G_\sigma(\omega+\nu)\delta_{\nu\nu'}\delta_{\sigma\sigma'} - G_\sigma(\nu)G_\sigma(\nu+\omega)F_{\sigma\sigma'}^{\nu\nu'\omega}G_\sigma(\nu')G_\sigma(\nu'+\omega). \quad (2.41)$$

The **full vertex** F contains the information of all possible scattering events between two propagating fermions, and can therefore be interpreted as the scattering amplitude between two quasi-particles, at least in the Fermi liquid regime, where one-particle excitations are still well defined. For convenience one also usually defines the bubble-like term, as

$$\chi_0^{\nu\nu'\omega} = -\beta G_\sigma(\nu)G_\sigma(\omega+\nu)\delta_{\nu\nu'}\delta_{\sigma\sigma'}, \quad (2.42)$$

where the spin index in the l.h.s. has been dropped, as we restrict to the paramagnetic case, so that Eq. (2.41) can be rewritten in compact form as

$$\chi_{\sigma\sigma'}^{\nu\nu'\omega} = \chi_0^{\nu\nu'\omega}\delta_{\sigma\sigma'} - \frac{1}{\beta^2}\sum_{\nu_1\nu_2}\chi_0^{\nu\nu_1\omega}F_{\sigma\sigma'}^{\nu_1\nu_2\omega}\chi_0^{\nu_2\nu'\omega}. \quad (2.43)$$

The two-particle full vertex F represents the fully connected part of the generalized susceptibility (2.41). Moreover, the set of those diagrams, can be further classified according to their **reducibility** property. Reducibility is an important concept in the diagrammatics and, in general for all diagrammatic techniques, it is of fundamental importance to make a clear distinction between *reducible* and *irreducible* diagrams. According, e.g., to Ref. [90], a diagram is classified as one-particle irreducible if it *cannot* be split into two parts by cutting a single internal line.

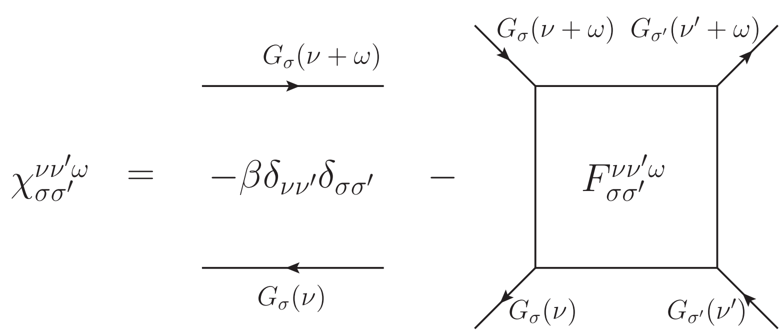

Figure 2.6: Diagrammatic representation of the generalized local susceptibility $\chi_{\sigma\sigma'}^{\nu\nu'\omega}$ in the ph notation, as defined in Eqs. (2.40a) and (2.41). In the interacting case, $\chi_{\sigma\sigma'}^{\nu\nu'\omega}$ is naturally decomposed into a bubble term $\chi_0^{\nu\nu'\omega}$, defined in Eq. (2.42), and the vertex corrections, expressed in terms of $F_{\sigma\sigma'}^{\nu\nu'\omega}$. After Ref. [158].

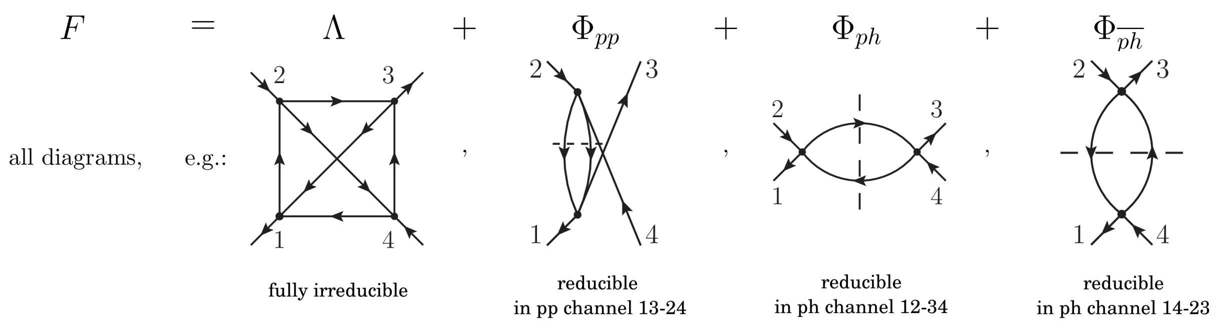

Figure 2.7: Parquet equation. Adapted after Ref. [158].

The self-energy corresponds per definition to the sum of all one-particle irreducible diagrams. At the two-particle level, the concept of reducibility becomes naturally more complex [158] and gives rise to a richer classification for the Feynman diagrams. We can indeed distinguish between:

- *Fully irreducible* diagrams, i.e., diagrams which cannot be separated into two parts by cutting *two* internal lines, which represents the two-particle counterpart of the self-energy diagrams at the one-particle level.

- *Reducible* diagrams. However, by cutting two lines, there is more than one possibility to separate a diagram. Hence, the concept of reducibility has to be referred to a specific *channel*. Each channel corresponds to a different way of separating (always pairwise) the four outer legs of a given diagram.

According to this classification, each diagram will be either fully irreducible, i.e., irreducible in all channels, or reducible in exactly one specific channel [158]. As a consequence, the full vertex can be expressed in terms of fully irreducible contributions (Λ) and reducible contribution in all the three channels (a particle-particle and two particle-hole) as

$$F = \Lambda + \Phi_{ph} + \Phi_{\overline{ph}} + \Phi_{pp}. \tag{2.44}$$

We omit, for the sake of simplicity, all spin and frequency indexes. Such a decomposition of F is known as **parquet equation** [161] and it is schematically illustrated in Fig. 2.7 with one low-order diagram shown for each of the four contributions. It is important to state that, being nothing more than a mere classification of diagrams, the parquet equations do *not* imply any kind of approximation.

In order to deal with the parquet equation, one can consider another significant subset of diagrams Γ_r, defined as

$$F = \Gamma_r + \Phi_r, \quad r = ph, \overline{ph}, pp, \tag{2.45}$$

corresponding to the diagrams *irreducible* in one specific channel $r = ph, \overline{ph}, pp$. This is easily understood, considering that each diagram included in F is either reducible or irreducible in a given channel. The Γ_r vertices can be directly computed from F by means of an integral equation, known as **Bethe-Salpeter equation**, as

$$F = \Gamma_r + \int \Gamma_r GGF, \tag{2.46}$$

where the integral symbol denotes the sum over all degrees of freedom (e.g., frequency, spin, $\ldots$). In fact, Eq. (2.46) does not add further information with respect to the definition of Γ_r (2.45): it follows immediately from that, considering that the set of the reducible diagrams Φ_r can be obtained by connecting Γ_r to the full vertex F via two Green's function lines. Such a construction is, by definition, reducible in channel r. Moreover, this decomposition is, obviously, not unique, as it can be performed independently for all channels.

It is important to notice the different channels (i.e., ph, $\overline{ph}$, and pp) are not completely independent, as they satisfy the so-called crossing symmetry [161], which is a direct consequence of the Pauli exclusion principle for fermions. Moreover, in the case of a $SU(2)$ symmetric Hamiltonan we consider here, as already discussed above, there are only three independent spin combinations, i.e. $\uparrow\uparrow$, $\uparrow\downarrow$, $\overline{\uparrow\downarrow}$. In this basis, two out of the three Bethe-Salpeter equation (2.46) are coupled (within each channel), so that it convenient to decouple them (analytically) performing a **spin diagonalization**, i.e., defining the (d)ensity, (m)agnetic, (s)inglet, and (t)riplet channels as

$$F_{d.m}^{\nu\nu'\omega} := F_{\uparrow\uparrow}^{\nu\nu'\omega} \pm F_{\uparrow\downarrow}^{\nu\nu'\omega}, \tag{2.47a}$$

$$F_{s,t}^{\nu\nu'\omega} := F_{pp,\uparrow\downarrow}^{\nu\nu'\omega} \pm F_{pp,\overline{\uparrow\downarrow}}^{\nu\nu'\omega}, \tag{2.47b}$$

where the subscript pp denotes that the relation in this form holds in the pp (frequency) notation. In an analogous way one defines also the (ir)reducible vertices Φ_r (Γ_r) as well as a fully irreducible vertex Λ, and the decoupled Bethe-Salpeter equations read, hence,

$$F_{d,m}^{\nu\nu'\omega} = \Gamma_{d,m}^{\nu\nu'\omega} + \frac{1}{\beta}\sum_{\nu_1} \Gamma_{d,m}^{\nu\nu_1\omega} G(\nu_1)G(\nu_1+\omega)F_{d,m}^{\nu_1\nu'\omega}, \tag{2.48a}$$

$$F_{s,t}^{\nu\nu'\omega} = \Gamma_{s,t}^{\nu\nu'\omega} - \frac{1}{2}\frac{1}{\beta}\sum_{\nu_1} \Gamma_{s,t}^{\nu_1\nu'\omega} G(\nu_1)G(\omega-\nu_1)F_{s,t}^{\nu(\omega-\nu_1)\omega}, \tag{2.48b}$$

where the factor two in the pp vertex functions arises due to the indistinguishability of identical particles [161]. An important remark: while Γ_r and Φ_r are, by definition, channel-dependent, this is not the case for the F and Λ, and even if one can formally define channel-dependent quantities, there is only two independent full vertex and fully irreducible vertex functions exist. More generally, all vertex functions in the d, m, s, and t channels are not completely independent, and several symmetry relations can be derived at all levels of diagrammatics. However, a comprehensive discussion of those symmetry relations, as well as a thoughtful derivation of the diagonalized Bethe-Salpeter equations above, is beyond the scope of this thesis, and we refer to Refs. [158, 161] for a detailed reading.

As already mentioned, in DΓA the AIM is a mere tool which can be exploited in order to calculate (numerically) the exact two-particle fully irreducible local vertex Λ. The vertex function extracted from the AIM will approximate the local one of the Hubbard model, assuming the equivalence between the impurity and the lattice local Green's function. In the following we show (i) how to combine the relation above in order to extract the fully irreducible local vertex Λ from an AIM, and (ii) how to use it in order to compute a non-local self-energy solving the parquet equations.

Including non-local spatial correlations within DΓA. In the following we discuss the complete flowchart of DΓA. It consists of two main blocks: one relying on the definition and the numerical solution of a proper AIM, in order to extract the two-particle fully irreducible local vertex, the other on the solution of the parquet equations in the reciprocal space of the original lattice, in order to extract the non-local DΓA self-energy.

As for DMFT, also within DΓA one needs an initial guess for the AIM (see also Sec. 2.1) associated to the lattice problem at hand, which translates into a guess for the self-energy entering the local Green's function (2.12). However, DΓA requires the knowledge of the generalized (local) susceptibility (2.40) in Matsubara representation, whose numerical evaluation is computationally heavier with respect to the evaluation of the (local) self-energy. It can reliably be obtained, e.g., within ED by means of the Lehmann representation (for an explicit expression see, e.g., Ref. [145]), though it is most likely limited to the one-band model, or within QMC, measuring the τ-ordered product (2.38), provided the asymptotic behavior is treated properly in the FT process [112, 162, 163], as discussed also in Appendix B.

In order to **extract the two-particle fully irreducible local vertex** Λ, by ''inverting'' the parquet equation (2.44), one needs to separate the full vertex F into its reducible (Φ_r) and irreducible (Γ_r) contributions in each channels. The full vertex function F is trivially evaluated by means of the definition (2.41), and an expressions for the irreducible vertex Γ_r can be derived, e.g., substituting the Bethe-Salpeter equations (2.48a) and (2.48b) in each channel into 2.41), yielding

$$\Gamma_{d,m}^{\nu\nu'\omega} = \beta^2(\chi_{d,m}^{-1} - \chi_0^{-1})^{\nu\nu'\omega}, \tag{2.49a}$$

$$\Gamma_{s,t}^{\nu\nu'\omega} = \beta^2\big[4(\chi_{s,t} \mp \chi_{0,pp})^{-1} \pm 2\chi_{0,pp}^{-1}\big]^{\nu\nu'\omega}. \tag{2.49b}$$

Once that F and the Γ_r's are known, the Φ_r's are accessible by means of Eq. (2.45). Hence, it is a trivial algebraic task to invert the parquet equation (2.44) in order to the fully irreducible vertex Λ, which remains the only unknown. This procedure is illustrated in Fig. 2.8 in the upper part of the DΓA flowchart.

In order to **evaluate the non-local self-energy** of the original lattice, one can employ the exact equation of motion

$$\Sigma_k(\nu) = U\frac{n}{2} - UT^2\sum_{\nu'\omega}\sum_{kq} F_{kk'q\,\uparrow\downarrow}^{\nu\nu'\omega} G_{k'+q}(\nu'+\omega)G_{k'}(\nu')G_{k+q}(\nu+\omega). \tag{2.35}$$

where $F_{kk'q}^{\nu\nu'\omega}$ is the *non-local* full vertex function corresponding to the local fully irreducible vertex Λ of the AIM. This means that one has to solve the parquet equation on a *coarse-grained* Brillouin zone for the lattice, in order to generate a momentum-dependent $F_{kk'q}^{\nu\nu'\omega}$. As the only

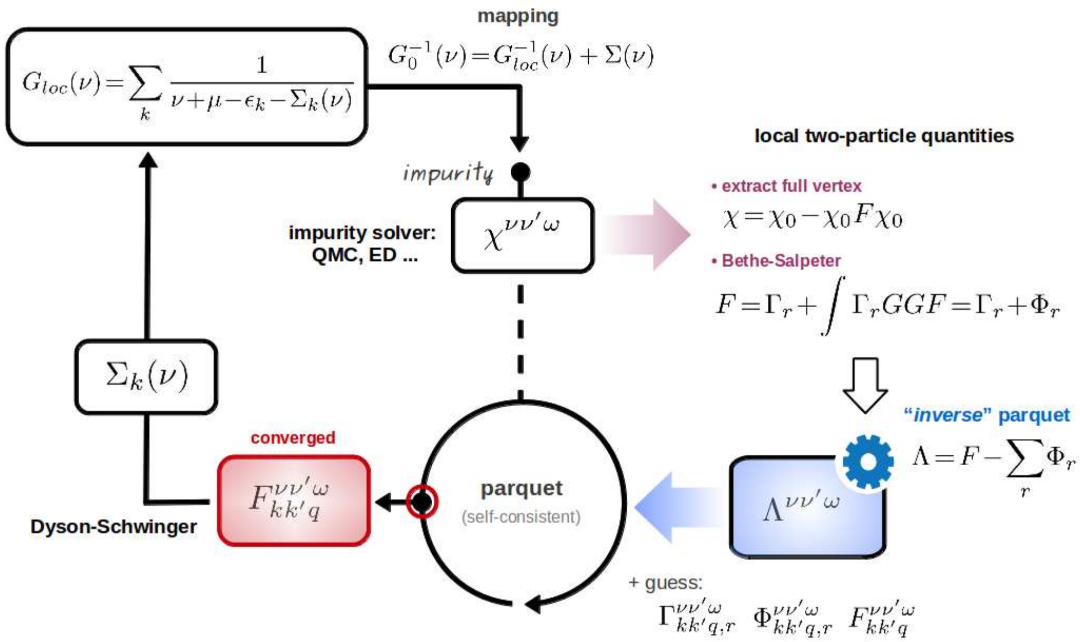

Figure 2.8: Flowchart of DΓA: the lattice problem is mapped onto an auxiliary AIM, use to obtain local two-particle vertex functions; the solution of the (inverse) parquet equation yields the two-particle fully irreducible local vertex Λ. The self-consistent solution of the parquet equation on the lattice, using Λ as input, yields the momentum-dependent two-particle full vertex, needed to compute the non-local lattice self-energy of DΓA.

known quantity is the local fully irreducible vertex Λ, one has to start from an educated guess for all momentum-dependent vertex functions, i.e., $\Gamma^{\nu\nu'\omega}_{kk'q,r}$, $\Phi^{\nu\nu'\omega}_{kk'q,r}$, and $F^{\nu\nu'\omega}_{kk'q,r}$ itself (usually they are set equal to the bare interaction U). The parquet equations are solved self-consistently: the momentum dependent quantity will flow till some convergency criterion is met, while the fully irreducible vertex will *not* be updated in the procedure. While this may seem to be a prohibitively expensive task (in particular if compared to the solution of the inverse parquet equation for the AIM) the solution of the parquet equations is indeed doable, and a solver was recently made available from the group of Jarrell [164, 165]. The procedure to obtain the non-local self-energy is illustrated in Fig. 2.8 in the lower part of the DΓA flowchart.

In principle. also the whole DΓA cycle should be performed self-consistently. This is obviously extremely expensive from the computational point of view. Thus, the previous calculations were performed within a one-shot (ladder) DΓA approximation [145] on top of a DMFT self-consistently converged loop. Obviously, this implementation is not independent on the initial conditions: e.g., it relies on the DMFT Neél temperature T_N^{DMFT}, which is intrinsically not accurate due to its mean-field nature. In particular in the $d=2$ case, $T_N^{\mathrm{DMFT}}>0$ (violating the theorem of Mermin & Wagner) resulting in an overestimation of antiferromagnetic fluctuation at finite T. This problem has been overcome however, by introducing a Moriyasque λ-correction to the susceptibility [147, 168].

2.4 Extension to nanoscopic systems

So far we provided the general concepts of how many-body effects in lattice model Hamiltonians are taken into account within DMFT and its extensions. We restricted to the case of the Hubbard model, but DMFT has been also successfully applied to other models, like the Falicov-Kimbal [169] or the Kondo lattice [170] models. In the following we discuss the applicability of those techniques to correlated nanostructures. After a brief introduction to generic issues in this context, we present the basic idea (Sec. 2.4.1) and the flowchart (Sec. 2.4.2) of a novel method we developed, which provides a flexible way to apply DMFT and its extensions to nanoscopic systems. To conclude, we also discuss similarities and differences with alternative methods reported in the literature (Sec. 2.4.3).

Independently on the model one is considering, as soon as the complexity of the effective low-energy model increases, performing many-body calculations becomes extremely challenging. The exponential growth of the Hilbert space of the auxiliary impurity problem to be solved, due to an increasing number of correlated bands in the relevant low-energy manyfold, or of sites in a cluster, imposes a severe limitation on the system size, even for the most advanced and efficient impurity-solver algorithms.

Hence, if one aims to address the problem of correlation effects at nanoscopic scales, i.e., for systems with a finite number of sites, it is clear that any exact treatment of the problem suffers from analogous scalings with the size of the Hilbert space, and therefore does not allow to deal with more than few coupled sites. The lack of a proper tool for a theoretical investigation of electronic correlations at the nanoscale motivated the development of a novel approximation scheme, based on DMFT and its extensions, which may be suitable to treat complex networks of correlated sites. However, the application of DMFT and its extensions at the nanoscale is not straightforward. In the lattice, one can take advantage of the translational invariance granted by the underlying periodic structure, and of the equivalence of lattice sites due to the infinite extension of the system, in order to define a local impurity problem, which is eventually allows one to perform the actual calculations. At the nanoscale, instead, one has to consider systems which are, due to their finite size, inhomogeneous, devoid of translational symmetry, and also quite far from the thermodynamic limit, which represents the usual DMFT framework. Those considerations challenge reliability of DMFT and its extensions for nanoscopic systems. requiring it to be tested.

2.4.1 The idea behind

In order to describe the method in details, let us proceed with the definition of the problem we aim to solve. We are interested in a nanoscopic system consisting of N sites (e.g., atoms) $i = 1, \ldots, N$ whose position in space is fixed[6] and where the electronic dynamics within the nanostructure is described by an inter-site hopping t_{ij}, and a local Coulomb repulsion U_i.

[6]i.e. no phononic, or molecular vibrational degrees of freedom are taken into account at this stage

Optionally, we consider the possibility of a hybridization $V_{i\eta k}$ between the nanostruture and M non-interacting environment $\eta = 1, \ldots, M$, describing, e.g., an adsorbent substrate or electrodes contacted to the nanostructure, that in the following will be in general referred to as ''leads''. The Hamiltonian of such a system reads, hence,

$$\mathcal{H} = -\sum_{ij}\sum_{\sigma} t_{ij} c^{\dagger}_{i\sigma} c_{j\sigma} - \mu \sum_{i}\sum_{\sigma} c^{\dagger}_{i\sigma} c_{i\sigma} + U \sum_{i} c^{\dagger}_{i\uparrow} c_{i\uparrow} c^{\dagger}_{i\downarrow} c_{i\downarrow} + \sum_{i\eta k}\sum_{\sigma} (V_{i\eta k} c^{\dagger}_{i\sigma} l_{\eta k\sigma} + V^{*}_{i\eta k} l^{\dagger}_{\eta k\sigma} c_{i\sigma}) + \sum_{\eta k}\sum_{\sigma} \epsilon_{\eta k\sigma} l^{\dagger}_{\eta k\sigma} l_{\eta k\sigma}, \tag{2.50}$$

where $c^{\dagger}_{i\sigma}$ ($c_{i\sigma}$) and $l^{\dagger}_{\eta k\sigma}$ ($l_{\eta k\sigma}$) denote the creation (annihilation) operators for an electron with spin σ on site i and in lead η state k with energy $\epsilon_{\eta k\sigma}$, respectively. In the most general case the Hubbard interaction can be inhomogeneous (e.g., in nanostructures made of different atomic species). For the sake of clarity, in Hamiltonian (2.50) we drop the orbital indexes. However, the generalization to multi-orbital problems is straightforward and below we will briefly highlight the corresponding modifications to the general scheme.

As discussed in the introduction to this section, it is clear that any exact treatment of Hamiltonian (2.50) becomes unfeasible as soon as the complexity of the nanostructure increases, hence, the basic idea behind the nano-DΓA is to reduce the full problem into a set of N auxiliary single-site Anderson impurity models (AIM). These local problems are defined in such a way that they result completely independent. Furthermore, when possible, any existing symmetry of the nanostructure can be exploited, reducing the number of auxiliary AIMs to one for each of the $N_{\text{ineq}} \leq N$ *inequivalent* atoms in the nanostructure. Since the numerical solution of the impurity problem is usually the bottleneck of the algorithm, through this approximation the overall computational effort is heavily reduced, because it depends only linearly on N_{ineq}, instead of the usual exponential scaling with the size of the Hilbert space. Moreover, in case of highly symmetric structures N_{ineq} may also be much lower than N. Note that this decomposition does not improve the scaling with the number of orbitals per atom, and the full multiplet structure have still to be taken into account when appropriate.

If using the AIM only to compute a local self-energy, as in DMFT, such decomposition makes it effectively possible to deal with a huge number of atoms in a reasonable calculation time. This corresponds obviously to neglecting non-local correlations within the nanostructure. However, those can indeed also be included -when needed- by extending the calculation of the AIM at the two-particle level, in the spirit of DΓA. In fact, as already discussed in Sec. 2.3.1, DΓA provides a systematic method to include non-local spatial correlations beyond DMFT by extracting purely local two-particle quantities from an auxiliary AIM. This means that, within this scheme, one can treat correlated nanostructures at different approximations level, i.e. including only local correlations ($n = 1$-particle, or nano-DMFT[7]) or correlations at all length scales ($n = 2$-particle or nano-DΓA). Evidently, like its bulk counterpart, the nano-DΓA approximation level is computationally more expensive than the nano-DMFT one. However, the latter will will be shown to be quantitatively reliable in a reasonably wide range of parameters.

[7]Being careful not to confuse it with the slightly different approach, reported in Ref. [171], see also Sec. 2.4.3.

2.4.2 Flowchart of nano-DΓA

The flowchart of nano-DΓA, shown in Fig. 2.9, consists of the following steps, described below in more details: (i) setting up of the nanostructure; (ii) definition of a suitable local problem; (iii) solution of the impurity model, and self-consistency loop.

Setting up the nanostructure. The system is completely identified by the Green's function of the whole nanostructure (including the leads), which, in the non-interacting case, can be analytically computed from Hamiltonian (2.50) without any approximation, e.g., by means of (a generalization to the multi-site case of) the standard path integral procedures [**?**]. For the sake of completeness we briefly recall its main steps. In Hamiltonian (2.50) both operators corresponding to the electrons on the impurity (correlated) sites and in the metallic (uncorrelated) leads appear, and they are connected through the hybridization term $V_{i\eta k}c^{\dagger}_{i\sigma}l_{\eta k\sigma}$. One can decouple the two electronic species performing a Gaussian integral in the corresponding Grassmann variables of the non-interacting fermionic degrees of freedom, yielding the effective action depending only on the correlated fermionic degrees of freedom

$$
\begin{aligned}
S^{\text{eff}} = & \int_0^{\beta} d\tau \left[\sum_{ij}\sum_{\sigma} c^{\dagger}_{i\sigma}(\tau)\Big\{(\frac{\partial}{\partial\tau}-\mu)\delta_{ij}-t_{ij}\Big\}c_{j\sigma}(\tau) + U\sum_i n_{i\uparrow}(\tau)n_{i\downarrow}(\tau)\right] \\
& + \int_0^{\beta} d\tau \int_0^{\beta} d\tau' \sum_{ij}\sum_{\sigma} c^{\dagger}_{i\sigma}(\tau)\Delta_{ij\sigma}(\tau-\tau')c_{j\sigma}(\tau'),
\end{aligned}
\tag{2.51}
$$

where the FT in the (Matsubara) frequency space of the hybridizaion function $\Delta_{ij\sigma}(\tau-\tau')$ reads

$$
\Delta_{ij\sigma}(\nu) = \sum_{\eta k} \frac{V_{i\eta k}V^{*}_{j\eta k}}{\nu-\epsilon_{\eta k\sigma}}. \tag{2.52}
$$

The Green's function can be formally computed from the effective action as

$$
G_{ij\sigma}(\tau) = -\frac{1}{\mathcal{Z}}\prod_{i'j'}\prod_{\sigma'}\int \mathcal{D}c^{\dagger}_{i'\sigma'}\mathcal{D}c_{j'\sigma'}\; c^{\dagger}_{i\sigma}(\tau)c_{j\sigma}(0)\;\mathrm{e}^{-S^{\text{eff}}[c^{\dagger},c]}, \tag{2.53}
$$

with the partition function $\mathcal{Z}$ defined as

$$
\mathcal{Z} = \prod_{i'j'}\prod_{\sigma'}\int \mathcal{D}c^{\dagger}_{i'\sigma'}\mathcal{D}c_{j'\sigma'}\;\mathrm{e}^{-S^{\text{eff}}[c^{\dagger},c]}. \tag{2.54}
$$

The Green's function is, in general, a matrix in the site (and possibly orbital) indexes, one can explicitly write the generic matrix element of its inverse in the (Matsubara) frequency space, as

$$
\left\{G^{-1}\right\}_{ij}(\nu) = (\nu+\mu)\delta_{ij} + t_{ij} - \sum_{\eta k}\frac{V_{i\eta k}V^{*}_{j\eta k}}{\nu-\epsilon_{\eta k}} - \Sigma_{ij}(\nu), \tag{2.55}
$$

where $\Sigma(\nu)$ is the self-energy matrix describing the interactions between the electrons on the nanostructure, and needs to be computed numerically. As in general we will refer to the high-temperature paramagnetic phase, and the Green's function is diagonal in spin, we omitted the

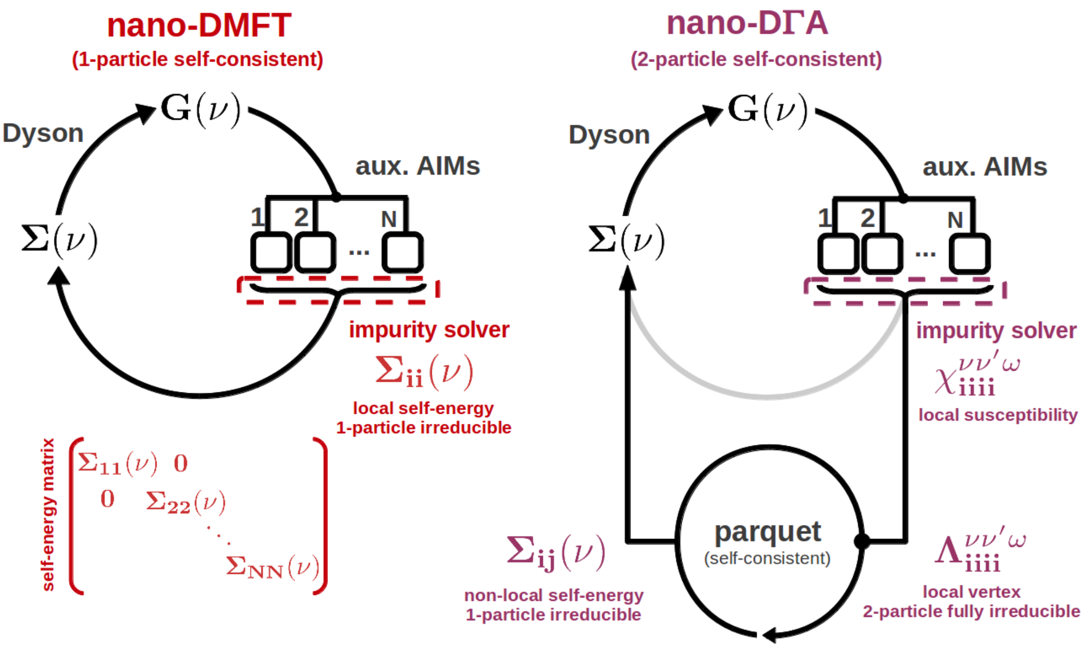

Figure 2.9: Flowchart of nano-DMFT (left panel) and nano-DΓA (right panel) self-consistency schemes. Given the (non-interacting) Green's function of the whole nanostructure, one can define a set of local (independent) auxiliary AIMs. In the case of the nano-DMFT, each local problem i yields a local one-particle irreducible self-energy $\Sigma_{ii}(\nu)$ (see Sec. 2.1). Collecting each site-dependent local self-energy, a (block-diagonal) self-energy matrix for the whole nanostructure is built, and the Green's function is updated by means of the Dyson equation. In the case of the nano-DΓA, each local problem i yields instead a two-particle generalized local susceptibility $\chi^{\nu\nu'\omega}_{iiii}$, which is used to extract the two-particle fully irreducible local vertex $\Lambda_{iiii}\nu\nu'\omega$. The latter represents the input for the self-consistent solution of the parquet equations, which yields a non-local one-particle irreducible self-energy $\Sigma_{ij}(\nu)$ (see Sec. 2.3.1 and 2.3.2). In the last step, a self-energy matrix for the whole nanostructure is built, and the Green's function is updated by means of the Dyson equation. As a reasonable initial guess for the nano-DΓA scheme, one may consider to use a converged nano-DMFT calculation (denoted by the grey line closing the nano-DMFT loop in the right panel).

spin index σ, reabsorbing it into the matrix notation. It is important to stress, that all the information about the geometry of the structure and of the leads is included in the hopping and the hybridization matrices. In practice, this means that it is straightforward to implement even complex nanostructures. In this respect, the input of the hopping (and of the hybridization) parameters may be provided from *ab-intio* calculations, e.g. a LDA projected to Wannier orbitals [172], allowing also realistic calculations of nanoscopic systems and possibly a quantitative comparison with experiments (see Sec. 2.2 for more details on how to merge many-body techniques with *ab-initio* calculations in the bulk systems).

Definition of a suitable local problem. In the Green's function (2.55) one can easily understand that non-locality arises from the non-local fluctuations generated from the interplay between the purely local Hubbard interaction and the geometry of the nanostructure itself, i.e., from the hopping channels t_{ij} between the correlated atoms (or even from higher order hybridization processes $V_{i\eta k}V^*_{j\eta k}$ between different atoms via a lead). Note that, due to the lack of translational invariance, it is, in general, not possible to define a local problem for the whole nanostructure as it is usually done for the lattice problem, and one has to find an alternative. Here, the basic idea of nano-DΓA comes into play, i.e., one reduces the complicated N-impurity Anderson model, defined by Hamiltonian (2.50), to a set of auxiliary AIMs. This task is achieved by means of the relation

$$\mathcal{G}_{0i}^{-1}(\nu) = \Big[\{G\}_{ii}(\nu)\Big]^{-1} + \Sigma_{ii}(\nu), \tag{2.56}$$

which represents essentially a real space generalization of the DMFT self-consistency condition for the bulk case. Specifically, the Weiss field $\mathcal{G}_{0i}(\nu)$, $i = 1, ..., N$, is built from the i-th block of the matrix Green's function $G(\nu)$ and from the corresponding local self-energy $\Sigma_{ii}(\nu)$. Each site i of the nanostructure is therefore coupled to its own dynamical bath $\mathcal{G}_{0i}(\nu)$ that contains the information about the environment of site i, i.e. the rest of the nanostructure. Moreover each local impurity problem is completely independent from the others and this allows one to restrict oneself only to the N_{ineq} AIMs for the inequivalent atoms of the nanostructure. In the multiband case Eq. (2.56) becomes a matrix equation with band indexes. The procedure described above is illustrated schematically in Fig. 2.10.

We recall that in the non-interacting case the self-energy is, obviously, zero, and therefore the decomposition (2.56) does not imply any approximation. In the interacting case, instead, the self-energy entering the Dyson equation (2.55) needs to be computed numerically from each of the auxiliary AIMs with the most convenient choice for the impurity solver.

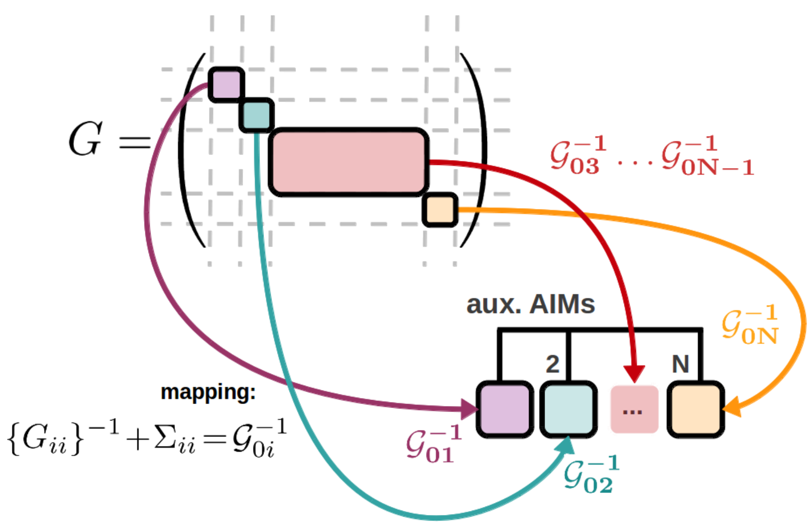

Figure 2.10: Mapping of the full problem onto a corresponding (set of) suitable local problem(s) in nano-DΓA.

Loop in the nano-DMFT fashion. Let us start with the description of the self-consistency loop at the nano-DMFT level, i.e. if one extracts from each of the auxiliary AIMs only a local self-energy $\Sigma_{ii}(\nu)$, $i = 1, \ldots, N_{\text{ineq}}$. This approximation implies that non-local correlations within the nanostructure are neglected.

The N_{ineq} inequivalent self-energies are then collected and a self-energy matrix in the site (and orbital) space is defined, where the inequivalent local self-energies are assigned to the corresponding diagonal elements (blocks), according to the symmetries of the system. In the general case the self-energy matrix reads, hence,

$$\Sigma(\nu) = \begin{bmatrix} \Sigma_{11}(\nu) & 0 & \cdots & 0 \\ 0 & \Sigma_{22}(\nu) & \cdots & 0 \\ \vdots & \vdots & \ddots & \vdots \\ 0 & 0 & \cdots & \Sigma_{NN}(\nu) \end{bmatrix},$$

as shown in the left panel of Fig. 2.9. In the simplest case, where all sites are equivalent, one would have a $N \times N$ matrix with all identical diagonal elements, and zero elsewhere.
The self-energy $\Sigma(\nu)$ is then plugged into the Dyson equation (2.55) in order to compute again the Green's function of the whole nanostructure, and the process is iterated self-consistently till convergence.

At this level, the approximation of completely neglecting non-local spatial correlations in nanoscopic systems, is not justified. However, before proceeding with the next approximation scheme, it is interesting to discuss some cases in which non-local spatial correlations are expected become negligible

- **non-interacting limit:** $U = 0$. Trivial limit because the solution of each auxiliary impurity model yields $G(\nu) = \mathcal{G}_0(\nu)$, corresponding to a identically zero self-energy.

- **decoupled sites:** $t_{ij} \to 0$, if the hybridization function is diagonal in the site indexes $\Delta_{ij}(\nu) \propto \delta_{ij}$. This can be considered the nanoscopic counterpart of the atomic limit in the lattice problem. Each of the site of the nanostructure is completely decoupled form the others, i.e., the Hamiltonian is separable and each term coincides with the Hamiltonian of the AIM.

- **strong hybridization:** $V_{i\eta k} \to \infty$, if each site is coupled to its own lead. The hybridization becomes the dominating energy scale, and each site is effectively decoupled from the rest of the nanostructure.

- **large coordination:** formally, z in a finite system cannot diverge, so that the limit $z \to \infty$ in which DMFT is exact, is not a well defined limit for the nano-DMFT. However, when the connectivity increases, non-local fluctuations are expected to become less relevant.

Beyond this limiting cases non-local spatial correlations may become significant. However, this does not mean *a priori* that far away from the limiting cases the nano-DMFT is not reliable:

indeed the definition of some generic validity criteria will be an important part of the testing phase of the method.

Loop in the nano-DΓA fashion. In order to include non-local spatial correlations beyond mean-field at the nanoscale, one needs to compute a two-particle fully irreducible local vertex for each of the inequivalent auxiliary impurity model. This is done in complete analogy to the case of the bulk DΓA (see Sec 2.3.2). The N_{ineq} local $\Lambda_{iiii}^{\nu\nu'\omega}$ represents the input for the parquet solver, as shown in the right panel of Fig. 2.9. The self-consistently solution of the parquet equations in **real space** yields the full non-local vertex $F_{jklm}^{\nu\nu'\omega}$, and the corresponding self-energy by means of the Dyson-Schwinger equation

$$\Sigma_{ij}(\nu) = U\frac{n_i}{2}\delta_{ij} - UT^2\sum_{\nu'\omega}\sum_{klm} F_{jklm}^{\nu\nu'\omega} G_{li}(\nu'+\omega)G_{ik}(\nu')G_{im}(\nu+\omega). \tag{2.57}$$

With respect to the bulk DΓA, however, no coarse-graining is involved in the parquet equations, which are solved in the full Hilbert space of the nanostructure. This means that, concerning nano-DΓA, one does not rely on any further conceptual approximation beyond the locality of the two-particle fully irreducible vertex.

2.4.3 Critical discussion & relation to alternative approaches

Above we have shown how one can describe non-perturbative local and non-local correlation effects at the nanoscale. However, there are several question that one would need to answer. Can DMFT provide a reasonable description of correalted nanostrucutures? In this context, which are the physical situation where non-local fluctuations are no longer negligible, and to what kind of physical phenomena could these give rise to? The extensive test phase of the method will provide useful information in this direction.
A limitation which is already known is that one cannot describe *non-local interactions* within this formalism. However, as already mentioned, the intrinsic diagrammatic nature of the method also allows for further improvements by means of the systematic inclusion of Feynman diagrams, as recently suggested in the context of the *ab-initio* DΓA [157].

Concerning related research lines, one should mention that the decomposition applied to the nanostructure, in the present scheme, is just a special realization of general technique already known in the literature, already applied to different kind of systems. In general, the idea is suitable to the study of inhomogeneous systems, and has been applied to, e.g., the study of bulk materials in the presence of two-dimensional interfaces by Potthoff and Nolting [173], as well as to the case of LDA+DMFT calculations with locally-inequivalent atoms within the unit cell (see, e.g., Ref. [272]). An approach for quasi one-dimensional systems, the chain DMFT, reported by Biermann *et al.* [174], relied on the decomposition to replace a system of weakly coupled (equivalent) chains by a single effective chain, coupled to a self-consistent bath. Another noticeable case is its application to ultracold atoms on optical lattices, using the so-called real-space DMFT (R-DMFT), by Snoek *et al.* [175], where the inhomogeneity comes from the external, spatially dependent, trapping potential, applied to an otherwise translationally invariant lattice. The present approach is similar to the R-DMFT, at least at the one-particle level. The main difference being that in our case each site may also coupled to a noninteracting bath, and a possible inhomogeneity in the system arises not due to an external potential but from the geometry or even the chemical composition of the nanostructure itself. Recently R-DMFT has been also applied in the contest of the two-impurity Anderson model to analyze the interplay between indirect magnetic exchange (RKKY interaction) and Kondo physics [176, 177].

The application of DMFT to nanoscopic systems, on the other hand, has been already attempted following alternative ways. A nano-DMFT scheme has been already proposed by Florens [171], relying however on a specific cayley-tree geometry. Realistic calculations of strongly correlated transition metal nanoscopic devices and of correlated adatoms on surfaces have also been carried out. In recent works, Jacob *et al.* [178, 179] introduced a *molecular* DMFT approach, which combines density functional theory (in the local density approximation) with many-body approaches. A contact device of $3d$-shell magnetic atoms is considered, where local and non-local electronic correlations are addressed within a cluster approach. The use of a OCA [109, 110, 111] impurity solver allows the analysis of low temperature Fano resonances in the transmission function for Fe, Co, and Ni devices. The interplay between orbital degrees of freedom and the spin fluctuation responsible for the Kondo effect was investigated by Surer *et al.* [180] in a Co impurity on a Cu (111) surface. Density functional theory and a Krylov (hybridization expansion) CT-QMC [93] allows one to accurately take local electronic correlations into account within the whole $3d$ multiplet.
Complementarily, the nanoscopic extension of DMFT and DΓA introduced above is suitable to study a large variety of systems, both for models and real materials. Moreover it also allows, when necessary, to overcome the limitation of considering only local correlations typical of the DMFT methods.

Chapter 3

Local and non-local correlations in molecular systems: a test for nano-DΓA

In this chapter we apply the nanoscopic extension of DMFT and DΓA, introduced in the last section, to quasi one-dimensional model systems. The aim is to investigate the effects of local and non-local correlations on electronic structure and transport properties, and to test the reliability of our method and to understand its strengths and its limitations. In this respect, the comparison with an exact numerical solution for the systems of choice is of fundamental importance for demonstrating the applicability of our method as a general and flexible scheme to deal with correlated nanostructures.

As mentioned in the previous chapter, despite some attempts to investigate correlation effects at the nanoscale, a reliable approximation that allows to deal with complex nanostructures made of several coupled correlated sites is still lacking. The nanoscopic extension of DMFT and DΓA we proposed in Sec. 2.4 is meant to fill this gap. From the practical point of view, as highlighted in its flowchart (see Fig. 2.9), the approach can be implemented at different levels of approximation: (i) the nano-DMFT, where the internal self-consistency is assured at the one-particle level only, and non-local spatial correlations are neglected, and (ii) the nano-DΓA which is fully self-consistent also at the two-particle level, and allows us to restore spatial correlations beyond DMFT. However, the applicability of DMFT and its extensions to nanoscopic systems is not straightforward, and its reliability is *a priori* not known. Hence, in the preliminary test phase, one needs to consider simple benchmark systems in order to understand to which extent, and under which conditions, each approximation employed is reliable.

3.1 Quasi one-dimensional molecules

In the preliminary test phase for nano-DΓA we focus on quasi one-dimensional (Q1D) molecular structures, which represent the ideal playground for an early stage analysis. In particular we focus on *benzene* (chemical formula C_6H_6) and *cyclo-octatetraene* (C_8H_8) molecules, which are significant from several points of view.

First of all, they fulfill an important requirement, crucial for a precise benchmark, i.e., the size of the Hilbert space of such systems is low enough to allow a numerically exact solution even in the interacting case, e.g., via ED of a low-energy effective Hamiltonian or QMC simulations. Moreover, a Q1D structure, such of those of C_6H_6 and C_8H_8, is probably one of the most challenging cases for many-body calculations in the framework of DMFT, since non-local spatial correlations are expected to be particularly relevant in such low-dimensional structures. In this sense, the existence of an exact benchmark allows for a quantitative analysis of the performance of both the nano-DMFT and nano-DΓA approximations.

At the same time, monocyclic hydrocarbons (also knows an *annulenes*), as well as more complex molecular structures, still raise both experimental and theoretical interests, as the delocalized π electrons play a role analogous to that of the conduction band in convenstional semiconductors. For instance, it is well known that electronic transport through benzene is peculiar due to quantum interference (QI) effects [181, 182], which are also significant in the presence of a magnetic field, giving rise to the Aharonov-Bohm effect [183, 184]. However it is also believed that strong electronic correlations modify quantitatively transport properties in the benzene molecule [185]. Recently it has also been shown that a benzene molecule contacted to metallic electrodes behaves as a single molecule transistor device [186, 187], with possibly huge impact on technological applications in the direction of, e.g., QI-controlled molecular electronics [188]. Another interesting feature that makes benzene somehow ‘‘special’’ with respect to cyclo-octatetraene, for instance, is its aromatic nature (see below), where a resonating valence bond (RVB) physics is also possibly playing a role [189].

As this chapter will be entirely devoted to the discussion of these two-systems within the nano-DΓA, in the following a brief description of them, as well as for the corresponding model Hamiltonian, is provided, while in Sec. 3.2 the numerical results are presented.

A brief introduction. Both benzene and cyclo-octatetraene are conjugated molecular systems, but as we will see their chemical nature is quite different.

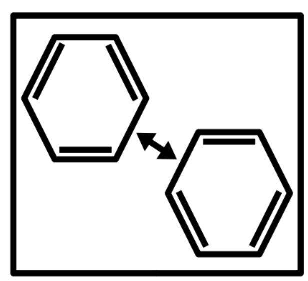

The **benzene** molecule is an aromatic hydrocarbon with molecular formula C_6H_6. It is nowadays understood that the tetravalent carbon atoms (configuration: [He] $1s^2 2s^2 2p^2$) are arranged at the vertices of a hexagonal planar ring. However, since its discovery the chemical structure of the molecule was greatly debated. Early theoretical investigations resulted in several prediction, and led eventually to the Kekulé formula [190, 191], where carbon atoms forms alternating single and double bonds with the nearest neighbors. This hypothesis was experimentally contradicted, as X-ray diffraction patterns show that all carbon-carbon bonds have the same length of 1.40 Å, intermediate between the single (1.35 Å) and double (1.47 Å) bond-length. Moreover, chemical analysis reveals that all hydrogen atoms have the same reactivity. Valence bond theory can not account for all the properties of the molecule, and the benzene structure is instead understood in terms of a *resonance hybrid* between two possible Kekulé structures. This property is also known as aromaticity and, according to the

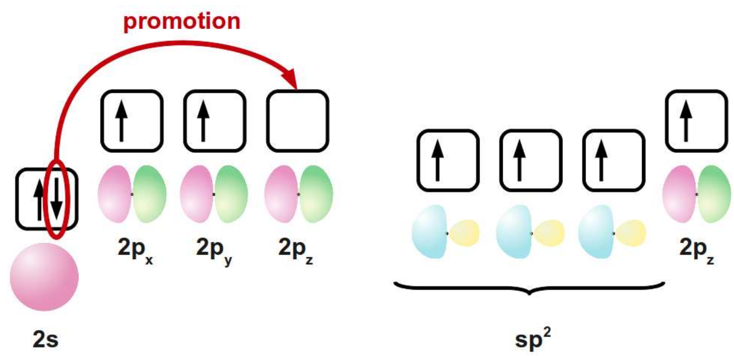

Figure 3.1: Hybridization mechanism in C atoms. An electron in excited from the closed $2s$ shell to one of the degenerate ps, allowing sp hybridization between the s and the remaining p orbitals.

Hückel's rule [192], is predicted to manifest in structures with a number of π electrons equal to $4n + 2$, with n being a non-negative integer. The latter follows from general consideration on basic chemical principles and can be explained in the framework of molecular orbital (MO) theory. In order to fulfill the octet rule (i.e., to reach a more stable configuration with a closed outer shell), carbon must use all the 4 electrons of its outer shell when bonding to other atoms. However, only unpaired electrons can bond, and carbon has a close $2s$ atomic orbital (AO). Since in carbon the gap between $2s$ and $2p$ AOs is fairy small compared to the binding energy of the GC or the C-H chemical bond, it is energetically favorable for the carbon atoms to promote an electron from the $2s$ to an unoccupied $2p$ AO, because the excitation energy will be compensated in the formation of the molecule. The process leads to the hybridization of $2s$ with $2p_x$ and $2p_y$ AOs, and their linear combination (LCAO) results into three degenerate sp^2 MOs (the mechanism is shown in Fig. 3.1). The sp^2 MOs are arranged, according to valence shell electron pair repulsion (VSEPR) theory [193], in a trigonal planar configuration, which allows them to be as far apart as possible form each other, and give rise to σ bonds with the hydrogen s and the nearest neighbor carbon atoms sp^2 orbitals. The remaining $2p_z$ AO of each carbon is directed perpendicularly to the sp^2 plane and tends to form π bonds with the other carbons' $2p_z$ AOs. While σ bonds are strong and σ electrons localized around the nuclei, π electrons are relatively mobile. This lead to the formation of a π electron cloud and to charge delocalization into a bonding MO shared among all carbon atoms of the benzene ring. This scenario is consistent with the unusual stability of the benzene molecule, and its tendency to favors substitution reaction of hydrogen atoms with other functional groups against addiction reactions, as well as with the other previously discussed properties.

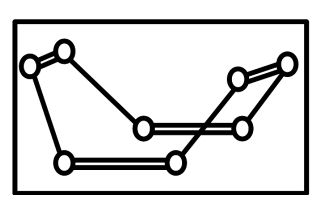

On the other hand, the **cyclo-octatetraene**, or **COT**, is an annulene with chemical formula C_8H_8. Because of its stoichiometric similarities to benzene, also the structure of COT raised some controversy. However, unlike benzene, this molecule is not aromatic and is characterized by *fixed* alternating single and double C-C bonds, which determine its non-planar *tub* conformation. In this case it is also worth stressing that a change in the valency of the molecule may have strong effects both on the spatial arrangement of the carbon atoms and on its electronic structure. For instance COT can react with potassium (K) to form a salt, K_2COT, containing the dianion COT^{2-} which has ten electrons and fulfills the Hückel's rule. As a consequence it acquires a planar structure and becomes aromatic.

A model Hamiltonian for π electrons. In chemistry, the Hückel method [194, 195, 196, 197] and its extension [198] are commonly used to predict the energy level (and the corresponding degeneracy) of MOs of π electrons in conjugated hydrocarbon systems (like ethene, benzene, or even graphite and carbon nanotubes). An effective electronic model for organic molecules can be derived performing electronic structure calculations restricting to the π orbitals [199], or according to the π-electrons effective field theory (π-EFT) by Barr *et al.* [200]). This follows from the observation that the main physical processes in the system are determined by the characteristic length (or equivalently, energy or time) scale set by the strength of the π bonds, and therefore, one expect that the only relevant degrees of freedom are those characterized by scale comparable to those.

Hence, both systems can be described by effective Hamiltonians for π electrons of the form introduced in the context of nano-DΓA, that we report below for the sake of convenience

$$\begin{aligned} H = &- \sum_{ij} \sum_{\sigma} t_{ij} c^{\dagger}_{i\sigma} c_{j\sigma} - \mu \sum_{i} \sum_{\sigma} c^{\dagger}_{i\sigma} c_{i\sigma} + U \sum_{i} c^{\dagger}_{i\uparrow} c_{i\uparrow} c^{\dagger}_{i\downarrow} c_{i\downarrow} \\ &+ \sum_{i\eta k} \sum_{\sigma} (V_{i\eta k} c^{\dagger}_{i\sigma} l_{\eta k\sigma} + V^{*}_{i\eta k} l^{\dagger}_{\eta k\sigma} c_{i\sigma}) + \sum_{\eta k} \sum_{\sigma} \epsilon_{\eta k\sigma} l^{\dagger}_{\eta k\sigma} l_{\eta k\sigma}, \end{aligned} \tag{3.1}$$

Here $c^{\dagger}_{i\sigma}$ ($c_{i\sigma}$) has to be interpreted as the creation (annihilation) operator of an electron with spin σ in the $2p_z$ Wannier orbital centered at the carbon atom. Here, μ denotes the equilibrium chemical potential, possibly including the effect of a gate voltage V_G. The Hubbard interaction U, taking into account the (local) Coulomb repulsion between the π electrons, could depend on the site index i, e.g., if the system is made of atoms of different species. However, here we will only consider cases in which the nanostructure is made of equivalent carbon atoms. The operators $l^{\dagger}_{\eta k\sigma}$ ($l_{\eta k\sigma}$) describes fermionic degrees of freedom of a non-interacting environment hybridized with the carbon atoms.

Though Hamiltonian (3.1) is physically sensible to describe annulenes structures, one has still some degrees of freedom, e.g., the choice of the hopping and hybridization structure. In the following we discuss explicitly the configurations that will be considered in the present work (see Figs. 3.2 and 3.3), keeping in mind that the main aim, at this stage, is not focused on realistic simulations but rather to test the reliability of the nanoscopic extension of DΓA on model structures.

• **Hopping structure:** for both the benzene and COT molecules we consider the hopping configuration where hopping processes are restricted to nearest neighbor sites only (''*NN t*'' in the following) with amplitude t, which sets the unit of energy.

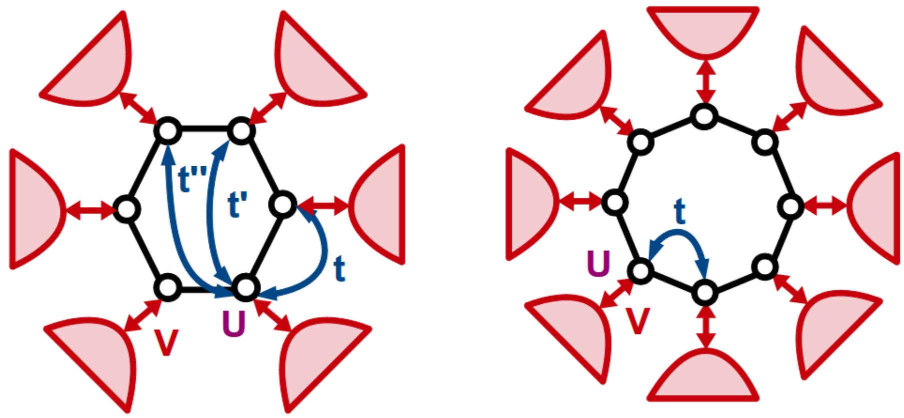

Figure 3.2: Schematic representation of the Q1D planar molecules considered for the numerical calculations and tests in this chapter. The connectivity within the nanostructure is determined by hopping channels t (between nearest neighbors), t' and t'' (longer range), and optionally each site can be connected to a metallic lead via an hybridization channel V. The Coulomb interaction between π-electrons is taken into account by an on-site Hubbard repulsion U.

In the case of the COT, the presence of single and double covalent bonds (and consequently its non-planar structure) would result in a slightly different overlap of AOs (i.e., hopping amplitudes). For the sake of simplicity we neglect this effect considering instead a planar structure where the carbon atoms occupy the vertices of a regular octahedra, as would be the case, e.g., for the COT^{2-} mentioned above.[1]

Moreover, it is also interesting to consider what happens in other hopping configurations, i.e., when non-zero longer range hopping parameters are introduced, as this is related to the connectivity within the nanostructure. In the following we will consider the hopping configuration where electrons can hop to any other site of the ring with *the same* hopping amplitude t (‘‘*all t*’’). Obviously, as the hopping amplitude is a measure of the overlap of orbitals belonging to neighboring atoms, the hopping amplitude is in general a decreasing function of the inter-site distance. However, from a purely mathematical point of view, this case is also of interest, and can be considered as the analog (on a finite system) of a *fully connected* lattice model.[2] In this sense, increasing the number of nearest neighbors is equivalent to increasing the dimensionality of the system: e.g., one can show that a Q1D benzene ring with hopping amplitudes $t' = t$ and $t'' = 0$ (‘‘*ttp*‘‘), corresponding to connectivity $z = 4$, is topologically equivalent to a 3-dimensional octahedra with nearest neighbor hopping t, also corresponding to $z = 4$ (and resulting in the same spectral function, as shown in Fig. 3.4). Analogously, the *all t* configuration can be mapped into a structure in a 5-dimensional space.

[1] It is interesting to notice that, in the context of realistic LDA+DMFT calculations, one would probably need a fully self-consistent scheme for this system: indeed, the change of orbital occupation and the fulfillment of the Hückel's rule, lead to a relaxation of the molecular structure and to the consequent change of the orbital overlap.

[2] e.g., the fully connected ($z = \infty$) Ising model, is often chosen as a valuable example to show that the *saddle point method* for the evaluation of the path integral of the partition function (mean-field approximation) leads to the exact solution [201, 202, 203].

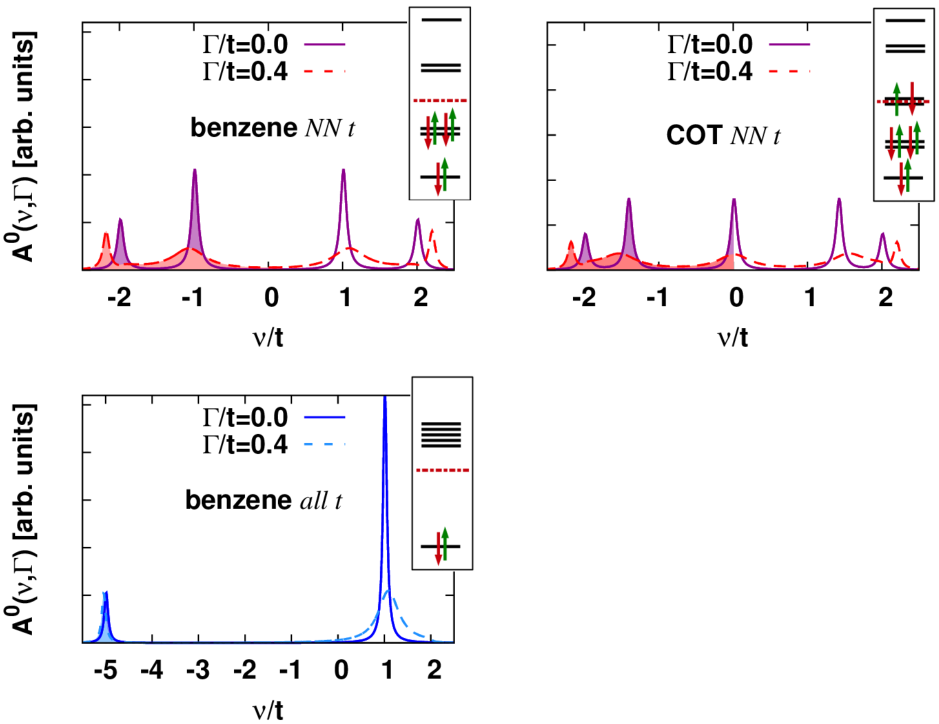

Figure 3.3: Spectral function $A^0(\nu, \Gamma)$ of the non-interacting benzene and COT molecules, for two values of the hybridization $\Gamma = 2\pi\rho V^2$, and different hopping topologies, as described in the text. The portion of the occupied spectrum (at $T = 0$) is denoted by color filling. In the case of the isolated molecule ($\Gamma = 0$) the relative height of the peaks reflects the respective degeneracy, and the width of the δ-like peaks is determined by a tiny artificial broadening. The insets show the corresponding MO picture of the isolated rings (the dashed red line marks the Fermi energy).

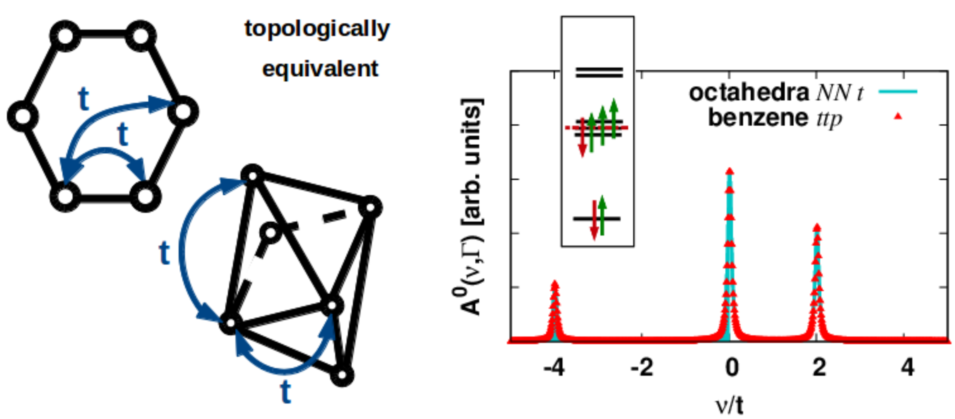

Figure 3.4: Spectral function $A^0(\nu, \Gamma = 0)$ of the non-interacting Q1D benzene ring in the *ttp* hopping configuration and of the 3-dimensional octahedra in the *NN t* one. In both case $z = 4$ and all sites are equivalent. The insets show the corresponding MO picture of the isolated rings (the dashed red line marks the Fermi energy).

It is worth to make few remarks concerning the non-interacting ($U = 0$) and isolated ($V = 0$) benzene and COT rings. Due to their finite size, they display a discrete energy spectrum, given by the eigenstates of a tight-binding Hamiltonian. In the *NN t* case, the spectrum is also particle-hole symmetric (with the conventional choice for the chemical potential $\mu = 0$) and both molecules are half-filled, with on average one electron per carbon atom $\langle n \rangle = 1$. However, the most important difference between (uncorrelated) benzene and COT molecules, is that the former is insulating with a gap $\Delta = 2t$ between the highest occupied molecular orbital (HOMO) and the lowest unoccupied molecular orbital (LUMO), while the latter presents a doubly degenerate peak exactly at the Fermi energy. In the *all t* case that we will consider for the benzene, the spectrum is no longer particle-hole symmetric, and the molecule has just a single level below the Fermi energy, corresponding to a filling of $\langle n \rangle = 1/3$ (at $T = 0$) and a five-fold degenerate unoccupied state above ϵ_F.

• **Hybridization:** in the following we will consider paramagnetic metallic leads, described by a flat, featureless, and symmetric DOS $\rho = 1/2D$, where we choose the half-bandwidth to be $D = 2t$. The assumption is quite reasonable, yet in principle, depending on the functional form of $\epsilon_{\eta k \sigma}$, the formalism can be extended to a generic DOS, including the possibility to consider also insulating, (anti-)ferromagnetic (of great interest in the framework of *spintronic* devices [204, 205]) and superconducting leads. On the other hand, if one aims at a quantitative prediction of (or to a comparison with experimentally measured) physical quantities, then a realistic description of the leads' electronic structure is mandatory [200].
Moreover, for the sake of simplicity, and to deal (at the beginning) with systems in which all sites are fully equivalent, we consider each site to be contacted to its own lead, so that the hybridization matrix has the diagonal form $V_{i\eta k} = V\delta_{i\eta}$, and it is independent on k.
The hybridization can also be treated exactly, tracing out the fermionic degrees of freedom of the leads, and yielding the so-called leads' self-energy, compare also with the corresponding expression (3.2), which reads

$$\Sigma_{ij}(\nu) = V^2 \sum_{\eta \mathbf{k}} \frac{1}{\nu - \epsilon_{\eta \mathbf{k}}} \delta_{ij} \delta_{\eta i}. \tag{3.2}$$

which corrects the π-electrons propagator: Re$\Sigma(\nu)$ is an energy shifts of the eigenstates and is zero in the limit $D \gg t$, while Im$\Sigma(\nu) = \pi \rho V^2 \equiv \Gamma/2$ gives a Lorentzian broadening of the peaks, due to scattering processes with electrons in the conduction band of the lead(s). The effect of the hybridization on the non-interacting spectral functions of the benzene and COT molecules is shown in Fig. 3.3, in the hopping topologies that will be discussed in the following.

• **Interaction:** we consider only the local contribution U of the Coulomb repulsion between π electrons. Although it is known that non-local contributions are not *a priori* negligible at the typical bonding inter-atomic distances, it has been suggested [200] to be a reasonable approximations in π conjugated molecules (for a related discussion, and a possible strategy for including non-local interaction terms see Ref. [200] and references therein). However, the task of determining *ab-initio* the value of the screened interaction in molecular junctions is, obviously, not trivial. A possibility would be to include it as a fitting parameter in order to reproduce fundamental quantities from experiments. However, in the following U will be considered as a parameter to be varied in order to analyze the role of electronic correlations in different regimes.

3.2 nano-DMFT approximation level: results

In the following we present our calculations at the one-particle approximation level (nano-DMFT). The main goal of this section is to understand if, and in which parameter regime, a DMFT approach is appropriate. Therefore, we report here calculations for local and non-local quantities sush as: site-dependent densities, double occupation, spectral function, self-energy and zero-bias conductance, we extensively compare the results to a numerically exact solution.

The impurity solver. Before starting the detailed discussion of our results, information about the algorithm used for solving the local problem (i.e., the single.site AIM) should be given. As already pointed out in Sec. 2.4, our scheme is *independent* of the impurity solver, and one has the freedom of choosing alternative numerical methods to solve the auxiliary AIMs, depending on the quantity and/or the parameter regime of interest.

Specifically, most of the numerical results presented in the following sections are obtained using a Hirsch-Fye (HF-QMC) algorithm [103] as impurity solver for both the nano-DMFT and the exact solution. Our choice of the impurity solver was aimed at mapping complex, possibly realistic, nanostructures, including also orbital degrees of freedom. Moreover, the availability of a HF-QMC for the exact solution[3] motivated us to employ the same algorithm also for solving the impurity problem in the nano-DMFT/DΓA approximations in order to have a quantitative comparison to the exact solution in a extremely controlled way.
This choice, however, restricts us to rather higher temperature with respect to the typical Kondo scale which may be expected in such systems. Hence, for future applications of the method, CT-QMC [93] will be adopted as an impurity solver (see the outlook, Sec. 3.5) allowing for an investigation of the low-temperature regime.

On the other hand, as far as the evaluation of two-particle quantities are concerned, an ED impurity solver revealed to be a better choice to properly treat the high-frequency asymptotic behavior of the vertex functions (cf. with Sec 3.4), yet this is also possible within state-of-the-art QMC solvers [112, 162, 163].

[3]Note that the isolated benzene of COT molecules can be solved exactly also by the direct diagonalization of the corresponding Hamiltonian. However, if infinitely-extended bulk leads are connected to the nanostructure, the diagonalization becomes unfeasible, while the system can still be treated within a QMC technique.

3.2.1 Benzene molecule

The following results have been partially published in the APS Journals ''Physical Review Letters'': PRL **104**, 073101 (2010) [206] and ''Physical Review B'': PRB **86**, 115418 (2012) [207].

We consider the model for the benzene molecule described above (left panel of Fig. 3.2) in the presence of an Hubbard interaction $U = 5t$, which is larger than the benzene gap $\Delta = 2t$, and may be representative of systems with poor screening (see, e.g., [208] and references therein).

Electronic structure. A general overview on the local physics of the system can be obtained considering the **on-site spectral function at the Fermi energy**, which can be estimated [121] directly from the local Green's QMC function at $\tau = \beta/2$ as

$$\overline{A(0)} = \int d\nu A(\nu) \cosh^{-1}(\nu/2T) \approx -\beta G(\beta/2), \tag{3.3}$$

where the relation on the r.h.s. becomes exact in the limit of $\beta \to \infty$ ($T = 0$). At finite T the hyperbolic function weighting the spectrum $A(\nu)$ is pinned around $\nu = 0$ ($\epsilon = \epsilon_{\mathrm{F}}$), and corresponds to averaging the spectrum over a frequency window of the order of the temperature T around the Fermi energy. The obvious advantage of using Eq. (3.3) is that one can extract this information directly from the QMC data, without the need of an analytic continuation. In Fig. 3.5 we compare our results for the on-site spectral function (left panel) and the site density and double occupation (right panel) between the nano-DMFT and the corresponding exact solution. We show the behavior of those local quantities as a function of the ratio between the hybridization strength V and the absolute value of the hopping amplitude t. Looking at the *NN t* topology, i.e., with hopping processes only involving nearest neighbor sites, one immediately observes that the agreement between the exact solution and nano-DMFT is very good when the hybridization V is large. This is understood considering that, in the limit $V \to \infty$, the hybridization becomes the dominating energy scale: each atom forms a bound state with its own lead and hopping processes within the benzene ring are not energetically favorable anymore. Hence, each site is characterized by a local dynamics, and non-local correlations become negligible. For the same reasons, one expects the opposite (molecular) limit $\Gamma = 0$, or equivalently $V/t = 0$, in which the benzene ring is isolated, to be the most difficult for nano-DMFT, and non-local correlations to be important. In fact, this seems to be the case: while the exact solution correctly predicts the benzene ring to be insulating, the nano-DMFT results show instead a small but *finite* spectral weight at the Fermi energy (cf. left panel of Fig. 3.5). Though the *quantitative* difference is not too large, the result shows that nano-DMFT suggests a *qualitative* different picture. Another indication that the nano-DMFT approximation breaks down at some value of V/t in the weak-hybridization limit, can be found in the behavior of the **double occupation** (main panel, right). In the *NN t* case, while nano-DMFT correctly reproduces the occupation and the system is half-filled on the whole hybridization range (inset), the double occupation are overestimated with respect to the exact solution in the weak-hybridization limit. In fact,

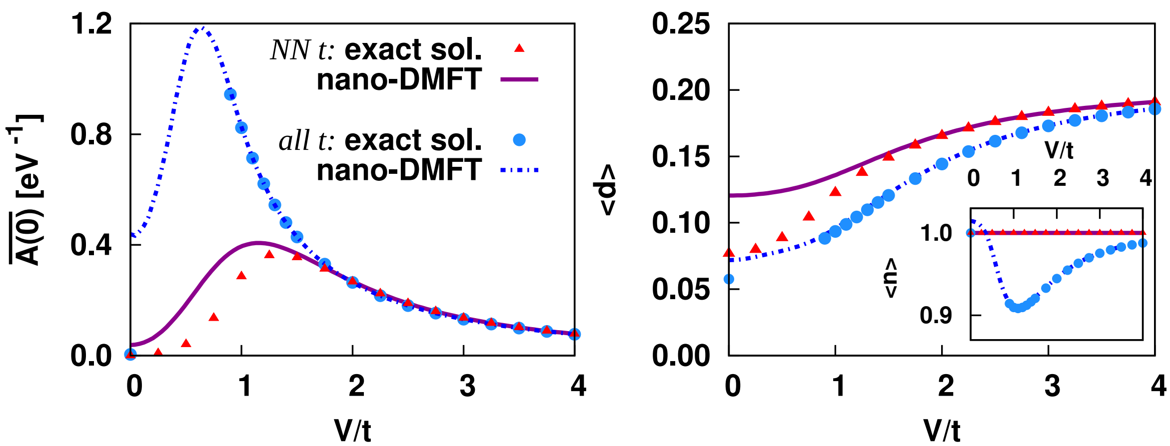

Figure 3.5: On-site spectral function $\overline{A(0)}$ (left panel), site densities $\langle n\rangle$, and double occupations $\langle d\rangle$ (right panel) as a function of V/t for the benzene ring. Note that all the sites are equivalent due to symmetry. The nano-DMFT results (lines) are compared to the exact solution (symbols) at $U=5t$ and $T=0.05t$, for both *NN t* and *all t* hopping configurations. Adapted after Ref. [207].

both the suppression of the spectral weight at the Fermi energy and of the double occupations in the exact solution are determined by non-local spatial correlations, which are missing at the nano-DMFT approximation level.

In light of the previous results, it is interesting to discuss the role of an enhancement of the connectivity, which, in a lattice model would lead to an improvement of the DMFT description of the system. This situation is realized in the benzene molecule for the *all t* case, in which hopping processes to all other sites of the molecule are allowed with the same hopping amplitude t, so that each site has effectively no longer two, but five nearest neighbors. Though not fully realistic, this situation is of theoretical interest, as far as the validation of our approximation schemes is concerned. The inclusion of longer range hopping has the additional effect of breaking the particle-hole symmetry of the molecule: in the isolated, non-interacting case, the system is *away* from half-filling for $\mu=0$, while in the non-interacting case, the site-occupation is only $\langle n\rangle=1/3$ (at $T=0$). In contrast, at the value of $U=5t$ there is a strong redistribution of spectral weight and at $\mu=0$ is almost half-filling. The deviation from half-filling is of the order of some percent, the actual value depending on the hybridization strength (as it can be observed in the inset of the right panel in Fig. 3.5). More noticeably, in the *all t* topology no substantial difference between DMFT and exact solution can be found in $\overline{A(0)}$, as well as in the single and double occupations, even in the intermediate region $V\simeq t$, where deviation were already visible in the *NN t* configuration. In this case, however, no exact QMC solution is available below the threshold of $V\sim 0.8t$ due to the well-known fermionic sign-problem. Therefore, we cannot check the molecular limit for the *all t* topology (at this value of U at least) with such an impurity solver. Nevertheless, the Hamiltonian of the isolated molecule can still be solved by an exact diagonalization of the local Hamiltonian. This exact diagonalization predicts an insulating state also for the *all t* topology, while the nano-DMFT solution is metallic and overestimates double occupation. This means that, despite the enhanced connectivity, non-local fluctuation become relevant at low enough hybridization, and the completely local approximation will eventually break down. Moreover, a comparison of the curves in the right panel of Fig. 3.5 shows that, while the *all t* hopping structure drives the system slightly away from half-filling, the value of $\langle d \rangle$ in the *all t* configuration is *always* smaller that in the *NN t* one, in the whole hybridization range. This suggests that the enhanced connectivity does not weaken (substantially) local electronic correlations, yet it washes away the non-local ones, resulting in a improved agreement between nano-DMFT and the exact solution.

Analysis of the self-energy. A deeper understanding of the origin of the observed agreement between the nano-DMFT and the exact solution is provided by the analysis of the respective self-energies for both hopping topologies. As before, let us begin discussing the *NN t* case first, referring to Fig. 3.6, where we plot the corresponding **self-energy in Matsubara representation**. In panels (a), (b), and (c) the imaginary part of the local self-energy (the real part is zero due to particle-hole symmetry, having subtracted the Hartree term), while in panels (c), (d), and (e) the non-local contribution to the self-energy are shown for different values of V/ts shown.

One can see that nano-DMFT nicely captures the local physics, accurately reproducing the exact self-energy at low (Matsubara) frequencies and thus providing a reliable estimate for the quasi-particle residue

$$Z = \frac{m}{m^*} = \left(1 - \frac{\partial \mathrm{Im}\Sigma(\imath\nu_n)}{\partial \nu_n}\bigg|_{\nu_n \to 0^+}\right)^{-1}, \tag{3.4}$$

where m^* is the effective mass, renormalized by the interaction. On the other hand the scattering rate is exponentially suppressed, due to the lack of excitation of the non-interacting benzene molecule, which is insulating (cf. Fig. 3.3). A different behavior is expected when the underlying spectrum is metallic, e.g., in the case of the COT molecule (see Sec. 3.2.2).

However, the slope of the local self-energy around zero frequency is evidently not enough to capture the full picture, and non-local elements of the self-energy are, in general, non-negligible with respect to the local ones. While non-local correlations are quickly suppressed with increasing hybridization (while the local ones remain sizable), thus providing a confirmation of the genuine agreement between nano-DMFT and the exact solution observed in Fig. 3.5, they play a pivotal role in the weak-hybridization regime.

This becomes clear analyzing more carefully the molecular limit $V = 0$. As already mentioned, in the non-interacting case $U = 0$, the isolated, half-filled, benzene molecule is a trivial band insulator, with a gap $\Delta = 2t \gg T$ given by the energy difference between the HOMO and LUMO. At finite U the situation is more complicated. While the estimate of $\overline{A(0)}$ (main panel of Fig. 3.5) in nano-DMFT is finite, though small, and corresponds to a semi-metallic behavior, the exact solution still predicts an insulating behavior. This imply that the restoration of the low-energy gap, with respect to the nano-DMFT, is due to large non-local contributions of the self-energy, as shown in panels (d), (e) and (f) of Fig. 3.6.

A better understanding of the suppression of the low-energy spectral weight in the isolated benzene molecule can be obtained by performing the **analytic continuation** of the Matsubara

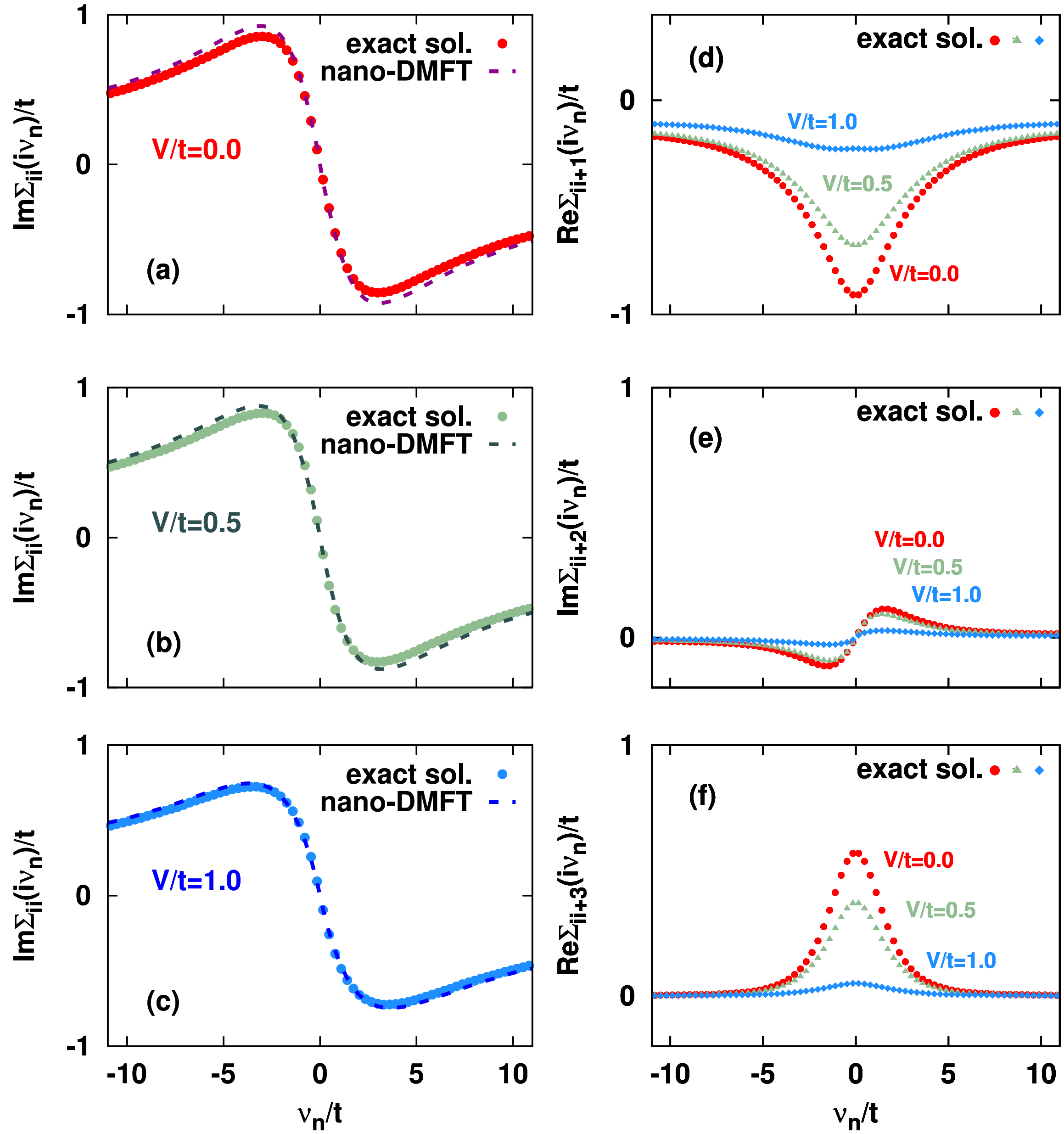

Figure 3.6: Self-energy in Matsubara representation for the benzene ring in the *NN t* topology at $U = 5t$ and $T = 0.05t$. In panels (a), (b), and (c) we show the evolution with V/t of the imaginary part of the local self-energy, comparing nano-DMFT (dashed lines) with the exact solution (symbols). Note that the real part is always identically zero due to the particle-hole symmetry at half-filling. In panels (d), (e), and (f) we show the non-local self-energies for nearest-neighbors (i,$i+1$), next-nearest neighbors (i,$i+2$), and next-next-nearest neighbors (i,$i+3$), respectively, obtained with the exact solution. All other non-local components of the self-energy are either identical to the ones shown here (since all sites are equivalent) or zero due to particle-hole symmetry. Also note that $\Sigma_{i\neq j}$ is, obviously, identically zero in nano-DMFT. Adapted after Ref. [207].

self-energy to the real axis, which whe show in Fig. 3.7 for the critical case of the isolated ($v=0$) benzene ring. The analytic continuation has been performed by means of a Padè interpolation of the QMC data[4] which allows to obtain both local and non-local (which are finite only within the exact solution) contributions of the self-energy.

Concerning the local self-energy (left panels), we can interpret the data in terms of a **Fermi liquid** (FL) **expansion** around the Fermi energy [90], yielding

$$\Sigma_{ii}(\nu) \sim -\alpha\nu + \imath\gamma(\pi^2 T^2 + \nu^2) + O(\nu^3), \tag{3.5}$$

where the coefficients α and γ control the quasi-particle *mass renormalization* and the *scattering rate*, respectively. The Fermi liquid expansion (3.5) is justified provided: i) quasi-particle excitations have a finite effective mass near the Fermi level, and ii) the damping of the quasi-particle is much smaller than the typical quasi-particle energy, i.e., $\gamma \ll |\nu|, T$. While one may be doubtful that those condition are fulfilled in the presence of a strong Hubbard interaction, one realizes that the nano-DMFT and the exact local self-energy, shown in the lower and the upper left panels of Fig. 3.7 respectively, look indeed FL-like, with a negative slope around $\nu=0$ ($\alpha>0$) and a negative and tiny damping factor $\gamma<0$. In general, the non-local self-energy is non-trivial function, and the corresponding expansion is complicated. Yet, observing the analytic continuation, shown in the right panels of Fig. 3.7, we may still extract useful information. One can notice that, due to the particle-hole symmetry, the (local and the) non-local terms of the self-energy $\Sigma_{ij}(\nu)$ display an alternating even/odd symmetry with respect to ν for the real/imaginary part, depending on the couple of indexes i and j. In particular, around the Fermi energy, the nearest-neighbor contribution $\Sigma_{ii+1}(\nu)$ is characterized by a large static contribution $\mathrm{Re}\Sigma_{ii+1}(\nu=0) \sim t$, while the imaginary part is at least $O(\nu)$. Similar observations also hold for the other self-energy contributions. Hence, to a first approximation, the most important effect of the non-local self-energy consist in a renormalization of the bare hopping amplitude: $t \to t + \mathrm{Re}\Sigma_{ii+1}(\nu=0)$. As those terms have the same sign, the overall effect is an enhancement of the effective hopping, which determines a further suppression of the spectral weight at the Fermi energy of the benzene ring in the presence of non-local correlations.

This mechanism is more easily conceived by briefly considering the case of a two-site system at half-filling, connected by an hooping t, for which the local spectral function around he Fermi energy can be written as

$$A(\nu \sim 0) \sim \frac{1}{\pi}\frac{\gamma(\pi^2T^2+\nu^2)}{\left[\nu+\alpha\nu-\imath\gamma(\pi^2T^2+\nu^2)\right]^2-(t+\xi)^2}, \tag{3.6}$$

where we used the brief notation $\xi = \mathrm{Re}\Sigma_{ii+1}(\nu=0)$. In the non-interacting case ($\alpha,\gamma,\xi=0$) the excitation spectra of the two-site system consists of two peaks, separated by a charge gap

[4] Particular care is needed as the QMC data are affected by statistical fluctuations, and may cause the Pade interpolation to yield non-analytic functions on the real frequency axis. While extremely accurate QMC data would be needed to obtain a physically sensible spectral function via analytic continuation, we expect the qualitative features of the self-energy discussed here to remain valid.

$\Delta = 2t$, so that its low-energy behavior resembles the one of the benzene molecule. The spectral function (3.6) shows that, even in case of a tiny quasi-particle dumping factor γ, the spectral weight at the Fermi energy can still be suppressed by large non-local correlations (cf. also with the spectral function in the left panel of Fig. 3.10 and the related discussion).

Another confirmation of our interpretation, comes also from the analysis of the self-energy in the *all t* configuration, shown in Fig. 3.8. In the upper panels we show the comparison between the nano-DMFT and the exact local self-energy at $V/t = 1$, i.e. very close to the lowest value of V/t accessible to the exact solution, the both imaginary part (and hence the quasi-particle residue) and the real part (and hence the filling) are accurately reproduced. Moreover, due to the higher connectivity with respect to the *NN t* hopping configuration, any non-local contribution of the self-energy is completely negligible with respect to the local ones, i.e., almost two order of magnitude smaller (and therefore not shown). In particular this happens also to the nearest

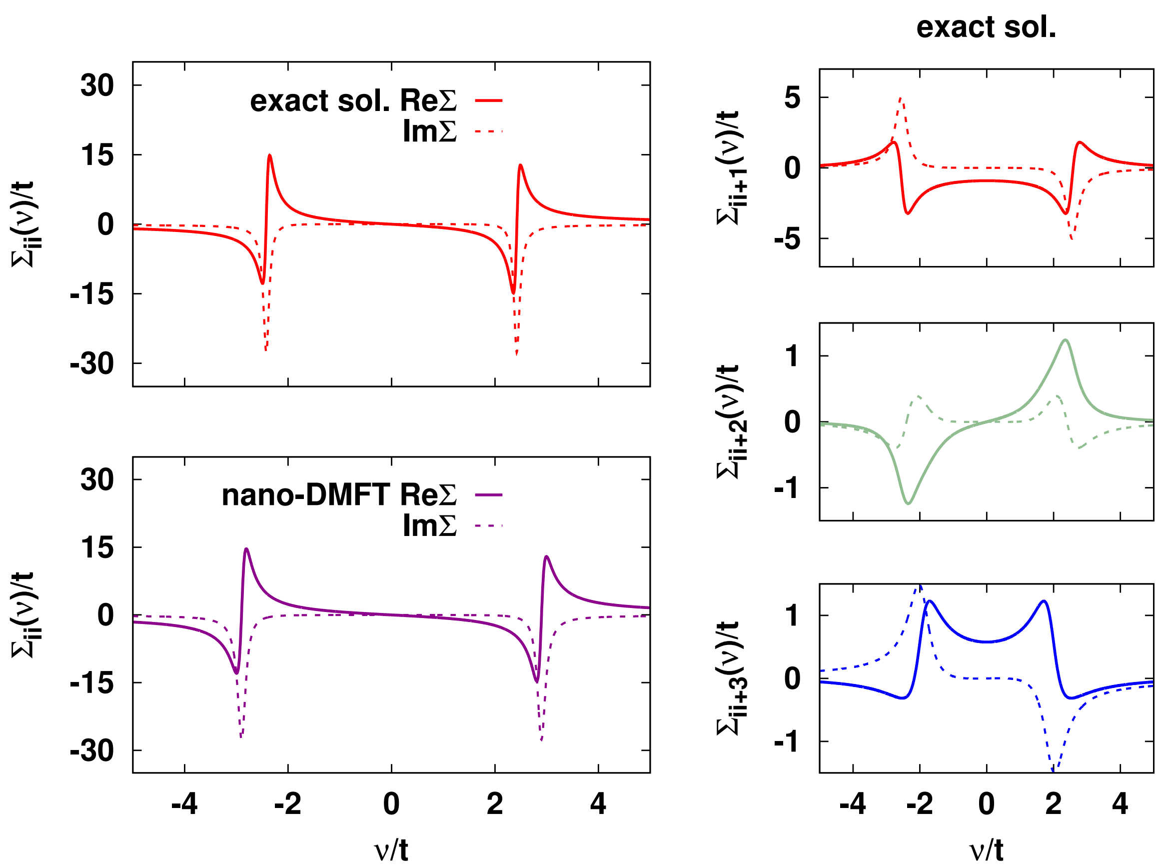

Figure 3.7: Analytic continuation on the real frequency axis of the real (full line) and imaginary (dashed line) self-energy for the benzene ring in the *NN t* topology at $U = 5t$, $T = 0.05t$, and $V/t = 0.0$. Left panels: comparison local self-energy between the exact QMC solution (upper panel) and nano-DMFT(QMC) (lower panel). Right panels: contributions of the exact QMC non-local self-energy for nearest-neighbors (i,$i+1$, upper panel), next-nearest neighbors (i,$i+2$, middle panel), and next-next-nearest neighbors (i,$i+3$, lower panel), respectively.

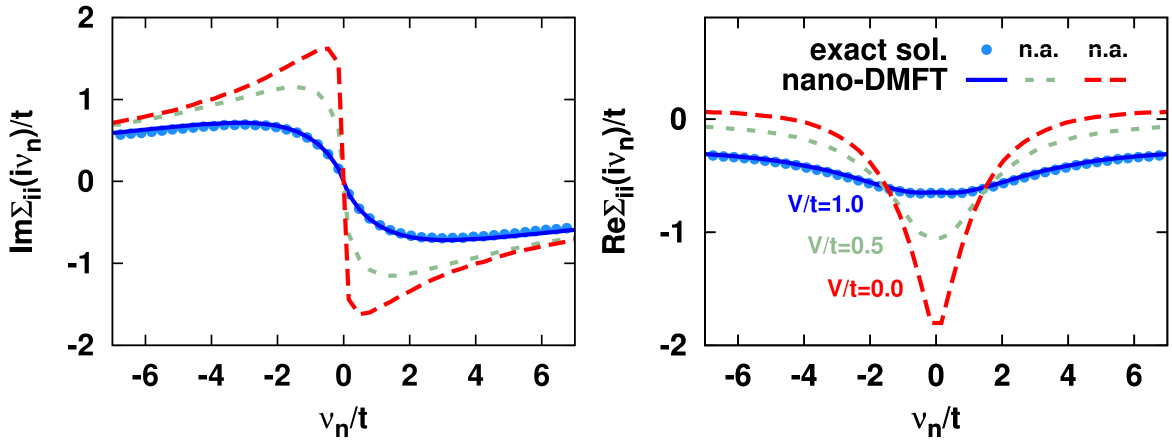

Figure 3.8: Local self-energy in Matsubara representation for the benzene ring in the *all t* topology at $U = 5t$ and $T = 0.05t$. comparing between DMFT (lines) and exact solution (symbols) at different V/t. Above $V/t \sim 0.8$, the exact local self-energy is accurately reproduced by nano-DMFT, while non-local contributions are negligible with respect to the local ones (not shown). Below this threshold, no exact QMC solution is available, but the evolution of the nano-DMFT self-energy shows that the system becomes more correlated. Adapted after Ref. [207].

neighbor self-energy at low-frequency,[5] in contrast to the *NN t* case. If one defines the ratio

$$\varsigma_{ij} := \frac{\Sigma_{ij}(\nu_n = \pi T)}{\max\limits_{n}\{\mathrm{Im}\Sigma_{ii}(\imath\nu_n)\}}, \tag{3.7}$$

then for $V/t = 1$ one finds $\varsigma_{ii+1}^{all\,t} \approx 0.01$ and $\varsigma_{ii+1}^{NN\,t} \approx 0.32$, where the latter values corresponds to the self-energy in panel (d) of Fig. 3.6).

Due to the sign-problem in the exact solution, we can study the evolution of the self-energy toward the molecular limit only within nano-DMFT. The results shows that the system becomes more correlated (γ increases) upon decreasing V/t, and that most likely also non-local correlations eventually arise. This also explains why, in the limit $V/t \to 0$, nano-DMFT overestimates $\overline{A(0)}$, in contrast with the exact ED value of $\overline{A(0)} = 0$, as shown in the left panel of Fig. 3.5.

[5]Note that, instead, the asymptotic value of $\Sigma_{i\neq j}(\imath\nu_n \to \infty) \to 0$ in all cases, as the only constant contribution is the Hartree term, which is purely local in the Hubbard model (local interaction).

Spectral function: analytic continuation of the QMC data. In order to have a better picture of the behavior of the system, not limited to the Fermi level, in Fig. 3.9 we show the evolution with V/t of the **one-particle spectral function** $A(\nu) = -\frac{1}{\pi}\mathrm{Im}G^r(\nu)$.

The spectra are obtained via analytic continuation on the real axis of the DMFT(QMC) data using a Padè interpolation and/or a Maximum Entropy method (MEM) [101]. A qualitative

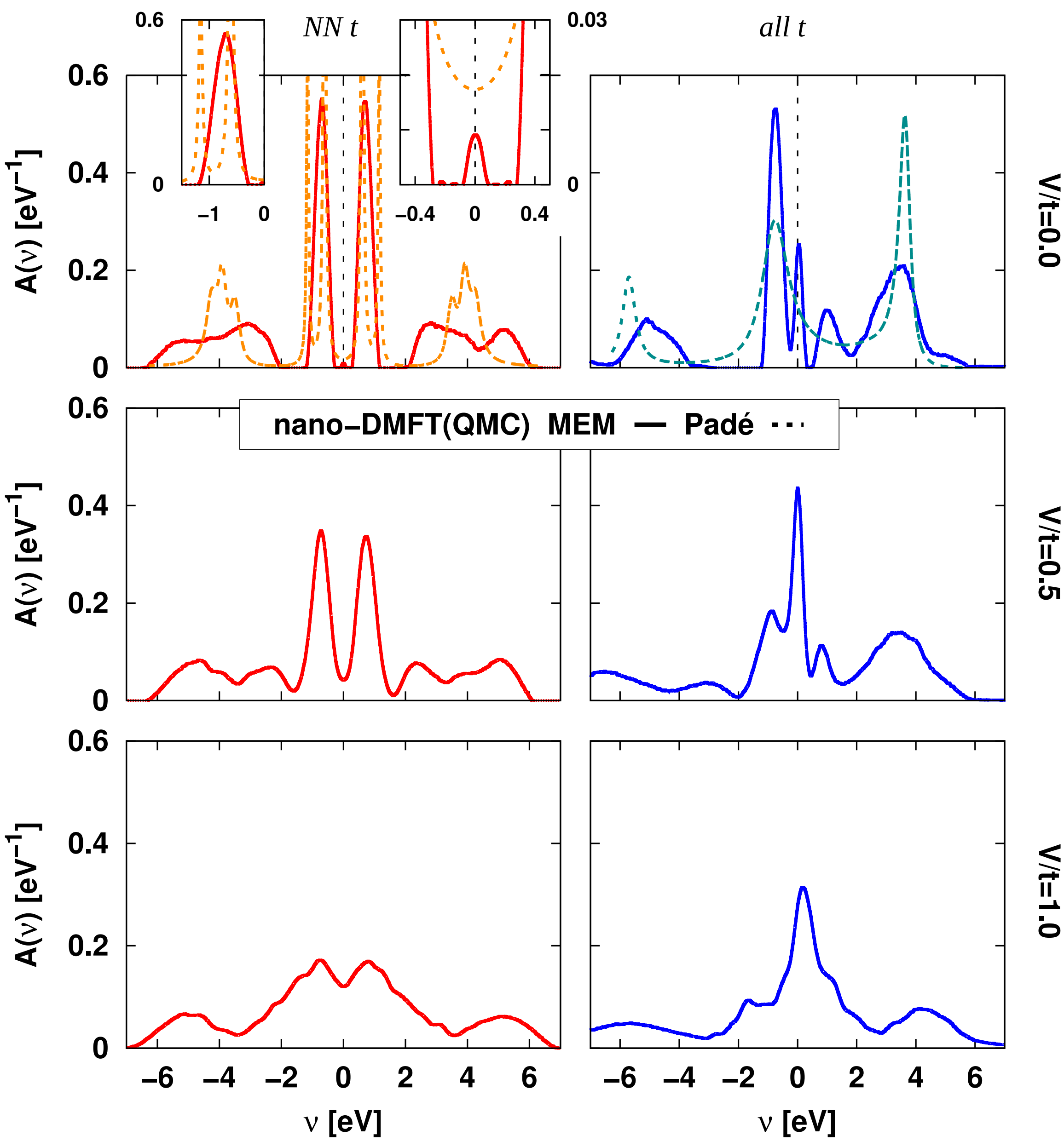

Figure 3.9: One-particle spectral function $A(\nu) = -\frac{1}{\pi}\mathrm{Im}G^r(\nu)$ for the benzene ring at $U = 5t$ and $T = 0.05t$. Left panels: evolution of $A(\nu)$ with V/t in the *NN t* (red/orange) and *all t* (blue/cyan) hopping configurations. The analytic continuation of the nano-DMFT(QMC) data has been performed with MEM (solid lines) and, only in the case $V/t = 0.0$, also with a Padé interpolation (dashed lines).

understanding of the effect of electronic correlations is already provided by a comparison to the non-interacting ones of the benzene molecule for both *NN t* and *all t* hopping configurations, shown in the left panels of Fig. 3.3 (where $\Gamma/t\sim 0.4$ corresponds to $V/t=0.5$).

In the *NN t* topology, $A(\nu)$ shares some similarities with the non-interacting spectrum: at $V=0$ (upper left panel of Fig. 3.9) the MEM predict two broad low-energy structures symmetric with respect of the Fermi energy, due of the particle-hole symmetry, while the Padè method resolves each structure into two peaks (see left inset) The overall effect of the interaction is to *shrink* the low-energy structure toward the Fermi energy, and the gap is filled with some spectral weight: a real filling in the Padè spectrum and a spurious tiny peak in the ME one (see right inset). At the same time, more structure appears at an energy scale comparable with U, which is identified with the lower and and the upper Hubbard bands. The coupling to the leads additionally contributes to the broadening of the spectrum, leading to a semi-metallic behavior. The redistribution of the spectral weight due to the interaction is instead more drastic in the *all t* topology. Already in the molecular limit ($V=0$), nano-DMFT predicts a metallic solution, which is in contradiction with the results of the exact diagonalization (cf. with the discussion of the left panel of Fig. 3.5). At finite V/t (middle and lower panels of Fig. 3.9), the hybridization to the leads favors the emergence of a resonance at the Fermi energy, which is a genuine many-body effect, arising from the interplay between U and V, and it would not exist in the absence of electronic correlations (cf. with the lower left panel of Fig. 3.3). At the same time, the hybridization induces an additional quasi-particle damping factor $\Gamma/2=\pi\rho V^2$, which also

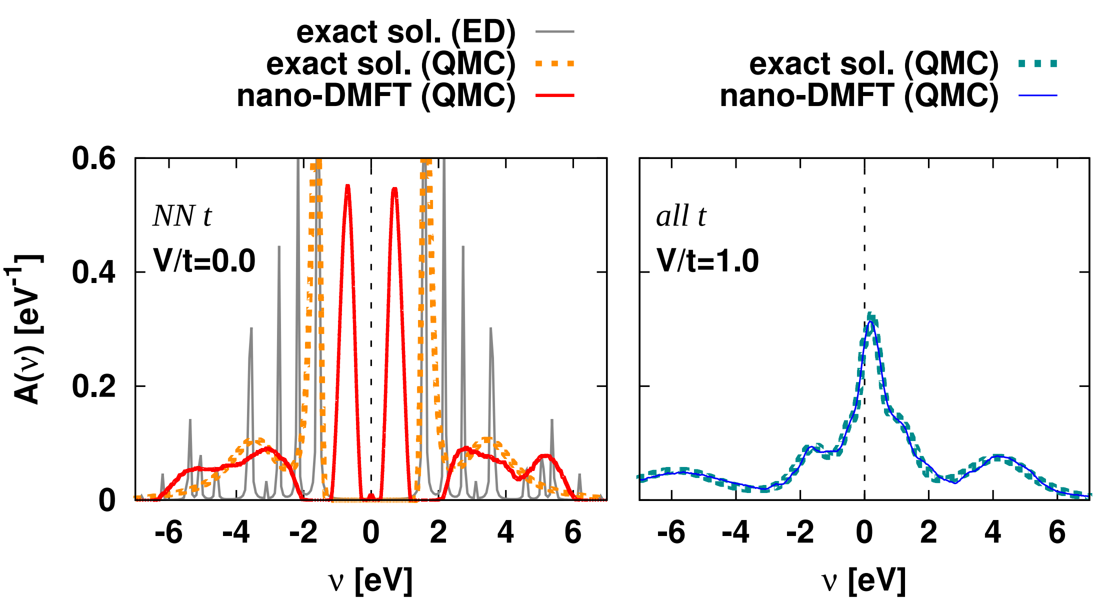

Figure 3.10: Comparison of the nano-DMFT and exact one-particle spectral function for the benzene ring at $U=5t$ and $T=0.05t$. Left panel: *NN t* hopping configuration at $V/t=0$, non-local spatial correlations matter. Right panel: *all t* hopping configuration at $V/t=1$, the system is dominated by local effects.

controls the width of the resonant peak. Hence, toward the limit in which the hybridization becomes the dominating energy scale, the spectral weight becomes more and more incoherent in both hopping configurations, and tend to lose almost all low-energy features.

The comparison between nano-DMFT and the exact solution can be performed also at the level of the one-particle spectral function. However, accumulating statistics to perform an analytic continuation of the exact QMC solution with the MEM is computationally quite costly, already for the case of the benzene molecule, while the Padè interpolation yields non-analytic spectra due to difficulties in the interpolation process (originating from the statistical fluctuation of the QMC data) for the non-local self-energies $\Sigma_{ij}(\imath\nu_n)$ for $|i-j|>1$.
Hence, we restricted to the comparison of the following two representative cases, one for each hopping configuration: (i) the molecular limit of the benzene molecule in the *NN t* configuration, and (ii) the *all t* configuration for $V/t=1$, i.e. at the lowest possible value of the hybridization for which the fermionic sign in the exact QMC solution is still close to one. Both the analytic continuation of the nano-DMFT(QMC) and exact QMC solution are obtained by means of MEM; for the isolated ring we provide, in addition, the one-particle spectral function obtained by ED of the Hamiltonian; the results are compared in Fig. 3.10. In the *NN t* case (left panel), we can see that nano-DMFT completely fails to describe the low-energy physics, predicting a small yet finite spectral weight (or a tiny peak in the MEM, compare also with the r.h.s inset of the upper left panle of Fig. 3.5), while both the QMC and ED exact solution remarkably yield the same amplitude for the gap: $\Delta\sim 2.5$ eV. In the *all t* case (right panel), where non-local spatial correlations are negligible, nano-DMFT not only predicts the correct low-energy physics, but it quantitatively reproduces the excitation spectra in the whole energy range.

Quantum transport in benzene junctions. Another interesting issue is the study of electronic transport in molecular junctions. As already mentioned, one expects QI to play an important role in ring structures, and it reflects itself in the presence of *antiresonances* in the transmission function. This interesting phenomenon has been addressed by several authors, yet neglecting electronic correlations [181, 182]. The reason for this is that QI seems to be mainly connected to the molecular topology. [182] As a consequence, the main qualitative features connected to QI are captured already by tight-binding, of Hartree-Fock kind of calculations. However, the importance of non-perturbative electronic correlations, and of their interplay with QI, in determining the transport properties of nanoscopic structures is well known, and has been the subject of intensive investigation [185, 209, 210, 211]. Moreover, the Coulomb interaction plays a pivotal role in the study of both equilibrium and non-equilibrium transport for molecules and atomic contacts in the Kondo regime [212, 213, 214, 215].

In the following we will study equilibrium conductance in benzene junctions, and we will see that QI effects are clearly visible even in the non-interacting limit $U=0$, while, in the presence of an on-site interaction, effects of local (and non-local) electronic correlations become important, in particular in the weak-hybridization regime $\Gamma\ll t$.

As it has been shown in Sec. 1.3.2 the **electronic conductance** $G(\epsilon)=e^2/h\mathcal{T}(\epsilon)$ through a nanostructure can be expressed in terms of the **transmission coefficient**, obtained from the retarded and advanced Green's function of the interacting region. For the sake of clarity, we report here the corresponding formula, obtained neglecting vertex corrections

$$\mathcal{T}(\epsilon) = \mathrm{tr}[\hat{\Gamma}_{\mathrm{L}}(\epsilon)\hat{G}^{a}(\epsilon)\hat{\Gamma}_{\mathrm{R}}(\epsilon)\hat{G}^{r}(\epsilon)]. \tag{1.82}$$

In the expression above, both the Green's functions $\hat{G}^{r,a}$ and the scattering amplitude $\hat{\Gamma}_{\mathrm{L,R}}$ are matrices in the sites indexes of the nanostructure. In this respect, further clarification is mandatory. In the literature the conductance through a benzene ring is usually calculated in the configuration where the molecule bridges two leads *only*. Depending whether the leads are connected to the nearest, next-nearest, or next-next-nearest (i.e. opposite) neighboring-sites of the benzene ring, those configuration are labeled as *ortho*-, *meta*-, and *para*-positions, respectively [181].

The realization of those configurations in the nanostructure we are considering is indeed possible, yet it breaks the symmetry of the structure, i.e. one will have two or three inequivalent sites, depending on the position of the leads. Hence, we decided to avoid this additional complication, and we considered a configuration in which each site of the benzene ring is equivalently coupled to its own lead with identical, energy independent, scattering amplitudes $\Gamma = 2\pi\rho V^2$. Even in this configuration, however, one can define and calculate a *two-terminal* conductance between sites L and R using the following form for the **scattering matrices**:

$$\left\{\hat{\Gamma}_{\mathrm{L}}\right\}_{ij} = 2\pi\rho V^2\delta_{Li}\delta_{jL}, \tag{3.8a}$$

$$\left\{\hat{\Gamma}_{\mathrm{R}}\right\}_{ij} = 2\pi\rho V^2\delta_{Ri}\delta_{jR}, \tag{3.8b}$$

where, in practice, the only non-zero element is located on the main diagonal, in the position corresponding to site L or R. Hence, when computing the conductance between a L and a R terminal, the form (3.8) for the scattering matrices implies $\Gamma = \Gamma_{\mathrm{L}} = \Gamma_{\mathrm{R}}$ and one can show that Eq. (1.82) simplifies to

$$\mathcal{T}(\epsilon) = \sum_{\sigma} \Gamma|G^{r}_{\sigma\mathrm{LR}}(\epsilon)|^2\Gamma. \tag{3.9}$$

Obviously, in the configuration we consider, the Green's function will still contain the information that *each* site is contacted to its own lead. Despite this does not have a dramatic effect on the conductance in the limit $\Gamma \ll t$, it is certainly of importance in the intermediate-to-strong-hybridization regime[6] or if one aims to a realistic description of transport properties of the system under analysis.

With the *caveat* that the Green's function is anyway modifed by the presence of additional leads

[6]This statement is based on the comparison the conductance as a function of the gate voltage V_G (for more detail see Sec. 3.2.3) in the leads' configuration discussed so far, and the one in which only two sites of the ring are connected to the leads. In the latter configuration the translational symmetry is explicitly broken by the inhomogeneous coupling of the molecule to the leads, and the atoms constituting the molecule are no longer equivalent ($N_{\mathrm{ineq}} = 3, 4, 2$ in the case of *ortho*-, *meta*-, and *para*-positions of the leads, respectively). As one expects, we have found that the simultaneous presence of six leads, instead of two only, yields a suppression of the conductance of the order of $O(\Gamma/t)$, due to the enhanced scattering rate for the propagating electrons.

beyond the one to which voltage is applied, in the following we nevertheless keep the usual literature nomenclature as we will refer to the *ortho*-, *meta*-, and *para*-position, corresponding to the transmission coefficient computed using Eq. (3.9) with the non-local elements of the Green's function $|G^{r}_{\sigma ij}(\epsilon)|^2$ for $|i-j|=1$, $|i-j|=2$, and $|i-j|=3$, respectively.
A last complication, that we should discuss before turning to the numerical results, is related to the choice of a QMC impurity solver. In fact, one does not have direct access to the non-local elements of the retarded (or advanced) Green's function, and has to rely on an analytic continuation of the self-energy, which is particularly unstable for the exact solution, as already discussed. If possible, one would rather pursue alternative ways, e.g. the method which has been recently reported by Karrash *et al.* [216] is indeed interesting: they showed that, in the case of the single-impurity Anderson model, the finite-temperature conductance on the real axis can be obtained directly from the Matsubara Green's function, by performing a continued fraction expansion of the Fermi function, *without* the need of any analytic continuation. A generalization of the method to extended systems, however, does not seem to be possible.
Due to the complications inherent to the analytic continuation, we cannot easily compute the full energy-dependent transmission coefficient, and we will, hence, consider only the **conductance at the Fermi energy** $G(\epsilon_F)=(e^2/h)\mathcal{T}(\epsilon_F)$, estimated as

$$G(\epsilon_F) = \frac{e^2}{h}\sum_{\sigma}\Gamma|G_{\sigma\mathrm{LR}}(\imath\nu_n \to 0)|^2\Gamma \approx 2\frac{e^2}{h}\left(2\pi\rho V^2\right)^2 |G_{\mathrm{LR}}(\imath\nu_n = \pi T)|^2, \tag{3.10}$$

where we drop the spin dependence of the propagator and explicitly include a factor 2 for the spin degeneracy. However, the presence of, e.g., (anti)ferromagnetic leads or a magnetic field, would obviously determine a spin-dependent conductance.

A quantitative estimate for the transmission coefficient (3.10) may be obtained extrapolating the Green's function in the limit $\imath\nu_n \to 0$ with some fitting procedure. In the results shown in the following we just consider the Green's function at the lowest Matsubara frequency, $\nu = \pi T$, which, though being a rough estimate at our relatively high-temperature, is sufficient for understanding the qualitative behavior of the conductance in the benzene junction. In Fig. 3.11, we show the equilibrium conductance at the Fermi energy $G(\epsilon_F) = (e^2/h)\mathcal{T}(\epsilon_{\mathrm{F}})$ through the benzene nanostructure in the *ortho*-, *meta*-, and *para*-positions for both *NN t* and *all t* hopping topologies. As a general remark, valid for all connections, we can see that $G(\epsilon_F)$ increases like V^4 at low values of the hybridization, as it could be expected treating the scattering amplitudes Γ in Eq. (3.10) perturbatively. As V increases, $G(\epsilon_F)$ exhibits a maximum due to the formation of a resonant peak of width $\Delta = \pi\rho V^2$ between each site and its own lead. This effect is a consequence of a non-perturbative interplay between the on-site interaction and the hybridization. In the *NN t* topology (upper panel), our calculation reproduces the reduction of the conductance in the *meta*-position, with respect to the *ortho*- and the *para*-position [181]. This effect is believed to be a generic characteristic of single-molecule junctions, and it has been explained in terms of QI, arising only from the molecule's topology and not directly related to the presence of electronic correlations [182]. On the other hand, many-body effects have been recently reported [185] to be responsible for the formation of transmission minima (''Mott nodes'') in

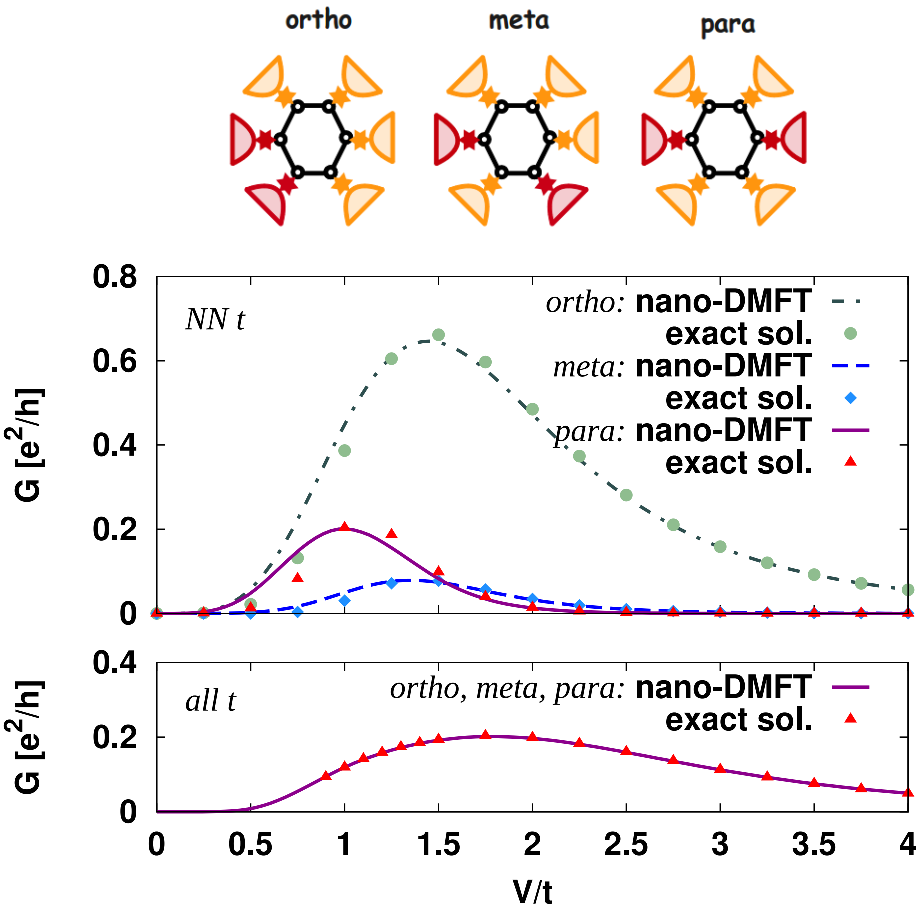

Figure 3.11: Conductance $G \equiv G(\epsilon_F)$ through the benzene ring as a function of V/t for *NN t* (upper panel) and *all t* (lower panel) hopping geometries at $U = 5t$ and $T = 0.05t$, comparing nano-DMFT (lines) and the exact solution (symbols). The *ortho*, *meta* and *para* labels refer to the conductance computed between two of the metallic leads, as shown schematically above the plots. In the *NN t* case, QI effect are clearly visible. In the *all t* case, instead, due to the symmetry of the problem all connections are obviously equivalent. Adapted after Ref. [207].

molecules with open shell configurations. Yet, this effect is not present in the *all t* topology (lower panel), and $G(\epsilon_F)$ is the same in all three contact positions due to the particular hopping structure (note that the criteria given in Ref. [182] to predict destructive interference relies on the assumption that only nearest neighbor hopping processes within the molecule take place).
The comparison between nano-DMFT and the exact solution shows that non-local correlations (beyond DMFT) are not important both in the limit in which the molecule is strongly coupled to the leads and when the connectivity is high. This, in the light of the results presented before, may not be surprising, since the conductance without vertex corrections is essentially a single-particle quantity.

If the suppression of $G(\epsilon_F)$ is not a direct consequence of electronic correlations, then we need to understand what is the influence of U (if any) on the profile of the zero-bias conduc-

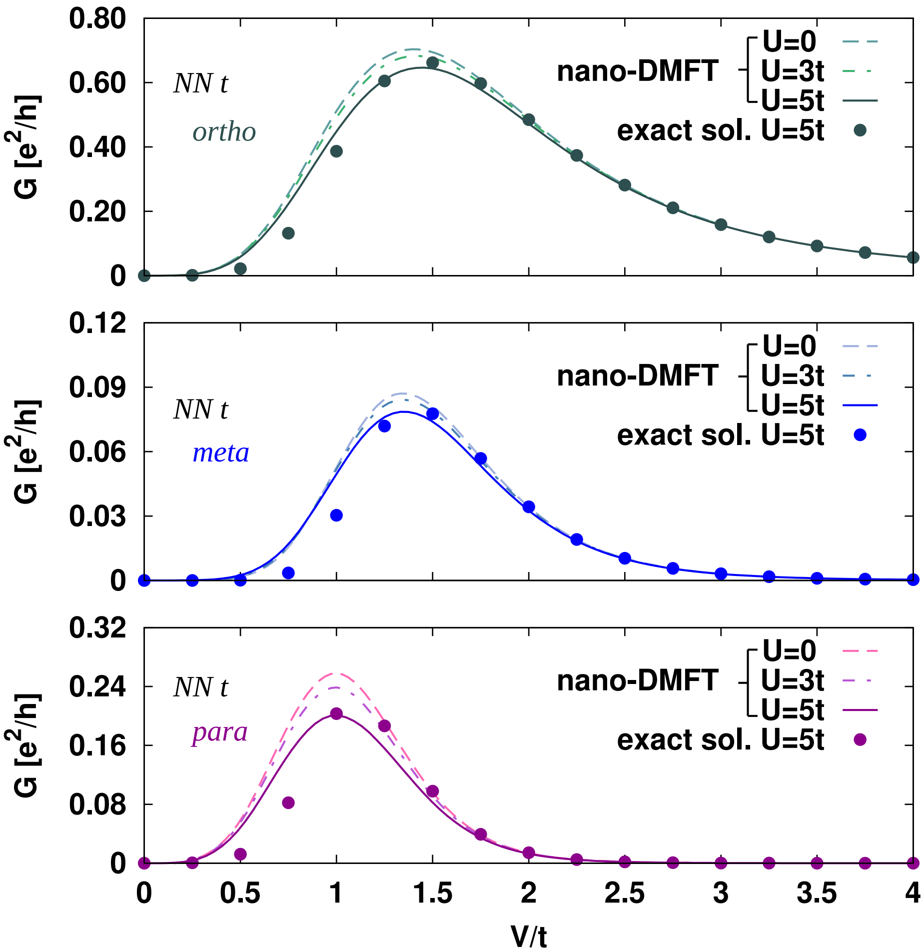

Figure 3.12: Evolution with U/t of the conductance through the benzene ring in the three contact positions of the *NN t* hopping configuration at $T = 0.05t$. Adapted after Ref. [207].

	$\Delta(U)$			
	ortho-	*meta-*	*para-*	position
$U = 3t$	$\sim 2\%$	$\sim 3\%$	$\sim 7\%$	
$U = 5t$	$\sim 7\%$	$\sim 9\%$	$\sim 22\%$	

Table 3.1: Percentage-wise reduction $\Delta(U)$, with respect to the non-interacting case, of the maximum value of the nano-DMFT two-terminal conductance in a benzene junction. The comparison of the data for different leads positions shows that, once QI are filtered out, the higher the order of hopping processes involved in transport through the molecule, the higher is the suppression of the conductance due to the local interaction. Adapted after Ref. [207].

tance. To this end, we report in Fig. 3.12 the results of our calculations at different values of U/t in the whole hybridization range, including the non-interacting case, where also nano-DMFT is obviously exact. As anticipated, the reduction of the conductance in the *meta*-position is observed already in the non-interacting case $U = 0$, supporting the hypothesis that it is a mere topological effect. The presence of a finite U leads only to quantitative changes, suppressing the conductance peak which appears in a hybridization regime $V \simeq t$, though this picture may change if vertex corrections are taken into account.

Already in the non-interacting case, the channel-dependent suppression of the conductance results from (i) a reduction arising from the length of the ‘‘conductance paths‘‘ between the corresponding leads, i.e., $G(\epsilon_F) \propto \mathrm{e}^{2|L-R|}$ and (ii) a topological reduction due to QI in the different channels. In order to get information on the **effect of correlations** *on top* of those effects, we compare the *percentage-wise* reduction $\Delta(U)$ of the conductance maximum at $U \neq 0$ with respect to its non-interacting value (at the same value of the ratio V/t). We find that the suppression, at a given value of U, increases with the distance between the sites through which the conductance is computed, i.e. $\Delta_{ortho} < \Delta_{meta} < \Delta_{para}$. This is understood considering that the Hubbard repulsion tends to localize the electrons in the molecule, and to penalize hopping processes, hence further suppressing the conductance through the dependence on the (interacting) non-local propagator. We summarize the corresponding values in Table 3.1. For similar reasons, when $V/t \gtrsim 1$ the ‘‘local’’ physics of the hybridization dominates over non-local hopping processes, and again the largest the distance between site L and R, the faster is the suppression of the conductance in the corresponding channel.

Moreover, nano-DMFT suggests that the effect of U is important only in the intermediate-hybridization regime $V \simeq t$ region. In the weak-hybridization regime the nano-DMFT curves for different values of U (almost) collapse onto one another, while the exact solution predicts a sensibly lower conductance all the way down toward the molecular limit. This suggests that, here, local correlations do not play any role in electronic transport, while non-local do. This aspect deserves further investigation: for instance one would be interested to see what happens if vertex correction to the conductance are included.

3.2.2 Cyclo-octatetraene molecule

The results presented in this section, concerning the COT molecule, are still unpublished.

The results presented so far for the benzene molecule show that nano-DMFT performs quite well, with some intrinsic limitation which are well understood in terms of the missing non-local spatial correlations. In order to have a wider picture of the behavior of Q1D molecules, and to understand how good nano-DMFT can describe them, we need to consider also different situations. Specifically, the physics of a benzene junction in the weak-hybridization regime is obviously dominated by the presence of a charge gap in the non-interacting DOS, and it would be interesting to investigate how our approximation scheme performs in the weak-hybridization regime, as we mentioned before, of a correlated metallic case. In this respect we have followed **two different paths**: (i) we considered another Q1D system, namely the **COT molecule**, introduced at the beginning of this chapter, and analyzed in detail below, and (ii) we introduced another control parameter, i.e., the **gate voltage** V_G, to be discussed in the next section.

Electronic structure of the COT molecule. The most striking difference between the COT and the benzene molecule is the existence, in the discrete, non-interacting spectrum, of a (doubly degenerate) peak lying exactly at the Fermi energy. In the presence of a local repulsion term (assuming it small enough not to invalidate the MOs picture), the lowest energy configuration would be the one with two singly-occupied degenerate orbitals at the Fermi energy, thus realizing an effective two-level $SU(4)$ AIM, relevant, e.g., for the description of carbon nanotubes QDs [217]. For the same reason, Kondo physics may be expected at low temperature.

As a first application of nano-DMFT to the COT molecule, let us consider the molecular limit $V=0$, which has both the advantage of getting rid of the hybridization energy scale, and to focus on a situation in which non-local correlation are expected to be maximal (according also to the analysis of the benzene molecule). The **one-particle spectral function** resulting from the MEM analytic continuation of the nano-DMFT(QMC) data, and the corresponding **Matsubara self-energy**, are shown in Fig. 3.13 for increasing values of U.
Let us start describing nano-DMFT results starting from the weak coupling regime, i.e. $U=t$. We show that the one-particle spectral function displays a peak at the Fermi energy[7] which is *disconnected* from the high-energy structure of the spectrum. The latter, however, is not entirely due to incoherent contribution of the Hubbard bands, as it will be even more clear observing the evolution of the spectral function with U, but originates also from the evolution with U of the non-interacting levels with eigenvalues (cf. with the upper right panel of Fig. 3.3). Moreover, we notice a quite peculiar behavior of the corresponding Matsubara local self-energy at low energy. In fact the absolute value of $\text{Im}\Sigma_{ii}(\imath\nu_n)$ decreases as $\nu_n \to 0^+$ down to approximately the last but one Matsubara frequency $\nu = 3\pi T$, while at lower energy it raises again. This determines a jump around $\nu=0$. This feature is still present also at higher

[7] Obviously, it cannot be a Kondo resonance with the leads, as $V=0$, but it may be a Kondo resonance à la DMFT within the C atoms of the COT ring.

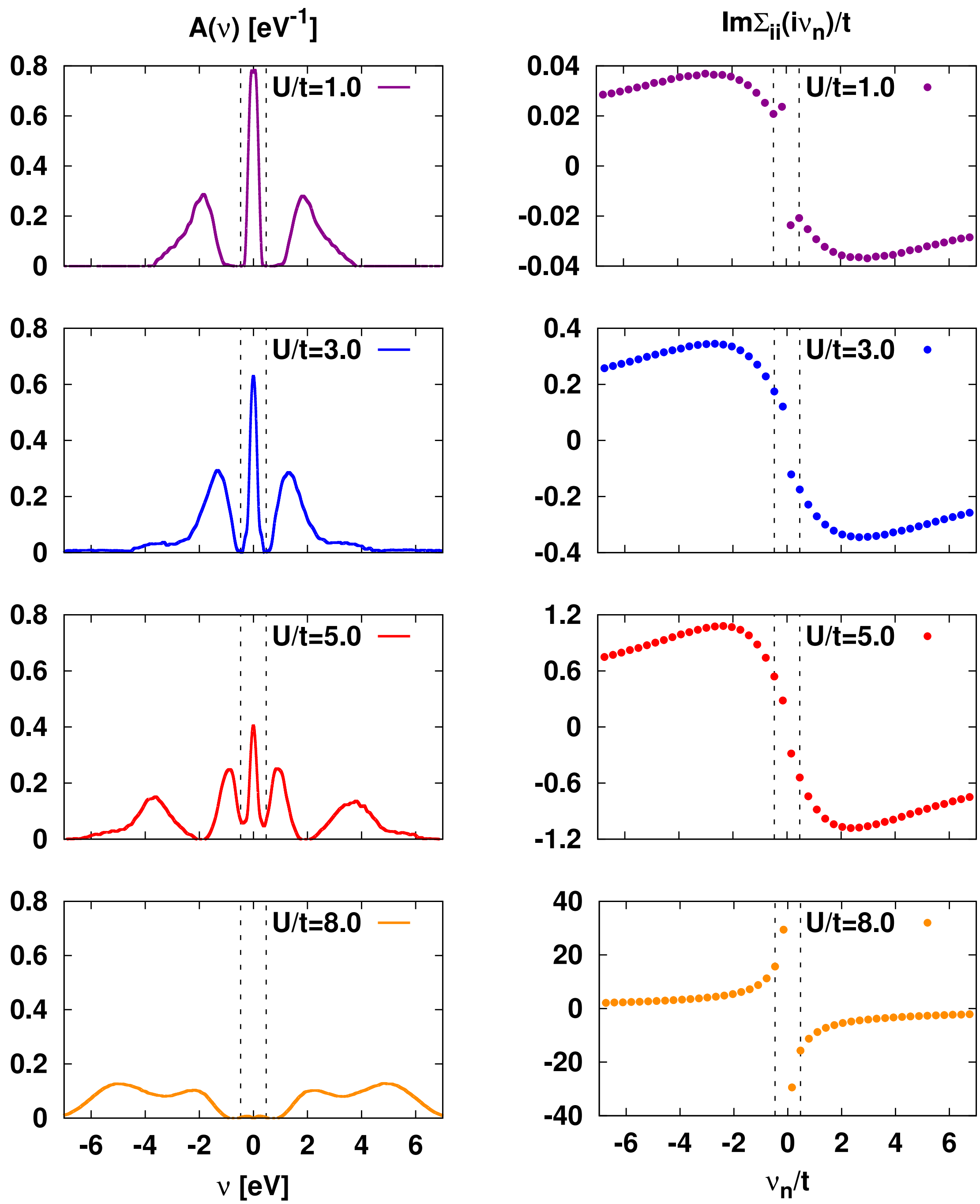

Figure 3.13: Interaction driven MIT within nano-DMFT for the isolated ($V = 0$) COT molecule in the *NN t* hopping configuration at $T = 0.05t$. Left panels: one-particle spectral function $A(\nu)$ obtained by MEM analytic continuation of the QMC data. Right panels: imaginary part of the local self-energy in Matsubara representation, the real part is identically zero due to particle-hole symmetry at half-filling. The black dashed line is a guide to the eye, indicating the $\nu = 3\pi T$.

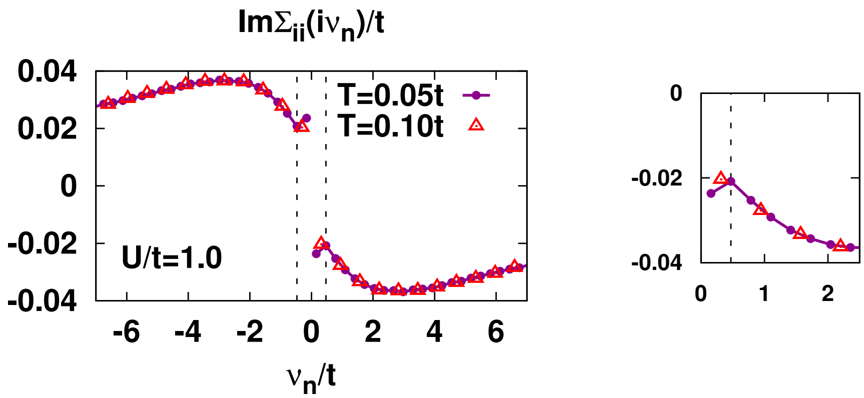

Figure 3.14: Left panel: temperature dependence of the imaginary part of the nano-DMFT self-energy in Matsubara representation for the isolated ($V=0$) COT molecule in the *NN* t hopping configuration for $U=t$. Right panel: zoom in the low-frequency range. The black dashed line is a guide to the eye, indicating the $\nu=\pm 3\pi T$ (at $T=0.05t$).

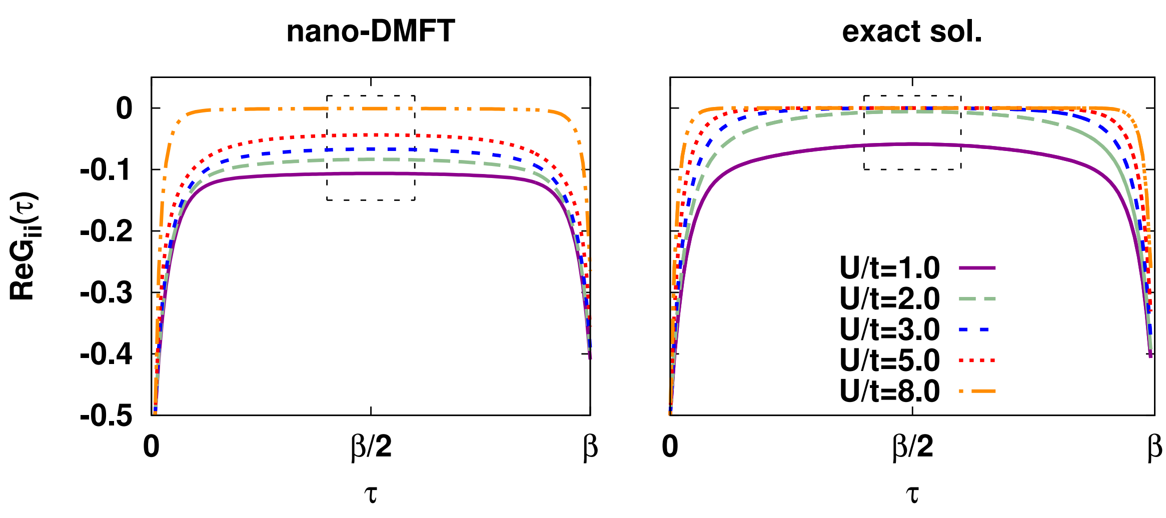

Figure 3.15: Local QMC Green's function $G_{ii}(\tau)$ in the imaginary time representation for the isolated ($V=0$) COT molecule in the *NN* t hopping configuration at $T=0.05t$ as a function of U/t. The black dashed lines highlight the suppression of the spectral function at the Fermi energy, estimated as $\overline{A(0)}=\beta G_{ii}(\beta/2)$. Left panel: in nano-DMFT the system continuously evolves into an insulator, MIT happening at a critical value of $U_c\sim 8t$. Right panel: in the exact solution $G(\beta/2)\sim 0$, within the systematic error $(\Delta\tau)^2$ error, already at $U/t=2t$.

temperatures, yet less evident (see Fig. 3.14). A similar behavior, can still be traced in the local self-energy also at $U = 3t$, and the spectrum is shrinking toward the Fermi energy (as in the case of the benzene molecule). At $U = 5t$ the situation is already much different: the low-energy structure of the spectral function is now composed by *three* connected peaks, which resembles a renormalized version of the spectral function at lower values of U/t, besides one can clearly observe the formation of Hubbard bands, at an energy scale comparable with U. In turn, the corresponding self-energy is smooth and linearly vanishing as $\nu_n \to 0^+$, suggesting the onset of a more conventional (but already strongly renormalized) FL ground state. Further increasing the interaction to $U = 8t$, the system undergoes a Mott-Hubbard MIT (more precisely a crossover), where the narrow peak at the Fermi energy has disappeared and the self-energy diverges, although still deviating from the atomic $\Sigma_{ii}(\imath\nu_n) \sim U^2/\nu_n$ behavior.

The next step would be to understand whether non-local correlations modify the nano-DMFT picture presented above. Obviously, obtaining the exact spectral function, accumulating statistics for the QMC is obviously even more costly than in the case of the benzene molecule, because the Hilbert space 2^{2N_s} of the system increases exponentially with the number of correlated sites N_s in the benzene and COT molecules. Nevertheless, one could extract an equivalent information by the QMC data, analyzing the U dependence of the nano-DMFT and the exact local Green's function in the imaginary time representation, as shown in Fig. 3.15. The relation between the local Green's function and the spectral weight at the Fermi energy, already given in Eq. (3.3), is reproduced here, for the sake of clarity:

$$\overline{A(0)} = \int d\nu A(\nu) \cosh^{-1}(\nu/2T) \approx \beta G(\beta/2). \tag{3.3}$$

If we analyze the nano-DMFT results, we can clearly see that (the absolute value of) $G_{ii}(\beta/2)$ is continuously decreasing with increasing U, until becoming zero around $U = 8t$, in correspondence of the MIT, somehow recalling the behavior of the DMFT solution of the (bulk) half-filled Hubbard model. On the other hand, in the exact solution, $G_{ii}(\beta/2)$ is significantly smaller than in the nano-DMFT case already at the lowest value of U/t considered here, and it is quickly suppressed with increasing U, for $U > U_c$. We could estimate the exact critical value to be $U_c \gtrsim 2t$. In this respect, however, we have to consider two sources of indetermination that affect the QMC data: (i) the systematic error due to the Trotter decomposition in the HF-QMC algorithm [103] that is of the order of $(\Delta\tau)^2 \sim 0.027$, in these calculations (recall that $\Delta\tau = \beta/L$ is the discretization step of the imaginary time domain); and (ii) the estimate of $\overline{A(0)}$ by means of Eq. (3.3) involves an integral over a finite frequency window of the order of the temperature T, so that we expect it to *overestimate* the real value of $A(0)$. A possible way to overcome this problems, would consist in extrapolating the results for $\Delta\tau \to 0$, as well as decrease the temperature. However, this is extremely costly within the HF-QMC: the overall numerical effort of the exact solution of the impurity problem grows as $2N_s(2N_s - 1){N_s}^2L^3$ (obviously nano-DMFT corresponds to $N_s = 1$) and $L^3 \sim 1/T^3$ upon temperature for a given $\Delta\tau$ [121]. An alternative, for future studies, would be to use a CT-QMC as impurity solver [93, 218] which does not suffer from the discretization error $\Delta\tau$ and scales only linearly with $\beta = 1/T$.

As the isolated molecule can be diagonalized exactly, in order to dispel the doubts arising from the interpretation of the QMC data, we decided to compare them with the ED one-particle spectral function, as shown in Fig. 3.16. The ED results show clearly that, already at $U = t$, there is no spectral weight at the Fermi energy, implying (i) that the peak observe in nano-DMFT is either an artifact of the MEM analytic continuation, unable to resolve sharp peaks, or it can exists only due to the absence of non-local correlations, and (ii) that even in the exact QMC solution, when non-local correlations are included, at our relatively high temperature, we are not able to resolve the charge gap, below a given threshold, only considering the estimate of $\overline{A(0)}$ provided by Eq. (3.3). As there is no symmetry that requires a peak to be present at the Fermi energy, this would suggest that the doubly degenerate eigenstates of the non-interacting COT molecule are split at an infinitesimal value of U. In this sense, the low-frequency behavior observed also in the self-energy of the nano-DMFT may be interpreted as the fingerprint of the presence of the gap, and the peak at the Fermi energy shown by the nano-DMFT spectral function may be an artifact of the MEM employed in the analytic continuation procedure. On the other hand, the situation changes considering the evolution to intermediate values of U/t: while the ED gap increases and becomes sizable increasing the interaction, nano-DMFT still displays a narrow peak at the Fermi energy, as the Hubbard bands start to appear. At the same time, the corresponding self-energy recovers gradually the usual behavior for a metallic solution (cf. Fig. 3.13). Eventually, at $U = 8t$, both the nano-DMFT and the exact ED solution are insulating, but nano-DMFT substantially underestimates the ED gap (which is of the order of $\Delta \sim 4$ eV) and therefore it cannot be expected, e.g., to yield a quantitative description of transport properties.

The above analysis not only provides for more insights about the real behavior of the system, but also allows us to better understand the nano-DMFT results. Indeed it seems possible that, in nano-DMFT, local correlations *alone* are able to open a gap for $U \lesssim t$, as it is reflected in the insulating-like behavior of self-energy at low-frequency. However, in the intermediate coupling regime, the system is metallic and is characterized by a proper QP peak and a linearly vanishing self-energy for $\nu_n \to 0$. Eventually the system undergoes a Mott-Hubbard crossover to an insulating state, as the interaction is further increased. The exact solution, on the other hand, is *always* insulating, and evidently such apparent ‘‘reconstruction’’ of the metallic state, observed in nano-DMFT, does not take place. This is very likely due to the effect of non-local spatial correlations.

Effect of the hybridization. Hitherto we have considered the COT in the molecular limit only. However, we know from the analysis of the benzene molecule, that the presence of the hybridization is supposed to suppress non-local spatial correlations, leading to an improvement of the nano-DMFT description of the system. Therefore, it is interesting to study the evolution of the system from the molecular limit to a weak-hybridization regime. In Fig. 3.17 the nano-DMFT and exact self-energy in the different regimes for relevant values of U/t are presented. At $V/t = 0$, the imaginary part of the exact QMC local self-energy is diverging for $\nu_n \to 0$ for all values of U/t considered. More in general, *all* imaginary components of the self-energy are

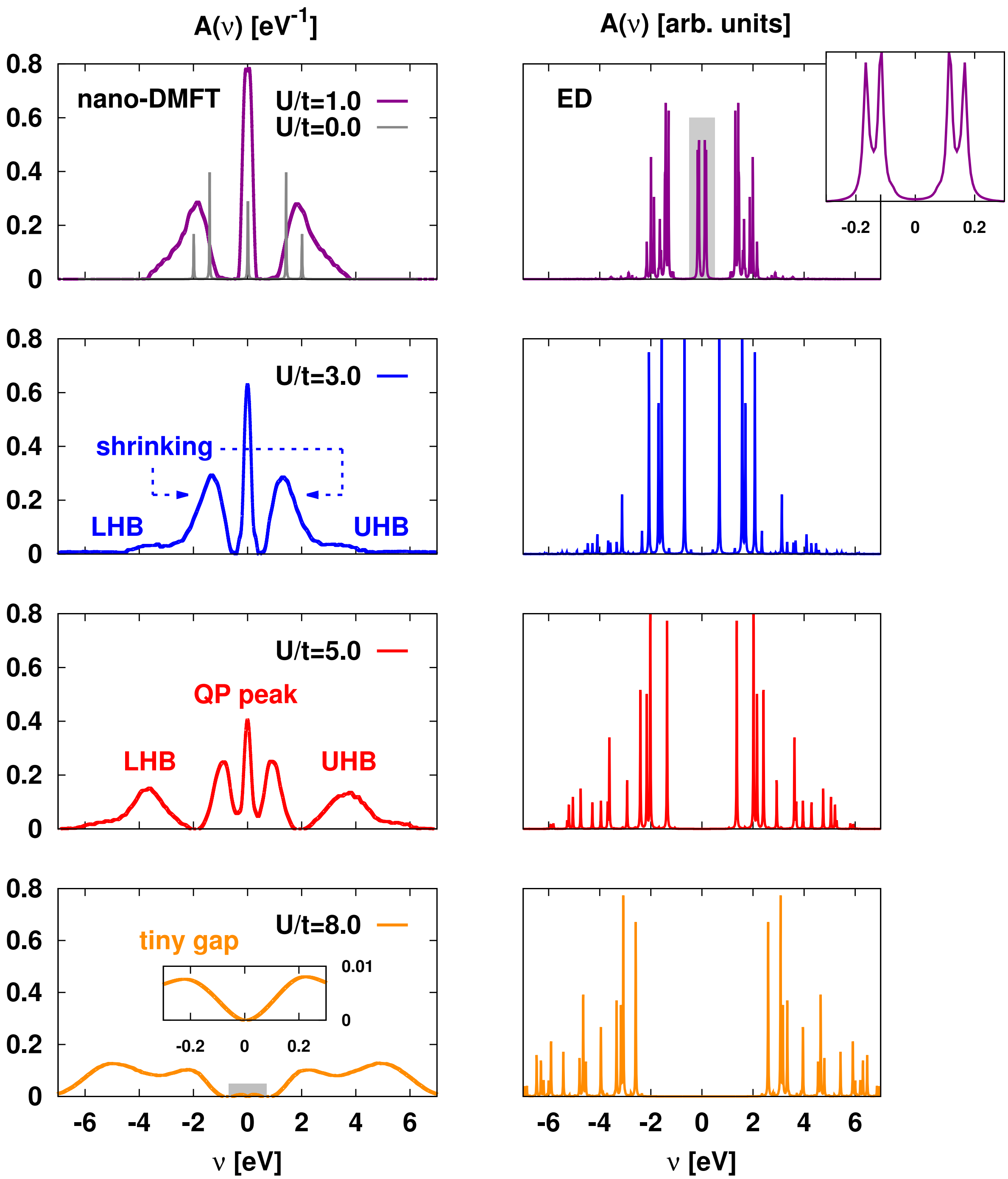

Figure 3.16: Comparison between the one-particle spectral function $A(\nu)$ as a function of U/t, for the isolated ($V=0$) COT molecule in the *NN t* hopping configuration at $T=0.05t$. Left panels: one-particle spectral function obtained by MEM analytic continuation of the QMC data. Right panels: one-particle spectral function obtained by exact diagonalization of the many-body Hamiltonian. Insets reproduce the low-energy structure of the spectra shaded in gray in the corresponding main panel.

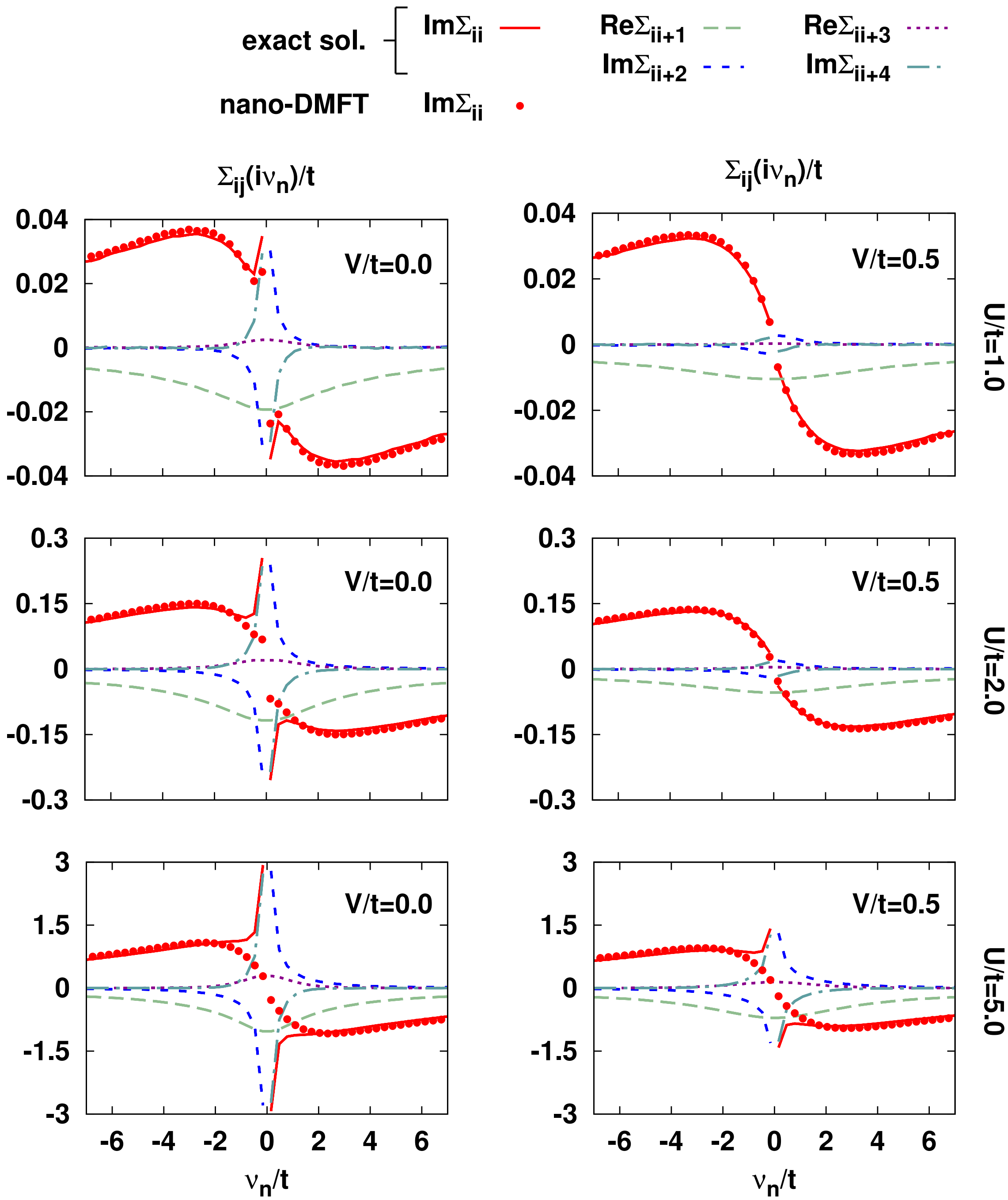

Figure 3.17: Comparison of the nano-DMFT (symbols) and exact (dashed lines) self-energy of the COT molecule in Matsubara representation in the *NN* t hopping configuration at $T = 0.05t$ for the representative cases of $U = t$ (upper panels), $U = 2t$ (middle panels), and $U = 5t$ (lower panels), at $V/t = 0$ (left) and $V/t = 0.5$ (right). All other contribution of Σ_{ij} are either equivalent to the one shown, or zero by symmetry.

either zero by symmetry or diverging, i.e., $\mathrm{Im}\Sigma_{ij}(\imath\nu_n \rightarrow 0) \rightarrow \infty$ for $j = i, i+2, i+4$. Let us note that this is completely different from what was happening in the benzene ring, where $\mathrm{Im}\Sigma_{ij}(\imath\nu_n \rightarrow 0) \sim 0$ for $j = i, i+2$ (cf. Fig. 3.6). As already discussed, instead, the nano-DMFT self-energy is not metallic-like in the weak coupling, while showing a metallic behavior in the intermediate coupling regime.
On the contrary, at finite V/t, in the weak coupling regime both the exact and the nano-DMFT local self-energy are metallic-like and linearly vanishing as $\nu_n \rightarrow 0$, while all non-local contributions are strongly suppressed with respect to the molecular limit. As the ratio V/U decreases (in the plot we show data for $U/t = 5$ at $V/t = 0.5$) non-local correlations are no longer negligible: the exact QMC solution is insulating, with the local self-energy displaying non-metallic behavior, while nano-DMFT is still metallic.
We can conclude that non-local spatial correlations, and their interplay with the local ones, are fundamental in order to estimate the correct critical value of the interaction U_c for the MIT (or crossover). The value of U_c is also strongly dependent on the ratio V/U. In particular, within the exact solution $U_c = 0$ for $V = 0$, which increases to a finite U_c value increasing V. On the other hand, nano-DMFT predicts U_c to be an increasing function of V/U, but generally overestimates it in the whole weak-hybridization regime investigated here.

3.2.3 Gate voltage dependence in transport through molecular junctions

The results presented in this section are still unpublished.

In an experimental setup, beside the source and the drain electrodes, the nanostructure can also be coupled to a gate electrode, that is used to induce a shift of the chemical potential of the system applying a gate voltage V_G. Besides being an easily tunable parameter, V_G also allows to extract information about the electronic structure of the system through the measurement of the conductance $G(\epsilon_F - eV_G)$.
For the sake of completeness, we should also mention that the electronic conductance is often also studied at non-equilibrium, both experimentally and theoretically, as a function of the bias voltage $V_{sd} = \mu_\text{s} - \mu_\text{d}$ (as discussed in Secs. 1.1 and 1.2). However, the theoretical description of transport properties out-of-equilibrium, would require an extension of the present formalism, involving the evaluation of the Green's function on the Keldysh contour [88]. Therefore, in this work, we deal with transport only within linear response.
Moreover, V_G also grants control on the system's density, which is often a critical parameter in determining the physics of a system. As a general statement, electronic correlations due to the Coulomb repulsion are expected to be most effective at half-filling, yet in a system with competing energy scales, interesting phenomena may take place also away from half-filling.
In the specific case of the benzene molecule, the application of a gate voltage, and hence, e.g., the addition/removal of one electron, has mainly two important effects:

- one can drive the molecule from a **spin-singlet charge-neutral state** $|0\rangle$ at half-filling, with a closed shell of doubly degenerate HOMOs, to a the **Kondo regime**, characterized by *two* doublets $|i\sigma\rangle$, as the additional electron/hole can be place in any of the orbitals $i = 1, 2$, with spin $\sigma = \uparrow, \downarrow$) [212, 213].

- the molecule does *not* **fulfill the Hückel's rule** ($4n + 2$ electrons, n non-negative integer) anymore, and loses its aromaticity, which could possibly reflect itself in strong changes in the structure of the spin-spin susceptibility.

Concerning the COT molecule

- in the *realistic* molecule , i.e., the one with alternating single and double covalent bonds between the C atoms (see Sec. 3.1), the addition/removal of an electron can also have important consequences on structure of the system itself. However, in our model COT system, consisting of a planar ring with equivalent bonds between all nearest neighbors, the effect of V_G is related to the change of the filling mostly.

In the following, we apply a gate voltage and investigate electronic and transport properties of Q1D systems also off half-filling. In Figs. 3.18 and 3.19 we show $G(\epsilon_F - eV_G)$ between opposite sites of the nanostructure, as well as the corresponding average density $\langle n(V_G)\rangle$ as a function of the gate voltage[8] for both the benzene and COT molecular junctions in the weak-hybridization regime and intermediate value of the interaction $U/t = 2$. The latter may be realistic if one considers that the on-site interaction on the carbon atoms of the molecule can be screened by the conduction electrons of the leads. Furthermore, in this situation, the interaction is of the order of the HOMO-LUMO charge gap which for the non-interacting benzeneis $\Delta = 2t$. This allows us to study the hybridization-driven MIT in the COT junction already in the weak-hybridization regime. This means that we will be able to explore, as a function of V_G, all correlation regimes, i.e., cases where electronic correlations are negligible, where local correlations are dominant, and where non-local ones also play an important role.

Let us start with the V_G analysis of the **benzene junction**. As already mentioned, one does not expect large correlation effects in the transport properties of the system if the chemical potential lies within the gap. This is confirmed by the data: when the hybridization is very weak, i.e. $V/t = 0.1$ (upper panels of Fig. 3.18), at $eV_G/t \sim 0$ the conductance is very low because of the gap, and the system is half-filled. Moreover, this physics, as well as the correct order of magnitude for the conductance, is already well described in a (non-interacting) tight-binding approximation, with only quantitative corrections to the conductance due to non-local correlations. This is shown in the inset on the left-hand side by the large contribution around $\nu_n \sim 0$ of the non-local (Matsubara) self-energy $\Sigma_{ii+1}(\imath\nu_n)$ (while the local one linearly vanishes because of the gap). The picture changes at large enough eV_G/t: one can see that the non-interacting conductance peaks are suppressed by the interaction, and the step-like variation of the site-density with V_G are smeared out, in addition to temperature effects already present in the non-interacting data. In the region of gate voltage $eV_G/t \gtrsim 1$, nano-DMFT overestimates the conductance (and some differences are also observed in the filling) and an analysis of the corresponding self-energy (inset on the right-hand side) shows a clear non-FL behavior similar to the one observed in the case of the COT molecule at half-filling. In this light, the suppression of the conductance would correspond to the presence of a (pseudo) gap in the spectral function of the interacting system, which nano-DMFT is not able to resolve. This also means that, concerning how the application of a gate voltage influences the reliability of nano-DMFT, there is not univocal tendency, and the quality of the results is strongly system-dependent and subject to the actual electronic structure.

Less surprisingly, instead, increasing the hybridization strength to $V/t = 0.5$ (lower panels of Fig. 3.18) leads to a better agreement between nano-DMFT and the exact solution in the whole range of gate voltages analyzed. Quantitative differences are still observed, but the broadening of the many-body resonances avoid the formation of (sizable) charge gaps in the spectral function (as confirmed by the self-energy in the inset). Therefore, we can conclude that in this regime, the nano-DMFT approximation is already sufficiently good, and correctly captures the physics of the system.

Similar results are observed when considering the **COT junction**. As we have seen before, in the limit $V/U \ll 1$ and at half-filling ($V_G = 0$) the exact solution predicts the system to be

[8]Note that, as the ($V_G = 0$) systems considered here fulfill particle-hole symmetry, we can restrict to the case $V_G > 0$ only.

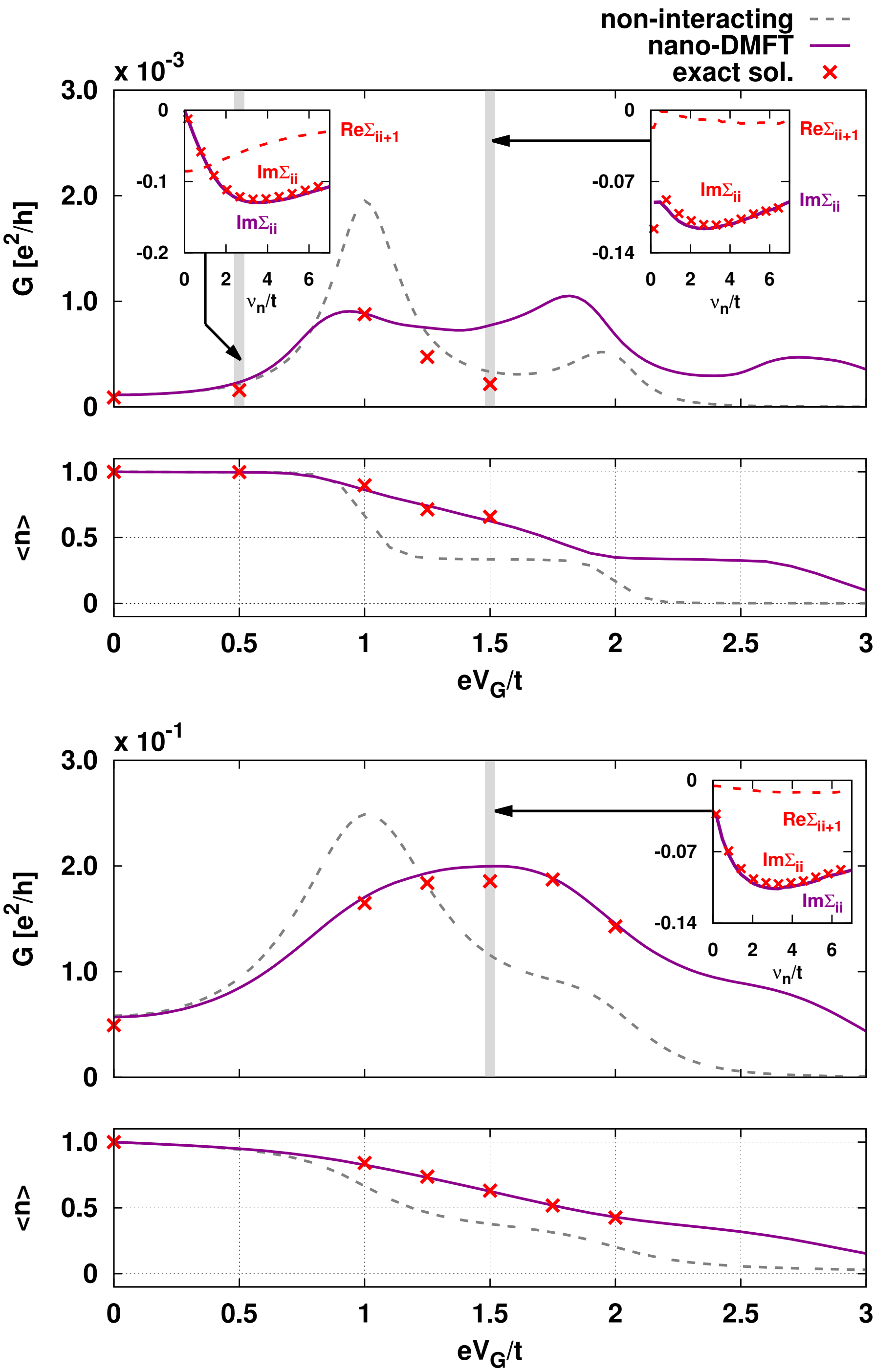

Figure 3.18: Zero-bias conductance $G(\epsilon_F)$ between opposite sites of the benzene ring and site density $\langle n \rangle$ as a function pf the gate voltage V_G, in the *NN t* hopping configuration for $U = 2t$, $T = 0.05t$, at $V/t = 0.1$ (upper panels) and $V/t = 0.5$ (lower panels). The insets show the local and non-local (between neighboring sites i, $i+1$) self-energy in Matsubara representation for selected values of eV_G/t, highlighted by the shaded area.

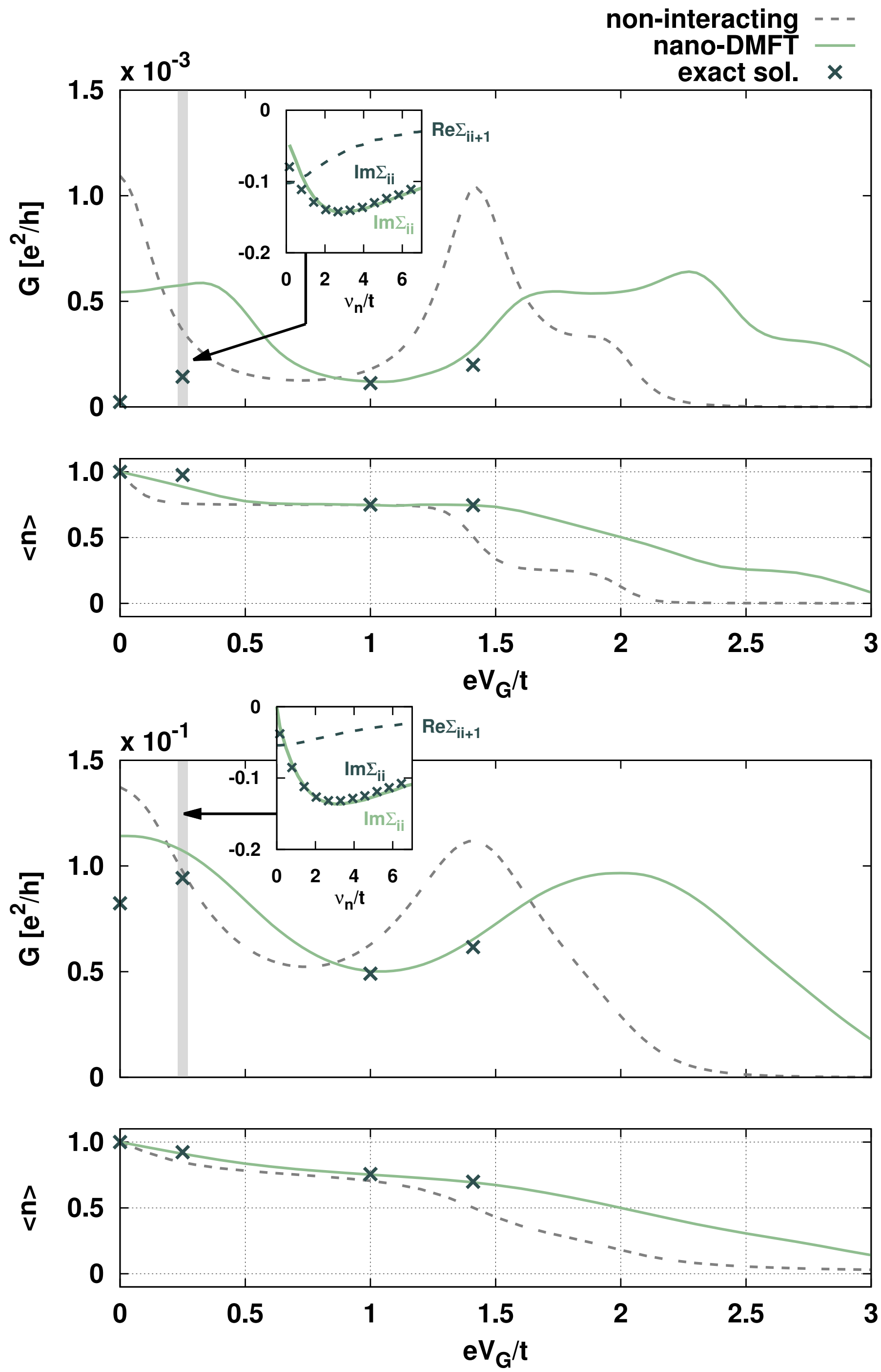

Figure 3.19: Zero-bias conductance $G(\epsilon_F)$ between opposite sites of the benzene ring and site density $\langle n \rangle$ as a function pf the gate voltage V_G, in the *NN t* hopping configuration for $U = 2t$, $T = 0.05t$, at $V/t = 0.1$ (upper panels) and $V/t = 0.5$ (lower panels). The insets show the local and non-local (between neighboring sites i, $i+1$) self-energy in Matsubara representation for selected values of eV_G/t, highlighted by the shaded area.

insulating, while nano-DMFT yields a narrow peak at the Fermi energy. This is also the case of the weak-hybridization regime, e.g., at $V/t=0.1$ (upper panels of Fig. 3.19) where nano-DMFT overestimates the conductance by roughly an order of magnitude in the low gate voltage regime. Again, in correspondence of an insulating state, the local (Matsubara) self-energy displays a non-metallic behavior at low-frequency, combined with large non-local contributions. Moving away from half-filling the agreement seems to improve, but the quality of the approximation still depends on the ratio eV_G/t. Increasing the hybridization (lower panels of Fig. 3.19) we observe that around $V_G\sim 0$ the difference between the nano-DMFT and the exact conductance is not as large as in the previous case, and indeed the corresponding local self-energy is linearly vanishing for $\nu_n\to 0$. The quantitative difference in the conductance is understood in terms of a suppression of the non-local Green's function due to non-local correlations, shown in the self-energy in the inset (for the case $V_G=0$ see also the full self-energy shown in Fig. 3.17). In this regime, although some quantitative difference is still visible, we observe that the nano-DMFT approximation provides a reasonable description of the conductance and of the site-density in the whole rang of eV_G/t values investigated.

3.3 Phase diagram of electronic correlations at the nanoscale

The results we discussed so far provide already good indications to understand the role of electronic correlations in Q1D molecules on a general ground. In fact, we can depict a schematic $U-V$ phase diagram shown in Fig. 3.20, where we identify three regions: a region (indicated as I in the phase diagram) where electronic correlations are not important, a region (II) where the system is dominated by local correlations, and a region (III) where non-local correlations beyond mean-field are non negligible with respect to the local ones.

Let us characterize those regions in more detail. In **region I**, located in the weak-coupling and/or at strong-hybridization regime, a qualitatively (and sometimes quantitatively as well) description of the system is provided already by a tight-binding (non-interacting) approach. In **region II** local correlations substantially modify the behavior of the system with respect to the non-interacting case. Here, the nano-DMFT scheme is rather accurate, at least concerning the one-particle quantities we have analyzed here, as non local spatial correlations are shown only to yield minor quantitative differences with respect to the exact solution. The actual extension of this region may depend on the system under consideration as well as on other parameters, as in the case of the gate voltage, discussed in the previous section. In **region III**, extended to the weak-hybridization and/or strong-coupling regime $U/V\gg 1$, including non-local spatial correlations beyond mean-field is crucial for the understanding of the physics of the system in study. This can be done, e.g., by means of nano-DΓA as will be shown in the next section. Moreover, one should notice that region III may extend even to not so large U/t, depending on the specific system considered (as we have explicitly shown in the case of the benzene and COT molecules).

In this picture, another element that can influence the respective extension of the different regions is the connectivity z: we have shown that, in the case of the benzene molecule, as the connectivity increases, non-local spatial correlations are significantly suppressed. In the phase diagram this corresponds to region II, where nano-DMFT performs well, extending to lower values of V/U or equivalently, in region III shrinking. In the limit of $z \to \infty$ non-local correlations are washed away, and nano-DMFT is exact.

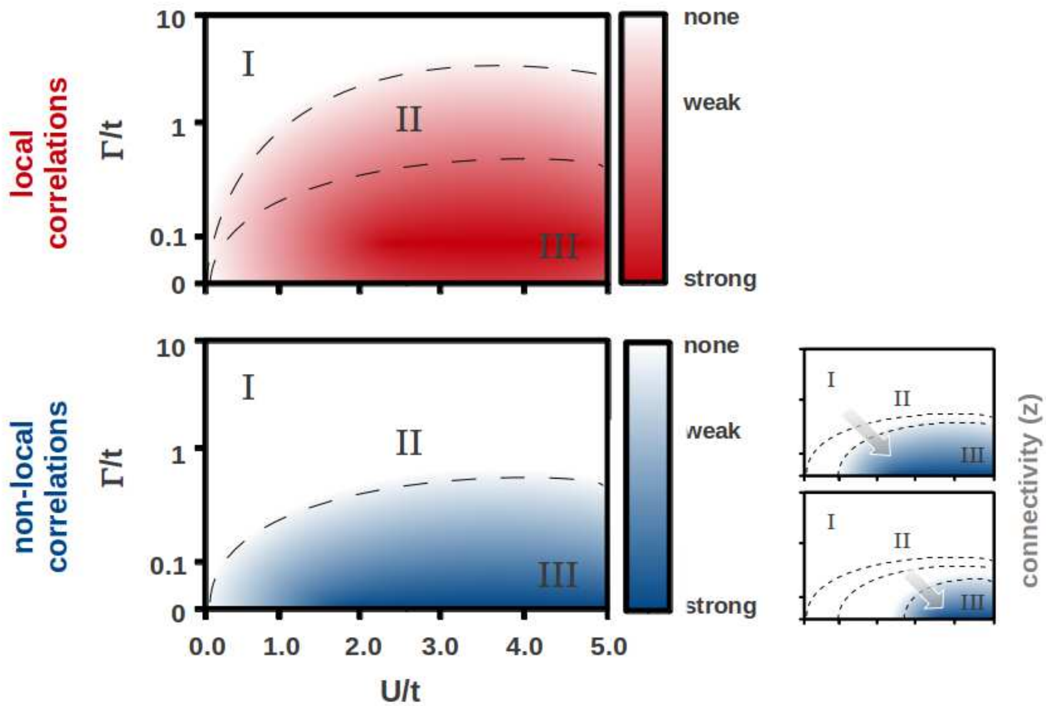

Figure 3.20: Qualitative phase diagram of electronic correlations obtained from the analysis of Q1D molecules. Strong correlations arise due to the presence of the local interaction U, while are suppressed by hybridization processes with the electrons of the non-interacting environment, controlled by the scattering amplitude $\Gamma = \pi\rho V^2$. Hence, the phase space can be divided into three regions (denoted above by roman numbers) depending on the ratio U/Γ: the black dashed lines are guides to the eye, and the separation between the different regions is smooth, as shown by the color gradient, indicating the strength of local (red) and non-local (blue) electronic correlations.
Non-local spatial correlations and are non-negligible in the weak-hybridization limit $\Gamma \ll t$, while, at a given value of U/t are rapidly suppressed as Γ/t increases: the system is dominated by local correlations and nano-DMFT a reliable approximation. Eventually the latter is also suppressed in the strong-hybridization limit and correlation effects are substantially taken into account already in perturbation theory (e.g., Hartree-Fock approximation).
As in general expected within mean-field theory, also the connectivity of the system play an important role, further suppressing non-local correlations, i.e., reducing the region of the phase diagram when those are important (lower right panels). In the limit $z \to \infty$ non-local correlations due to U vanish.

3.4 Including non-local spatial correlations

The results presented in this section, i.e., the evaluation of the local vertex functions and the corrsponding nano-DΓA results for Q1D molecules are still unpublished.

The comparison between DMFT and the exact solution in the benzene and COT rings allowed us to get an overview on its reliability and to understand that there exist well defined parameter regimes where non-local correlations are non-negligible. In the following we apply nano-DΓA to both the benzene and COT molecules, thus including non-local correlations beyond mean-field. Specifically, we limit to the molecular limit $V = 0$ and at half-filling, where (non-local) electronic correlations are expected to be most important.

The results presented in the following represent the first application of the idea behind DΓA, in which all channels (both *ph* channels and the *pp* one) are indeed treated on equal footing, by means of the parquet formalism. Previous DΓA results reported so far [145, 147, 168] relied on the *ladder* approximation. The ladder assumes the irreducible vertex function $\Gamma_r^{\nu\nu'\omega}$ to be local only in a specific channel, and the corresponding non-local correlations are introduced via ladder resummation of diagrams. Besides being of easier implementation, the ladder-DΓA is only suitable for systems in which one of the channels is expected to be dominant over the others, as in the case, e.g., of the magnetic channel in the bulk (cubic) Hubbard model close to the AF transition.
As already discussed, the heart of DΓA is the local two-particle fully irreducible vertex, which is extracted from the AIM, as described at the end of Sec. 2.3.2. Analogously, in its nanoscopic extension, nano-DΓA, a local fully irreducible vertex $\Lambda_{ii}^{\nu\nu'\omega}$ can be extracted from each of the inequivalent auxiliary AIMs defined for a given nanostructure. In both cases we considered so far, i.e. the benzene and the COT molecule, all carbon atoms are equivalent, and so are all local two-particle fully irreducible vertices, so that we actually need to calculate only one of them, thus mitigating the computational workload of the whole calculation.

Evaluation of the two-particle vertex functions: technical details. Before we discuss our nano-DΓA results, it is worth giving some technical details on how the fully irreducible local vertex has been obtained here. Here, we consider the result of a *converged* nano-DMFT loop as the input for a the nano-DΓA one-shot calculation. The implementation of a fully self-consistent nano-DΓA scheme is not yet available, and will be part of future projects.

The nano-DMFT results are obtained with an HF-QMC impurity solver, where the asymptotic behavior of one-particle quantities, i.e. the Green's function and the local self-energy is properly treated in order to minimize numerical errors due to the discrete FT (cf. also Appendix B). On the other hand, at the two-particle level, many technical issues arise from the statistical QMC sampling of the generalized susceptibility (2.38). In particular, the accurate and efficient treatment of its asymptotic behavior still represents a significant challenge, despite the attempts

recently reported in this direction [162, 163, 219]. In fact, asymptotical instabilities for the generalized susceptibility would yield low-quality results for the vertex function due to the inversion of $\chi^{\nu\nu'\omega}$ in the Bethe-Salpeter equations, e.g., in the form (2.49a) and (2.49b).
Hence, our strategy consists in computing two-particle quantities of the converged AIM with an ED impurity solver. In order to do so, we need to fit the Anderson parameters $\{V_\ell, \epsilon_\ell\}$ in order to define a *discrete* hybridization function of a system consisting in N_s sites (one impurity and N bath sites) which reproduces the hybridization function of the original AIM

$$\Delta(\nu) = \sum_{\ell=1}^{N} \frac{V_\ell V_\ell^*}{\nu - \epsilon_\ell}, \tag{3.11}$$

and can be used for the ED setup. Exploiting symmetries allow to lower the number of independent fitting parameters, e.g. at half-filling, where the hybridization function fulfills the condition $\Delta(\nu) = \Delta^*(-\nu)$, it is reduced by a factor of two. Besides the error arising due to the discretization of the bath, one can exactly evaluate the generalized susceptibility (2.40) directly in the (Matsubara) frequency space, thus avoiding the nasty step involving the FT.
The ED results presented in the following have been performed together with G. Rohringer with $N_s = 5$ sites in the AIM (including the impurity site), keeping (at least) 160 (positive) fermionic and bosonic Matsubara frequencies, which has required, for each determination of the generalized susceptibility, a parallel calculation of about 100.000 CPU hours on the Vienna Scientific Cluster (VSC). This allowed for a precise calculation of the (Matsubara) frequency structure of the two-particle reducible and irreducible vertex functions (see also Ref. [158] for further details).

The ED fully irreducible vertex is the input for the parquet equations. In practice, the solution of the parquet equations is subject to numerical errors, e.g., arising from the inversion of the Bethe-Salpeter equation, and mainly due to the finiteness of the frequency grid on which the calculation is performed. This leads to a violation of the crossing symmetries [165], which would be instead fulfilled by an exact solution of the parquet equations. In turn, the symmetry violations lead to numerical instabilities beyond the weak-coupling regime, which become more and more severe as the temperature is lowered. In this respect, the enforcement of the crossing symmetries at the level of the full vertex $F^{\nu\nu'\omega}$ seems to improve substantially the algorithm and allows one to reach converged solutions also beyond the weak coupling regime [165]. In the actual algorithm of the nano-DΓA, used to obtain the results presented in the following, the enforcement of the crossing symmetry is not yet implemented. However, this was already enough to analyze regions of the parameters' space which are relevant in the present context. Further improvements of the whole computational scheme are certainly possible, as e.g., the implementation of semi-analytical asymptotic behavior of the two-particle quantities [219, 166]. This, as will be discussed in the outlook, is expected to further improve the scheme form both the accuracy and efficiency point of views.

3.4.1 One-shot nano-DΓA results

In the following we show the ED results for the local two-particle fully irreducible vertex in the four different channels: (d)ensity, (m)agnetic, (s)inglet, and (t)riplet (as defined in Sec. 2.3.2) and its effect on physical quantities obtained within the anno-DΓA scheme. However, it is worth stressing once again that, being the fully irreducible vertex irreducible in *every* channel by definition, each vertex is just one of the equivalent combinations of the only two independent quantities: $\Lambda_{\uparrow\downarrow}$ and $\Lambda_{\uparrow\uparrow}$, according to the following convention

$$\Lambda_{d,m} = \Lambda_{\uparrow\uparrow} \pm \Lambda_{\uparrow\downarrow}, \tag{3.12a}$$

$$\Lambda_s = 2\Lambda_{\uparrow\downarrow} - \Lambda_{\uparrow\uparrow}, \qquad \Lambda_t = \Lambda_{\uparrow\uparrow}. \tag{3.12b}$$

As for the high-frequency asymptotics of the fully irreducible vertex, we expect this to be *always* given by the lowest order contribution, i.e. proportional to the bare interaction U, as it was explicitly discussed in Ref. [158], for a DMFT calculation of the bulk 3-dimensional Hubbard model. This property is evidently connected to the intrinsic fully irreducible nature of the vertex, as all the high-frequency contributions to the asymptotics, beyond the bare U, are originated by reducible diagrams. Here we will show that this property holds, as expected, even in the ‘‘extreme’’ case of Q1D systems.

Benzene molecule. Let us start the discussion of the results for the two-particle fully irreducible local vertex for different values of U/t, shown in Figs. 3.21-3.24 with respect to its asymptotics, i.e., $\Lambda_d^{\nu\nu'\omega}-U$, $\Lambda_m^{\nu\nu'\omega}+U$, $\Lambda_s^{\nu\nu'\omega}-2U$, and $\Lambda_t^{\nu\nu'\omega}$.

At $U = t$, due to the presence of the charge HOMO-LUMO gap $\Delta = 2t$ at the Fermi energy of the non-interacting DOS of the benzene molecule, the changes of the fully irreducible vertex with respect to U are tiny (and therefore the corresponding plot is not shown). In this case, to obtain accurate results for the asymptotic behavior of the fully irreducible vertex is challenging even in the case of ED, and shows that one is indeed bound to the knowledge of the susceptibilities in a huge frequency range in order to perform numerically stable inversions of the Bethe-Salpeter equation(s), making evaluation of the susceptibility numerically demanding.

In the case $U = 2t$, the local two-particle fully irreducible vertex is shown in Fig. 3.21. The frequency structure of the vertex evidently resembles what we expect from the analysis of two-particle vertex functions in the AIM reported in Ref. [158]. Although in this case we achieve stable results for the inversion of the Bethe-Salpeter equation(s), the overall frequency dependence of $\Lambda^{\nu\nu'\omega}$ is rather weak, and does not represent a quantitatively important correction to the static contribution in each channel: e.g., the scale in the upper left panel of Fig. 3.21 has to be compared to $U\!=\!2t$.

Those results can be more precisely analyzed if considering one-dimensional slices of the the vertex, as, e.g., as shown in Fig. 3.22 along the line $\nu' = \pi T$, for $\omega = 0$ (upper panels) and $\omega = 20\pi T$ (lower panels). Although the system is supposed to be already beyond the weak-coupling regime, due to the weak deviation from the asymptotic at finite frequency it is interest-

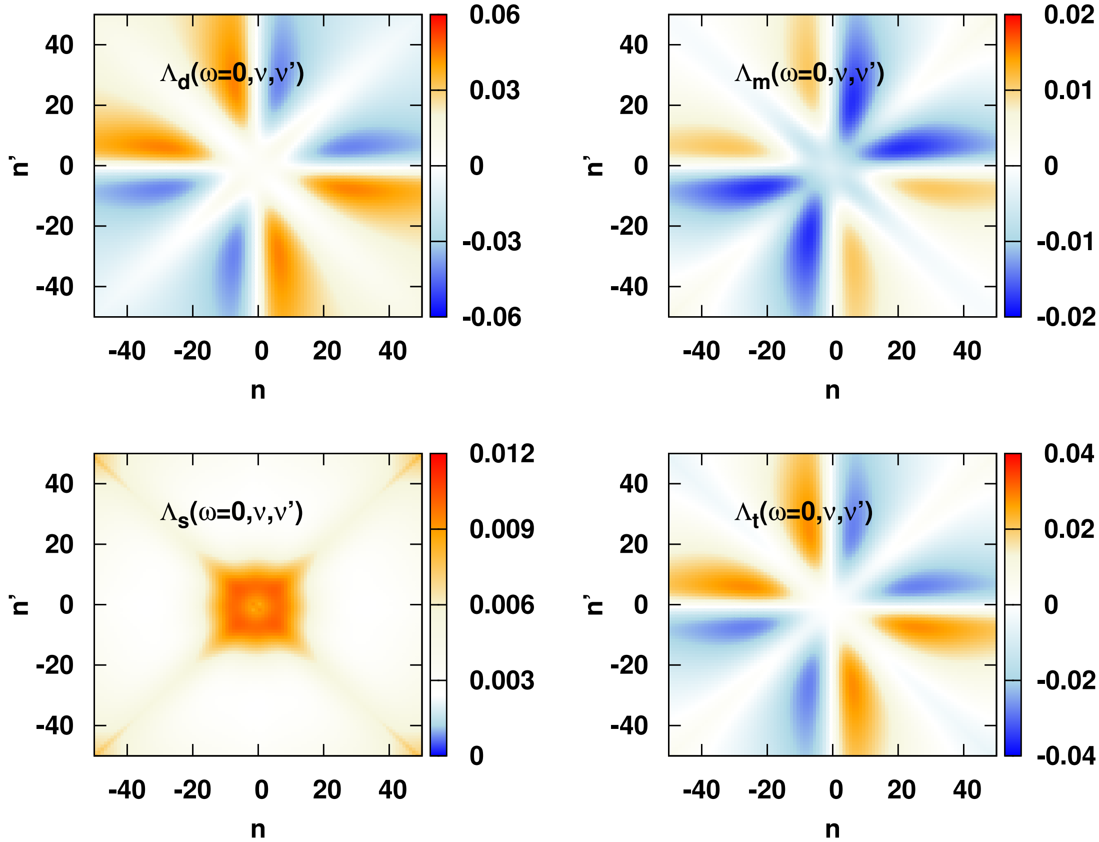

Figure 3.21: Local two-particle fully irreducible vertex $\Lambda^{\nu\nu'\omega}$ in Matsubara representation for the isolated ($V=0$) benzene ring in the *NN t* hopping configuration, at $U=2t$ and $T=0.05t$. In each panel a representation of the vertex is plotted and the corresponding asymptotics is subtracted, i.e. we plot: $\Lambda_d^{\nu\nu'\omega}-U$ (upper left), $\Lambda_m^{\nu\nu'\omega}+U$ (upper right), $\Lambda_s^{\nu\nu'\omega}-2U$ (lower left), and $\Lambda_t^{\nu\nu'\omega}$ (lower right) for $\omega=0$ as a function of the Matsubara indexes of the fermionic frequencies.

ing to compare $\Lambda^{\nu\nu'\omega}$ to the corresponding perturbative expansion in the Hubbard interaction: beyond the lowest order contribution of $O(U)$, determining the asymptotics in each channel, we also include the next term in the expansion, i.e., the U^4 contribution given by the *envelope* diagram(s), in analogy to Ref. [158]. For the sake of simplicity, we also restrict ourselves here to the density and magnetic channels only, which already contains the full information carried by $\Lambda_{\uparrow\uparrow}$ and $\Lambda_{\uparrow\downarrow}$.

Concerning the contributions at $\omega=0$, the numerical data for $\Lambda_d^{\nu\nu'\omega}$ qualitatively resemble the contribution of the envelope diagram $\Lambda_{\text{env}}^{\nu\nu'\omega}$, stemming from perturbation theory, while for $\Lambda_m^{\nu\nu'\omega}$ the numerical data qualitative deviates from the predictions of perturbation theory. At finite ω, e.g., $\omega=20\pi T$, the agreement seems to systematically improve.

Besides quantitative deviations on the scale appear to be substantial, they are still negligible with respect to the bare interaction U: indeed, the weak frequency dependence of the fully irre-

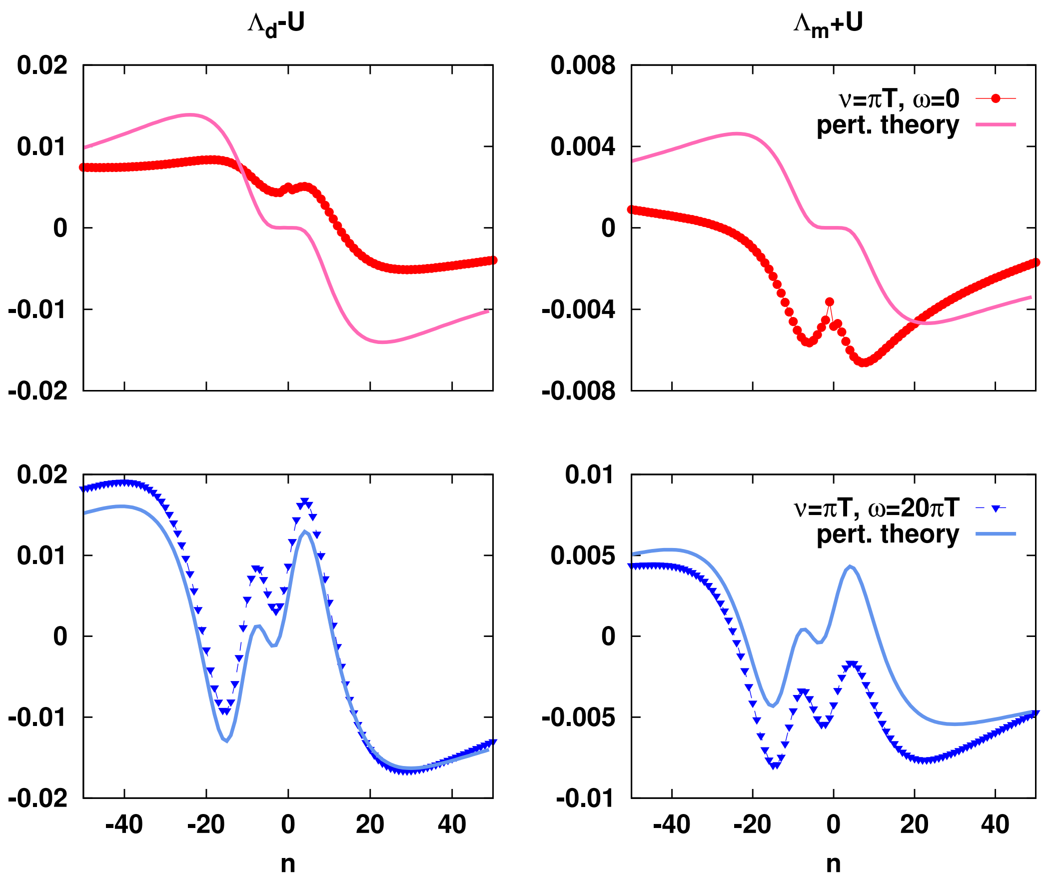

Figure 3.22: One-dimensional slice along the line $\nu' = \pi T$ of the local two-particle fully irreducible vertices $\Lambda^{\nu\nu'\omega}_{d,m}$ in Matsubara representation, for the isolated ($V = 0$)) benzene ring in the *NN t* hopping configuration, at $U = 2t$ and $T = 0.05t$. We compare the numerical results for $\omega = 0$ (upper panels) and $\omega = 20\pi T$ (lower panels) as a function of the Matsubara indexes of the fermionic frequency ν, to fourth-order perturbation theory (envelope diagram).

ducible vertex in this regime of parameters, suggests that an approximation such as the parquet approximation (PA), in which the (frequency dependent) vertex is approximated with its static contribution only, should already capture most of the physics contained in the full nano-DΓA approach.

At $U = 5t$ instead, in Figs. 3.23, when the energy scale set by the interaction is larger than the one set by the non-interacting HOMO-LUMO gap, the situation is different. The fully irreducible vertex displays a clear low-frequency structure, whose amplitude is no longer negligible with respect to the asymptotics, and rapidly decays to the corresponding asymptotic values at higher frequency. Furthermore, it is interesting to notice that, looking at the triplet channel would suggest a rather smooth evolution of $\Lambda^{\nu\nu'\omega}_{t} = \Lambda^{\nu\nu'\omega}_{\uparrow\uparrow}$ increasing the interaction beyond weak coupling, besides the characteristic energy scale changing according to the bare interaction U. However, this is not the case for the other channels, in which also $\Lambda^{\nu\nu'\omega}_{\uparrow\downarrow}$ appears. At high values of U/t, e.g., in the singlet channel, the vertex displays a more complex structure,

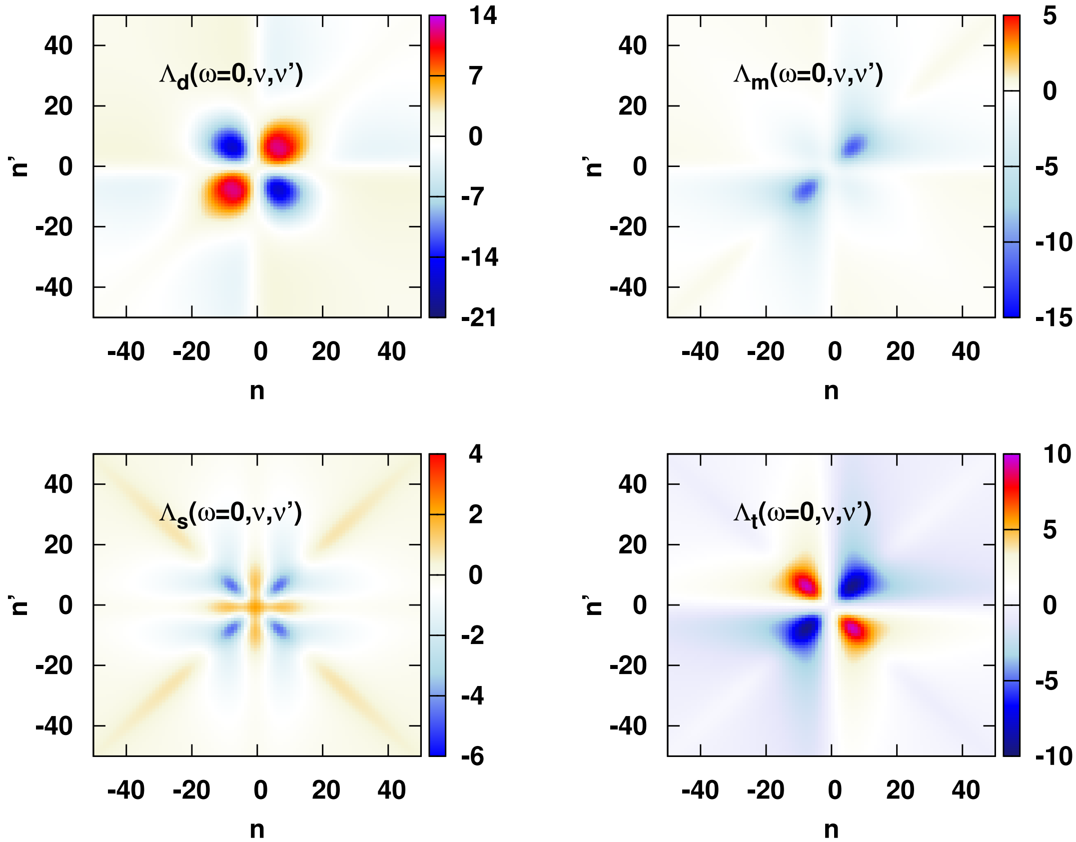

Figure 3.23: Same as for Fig. 3.21, but at $U = 5t$.

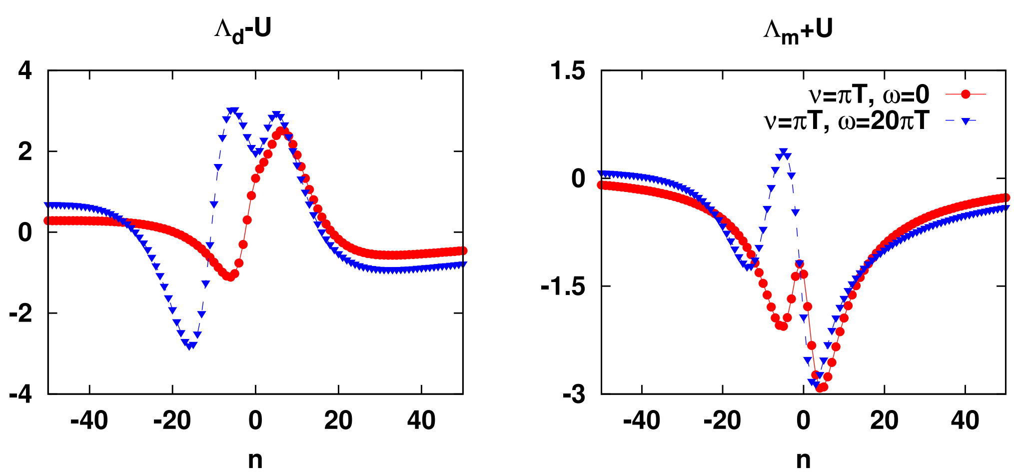

Figure 3.24: One-dimensional slice along the line $\nu' = \pi T$ of the local two-particle fully irreducible vertices $\Lambda^{\nu\nu'\omega}_{d,m}$ in Matsubara representation, for the isolated ($V = 0$) benzene ring in the *NN t* hopping configuration, at $U = 5t$ and $T = 0.05t$. Perturbation theory can no longer describe the numerical results, shown for $\omega = 0$ (upper panels) and $\omega = 20\pi T$ (lower panels) as a function of the Matsubara indexes of the fermionic frequency ν.

with both positive and negative peaks (with respect to the asymptotics) while in the density channel the sign of the whole structure is reversed.
The changes of the frequency structure of the vertex beyond weak coupling are evident considering the one-dimensional slices of the the vertex along the line $\nu' = \pi T$, for $\omega = 0$ and $\omega = 20\pi T$, as shown in Figs. 3.24, and its features cannot be described anymore by the envelope diagram contributions, which are negligible with respect to the numerical data (and therefore not shown). The origin and the interpretation of the non-perturbative topological evolution of the local fully irreducible vertex requires further investigations, but may be interpreted as precursors of the Mott transition [167].

The calculation of the fully irreducible vertex is, however, only the first step of nano-DΓA. In order to include non-local correlations with nano-DΓA we need to solve self-consistently the inverse parquet equations for which $\Lambda^{\nu\nu'\omega}$ represents the input. The real space Dyson-Schwinger equation (2.57) involving the converged full vertex $F^{\nu\nu'\omega}$ yields the nano-DΓA self-energy, which allows to calculate other quantities of interest.

Considering the weak frequency dependence of the fully irreducible vertex in the weak coupling limit ($U = t, 2t$), we perform the calculations both in the PA ($\Lambda = U$) and the DΓA level (full $\Lambda^{\nu\nu'\omega}$). In the strong coupling regime, instead, the parquet solver revealed to be unstable and no properly converged solution could be obtained at higher values of U, due to numerical violations of the crossing symmetries [165].
Let us start with a direct comparison of the nano-DΓA self-energy (between nearest neighbors $i, i+1$) to the nano-DMFT and the exact ones, shown in the upper panel of Fig. 3.25 in the $U = 2t$ case. Already the level of PA, the nano-DΓA represents a substantial improvement in comparison to nano-DMFT (in which non-local self-energies are identically zero) and it is in very good agreement with the exact solution. Considering the full (but rather weak) frequency dependence of the fully irreducible vertex does not provide any further sizable improvement with respect to the PA. The effect of non-local correlations can be also explicitly seen in the local Green's function in the imaginary time representation, shown in the lower panel of Fig. 3.25, where we compare the results obtained using the self-energies of the upper panel. In this case, though the difference exists only on a quite small scale, the improvement of nano-DΓA over nano-DMFT is qualitatively remarkable: clearly, the presence of non-local spatial correlations is crucial in restoring the charge gap of the isolated interacting benzene molecule.

The results shown so far look quite satisfactory, and give reassuring indication of the reliability of the method for including non-perturbative non-local correlations beyond nano-DMFT. However, the analysis of response functions, and their comparison within all the approximation levels discussed so far, is also important and represents, hence, one of the main aims of future works. Moreover, we also need to understand where does the (small) residual difference between nano-DΓA and the exact solution comes from. It may arise from numerical precision issues, e.g., the finiteness of the frequency range in which the parquet and Bethe-Salpeter equation are solved, or it may also be due to a momentum dependence of the fully irreducible vertex in Q1D systems.

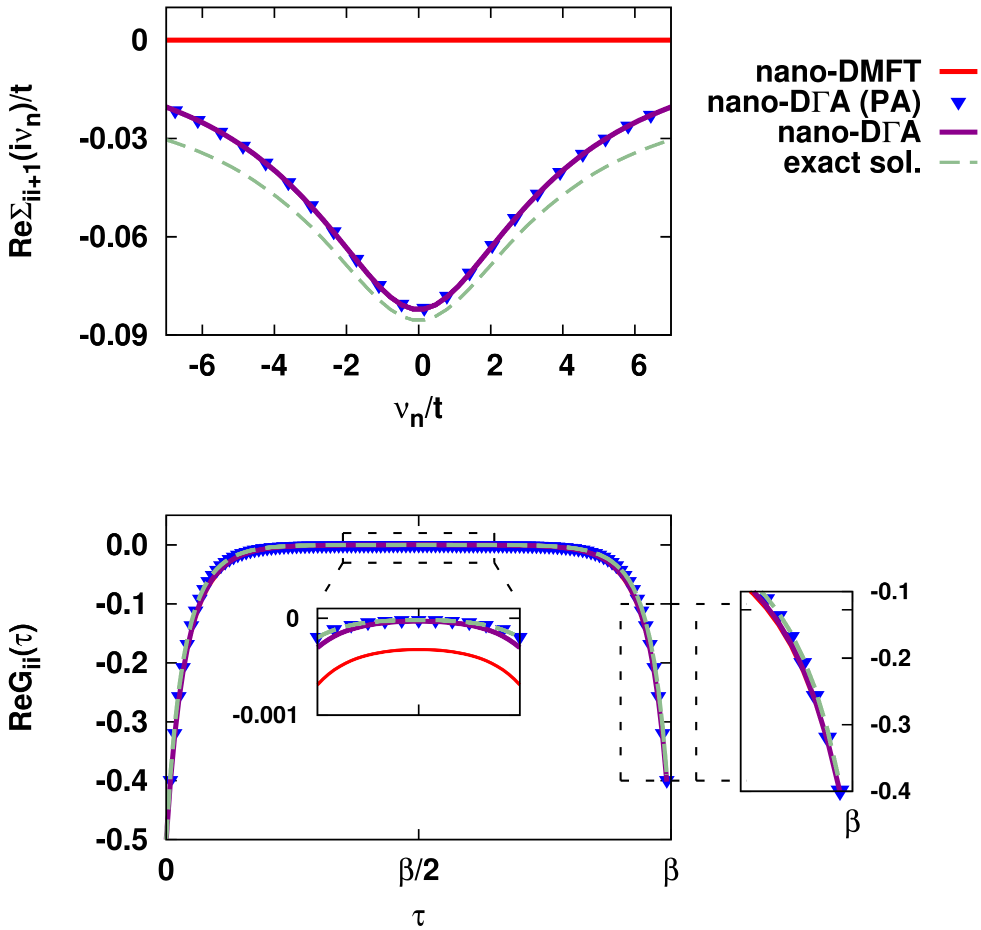

Figure 3.25: Comparison between nano-DMFT, nano-DΓA and the exact solution for the isolated ($V=0$)) benzene ring in the *NN t* hopping configuration, at $U=2t$ and $T=0.05t$. Upper panel: non-local self-energy (between nearest neighbors i, $i+1$) in Matsubara representation. Lower panel: local Green's function $G_{ii}(\tau)$, where only the nano-DΓA(PA) has been reported because it was essentially indistinguishable from the nano-DΓA. Inset: zoom of the highlighted region.

COT molecule. In the case of the benzene molecule the very good agreement between nano-DΓA and the exact solution, was observed already at the PA level. What is still needed to be investigated is the importance of the frequency dependence of the fully irreducible vertex in a case where it is not negligible. An analysis of $\Lambda^{\nu\nu'\omega}$ in the COT molecule, in analogy with the case of the benzene one, provides useful insights in this direction. In fact, we have seen in the previous sections, the isolated COT molecule is metallic both in the non-interacting case and within nano-DMFT at weak-to-intermediate coupling, while within the exact solution it is insulating. In this sense, one expects that the fully irreducible vertex could carry the information the system needs to open the charge gap.

In the he COT, however, the covergence of the parquet equations at $T=0.05t$, as usual, is quite problematic, due to the numerical violation of the crossing symmetry, already at the level of PA. Therefore, in this case we were forced to consider a higher value of the temperature, namely $T = 0.10t$, at which the parquet convergence is smooth up to the interaction values of approximately $U = 4t$.

We performed calculations at $U = 3t$, for which the corresponding fully irreducible vertex, calculated from a converged nano-DMFT loop is shown in Fig. 3.26. The fully irreducible vertex displays now a non-negligible frequency dependence in comparison to the static contribution. Remarkably, its frequency structure still resembles the one of the vertex of the benzene molecule at weak coupling, i.e., the one that can still be qualitatively understood by means of perturbation theory (envelope diagrams) [158, 167]. At the same time its asymptotics is well behaved, clearly displaying the typical *butterfly* structure expected for $\Lambda^{\nu\nu'\omega}_{d,m}$, and reported also in Ref. [158] in the metallic phase of the $d = 3$ Hubbard model.

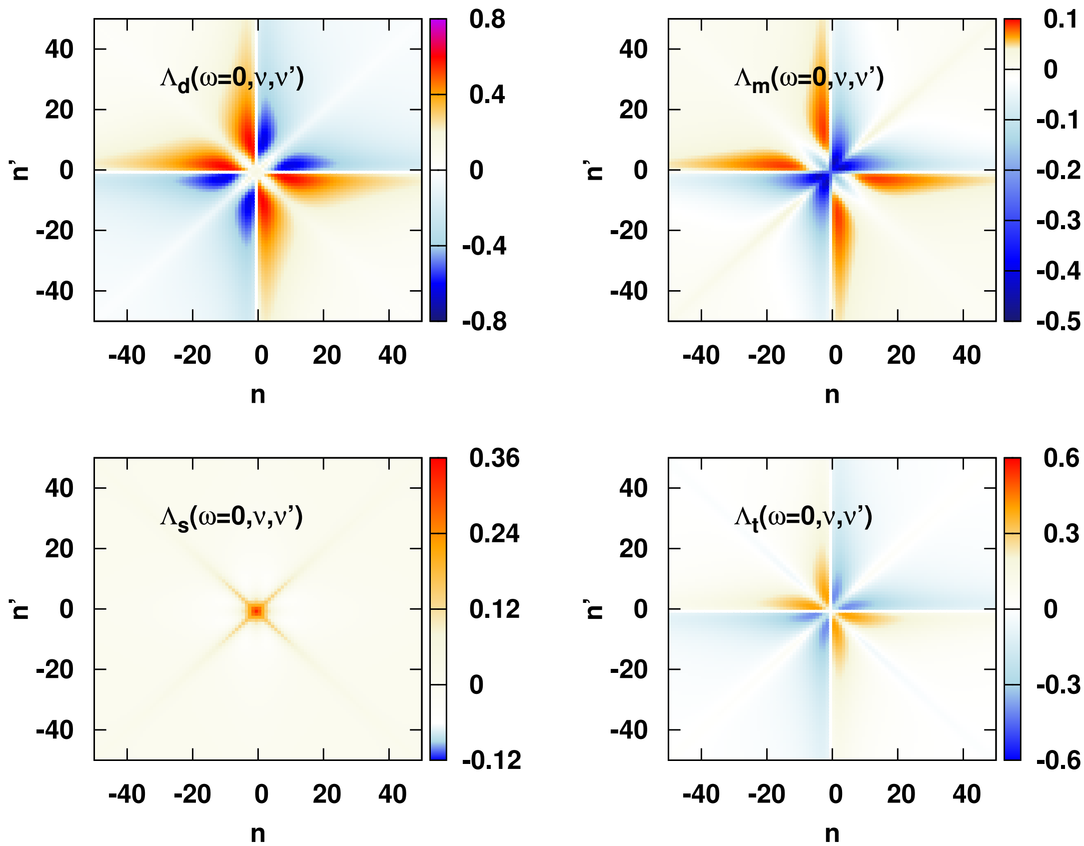

Figure 3.26: Local two-particle fully irreducible vertex $\Lambda^{\nu\nu'\omega}$ in Matsubara representation for the isolated ($V = 0$)) COT ring in the *NN t* hopping configuration, at $U = 3t$ and $T = 0.10t$. In each panel a representation of the vertex is plotted and the corresponding asymptotics is subtracted, i.e. we plot: $\Lambda^{\nu\nu'\omega}_{d} - U$ (upper left), $\Lambda^{\nu\nu'\omega}_{m} + U$ (upper right), $\Lambda^{\nu\nu'\omega}_{s} - 2U$ (lower left), and $\Lambda^{\nu\nu'\omega}_{t}$ (lower right) for $\omega = 0$ as a function of the Matsubara indexes of the fermionic frequencies.

A one-dimensional slice of the the fully irreducible vertex along the line $\nu' = \pi T$ for $\omega = 0$ and $\omega = 20\pi T$, is shown in Fig. 3.27: The significant frequency structure observed cannot be well reproduced by perturbation theory. Instead, we highlight in the insets the low-frequency feature of $\Lambda^{\nu\nu'\omega}$ which are not clearly visible in the full range. We notice a cusp at $\nu = 0$ in $\Lambda_m^{\nu\nu'\omega}$ which persists also at finite ω, and a wiggle in $\Lambda_d^{\nu\nu'\omega}$ which is instead washed away at a high enough value of ω. Those features appearing in the low-frequency range are probably the most relevant for describing the low-energy physics of the system. Tracing back their origin (which is evidently no longer related to the lowest order diagrams) is, however, absolutely not trivial.

One needs to understand what is the effect of the frequency structure of vertex on the nano-DΓA results for physical properties of the COT molecule. In Fig. 3.28 we show the non-local self-energy (between nearest neighbors i,$i+1$, shown in the upper panel) as well as the local Green's function in the imaginary time representation (lower panel), comparing nano-DMFT, nano-DΓA and the exact solution. In the case of the self-energy, a large part of the spatial correlations arise already in the PA, i.e., from the lowest order contribution of $\Lambda^{\nu\nu'\omega}$. Including the frequency structure of the fully irreducible vertex further improve the agreement, but non-local spatial correlations are still sensibly underestimated by nano-DΓA. The same conclusion can be inferred from the estimate of $A(0)$ provided by $G(\tau=\beta/2)$: in contrast to the benzene molecule, in the COT molecule non-local correlations included in nano-DΓA do not seem to be enough to open a charge gap.

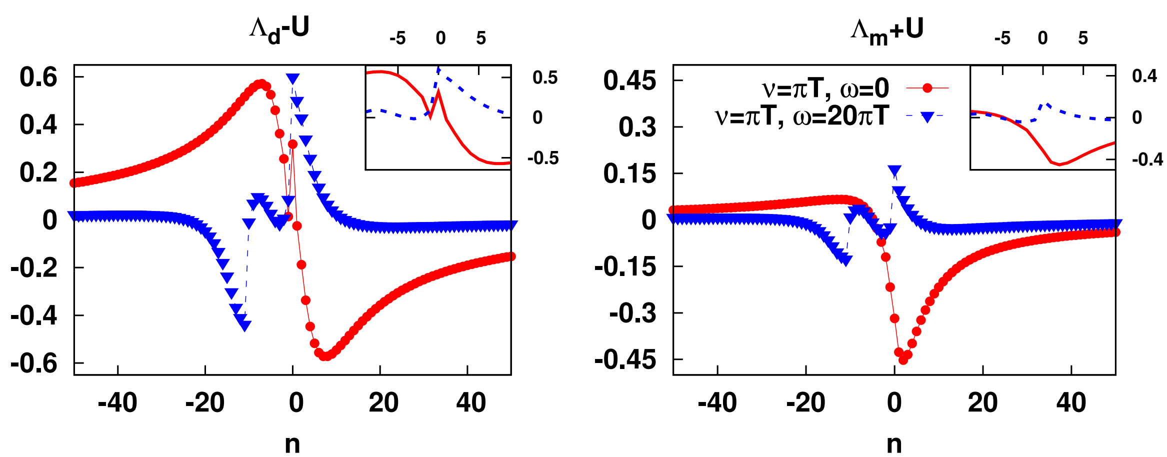

Figure 3.27: One-dimensional slice along the line $\nu' = \pi T$ of the local two-particle fully irreducible vertex $\Lambda^{\nu\nu'\omega}$ in Matsubara representation for the isolated ($V = 0$) COT ring in the *NN t* hopping configuration, at $U = 3t$ and $T = 0.10t$. In each panel a representation of the vertex is plotted and the corresponding asymptotics is subtracted, i.e. we plot: $\Lambda_d^{\nu\nu'\omega} - U$ (left), $\Lambda_m^{\nu\nu'\omega} + U$ (right) for $\omega = 0$ and $\omega = 20\pi T$ as a function of the Matsubara indexes of the fermionic frequency ν. Insets: the features of the vertex in the low-frequency region are highlighted.

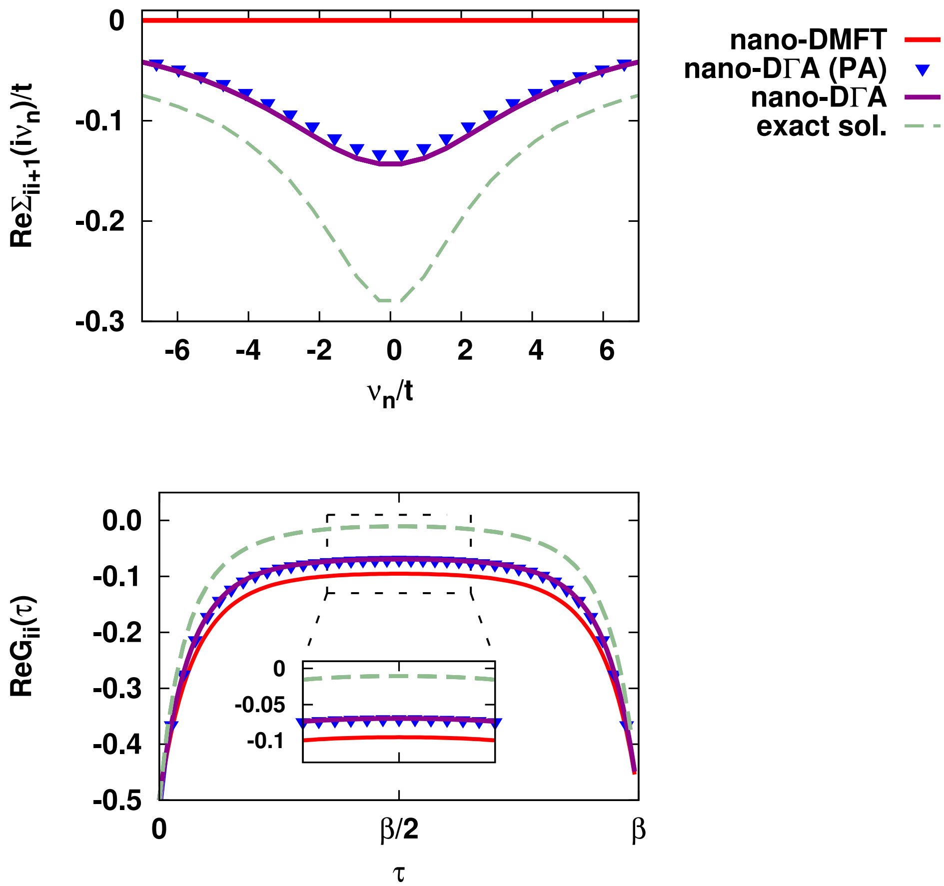

Figure 3.28: Comparison between nano-DMFT, nano-DΓA and the exact solution for the isolated ($V = 0$) COT ring in the *NN t* hopping configuration, at $U = 3t$ and $T = 0.10t$. Upper panel: real part of the on-local self-energy (between nearest neighbors i, $i + 1$) in Matsubara representation. Lower panel: local Green's function $G_{ii}(\tau)$ in the imaginary time representation.

Possible improvements in this respect may be expected by achieving a fully self-consistent nano-DΓA calculation, while it also possible that non-local correlations arising from a purely local fully irreducible vertex, while improving with respect to the description of nano-DMFT, are still not enough to accurately reproduce the exact solution.

In this respect the results presented above partially unveil the, so far unexplained, role of the frequency dependence of the fully irreducible vertex in the parquet equations in the context of nanoscopic systems. The results obtained call for further investigation in different parameter regimes, e.g., extending the analysis to systems with a finite hybridization to non-interacting environment. Another possibility concerns the direct calculation of the *exact* two-particle fully irreducible vertex, in order to observe its momentum structure: indeed, the DΓA aims mainly at treating $d = 2, 3$-dimensional systems, and it is possible that in the Q1D case considered here the assumption of the locality of the vertex is partially violated. While it is obviously a challenging task, it is still doable for Q1D system with a not too extended Hilbert space. Moreover, it may provide useful information about the limit of validity of nano-DΓA, as well as suggest possible parametrization of the vertex function, similarly to what has been reported in the context of functional renormalization group (fRG) technique [220].

3.5 Outlook

The analysis of electronic structure and transport properties in Q1D correlated systems represents the ideal testbed for the nanoscopic version of DMFT and of its diagrammatic extension, DΓA. We have described the parameter dependence of several physical quantities in different regimes, aiming to provide a general picture of the role of local and non-local electronic correlations. Moreover, the results presented so far showed that the inclusion of local and non-local spatial correlations in nano-DMFT and in nano-DΓA is possible. At the same time, these results point out other challenging problems and certainly require further investigations. In the following we briefly discuss other possible studies and extensions of the methods employed here.

Possible applications. According to the general criteria discussed in Sec. 3.3, even in low-dimensional systems, nano-DMFT can perform extremely well in a wide range of parameters, namely for large enough values of V/U and/or for high enough connectivity. At the same time it is quite flexible and fast, compared to an exact solution. Hence, nano-DMFT is expected to be an optimal and reliable tool to investigate higher dimensional nanostructure made of several atoms, for which an any exact solution in the presence of electronic correlations is numerically challenging or even prohibitive. In this respect, in the following chapters we will show applications of the method in the one-particle self-consistent approximation level, ranging from quantum junctions to realistic nanocluster of magnetic transition metal oxides.

On the other hand, we have shown that restoring non-local correlations beyond mean-field in a nano-DΓA fashion may improve the physical description of the system when the above criteria are not met. However, in order to understand to which extent the two-particle approximation level can be trusted, and in order to understand its limitations, we need to study the system presented so far (and possibly others) in a wider range of parameters. In this context, we plan to compute the exact two-particle fully irreducible vertex for the benzene and the COT molecules, in order to analyze its momentum dependence, which we consider an important step toward a deeper understanding of electronic correlations at the two-particle level.

Algorithmic development. As the method has been recently established, there is still room for technical improvements in several directions.

Concerning the **impurity solver**, modern QMC can deal with multi-orbital systems and it is often used in combination with *ab-initio* input for real material, but has the disadvantage of relying on problematic analytic continuation procedures in order to obtain physical quantities

on the real axis. On the other hand, ED impurity solvers avoid this issue, but are not suitable for systems with many degrees of freedom.
In addition, the HF-QMC algorithm mainly used to produce the results presented above poses severe limitation to the regime of low temperatures accessible, while in many cases of interest nanoscopic systems are expected to display, e.g., Kondo effect, at an energy scale which are exponentially small in the coupling constant. We plan to improve in this sense, adopting a new generation of CT-QMC impurity solver [93].

Concerning the **computation** of **two-particle quantities** we plan progresses from two point of views. On one hand, the knowledge of the local vertex functions allows us to compute vertex corrections for (nano-)DMFT/DΓA transport properties, e.g., conductance, optical conductivity in electronic transport and Seebeck coefficient in thermal transport. This represents a topic of forefront research, as effect of vertex corrections are typically neglected, except for sporadic investigations [89, 221, 222].
On the other hand, we need to improve the quality and the efficiency of the calculation of the vertex functions, in order to establish the approach to be widely applied to all cases of interest. We expect to make important steps forward in both directions implementing a semi-analytic method to access high-frequency asymptotic behavior for the local quantities in the impurity solver, extending the approach by J. Kuneŝ [219], as also explained in Ref. [158]. Eventually one would like to apply a similar idea also to non-local vertex functions in the parquet solver, though the possibility of an actual implementation in this respect is still to be confirmed.

Further improvements to the actual available version of the **parquet solver** are also mandatory for the nano-DΓA: the implementation of the solver in real space, in order to apply nano-DΓA also to non-translationally symmetric nanostructures; the implementation of more general routines able to deal with system out of half-filling, in the presence of hybridization, and in the case of site-dependent local fully irreducible vertex.

Chapter 4

Local Mott-Hubbard crossover in mechanically controlled break junctions

In this chapter we analyze correlation effects in a narrow of a 3-dimensional structure (or constriction), which is realized in the experiments involving e.g., a mechanically controlled break junction (MCBJ) or a scanning tunneling microscope (STM). In particular we focus on the relaxation of the electronic structure associated to a change of the size of the tunneling gap, and hence of the tunneling barrier, simulating the MCB process.
We show that the non-perturbative effects of a local Coulomb repulsion, present on the atoms in the neighborhood of the constriction, can drive a metal-to-insulator transition, localized on the atoms occupying the sharp edges of the junction. The observed local ''Mott-Hubbard'' crossover seems to be a general feature of sharp quantum junctions.

In the previous chapter we have applied the nano-approximation to include (both local and non-local) dynamical correlation effects in Q1D molecules, connected to bulk non-interacting environments (leads). In the description of the hybridization between the molecule and the leads, we restricted ourselves to the case in which the latter are characterized by one orbital with a flat, featureless DOS. This is quite a standard approximation in model calculations, where one is not particularly interested in the microscopic details of the electrodes' bandstructure, and may be sufficient in the case of GaAs heterostructure QDs, where the role of the semiconductor is mainly restricted to a charge reservoir. On the other hand, in quantum junctions (QJ), a microscopic description of the contacts plays a critical role.

4.1 Transport in quantum junctions: theory vs. experiments

As we have already mentioned in Sec. 1.1, experiments suggest a strong dependence of the tunneling current, and hence of the conductance, on the properties of the chemical bonding necessary to form a stable molecular junction. We have also mentioned the role of anchoring (and side) groups [44] which modify the properties of the molecule and of its hybridization to the electrodes. Obviously, a quantitative description of transport properties in such molecular

devices requires the energy spectrum of the whole junction and the hybridization between its components, i.e., molecule and electrodes, which is determined by the (e.g., LCAO) orbital overlap to be realistically taken into account.
There is no doubt that the spatial arrangement of the atoms forming the junctions influences the tunneling current. While in the experiments, there is, obviously, a certain degree of uncertainty coming from the impossibility to resolve the precise atomic configuration of the junction, within model calculations this issue can be quantitatively addressed. A recent interesting study in this direction has been reported by Berthod and Giamarchi [223], where they analyze the conventionally assumed proportionality between the differential conductance $G = dI/dV_{\mathrm{SD}}$ and the local DOS of the junction. There it is shown that, already in an exactly solvable (non-interacting) tight-binding picture, the electronic structure of the junction plays a fundamental role in determining the conductance. They also consider transport beyond the *quantum point contact* (QPC) picture, i.e., where tunneling processes involve lone atoms at the edge of the electrodes, and in particular they show that in the presence of several tunneling channels between *extended* regions of the source and the drain (planar junctions), some features of the local DOS can be washed out, e.g., by quantum interference between different channels.
Beautiful results were also reported by Palotàs *et al.* [224, 225] who developed an *ab-initio* package for STM simulations, showing that tips made of different materials (i.e., with a different electronic structure) yield different STM images.
The state-of-the-art for theoretical calculation of QJs relies on *ab-initio* description of the contacts within DFT, usually combined with non-equilibrium Greens's function (NEGF) technique in the Keldysh formalism (see Ref. [226] for a recent review) to address transport properties. However, DFT methods tend to overestimate the conductance with respect to the experimental values: e.g., in calculations done for a single $1,4$-BDT molecule bridging Au(111) surfaces (see Ref. [227] and references therein) a value of $G = 0.24\ G_0$ for the conductance at the Fermi energy [227], which is orders of magnitude higher than the experimental ones, discussed in Sec. 1.1, although the latter is extremely sensitive to the experimental technique employed.

A possible explanation for the discrepancy between theory and experiment can be ascribed to many-body effect beyond DFT, as, e.g., recently pointed out by Delaney and Greer [228]. Indeed, this eventually represents the main motivation for the development of the nanoscopic extension of DMFT, that we introduced here, or alternative approaches [178, 179], within which the structure of the junction can be modeled or taken into account *ab-initio*, interfacing with DFT, together with strong electronic correlations.

In particular, here we want to draw the attention to the role of atomically *sharp* contacts, which are formed, e.g., in mechanically controlled break junction (MCBJ) or scanning tunneling microscope (STM), which are widely employed in transport experiments (see also Sec. 1.1.2 for a brief discussion about their experimental realization). In the presence of a narrow contact region, quantum confinement may also play a role, and strong electronic correlations between spatially constrained electrons may arise *also* in the electrodes. As electronic correlations induce changes in the electronic structure of the system, one may also expect this to drastically affect the transport properties of the junction beyond the predictions of a Fermi liquid or DFT picture. If this is the case, it would be of crucial importance to consider the effects of electronic correlations also in the interpretation of tunneling experiments.

4.1.1 Modeling sharp junctions

In the following, we introduce model structure considered here in order to study sharp QJs. In particular we discuss in detail a possible realization of a MCBJ, that will consider for the analysis of the data presented in Sec. 4.2, within nano-DMFT. We also show that the model, with minor modification, is suitable to describe a STM: in this respect, preliminary analysis is already ongoing and a brief discussion is contained in the outlook (Sec. 4.3) at the end of this chapter. A schematic representation of the MCBJ and STM structures is given in Fig. 4.1 in order to clarify the description presented below.

General discussion. In order to describe a MCBJ, we need to consider a spatially extended and inhomogeneous structure, consisting of two identical 3-dimensional structures, representing the electrodes, separated by a distance Δd, often referred to as *tunneling gap*. As already mentioned, in a MCBJ molecules can be adsorbed into the gap, forming stable tunneling contacts, and allowing for the observation of electronic transport through molecular systems. Here however, in order to keep the complexity of the system low, we restrict to the analysis of correlation effects in a structure where the contacts are separated by a vacuum barrier, i.e., a QJ *without* any molecule adsorbed into the tunneling gap. The advantage, in prospective for our analysis, is that all correlation effects are with no doubt arising from the sharp contacts, and not from the confined system bridging the junction.
Although one has some degree of freedom in the spatial arrangement of the atoms in the junction, here we will restrict to the case in which the QJs consists of N atoms ordered according to a simple body-centered cubic (*bcc*) lattice symmetry. Hence, each half of the QJ develops symmetrically along the axis of the junction, and is made of a *tip* atom, occupying the sharp junction of the electrode, and N_ℓ layers, where each layer labeled $\ell = 1, ..., N_\ell$ (increasing with the distance from the *tip* atom) contains $(\ell + 1)^2$ atoms. Obviously the metallic road which is broken in the MCBJ process is infinitely long, i.e., its length $\mathcal{L}$ is large compared to the *bcc* lattice constant. and we mimic this allowing each of the correlated atoms in the outermost layers to hybridize with non-interacting environments, described by a flat, featureless, and symmetric DOS. Indeed, one expects electronic correlations to be induced by the spatial confinement of the electrons in the narrow region of the atomic contact, and Coulomb interaction to be strongly renormalized by an efficient metallic screening already a few Å away from the edges of the tunneling gap. Although this argument may seem rather naïve, we shall see that, even considering a structure with a few correlated layers, strong correlation effects mainly affect the lone *tip* atoms, i.e., the atoms localized at the sharp edges of the two facing structures.
For the sake of simplicity in the following we will refer to this realization as $\mathcal{J}^{[N_\ell+1]}$ **structure**, i.e., containing N_ℓ layers in addition to a *tip* atom. We will assume a single-band model, which

may be suitable for Cu or Co junctions, though orbital selective tunneling processes will probably also play a role in steel (Fe alloy) or materials where the full orbital multiplet structure needs to be taken into account. Hopping processes within the structure are allowed between nearest neighbor sites, with amplitudes t and t', for inter-layer and intra-layer processes, respectively, and t' will set the unit of energy. Hopping processes between the two facing structures are instead allowed only between the *tip* atoms occupying the sharp edge of each structure: in this quantum point contact realization, this hopping, defined by the parameter t_{QPC}, allows us to directly control the size of the nano-gap $\Delta d \equiv d_{\text{QPC}}$ by changing the distance between the structures. Each atom belonging to the outermost layer of each structure half ($\ell = 4$: in short L and R) is connected via hybridization channels $V_{i\eta k} = V\delta_{i\eta}$, with $V = t'$, to its own non-interacting lead described by a flat, featureless, DOS $\rho = 1/2D$, the half-bandwidth arbitrarily fixed to the value $D = 2t'$. Instead of a flat DOS, one could have, maybe more consistently assumed a 3-dimensional *bcc* one for the non-interacting environment, but this is not expected to qualitatively modify the results presented below.

Hamiltonian for QJs. The junction discussed above can then be formally described by the usual multi-impurity Anderson Hamiltonian, that we report below for the sake of clearness,

$$
\begin{aligned}
H = & -\sum_{ij}\sum_{\sigma} t_{ij} c^{\dagger}_{i\sigma} c_{j\sigma} - \mu \sum_{i}\sum_{\sigma} c^{\dagger}_{i\sigma} c_{i\sigma} + U \sum_{i} c^{\dagger}_{i\uparrow} c_{i\uparrow} c^{\dagger}_{i\downarrow} c_{i\downarrow} \\
& + \sum_{i\eta k}\sum_{\sigma} (V_{i\eta k} c^{\dagger}_{i\sigma} l_{\eta k\sigma} + V^{*}_{i\eta k} l^{\dagger}_{\eta k\sigma} c_{i\sigma}) + \sum_{\eta k}\sum_{\sigma} \epsilon_{\eta k\sigma} l^{\dagger}_{\eta k\sigma} l_{\eta k\sigma},
\end{aligned}
\tag{4.1}
$$

where $c^{\dagger}_{i\sigma}$ ($c_{i\sigma}$) has to be interpreted as the creation (annihilation) operator of an electron with spin σ in a Wannier orbital centered on the correlated atom i (in a multi-orbital case, i would be a combined site and orbital index). The chemical potential can include a gate voltage V_G, and the Hubbard interaction U_i could depend on the index i, yet, for the sake of simplicity, we will not consider this possibility in the following. The operators $l^{\dagger}_{\eta k\sigma}$ ($l_{\eta k\sigma}$) describes fermionic degrees of freedom of a non-interacting environment hybridized with some of the atoms in the junction. In Fig. 4.1 a schematic representation of the structures considered in the following is provided.

Comment on the configurations considered. In order to get rid of possible finite size effects, i.e., to have a system which may be representative of the experimental one, we considered a $\mathcal{J}^{[5]}$ structure, i.e., where each half of the QJ consists of a *tip* atom and $N_\ell = 4$ additional layers, corresponding to $N = 110$ atoms overall (and $N_{\text{ineq}} = 14$ inequivalent ones). Moreover, we analyzed the $\mathcal{J}^{[5]}$ structure in two different hopping configurations: a ‘‘homogeneous’’ case with $t = t'$, and an inhomogeneous’’ one, with $t = 2.5t'$. In both cases, we observed that electronic correlations to drive the system toward a Mott-Hubbard crossover, localized at the *tip* atom(s) and characterized by deviations from the usual exponential behavior of the conductance as a function of the tunneling barrier.

In order to test the stability of the result with the size of the system, we considered also structures with less than $N_\ell = 4$ layers. In particular, we analyzed in detail a $\mathcal{J}^{[2]}$ structure, consisting of a *tip* atom and only one additional layer for each half of the QJ, corresponding to $N = 10$ atoms overall (and only $N_{\rm ineq} = 2$ inequivalent ones: the *tip* and the *layer I* atoms). It is worth stressing that, in this realization, each of the four equivalent *layer I* atoms is connected to the *tip*, to the nearest neighbor *layer I* atoms, and to its own lead. In the present context, this system is interesting for several reasons, that we anticipate here.
One important issue is to understand whether the presence of many correlated layers contributes to the emergence of the local Mott-Hubbard crossover: as we shall see the answer is ‘‘no’’ (but not without reserve, as will be shown in detail in Sec. 4.2, in the analysis of the results). However, taking at least one layer into account allows to show that the phenomenon is correlation-driven and manifest itself *only* if all the atoms in the system are close to half-filling (more details about this issue are also postponed to Sec. 4.2). Moreover, the reduced size of the Hilbert space (e.g., with respect to the $\mathcal{J}^{[5]}$ structure) allows the exploration of a wider parameter range with limited computational effort. A direct comparison with an exact solution would have been of great importance, but it is unfeasible: due to the coupling to the leads, in the case of an ED, or due to a severe sign-problem originating from the complicated hopping structure, in the case of QMC.

Setting up a STM tip. A STM can be modeled analogously, and the scanning electrode is shaped as a single-cone-like structure, i.e., as one of the halves of the structure described above. The atoms belonging to the outermost layer hybridize with non-interacting environments, representing the rest of the semi-infinitely extended microscope, also in this case described by a flat, featureless, and symmetric DOS. In contrast to the MCBJ structure, the *tip* atom occupying the sharp edge is directly connected to the *sample*, via a single hopping or hybridization channel. However, the flexibility of nano-DMFT (and extensions) also leaves room for exploring other setups besides this one, e.g.: i) one can consider also the sample as a spatially extended lattice and include more tunneling channels between those lattice sites and the *tip* atom of the scanning electrode, or ii) one can include adatoms between the sample and the scanning electrode (EME setup).

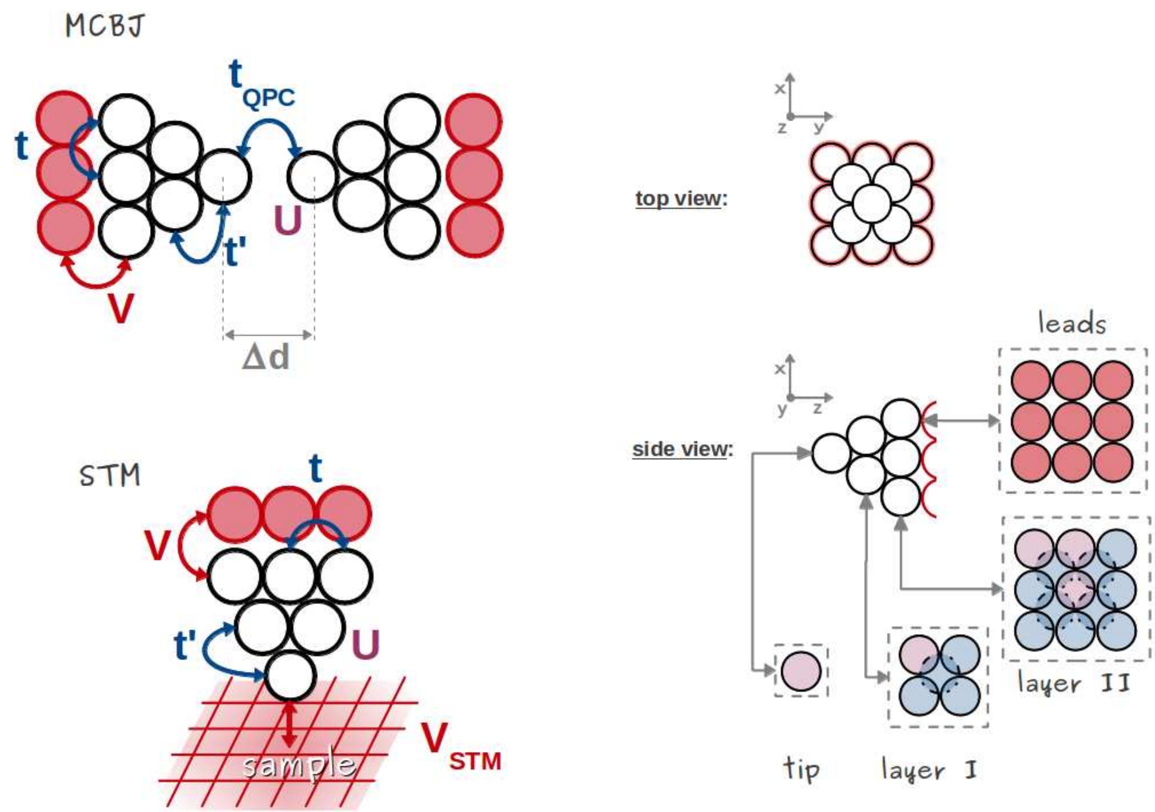

Figure 4.1: Left panels: schematic representation of the 3-dimensional QJs considered: a mechanically controlled break junction (MCBJ, above) and a STM (STM, below). Right panel: a top view (above) and a side view (below) show more details about the structures of th QJs, the color coding denotes inequivalent (violet) and equivalent (cyan) atoms, due to *bcc* lattice symmetry, and non-interacting environments (red).

In the representative realization of QJ shown here (denoted as $\mathcal{J}^{[3]}$ in the text) the *unit structure* of the system consists of a *tip* atom two layers, denoted as *layer I* and *layer II*, where electrons, due to spatial confinement, experience an on-site Hubbard repulsion U. The correlated atoms of the unit structure are connected by nearest neighbor hopping channels t (intra-layer) and t' (inter-layer). Each atom belonging to the outermost layer (i.e., the furthest from the tip) is also connected via an hybridization channel V to a non-interacting environments, describing the bulk of the junction (where an effective metallic screening of the interaction is assumed, see text for further details).

In the case of a MCBJ, the junction is made of two facing unit structure, separated by a tunneling gap Δd, whose size determines the inter-*tip* hopping amplitude t_{QPC}. In the case of a STM, the *tip* is connected to a sample via an hybridization channel V_{STM} (or possibly a hopping channel, t_{STM}, depending on the details to the sample).

4.2 nano-DMFT results

The results concerning the MCBJ, presented in the following, are partially published in the APS Journals ''Physical Review Letters'': PRL **104**, 073101 (2010) [206] and ''Physical Review B'': PRB **86**, 115418 (2012) [207].

In the following we present the nano-DMFT analysis of correlation effects in transport properties of MCBJ: after discussing how to simulate the MCB process, we show how the conductance profile is affected by the presenze of electronic correlation through the analysis of the electronic structure and electronic properties of the system. Considering different realization of the MCBJ allow to identify universal properties of the phenomenon, i.e., independently on the details of the parameters of the model, and discuss the role of size effects.

4.2.1 What happens in the MCB process?

Here, we essentially address the problem of the relaxation of the electronic structure of the system by changing the size of the tunneling gap Δd between the *tip* atoms at the edge of the two facing structures. The physical motivation is to identify possible correlation effects, analyzing the dependence of the conductance on the size of the tunneling gap. While in the experiments, the MCB process is reasonably associated with a rearrangement of the electrodes' lattice structure. Although the appropriate lattice structure could be obtained *ab-initio* at any size of the tunneling gap, for the sake of simplicity we will consider it to be frozen. In the model calculations we carried out, we can obtain an estimate the distance d_{QPC} between the *tip* atoms from t_{QPC}, i.e., the overlap of the electrons' atomic-like wave functions of the *tip* atoms. For the tunneling amplitude between two atoms, the following following functional dependence (see e.e.g, Ref. [231] and references therein) can be assumed

$$t_{\text{QPC}}/t' = \left(\frac{1}{d_{\text{QPC}}/a}\right)^{\alpha} \exp(1 - d_{\text{QPC}}/a), \tag{4.2}$$

where $\alpha = l + l' + 1$, being l and l' the angular momentum quantum numbers associated to the orbitals involved in the tunneling process. Here a defines the unit of length, and it is chose so that $t_{QPC}/t' = 1$ corresponds to $d_{QPC}/a = 1$. While the above relation is reasonable in at long distances, it evidently brakes down in the limit $d_{QPC}/a \ll 1$, where t_{QPC}/t' would diverge. A more general expression would require a detailed knowledge of the microscopic mechanism dominating transport on that length scale, which is highly non-trivial. In the following we estimate d_{QPC} according to Eq. (4.2) with $l = l' = 2$, i.e., assuming a d-like orbital character for the correlated atomic orbitals. In this respect, note that the physical phenomenon (i.e., the local Mott-Hubbard crossover) that will be discussed in the following *is not* affected by the exact estimate of d_{QPC}, e.g., on the character of the orbital involved. However, it is convenient to introduce a length scale: in fact, the (correlation-driven) deviation from an usual exponential behavior of the zero-bias conductance on the width of the tunneling barrier is best observed considering a function $G(\epsilon_F, d_{\text{QPC}}[t_{QPC}])$.

As it has been shown in Sec. 1.3.2 the **electronic conductance** $G(\epsilon) = e^2/h\mathcal{T}(\epsilon)$ through a nanostructure can be expressed in terms of the **transmission coefficient**, obtained summing over all possible transmission channels

$$\mathcal{T}(\epsilon) = \sum_{\sigma} \sum_{i\in\mathrm{L}} \sum_{i\in\mathrm{R}} \Gamma_i |G_{\sigma ij}(\epsilon)|^2 \Gamma_j, \tag{4.3}$$

where i and j run over the indexes of the correlated atoms sitting in the outermost layers of the L (left) and R (right) half of the QJ. As already discussed, the choice of a QMC impurity solver pose several problems in the evaluation of the Green's function on the real frequency axis. Hence, also in this case we will limit to consider of the conductance at the Fermi energy. With the form (3.8) of the scattering matrix for the two-terminal conductance, one can estimate the conductance at the Fermi energy as

$$G(\epsilon_F) = \frac{e^2}{h}\mathcal{T}(\epsilon_F) \approx 2\frac{e^2}{h}(2\pi\rho V^2)^2 \sum_{i\in\mathrm{L}} \sum_{i\in\mathrm{R}} |G_{\mathrm{ij}}(\imath\nu_n{=}\pi T)|^2. \tag{4.4}$$

Hence, the conductance depends in a non-trivial way on t_{QPC}, through the non-local propagator connecting the atoms belonging to the outermost layers of the two halves of the MCBJ.

Electronic structure: non-interacting case. Useful insights on the physics of the system can be gained analyzing the electronic structure of the inequivalent atoms in the MCBJ already in the non-interacting case. This can be done considering their **local spectral function** $A(\nu, \Gamma)$, which can be obtained exactly by the (trivial) analytic continuation on the real frequency axis of the non-interacting Green's function. Here, the dependence on the scattering rate Γ is explicit to remind that not all the sites of the structure are directly connected to a lead.
Hence, in Fig. 4.2 and 4.3 we show the local spectral function of the *tip* and of the only inequivalent atom of *layer 1* in all the realization of QJ discussed above. For each atom we compare $A(\nu, \Gamma)$ for representative values of the ratio t_{QCP}/t', namely $t_{\mathrm{QPC}}/t'{=}0$ corresponding to the extreme case where the two halves of the QJ are far apart and the Wannier orbitals' overlap is vanishing, $t_{\mathrm{QPC}} = t'$, and $t_{\mathrm{QPC}} = 2.25t'$, which would describe a situation where the *tips* are strongly bound. While the latter value may be unrealistic, it represents an interesting limit of the model in the presence of electronic correlations, as we will see in the following.
It is immediately clear that, already in the non-interacting limit, the local spectral function of any of the atoms of the QJs is more complicated than the ones of the Q1D molecules, and already an artificial Lorentzian broadening ($\delta \approx 0.1t'$) causes the tails of the peak to merge, creating a *continuum* local DOS, with a bandwidth $W \approx 4t'$. This means that the level spacing $\Delta\epsilon$ is not the dominating energy scale, and hence the system is not expected to behave as a QD: in particular, this explains why, in the following we will not be able to observe conductance quantization (only expected at temperatures $T \ll \Delta\epsilon$).
The most important detail, however, is the following feature, shared by all realizations of MCBJ: while the spectral function of the *tip* atom is very sensitive to variation of t_{QPC}, as one would expect, this has (almost) no repercussion on the *layer* atoms (although we show only the atom

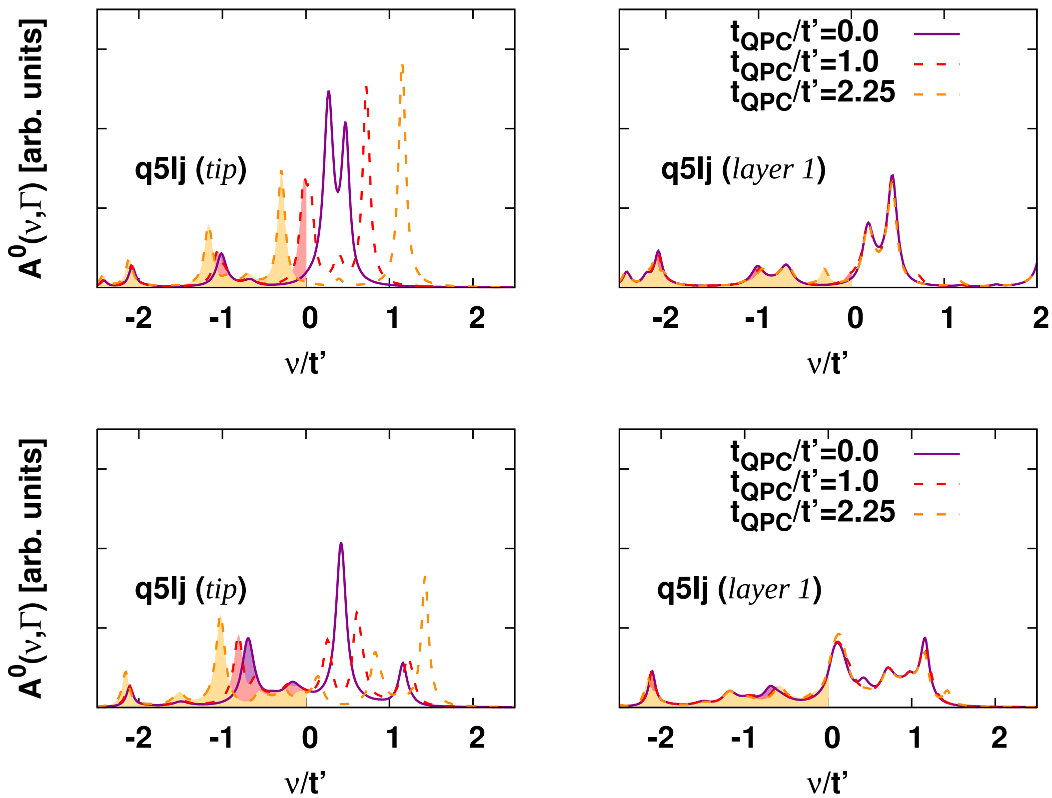

Figure 4.2: Spectral function $A^0(\nu,\Gamma)$ of the non-interacting Q5LJ in the hopping configuration corresponding to $t = 2.5t'$ (upper panels) and $t = t'$ (lower panels). The portion of the occupied spectrum (at $T = 0$) is denoted by color filling, and the width of the δ-like peaks is determined by an artificial broadening. Left panels: local spectral function of the *tip* atom ($\Gamma = 0$). Right panels: local spectral function of the first *layer* atom ($\Gamma = 0$).

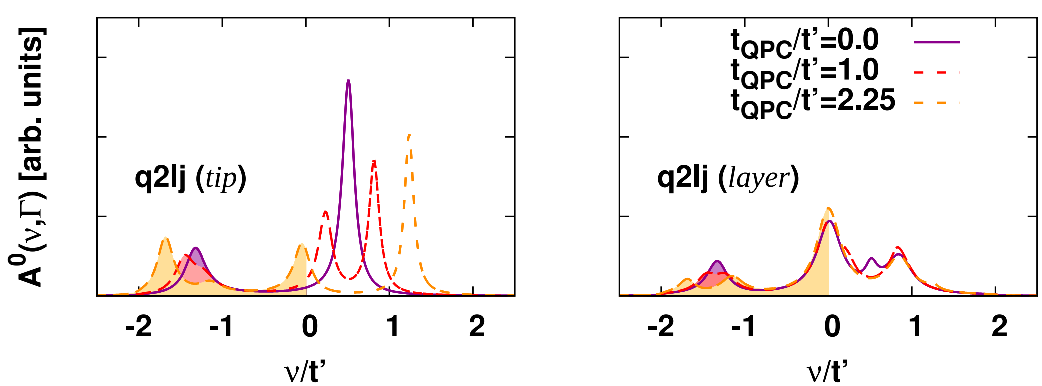

Figure 4.3: Spectral function $A^0(\nu,\Gamma)$ of the non-interacting Q2LJ in the $t = t'$ hopping configuration. The portion of the occupied spectrum (at $T = 0$) is denoted by color filling, and the width of the δ-like peaks is determined by an artificial broadening. Left panel: local spectral function of the *tip* atom ($\Gamma = 0$). Right panel: local spectral function of the only *layer* atom ($\Gamma = 0.1t'$).

belonging to the layer closest to the *tip*) which is not obvious. It is also important to notice that, at $U = 0$, the t_{QPC}-dependent relaxation of the *tip*'s electronic structure is accompanied by a strong variation of the site-density $\langle n \rangle$. The change in $A(\nu, \Gamma)$, and the corresponding variation of $\langle n \rangle$, suggests that already in the *absence* of electronic correlations, the relaxation of the electronic structure of the junction has a strong influence on the tunneling current. We shall see that, in the presence of electronic correlations it may have even more dramatic effects and lead to unexpected phenomena.

Local Mott-Hubbard crossover. Let us consider now what happens in the presence of a local Coulomb repulsion $U = 10t' \approx 2.5W$. We estimate the conductance G through the $\mathcal{J}^{[5]}$ structure according to Eq. (4.4), as discussed above, for both the "homogeneous" and "inhomogeneous" hopping configurations. The dependence of G on t_{QPC} (or equivalently, on d_{QPC}) is shown in the upper panels of Fig. 4.4, comparing the finite U and the non-interacting $U = 0$ results. Let us begin with some consideration about the non-interacting case: in a tunneling process, the tunneling current is expected to drop exponentially with the width of the potential barrier. In the situation we are considering, the barrier consists of vacuum or, more in general, of a dielectric medium present between the *tip* atoms of the two symmetric structures of the QJ. Indeed, on a semi-log scale, a linear decrease of the conductance G as d_{QPC} increases is actually observed for distances $d_{QPC}/a > 1$. While in the homogeneous case ($t = t'$) an exponential

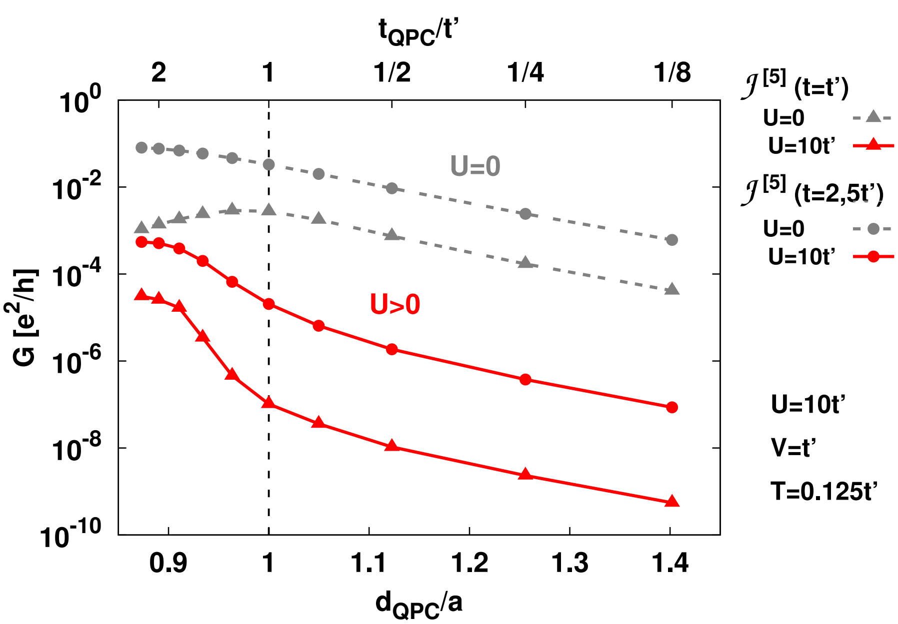

Figure 4.4: Conductance G through the $\mathcal{J}^{[5]}$ structure as a function of t_{QPC} and d_{QPC}, where the dependence (4.2) is assumed. The results for $t = 2.5t'$ (triangles) and $t = t'$ (circles), at $T = 0.125t'$, in the presence of electronic correlations ($U = 10t'$, red solid line) are compared to the non-interacting case (grey dashed line) on a semi-log scale (and log-log for t_{QPC}), highlighting the faster than exponential drop of the G in the MCB process.

drop of G with $d_{\rm QPC}$ is observed also at shorter distances, in the inhomogeneous one ($t=2.5t'$) the conductance displays a *maximum* upon decreasing $d_{\rm QPC}$: this behavior may be related to the formation of a bonding and anti-bonding pair of "extended" orbitals originated by the overlap of the localized *tips* orbitals. In the presence of electronic correlations, the conductance is in general suppressed with respect to the non-interacting value, at *any* value of $d_{\rm QPC}$, yet conserving the exponential behavior in the tunneling regime $d_{\rm QPC}/a\lesssim 1$, with an *universal* exponent β: $G(d_{QPC})\propto \exp(-\beta d_{\rm QPC}/a)$, which does not seem to depend on the microscopic details of the structure, i.e., U, t, and t'.

However, in an intermediate regime $d_{\rm QPC}/a\gtrsim 1$ (or $t_{\rm QPC}/t'\gtrsim 1$), the conductance clearly shows a **change of the exponent** β, reflected in a **non-linear behavior** of $G(d_{\rm QPC})$ in the logarithmic plot of Fig. 4.4, in both hopping configurations. The faster than exponential conductance behavior alone, although suggesting this phenomenon to be correlation-driven, is not sufficient to prove this statement. Hence, one can investigate the effect of electronic correlations on the evolution with $t_{\rm QPC}$ of **local quantities**, such as the **site-dependent density** $\langle n\rangle=\langle n_\uparrow+n_\downarrow\rangle$ and the **double occupation** $\langle d\rangle=\langle n_\uparrow n_\downarrow\rangle$, or the local **spectral function at the Fermi energy** $\overline{A(0)}$. One realizes immediately that, as in the non-interacting case, the change of $t_{\rm QPC}$, associated to the MCB process, mainly influences the *tip* atoms only, and not the other inequivalent atoms of the $\mathcal{J}^{[5]}$ structure: in Fig. 4.5 we show the results for the *tip* and *layer I* inequivalent atoms for both $t=2.5t'$ (left block of panels) and $t=t'$ (right block of panels), according to the labels in the plots. In order to understand the behavior of the *tip* atoms(s), it is fundamental to notice that, in the non-interacting case, the site-dependent density $\langle n\rangle$ displays a non-trivial dependence on $t_{\rm QPC}$, and it is spatially strongly inhomogeneous, i.e., its value varies sensibly from atom to atom in the junction. At $U=10t'$ instead, the *tip* are half-filled, as well as all other atoms in the $\mathcal{J}^{[5]}$ structure[1] (see e.g., *layer I* atom) *independently* on $t_{\rm QPC}$. This means that the evolution of $\langle d\rangle$ with $t_{\rm QPC}$ in the non-interacting case is only reflecting the variation of the density, i.e. $\langle d\rangle=\langle n_\uparrow n_\downarrow\rangle=\langle n^2\rangle/4$ (in the paramagnetic case). On the other hand, when the density is fixed at half-filling, the suppression of $\langle d\rangle$ upon decreasing $t_{\rm QPC}$ is the hallmark of the enhancement of electronic correlations due to the MCB process.
Analogously, density fluctuations can induce strong dependence of $\overline{A(0)}$ on $t_{\rm QPC}$, due to an asymmetric evolution of the non-interacting spectral function with respect to the Fermi energy. At $U=10t'$ and half-filling instead, the suppression of $\overline{A(0)}$ corresponds to a shift of the spectral weight from the Fermi energy to the incoherent Hubbard bands.

Further confirmation of the validity of this picture comes form the site-dependent nano-DMFT **local self-energy**, shown in Fig. 4.6 for the *tip* and *layer I* inequivalent atoms of the $\mathcal{J}^{[5]}$ structure for both $t=2.5t'$ and $t=t'$ hopping configurations. Each self-energy is compared at two selected values of $t_{\rm QPC}/t'$, representative of two extreme cases of the MCB process: one

[1] let us note here, that in the $t=t'$ configuration, the *tip* atom is *not* exactly half-filled in the whole range of $t_{{\rm QPC}/t'}$: indeed, this could explain why the deviation from the plain exponential behavior are less evident with respect to the $t=2.5t'$ case, as will be more clear in the following.

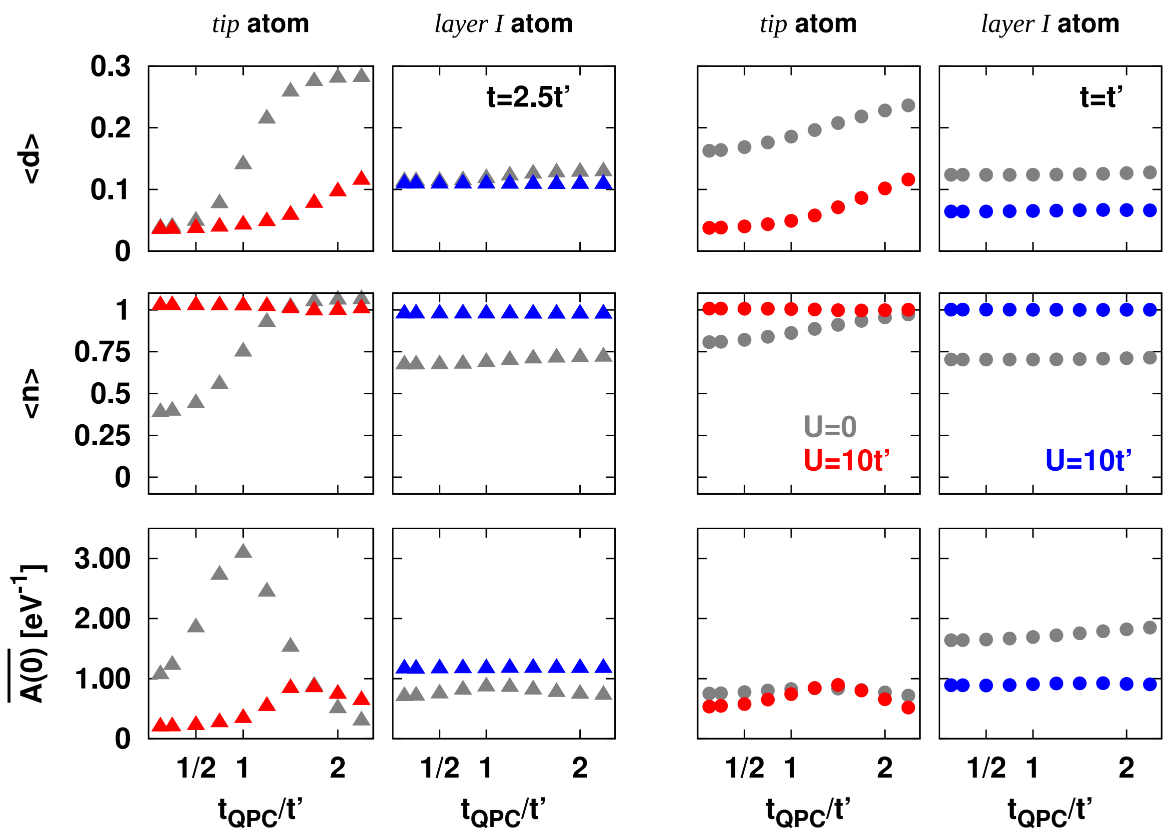

Figure 4.5: Evolution with $t_{\rm QPC}$ of the site-dependent density $\langle n \rangle$ (upper panels), double occupation $\langle d \rangle = \langle n_\uparrow n_\downarrow \rangle$ (middle panels), and $\overline{A(0)}$ (lower panels), limited to the *tip* (red symbols) and *layer I* (blue symbols) inequivalent atoms of the $\mathcal{J}^{[5]}$ structure. The results in the presence of electronic correlations ($U = 10t'$, color symbols) for $t = 2.5t'$ (triangles) and $t = t'$ (circles), at $T = 0.125t'$, are compared to the ones of the non-interacting system (grey symbols).

corresponding to the "contact" regime, i.e., when the inter-*tip* hopping is of the same order of magnitude of t' (precisely, $t_{\rm QPC}/t' = 1.5$ is shown), and one deep in the tunneling regime, where the overlap between the *tip*s' Wannier functions is substantially reduced ($t_{\rm QPC}/t' = 0.25$). In both hopping configurations, the imaginary part of the local self-energy of the *tip* atom becomes more and more insulating-like as $t_{\rm QPC}/t'$ is lowered, consistently with the decrease of the double occupations $\langle d \rangle$ at this site, while the *layer I* atom is metallic-like and almost $t_{\rm QPC}$ independent. Moreover, one can notice that in the case $t = 2.5t$ the *tip* self-energy (shown in the upper left panel of Fig. 4.6) is larger than the corresponding one for $t = t'$ (lower left panel) and it is probably directly related to size of the drop of the conductance G, shown in Fig. 4.4, which seems to be steeper in the former hopping configuration than in the latter one.

In conclusion, we have observed deviations in the dependence of the exponential decay of the conductance with the size of the tunneling gap in a MCBJ. While considering only transport properties may lead to misinterpretations, the scenario provided by the analysis of several

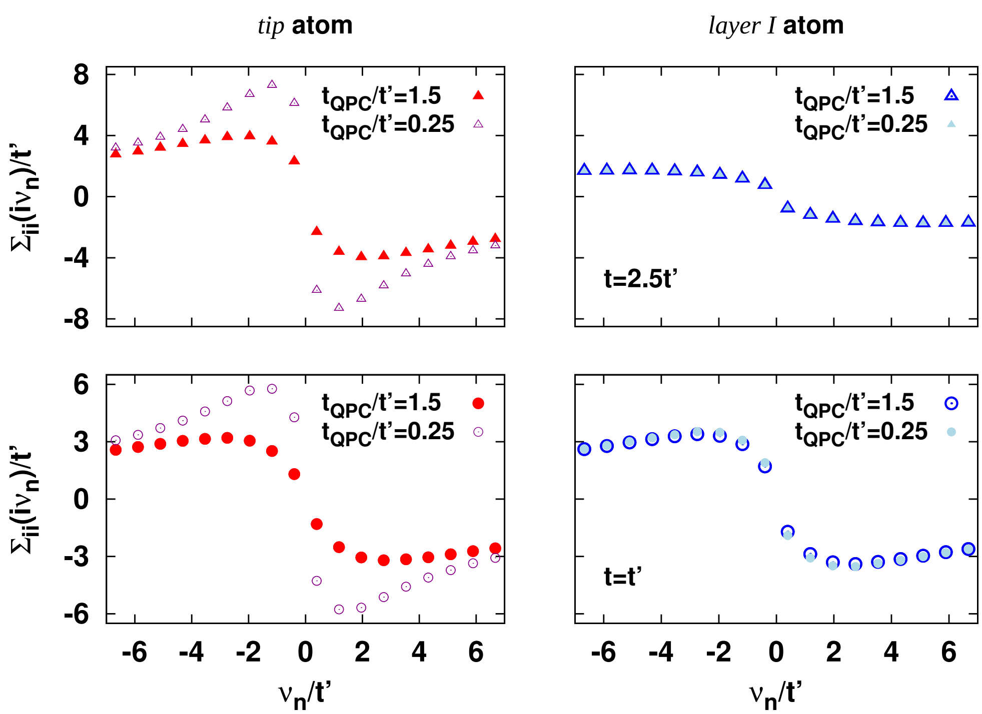

Figure 4.6: Evolution with t_{QPC} of the local nano-DMFT self-energy Σ_{ii}, at $U = 10t'$ and $T = 0.125t'$, for $t = 2.5t'$ (triangles) and $t = t'$ (circles), limited to the *tip* (red/violet symbols) and *layer I* (blue/cyan symbols) inequivalent atoms of the $\mathcal{J}^{[5]}$ structure.

spatially-resolved local quantities clearly show that the phenomenon is correlation-drive, and that can be entirely ascribed at the rearrangement of the electronic structure of the lone *tip* atoms: electronic correlations, due to spatial confinement of the electrons in the narrow restriction of a sharp QJ, are enhanced by increasing the tunneling gap, and induce a local **metal-to-insulator Mott-Hubbard crossover** of the *tip* atoms, which dramatically influence non-local transport quantities through the QJ in an absolutely non-trivial way.

4.2.2 Universal features of the local Mott-Hubbard crossover

The next question we aim to answer is whether this phenomenon can be regarded as a general feature of atomically sharp quantum junctions. In order to proceed, we will focus on the $\mathcal{J}^{[2]}$ structure: which allows to understand if the presence of several layers of correlated atoms is a necessary condition to observe the local Mott-Hubbard crossover. Obviously, considering the $\mathcal{J}^{[2]}$ structure represents a huge reduction of the numerical workload with respect to the $\mathcal{J}^{[5]}$ one, and as the self-consistent solution of the nano-DMFT equations in this case require a limited computational effort, it allows us to explore a wide range of parameters.

Critical threshold for the Mott-Hubbard crossover. In the following we will proceed as before, i.e.: first we show the fingerprint of the local Mott-Hubbard crossover in the conductance G through the $\mathcal{J}^{[2]}$ structure, and then we will interpret the results analyzing the local quantities of the only two inequivalent atoms.

The dependence of G on t_{QPC} (or equivalently, on d_{QPC}) is shown in Fig. 4.7, comparing the results for different values of the local interaction U, including the non-interacting case $U = 0$. Moreover, as we have seen no qualitative difference arising from different hopping structures, here we limited ourselves to the homogeneous ($t = t'$) hopping configuration.

There are mainly two elements to be noticed here: (i) the universality of the exponential behavior in the tunneling regime, and (ii) the existence of a **critical value** of the interaction U_c for the hallmark of the Mott-Hubbard crossover to be observed in the conductance.

In fact, we can see that the exponent β, determining the exponential decrease of G at distances $d_{\mathrm{QPC}}/a \gtrsim 1$ (as previously discussed) is the same for both the $\mathcal{J}^{[2]}$ and the $\mathcal{J}^{[5]}$ structure, and is U/t' independent, although the conductance is progressively suppressed by increasing U/t'. Those universal features are shown in Fig. 4.7, where the corresponding data are compared.

However, in the regime $d_{\mathrm{QPC}}/a \lesssim 1$ (that we called contact regime) the profile of the conductance strongly depends on the structure and interaction parameters. The data for the $\mathcal{J}^{[2]}$ structure, however, show that the change of β is weak or even absent in the weak-to-intermediate coupling regime $U \sim W \approx 4t'$, while is well pronounced, e.g., at $U = 10t'$. The change in the

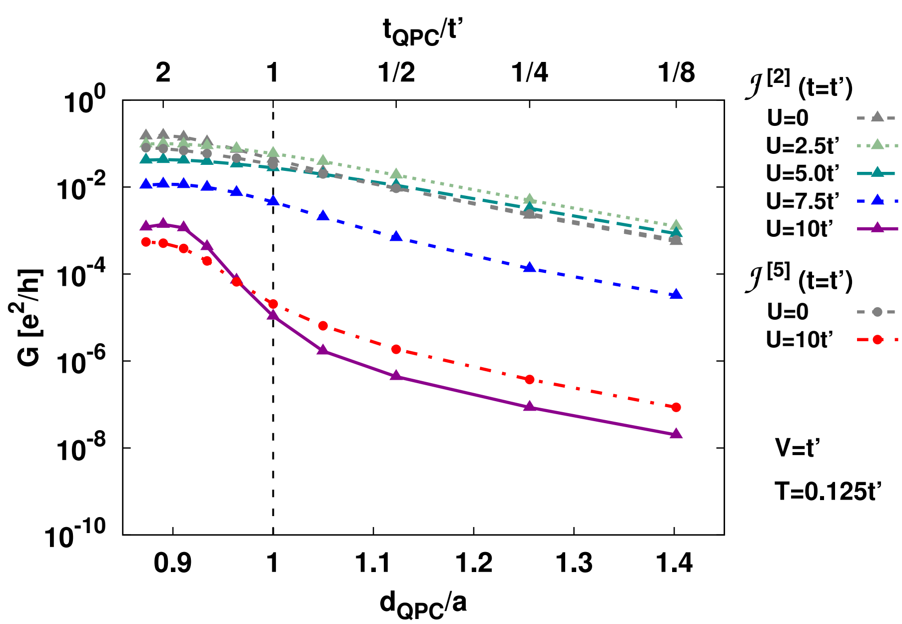

Figure 4.7: Comparison between the conductance G through the $\mathcal{J}^{[2]}$ (triangles) and the $\mathcal{J}^{[5]}$ (circles) structures as a function of t_{QPC} and d_{QPC}, where the dependence (4.2) is assumed. The data at different values of the interaction U/t', for $t = t'$ at $T = 0.125t'$, are compared, highlighting the faster than exponential drop of the G in the MCB process, taking place only above a critical value of the local interaction.

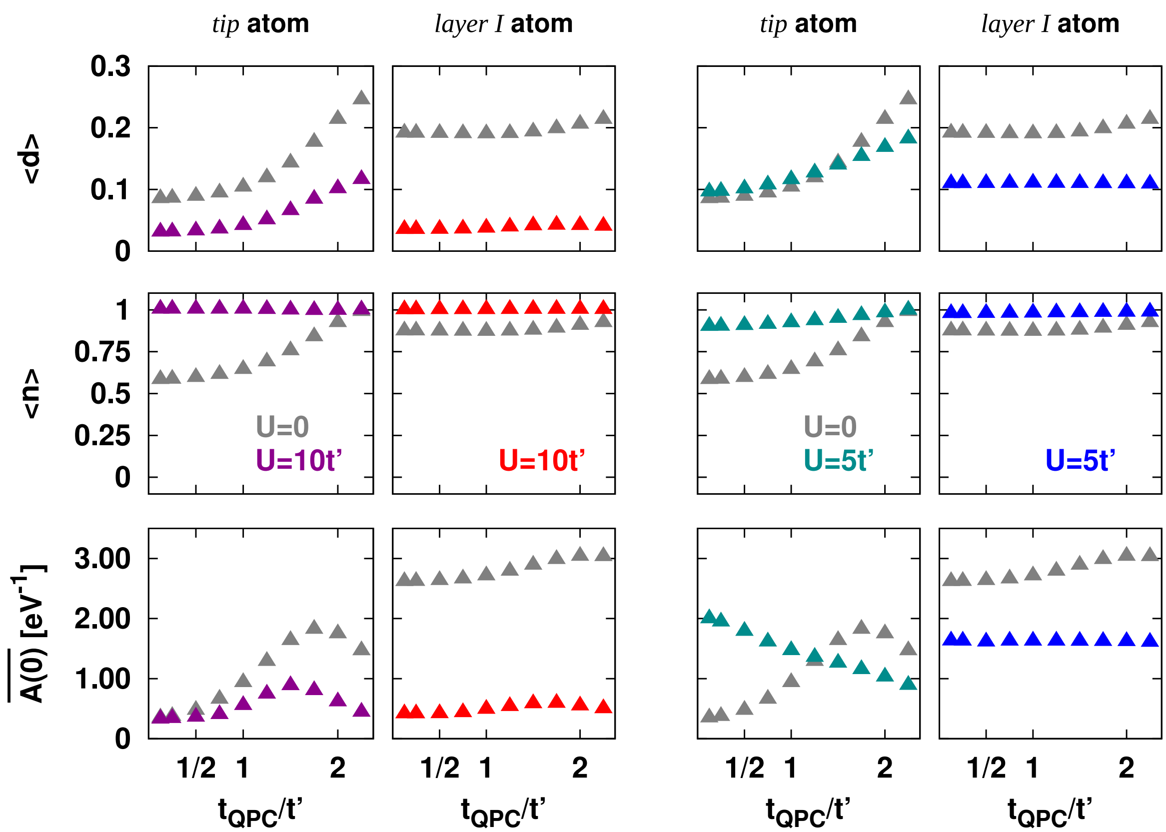

Figure 4.8: Evolution with $t_{\rm QPC}$ of the site-dependent density $\langle n \rangle$ (upper panels), double occupation $\langle d \rangle = \langle n_{\uparrow} n_{\downarrow} \rangle$ (middle panels), and $\overline{A(0)}$ (lower panels), for both the *tip* (violet/cyan symbols) and *layer I* (red/blue symbols) inequivalent atoms of the $\mathcal{J}^{[2]}$ structure. The results in the presence of electronic correlations $U = 10t'$ (left panels) and $U = 5t'$ (right panels) for $t = t'$, at $T = 0.125t'$, are compared to the ones of the non-interacting system (grey symbols).

exponent is also more pronounced in the $\mathcal{J}^{[2]}$ structure with respect to the $\mathcal{J}^{[5]}$ one, and this can be ascribed to finite size effects, responsible for quantum charge fluctuations in the atoms of the $\mathcal{J}^{[2]}$ structure.

Hence, in Fig. 4.8 we analyze local quantities of the *tip* and *layer I* atoms for two representative values of the interaction U/t', comparing the results to the corresponding non-interacting ones. As in the case of the $\mathcal{J}^{[5]}$ structure, also here the physics of the system can be understood considering the role of charge fluctuations induced by the change of $t_{\rm QPC}$ in MCB process. At $U = 5t'$ (right panels) the *tip* atom becomes half-filled only in the limit $t_{\rm QPC}/t' \gg 1$, so that $\overline{A(0)}$ increases as $t_{\rm QPC}/t' \to 0$: as a consequence no change in the exponential behavior of the conductance can be observed in the MCB process. On the other hand, at $U = 10t'$ the *tip* atoms stays half-filled on the whole range $t_{\rm QPC}$ and the strong electronic correlations induce a Mott-Hubbard suppression of the spectral weight at the Fermi energy, as well as the change in the exponent β on the exponential dependence of the conductance G on the distance $d_{\rm QPC}$, i.e., on

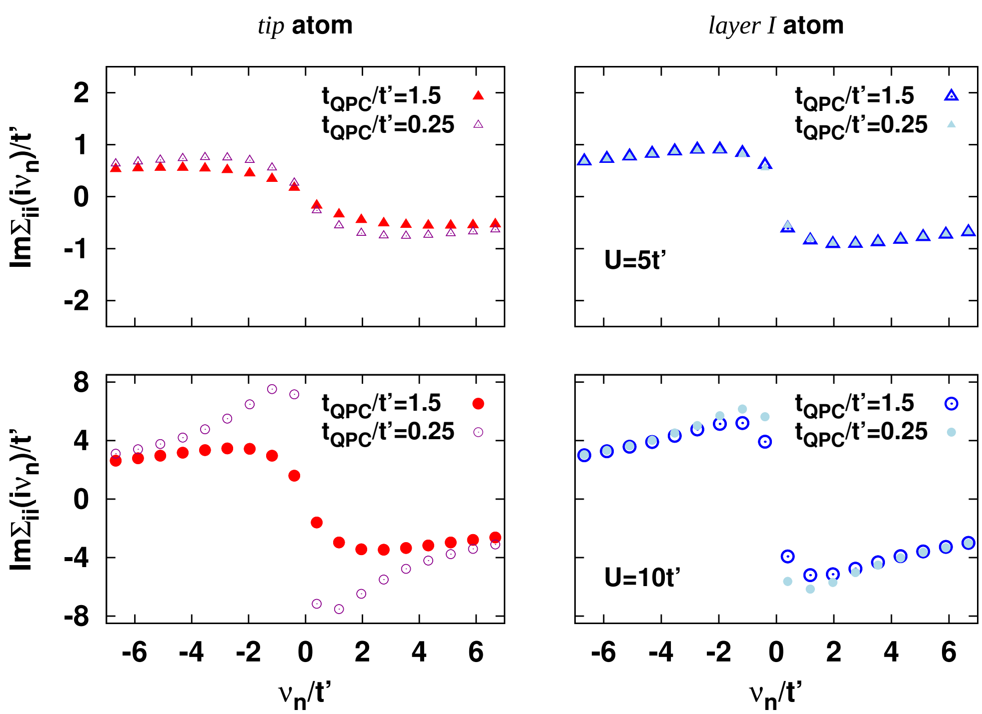

Figure 4.9: Evolution with t_{QPC} of the local nano-DMFT self-energy Σ_{ii}, at $U = 10t'$ and $T = 0.125t'$, for $t = t'$ (triangles) and $t = t'$ (circles), limited to the *tip* (red/violet symbols) and *layer I* (blue/cyan symbols) inequivalent atoms of the $\mathcal{J}^{[2]}$ structure.

the size of the tunneling gap. A similar argument can also be applied to the local quantities of the *layer I* atoms, which yet still maintain a weak t_{QPC} dependence, in contrast to the case of the $\mathcal{J}^{[5]}$ structure. This can reasonably be ascribed, e.g., to finite size effect, suggesting that *layer I* is only weakly affected by the *tip* atom, but there is some difference between *layer II* being sorrelated sites or non-interacting leads.

In this respect, important information, enclosed in the site-dependent nano-DMFT **self-energy**, is shown in Fig. 4.9 for both the *tip* and *layer I* inequivalent atoms of the $\mathcal{J}^{[2]}$ structure. Already at $U = 5t'$, i.e., when spatial charge fluctuations induced by the change of t_{QPC}/t' in the MCB process are still allowed, and the site-dependent density is not yet locked at half-filling, the imaginary part of the *tip* atoms' local self-energy shows only a weak insulating tendency, while one of the *layer I* atoms is t_{QPC} independent. At $U = 10t'$, instead, each atom in the structure is half-filled, and strong electronic correlations are enhanced in the MCB process, contributing to a faster than exponential suppression of the conductance as t_{QPC}/t' is decreased. The phenomenon can still be mainly ascribed to the *tip* atoms, whose imaginary part of the local self-energy displays a remarkable insulating tendency, compared to the weak changes in the *layer I* atoms' one, as $t_{\mathrm{QPC}}/t' \to 0$.

Dependence on the size of the junction. A systematic analysis of junctions of different size also supports our claims of universality of correlation-driven phenomena induced by the MCB process are physically sensible. We compute the conductance through a serie of $\mathcal{J}^{[N_\ell+1]}$ structures, which only differ in the number N_ℓ of correlated layers beyond the *tip* atom in each of the unit structure of the MCBJ, and in Fig. 4.10 we compare the results obtained for $N_\ell = 1, 2, 3, 4$ at $U = 10t'$. The comparison confirms that the functional dependence of G on $d_{\rm QPC}$ is (almost) *independent* of N_ℓ in the tunneling regime ($d_{\rm QPC}/a \gtrsim 1$). It is noticeable that, for $N_\ell > 1$, also the conductance profile in the contact regime ($d_{\rm QPC}/a \lesssim 1$) does not change qualitatively as N_ℓ is increased suggesting that the layers far from the *tip* do not play a relevant role in determining the conductance profile. However, increasing the number of layers N_ℓ determines a quantitative suppression of the conductance with the size of the junction.

We can also consider the layer-resolved local spectral weight at the Fermi energy $\overline{A(0)}$ in all the structures discussed above. In each of the panels of Fig. 4.11 we show $\overline{A(0)}$ for all inequivalent atoms of the corresponding $\mathcal{J}^{[N_\ell+1]}$ structure as a function of the layer label ℓ: here, L and R denote the outermost left and right layers of the structure, respectively, while the *tip* atoms are in the middle. The values of $\overline{A(0)}$ that we show for two values of $t_{\rm QPC}/t'$, are representative of the contact ($t_{\rm QPC}/t' = 1.5$) and tunneling ($t_{\rm QPC}/t' = 0.25$) regimes. As already discussed, one can see, e.g., in the $\mathcal{J}^{[5]}$ structure (upper left panel of Fig. 4.11), in the MCB process, $\overline{A(0)}$ show (almost) no dependence on $t_{\rm QPC}/t'$ in each of the layer atoms, while it is

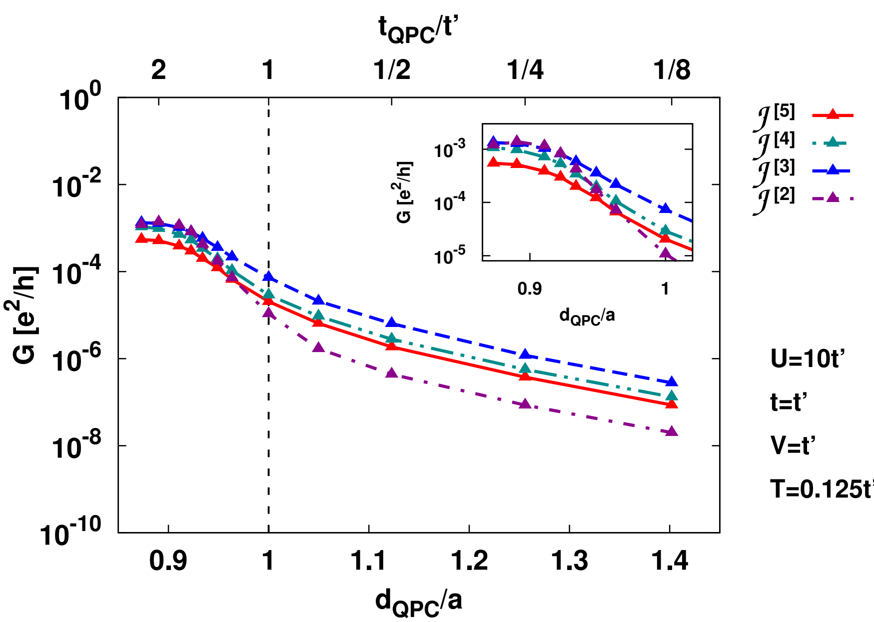

Figure 4.10: Main panel: Comparison between the conductance G through $\mathcal{J}^{[N_\ell+1]}$ structures as a function of $d_{\rm QPC}$ (and $t_{\rm QPC}$), for $t = t'$ and $U = 10t'$, at $T = 0.125t'$. All structures share a universal exponent β in the tunneling regime $d_{\rm QPC}/a \gtrsim 1$, independently on the number of correlated layers N_ℓ, as well as a qualitative behavior in the contact regime $d_{\rm QPC}/a \lesssim 1$, with the exception of the $N_\ell = 1$ case, where finite size effects connected to charge fluctuation in the *layer I* atoms play a relevant role. Inset: highlight of the contact region $d_{\rm QPC}/a \lesssim 1$.

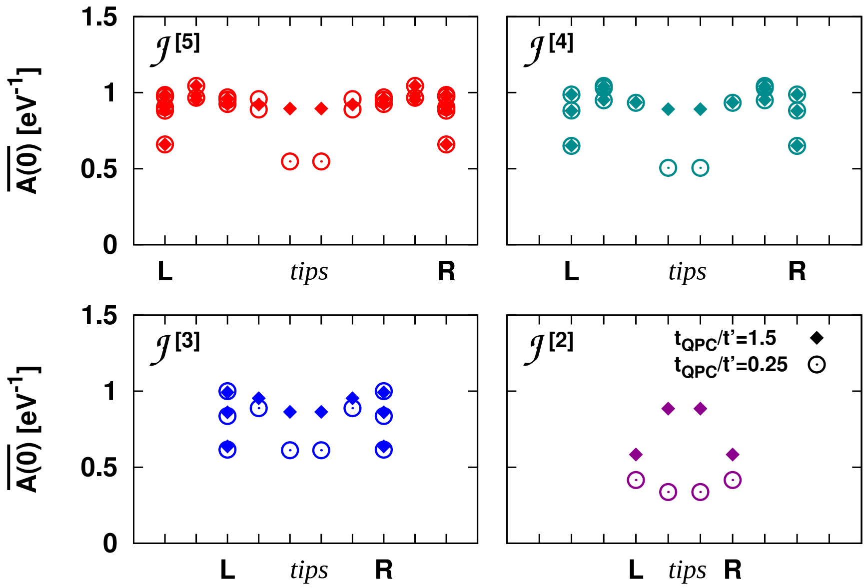

Figure 4.11: Layer-resolved $\overline{A(0)}$ for $\mathcal{J}^{[N_\ell+1]}$ structures consisting of $N_\ell = 1, 2, 3, 4$ correlated layers, for $t = t'$ and $U/t' = 10t'$, at $T = 0.125t'$. The suppression of the *tip* atoms' local spectrum $\overline{A(0)}$ is clearly observed comparing the data for two representative values of $t_{\mathrm{QPC}}/t' = 1.5$ (diamonds) and $t_{\mathrm{QPC}}/t' = 0.25$ (cirles), and it is stabilized as N_ℓ increases.

significantly suppressed in the *tip* atom. A similar behavior is also observed in the $\mathcal{J}^{[4]}$ (upper right panel) and $\mathcal{J}^{[3]}$ structures (lower left panel), yet with a slight tendency of fluctuations in the value of $\overline{A(0)}$ to increase as the size of the MCBJ is reduced. In the extreme case $\mathcal{J}^{[2]}$ (lower right panel), the suppression of $\overline{A(0)}$ with t_{QPC}/t' is sensibly stronger with respect to the other structures, and also affect the *layer I* atoms, which are also the outermost ones, here.

In conclusion, we have shown that faster than exponential suppression of the conductance with the size of the tunneling gap in a MCBJ is an universal feature of those kind of systems. We have ascribed this phenomenon to a Mott-Hubbard crossover involving the lone *tip* atoms, i.e., to the rearrangement of the local electronic structure induced by local electronic correlations. A necessary condition for the phenomenon to manifest requires all the atoms of the structure to be at (or close to) half-filling: as this tendency is supported by the presence of a local Coulomb repulsion, it results in a threshold value of the Hubbard interaction U_c to observe deviation for the expected exponential behavior of the conductance.

We have analyzed the dependence of the phenomenon on the size of the QJ considering several $\mathcal{J}^{[N_\ell+1]}$ structures, which differs only for the number of correlated layers N_ℓ beyond the *tip* atoms in each unit structure of the MCBJ. The general behavior of the conductance and of the layer-resolved local quantities is qualitatively the same in all the structures considered so far and confirms that the phenomenon is a robust feature of MCBJ.

4.3 Outlook

The above analysis rises also some questions which may be worth further investigation, as discussed in some detail in the following.

So far we have not yet mentioned the possibility of including non-local correlations beyond nano-DMFT. Although non-local spatial correlations in the 3-dimensional structures considered above are *not* expected to play a determinant role due to the higher connectivity with respect to, e.g., the Q1D molecules discussed in the previous chapter, the mere suspicion is not enough to discard the possibility. However, the calculation of a $\mathcal{J}^{[N_\ell+1]}$ structure within nano-DΓA requires: (i) to evaluate N_{ineq} inequivalent fully irreducible vertex functions and (ii) to solve the parquet equations in the Hilbert space of the whole system. In this respect, to perform a calculation at the two-particle level *without* the efficiency improvements discussed in Sec. 3.5, requires a prohibitively computational effort, with the present implementation of nano-DΓA.

Another important issue in this direction is including **vertex corrections** in the conductance, which requires the knowledge of the appropriate two-article vertex function. How would the scenario depicted above change? May one expect the features of the conductance, induced by Mott-Hubbard crossover, to be possibly enhanced?

It is interesting to notice that the Mott-Hubbard crossover can also be observed in the "extreme" case of a $\mathcal{J}^{[0]}$ structure, consisting only of the *tip* atoms, i.e., in the **two-impurity Anderson Model** (TIAM), as a function of the hopping parameter. However, the system is particle-hole symmetric and half-filled at *any* value of t_{QPC} (provided $\mu = 0$ as in all cases discussed above) thus favoring the development of the local Mott-Hubbard crossover, although a possible non-trivial dependence on the filling $\langle n \rangle$ can be observed changing the on-site energies of the impurities. Moreover, due to its reduced Hilbert space, compared to all other $\mathcal{J}^{[N_\ell+1]}$ structures, a complete nano-DΓA study of the TIAM, including non-local spatial correlations and vertex corrections to the conductance, would certainly be doable even within the actual numerical implementation of the method.

Another possible application, that we have partly already anticipated, concerns with the possible existence of a **local Mott-Hubbard crossover in a STM**. In particular, how does the rearrangement of the local electronic structure of the scanning tip of an STM induced by a change in the tunneling gap (if any) influence the tunneling current? And more generally: how reliable is the assumption that the real space profile of the tunneling current reflects locally the spectral function of the sample? In this sense, nano-DMFT (and its extensions) can be a suitable tool to shed light on those issues.

Obviously, the nano-DΓA is flexible enough to allow plenty of different applications. However, in order to achieve a quantitative comparison with experiments, an *ab-initio* description of quantum transport through complex *correlated* nanostructure seems to be mandatory, e.g., as an extension of the recently introduced *ab-initio* DΓA [157].

Chapter 5

Effects of size reduction on half-doped manganite $La_{0.5}Ca_{0.5}MnO_3$

Recent experimental evidence suggests the destabilization, upon size reduction, of the antiferromagnetic and charge-orbital order in the half-doped manganite $La_{0.5}Ca_{0.5}MnO_3$, in favor of a ferromagnetic metallic phase. The size-induced changes of the crystal structure are suggested to be responsible for this phenomenon. Hence, we investigate the effects of size reduction merging ab-initio and many-body methods. We perform a DFT+DMFT analysis of the bulk as well as of a defect-free nanocluster in isolation, considering the full structural optimization of the experimentally measured crystal structure. The present theoretical analysis is remarkably compatible with the experimental scenario, and interestingly predicts the correlation-driven stability of the charge-orbital state in bulk $La_{0.5}Ca_{0.5}MnO_3$, even in the absence of long-range magnetic order. We also show size reduction to be different from the application of hydrostatic pressure. Finally, we consider a model finite-size structure, characterized by the optimized parameters of the nanocluster, in order to perform a systematic analysis as a function of system size: preliminary nano-DMFT results suggest the onset of an orbital-selective Mott transition, driven by an external gate voltage.

Manganese oxides, widely known as *manganites*, have been one of the main areas of research within the strongly correlated electrons community since the experimental observation of a colossal magnetoresistance (CMR) effect [232], i.e., the overwhelming relative change of the electrical resistance upon the application of an external magnetic field.
Indeed, manganites are fascinating compounds, and display a complex phase diagram as a function of temperature [233, 234], pressure [235], magnetic field [233, 236], and doping [237], characterized by spin, charge, and/or orbitally ordered phases. The properties of the ground state are determined by the interplay of several competing energy scales, possibly including electron-phonon and Coulomb interaction. Besides many experimental and theoretical investigations carried out for the manganites, the origin of the CMR regime and the nature of the paramagnetic insulating (PI) phase are still unclear. In particular, among the proposed scenarios, it was suggested that this physics may arise due to the presence of intrinsic inhomogeneities

and their strong tendency toward phase separation on the nanoscale [238], or due to the localization of charge carriers through lattice polarons [239, 240, 241, 242]. Hence, the knowledge of the ferromagnetic metallic (FM) phase alone is, *not* sufficient to understand the CMR effect, which requires the knowledge of the competing phases as well.
Recently, another parameter to tune the physical properties of materials, namely size, became part of the scenario: size control is attractive from a technological point of view, as it can be achieved chemically, at relatively low-costs. While for strongly correlated materials, theoretical modeling of size-driven phenomena are rare, we pursued a study of the effect of size reduction on the structural and electronic properties of half-doped manganite $La_{0.5}Ca_{0.5}MnO_3$. The present theoretical analysis, supported by evidences from different experimental techniques suggests size control to be a suitable tool to tune electronic properties for functional material, with a possible impact on technological applications.

5.1 About mixed valence manganites

It is worth to recall some basic properties of the mixed valence manganites, mainly considering the $La_{1-x}Ca_xMnO_3$ compound, in order to establish a basic knowledge and ease the understanding of the theoretical analysis presented in the following. By contrast, a in-depth review on the vast field of manganites is certainly beyond the scope of the present work, and we rather refer to review articles [238, 243] for a deeper reading.
The field of manganites can be dated back to the 1950's, when Jonker and van Santen reported the existence of ferromagnetic metallic (FM) phase in mixed crystals of manganese oxides $LaMnO_3$-$CaMnO_3$, $LaMnO_3$-$SrMnO_3$, and $LaMnO_3$-$BaMnO_3$, [236]. However, the interest of a wide portion of the scientific community was only raised in the 1990s, due to the experimental observation of a large magnetoresistance (MR) effect. Indeed, the relative change in resistivity $|\Delta R/R(0)| = |R(H)/R(0) - 1|$ upon the application for a magnetic field H was way higher than the one observed in artificial magnetic/non-magnetic multilayer systems: up to 60% at room temperature in thin films [233, 234]. The enthusiasm for possible technological application was however weakened by experimental evidences [233] suggesting that a higher MR could be obtained only at the expense of lowering, sensibly below room temperature, the Curie temperature T_C, which determines the onset of the FM phase. At the same time, the relatively high magnetic field necessary to induce the MR achieved, $H \gtrsim 1$ T, in contrast to $H \sim 0.01$ T required by artificial multilayer systems, prevents manganites to be suitable for magnetic data storage applications [238].

Crystal $\&$ electronic structure. The manganese oxides are characterized by the generic chemical formula $R_{1-x}A_xMnO_3$, where R is a trivalent rare-earth-metal element and A is a divalent alkali-earth-metal element. The oxygen is in a O^{2-} oxidation state and the relative fraction of Mn^{4+} and Mn^{3+} is determined by the dopant concentration x, determining the mixed valence nature of the compound. In the ideal **perovskite** cubic unit cell, the rare earth atoms (or the alkali, if any) sit at cube corner positions $(0, 0, 0)$, while the Mn atom sits at body center position $(1/2, 1/2, 1/2)$ and oxygen atoms sit at face centered positions $(1/2, 1/2, 0)$. The five-fold degenerate $3d$ orbitals of the isolated Mn ion are split, due to the mixing with the surrounding oxygen octahedral environment, into two manifolds: the lower energy t_{2g} orbitals (d_{xy}, d_{xz}, and d_{yz}) and higher energy e_g orbitals (d_{3z^2-r2} and $d_{x^2-y^2}$) as predicted within ligand field theory.[1] The t_{2g} manifold lies below the Fermi energy, and the Hund's exchange favors the population of the t_{2g} orbitals with three electrons in a $3/2$ spin state (Hund's rule), while the e_g orbitals contain either one or zero electrons, depending on the valence of the Mn atom: Mn^{4+} are in a d^3 configuration, while Mn^{3+} are in a d^4 configuration. As the energy cost of a double occupation within the t_{2g} manifold is, due to the Coulomb repulsion, larger than the crystal field splitting, the additional electron determines an asymmetric occupation of the electronically degenerate e_g states. As a consequence, the surrounding oxygen octahedra undergoes a static distortion (Jahn-Teller effect) and elongates along the c-crystallographic direction, removing the degeneracy and further lowering the symmetry of the system, in order to minimize the energy of the system. See also the upper panels of Fig. 5.1 for a schematic representation of the crystal field and Jahn-Teller splittings.

Onset of charge, spin $\&$ orbital ordered phases. Each manganite compound displays a complex phase diagram, determined by the competition of structural and electronic phases: the termperature versus Ca doping phase diagram of $La_{1-x}Ca_{1-x}MnO_3$ is shown in the lower panel of Fig 5.1 for the sake of copleteness.

As already mentioned, the FM phase plays an important role for the realization of a MR effect (an explanation is provided in the related paragraph at the end of this section) and it has been widely investigated in the past. Its origin is conventionally owed to the **double-exchange** mechanism [244, 245], which allows the charge to move in manganites by the generation of a spin polarized state. The Mn e_g orbitals are delocalized due to a strong hybridization with the O $2p$, and charge transfer is hence allowed via the following process:

$$\mathrm{Mn}^{3+}_{\uparrow}\mathrm{O}_{\uparrow\downarrow}\,\mathrm{Mn}^{4+} \longrightarrow \mathrm{Mn}^{3+}_{\uparrow}\mathrm{O}_{\downarrow}\,\mathrm{Mn}^{3+}_{\uparrow} \longrightarrow \mathrm{Mn}^{3+}\mathrm{O}_{\uparrow\downarrow}\,\mathrm{Mn}^{3+}_{\uparrow}, \tag{5.1}$$

i.e., the initial and final states are connected by a virtual state due to tunneling processes through the oxygen bridging nearest neighbor Mn atoms. The effective tunneling amplitude t for the double-exchange process is proportional to the Mn $3d$ and O $2p$ overlap: $t \propto |t_{dp}|^2/\Delta$, where Δ is the charge transfer energy between the configurations in the process (5.1).
The t_{2g} orbitals, on the contrary, do not hybridize with the O's p and are localized. In the presence of a local Hund's exchange $\mathcal{J}$ between the e_g and t_{2g} electrons on the Mn atoms, an effective FM exchange develops between the localized t_{2g} spins belonging to nearest neighbor

[1] The ligand electron pair, located a the edges of the O octahedra repel with the electrons in the d orbitals of the Mn: hence, the d-orbitals pointing toward the ligands (i.e., the e_g) are higher in energy with respect to the ones pointing between them (i.e., the t_{2g}).

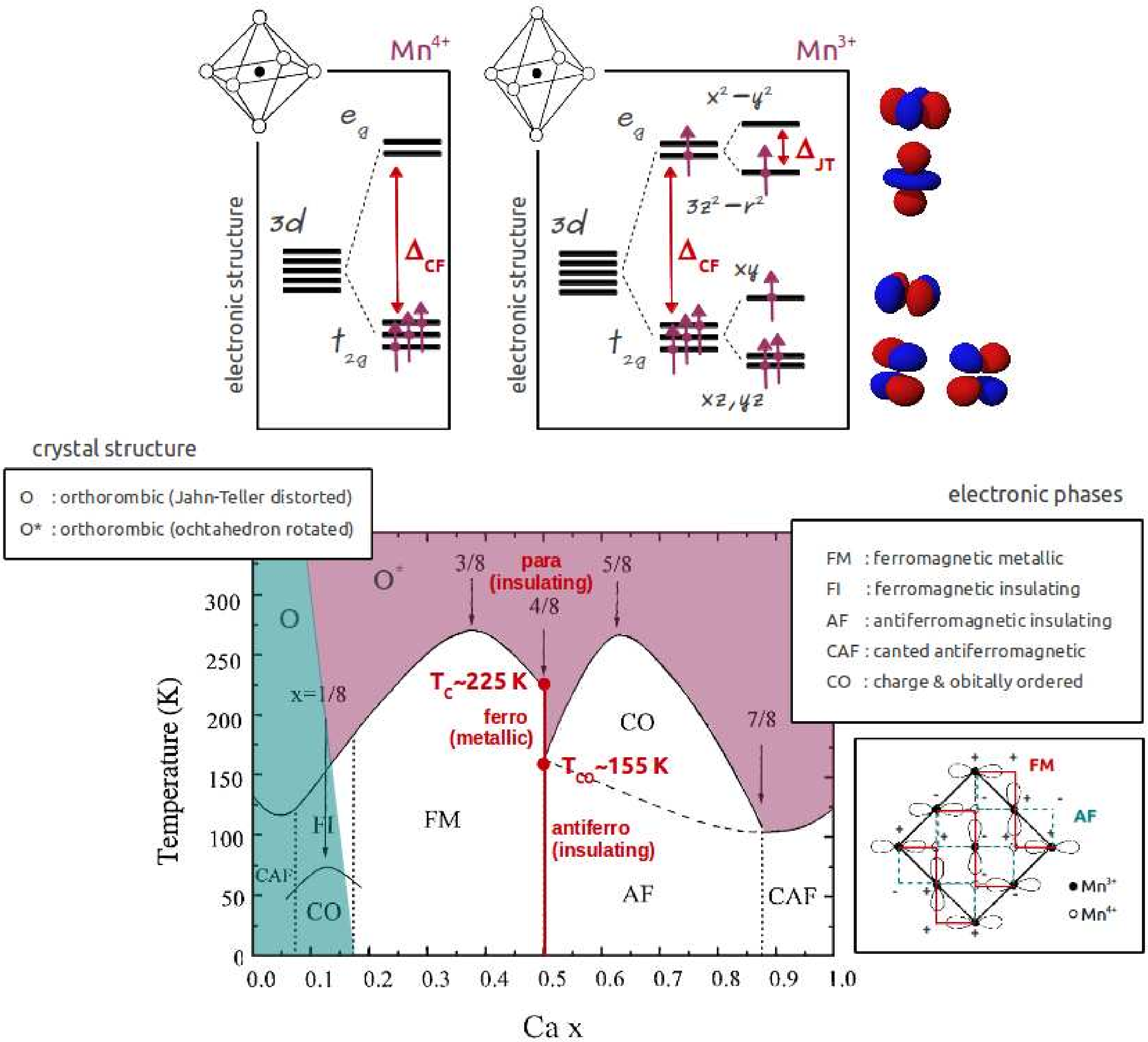

Figure 5.1: Upper panels: crystal field splitting of the five-fold degenerate $3d$ manifold into lower t_{2g} and higher e_g levels. Mn^{3+} atoms, due to the asymmetric filling of the e_g manifold, are Jahn-Teller active, and undergo an elongation of the MnO_6 octahedron, determining further splittings in both manifolds. The $3d$ orbitals are sketched on the right-hand side: the red/blue color coding indicates positive/negative charge, respectively. Lower panel: temperature versus Ca doping x phase diagram for the $La_{1-x}Ca_xMnO_3$ compound, the colors highlight the different crystal structures, while the electronically ordered phases are separated by black (solid or dashed) lines. The red solid line is a guide to the eye tracing the temperature evolution of the half-doped compound from a high-temperature paramagnetic insulating phase, through a FM metallic one (below T_C) to an AF insulating and CO state (below T_{CO}). The right-hand side inset shows the complex charge, orbital, and magnetic order in the CO phase. Adapted after Ref. [238].

Mn, and it is mediated by the hopping processes of the itinerant e_g electrons. Indeed, in the range $0.2 < x < 0.5$, a stable FM phase is observed also in the bulk $La_{1-x}Ca_xMnO_3$ compound.

However, many manganite compounds, including $La_{1-x}Ca_{1-x}MnO_3$, display also features which indicate strong deviations from double-exchange behavior. The charge and orbitally ordered state observed in the bulk half-doped manganite $La_{0.5}Ca_{0.5}MnO_3$ is one of the fascinating phenomena exhibited by those compounds. Bulk $La_{0.5}Ca_{0.5}MnO_3$ displays a charge-ordering (CO) transition at $T_{CO} = 155$ K, associated with a real space ordering of Mn^{3+}/Mn^{4+} species in a $1:1$ pattern. It is accompanied by orbital ordering (OO) and a structural change from orthorhombic to monoclinic symmetry, giving rise to an insulating ground state [247, 248, 249, 250, 251]. Below 155 K, the crystal structure is of monoclinic symmetry ($P2_1/m$) and an AF order sets in [252]. The magnetic structure is characterized by the so-called ‘‘CE’’ order, consisting of zigzag FM chains that are coupled AF in the crystallographic ac plane. The ac planes are stacked AF along the crystallographic b-direction. A noteworthy feature of the crystal structure concerns the Jahn-Teller distortions: while Mn1 atoms display sizable distortions, with two long bonds along the FM chain and four short bonds, the Mn2 atoms on the zigzag chains display instead negligible distortions, with nearly similar Mn-O bond lengths. Moreover, the average Mn2-O distance is smaller than that of Mn1-O [247].

Being at the edge of a strongly first order transition upon cooling [246], and bridging two phase characterized by completely different order, the CE and the FM ones, the half-doped $La_{0.5}Ca_{0.5}MnO_3$ represents a peculiar system susceptible to external perturbations. Indeed, the insulating CO state has been reported to be destabilized, in favor of a FM metallic phase, by various means, including magnetic field [253], doping, biaxial strain, pressure [254], and electric field [255]. Recently, a few experimental studies on $La_{0.5}Ca_{0.5}MnO_3$ [256, 257, 259], as well as on $La_{0.9}Ca_{0.1}MnO_3$ [258] and $Pr_{0.5}Ca_{0.5}MnO_3$ [259], reported that the destabilization of the CO state can be achieved even through size reduction. The route through size control also opens up the possibility of exploring the tunability of the CO-OO state and of the associated MIT between the FM and CE ordered phases.

The origin of MR effect: insights from multilayer systems. While the underlying mechanism controlling the CMR in the CO AF phase of half-doped in manganites is still a matter of debate [238], it is interesting to discuss the MR effect in the context of trilayer systems, e.g., following the simple arguments of Ref. [261]. It shows that the coexistence of FM and AF tendencies may give rise to the MR effect, and suggests a similar behavior may be determined by the destabilization of the CO order in the half-doped manganite $La_{0.5}Ca_{0.5}MnO_3$.

It is well-known that impurities in metals are screened by the surrounding conduction electrons, inducing oscillations in the electron density that decays as a function of the distance from the impurity (Friedel’s oscillations). Analogously, the presence of a magnetic impurity induces decaying oscillation in the spin polarization of the electron density, which can influence the spin orientation of a neighboring impurity. Hence, the exchange coupling between the impurity magnetic moments will result into a FM or AF alignment, depending on their relative distance.

The discovery of AF coupling between the iron layers of a Fe/Cr/Fe trilayer system [260] can be remarkably explained in this terms, where the thickness of the non-magnetic (NM) layer affects the nature of the magnetic exchange.
The presence of FM iron layers stacked AF, i.e., with an alternating magnetization, determines a MR effect. below we provide an intuitive explanation of the phenomenon restricting, for the sake of simplicity, to a model FM/NM/FM trilayer system.
Let us consider the electrical current flowing through the system, carried by the conduction electrons. In a FM background, the resistance experienced by spin up and spin down carriers within a given layer will differ, as well as the resistance originating by scattering processes at the FM/NM interface. On the other hand, within the NM layer, electrons in both spin channels experience the same resistance, but generally this is low compared to the one within the FM layers, and here will hence be neglected. For the sake of simplicity we will include the resistance through the FM layer and due to the scattering at the interface in the effective parameters $R_{\uparrow}$

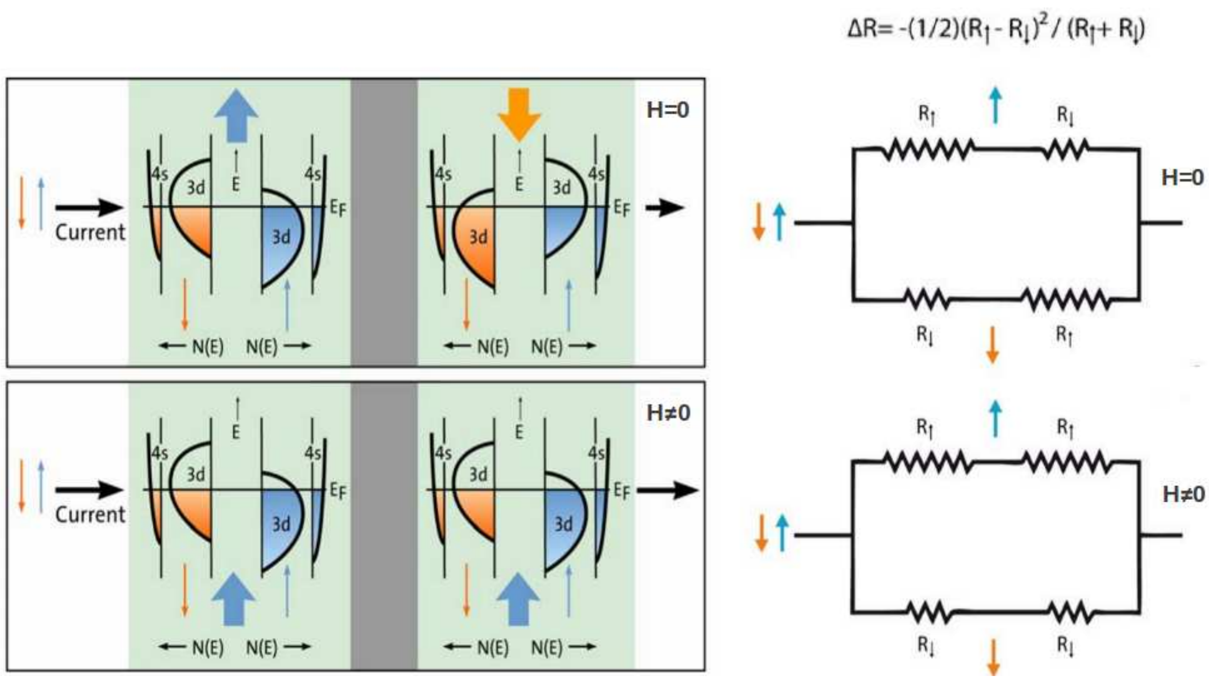

Figure 5.2: Left panels: schematic illustration of the electronic structure of a trilayer system, made of two FM layers (light green) separated by a NM layer (grey). Sample DOS $N(E)$ of $3d$ and $4s$ orbitals for the spin up (blue) and spin down (orange) components are shown: the magnetization caused by an excess population in one of the the spin channels is indicated by the thick arrows above/below the DOS. At zero magnetic field ($H = 0$, upper panel) the FM layers are stacked AF, i.e., with magnetization pointing in opposite direction. In the presence of an external magnetic field ($H \neq 0$, lower panels) each FM layers have the same polarization, inducing a negative MR $\Delta R = R(H) - R(0)$. Right panels: circuit representation of the trilayer system. In a FM background the effective parameter R_σ taking into account the resistance due to charge transport within the FM layer and the one originating by scattering processes at the FM/NM interface will be different for the two spin components. After Ref. [261].

and $R_\downarrow$, labeling the resistance in the different spin channels.

Under those conditions one can calculate the overall resistance experienced by a current flowing through the system, which is conveniently obtained considering the spin up and spin down components of the current separately. In the configuration in which the FM iron layers are AF stacked, which is realized in the absence of an external magnetic field, $H = 0$ (upper panels of Fig. 5.2) the spin up component of the current will experience a resistance $R_\uparrow$ (transport within the left-hand side FM layer and through the NM/FM interface) and a resistance $R_\downarrow$ (transport through the NM/FM interface and within the right-hand side FM layer), i.e., it experiences an overall resistance $R_\uparrow + R_\downarrow$. Analogously, for the spin down component the magnetic environment results to be ''reversed'', but the overall resistance that it experiences is $R_\downarrow + R_\uparrow$, i.e., identical to the spin up component. Combining the resistances in parallel, it yields an overall resistance at zero field $R(0) = \frac{1}{2}(R_\downarrow + R_\uparrow)$. In the presence of a magnetic field H instead, the FM iron layers are FM stacked (lower panels), so that the spin up and spin down components of the current experience a resistance $2R_\uparrow$ and $2R_\downarrow$, respectively, yielding an overall parallel resistance $R(H) = 2R_\uparrow R_\downarrow/(R_\uparrow + R_\downarrow)$. The MR is, hence determined by $\Delta R = R(H) - R(0) = -\frac{1}{2}(R_\uparrow - R_\downarrow)^2/(R_\uparrow + R_\downarrow)$, so that the larger the difference between the resistances of the individual spin components, the higher the MR.

As already discussed, charge transport in manganites is associated to the double-exchange process, and it is realized by effective Mn-Mn hopping processes through the bridging O atoms. One may hence expect a similar behavior: in the AF phase the system is insulating, and the resistance is huge, while in the FM metallic one, carriers are mobile and experience a lower resistance. The main issue relies on the possibility to trigger the transition, e.g., by the destabilization of the AF insulating phase by means of a reasonably weak external magnetic field, at a temperature which is easily accessible for applications (most likely room temperature). While in the bulk those conditions are not met, the recently reported effect of size reduction include, e.g., a lowering of the field required to melt the CO ordering [259].

5.2 Realistic model for manganites

The onset of the CE magnetic ordering in doped manganites cannot be explained within the double exchange model, and more recent theoretical analyses had invoked an important role played by the Jahn-Teller distortions, occurring at the Mn^{3+} ions, together with the Coulomb interaction [262, 263, 264]. Hence, in the following we study the effect of size reduction on the CO-OO state of $La_{0.5}Ca_{0.5}MnO_3$ (hereafter LCMO) by using a combination of DFT and DMFT: by extracting an *ab-initio* bandstructure through the self-consistent solution of th Kohn-Sham equations, one is able take into account, e.g., Jahn-Teller distortions, while DMFT allows to include strong electronic correlations beyond DFT, entailed by local Coulomb interactions.

For the DFT calculations, we used a combination of two methods: (a) plane-wave-based pseudopotentials and (b) muffin-tin orbital (MTO) based on linear muffin-tin orbital [127] and Nth order MTO (NMTO) [128]. For (a) we used projected augmented wave (PAW) pseudopotentials with an energy cutoff of 450 eV and performed calculation within a spin polarized generalized gradient approximation (GGA) [125] as implemented in the Vienna *ab-initio* Simulation Package (VASP) [265, 266, 267, 268]. From a self-consistent DFT calculation, a low-energy model, consisting of two e_g orbitals per Mn ion, was constructed using the NMTO **downfolding** technique. The following Hubbard Hamiltonian was defined in the downfolded NMTO basis

$$\begin{aligned}\mathcal{H} = &\sum_{imjm'}\sum_{\sigma\sigma'} t_{imjm'} c^{\dagger}_{im\sigma} c_{jm'\sigma'} - \Delta\epsilon \sum_{im}\sum_{\sigma} n_{im\sigma} \\ &+ U \sum_{im} n^{\dagger}_{im\uparrow} n_{im\downarrow} + \sum_{imm'}\sum_{\sigma\sigma'} (U' - J\delta_{\sigma\sigma'}) n_{im\sigma} n_{m'\sigma'} - \mathcal{J} S \sum_{im} (n_{im\uparrow} - n_{im\downarrow}),\end{aligned} \tag{5.2}$$

where t_{imjm} are the elements of the one-particle GGA Hamiltonian in the downfolded NMTO Wannier orbitals; the Coulomb interaction between e_g electrons is parametrized in terms of an intra-orbital Coulomb interaction $U=5$ eV and a Hund's exchange $J=0.75$ eV, taken from the literature [269] and represent realistic values for doped manganites. In case degenerate orbitals, e.g. the t_{2g} orbitals in a cubic symmetry, the Hamiltonian has to be invariant under orbital rotation, yielding the relation $U' = U - 2J$, which is, however, often considered a sensible choice also when the degeneracy is only fulfilled approximately [121], as in the present case, where the e_g are split by the Jahn-Teller crystal field. Furthermore, the e_g orbitals are coupled to a (classical) spin representing the half-filled and localized t_{2g} electrons by $\mathcal{J}=1.35$ eV [262]. Hamiltonian (5.2) was solved within DMFT(HF-QMC) in the same spirit as previously carried out in Ref. [262] in the context of pure $LaMnO_3$. Finally, $\Delta\epsilon$ is the parameter that takes into account the site-dependent double-counting corrections [129] (see below).

With respect to the standard DFT+DMFT method, the present case exhibits further complications. Among the eight Mn atoms contained in the LCMO monoclinic unit cell, one can identify three **locally inequivalent** types of **Mn atoms**: there are two pairs of ‘‘trivalent’’ (i.e., Mn^{3+}-like) atoms, Mn1(1) and Mn1(2), and four ‘‘tetravalent’’ (i.e., Mn^{4+}-like) Mn2 atoms. Any exact treatment of non-local correlation effects within the LCMO unit cell, e.g., in the same fashion as in Ref. [141] in the context of monoclinic VO_2, is hardy feasible. Therefore, we employ a *two-fold approximation*: we neglect the inter-orbital elements of the local Green's function at each Mn site, and we also neglect non-local spatial contributions between Mn sites i and j within the unit cell. Hence, for each of the inequivalent Mn atoms one can define an auxiliary two-orbital AIM. The solution of each auxiliary impurity problems yields a purely local self-energy, as shown in Fig. 5.3. Considering that, within this approximation, to each equivalent atoms corresponds the same local self-energy, one can define a matrix self-energy for the whole unit cell, which is diagonal both in the site and the orbital indexes. The self-energy is used to update the Green's function and the previous steps are iterated till self-consistency. This procedure formally corresponds to the multi-orbital generalization of the approximation scheme already introduced in Sec. 2.4 in the case of finite systems, applied here to the LCMO unit cell.

Moreover, due to the presence of inequivalent Mn atoms, it was necessary to explicitly consider a *site-dependent* **double counting corrections**, in terms of a site-dependent density and an average Coulomb interaction defined as [121]

$$\Delta\epsilon \rightarrow \tilde{U} = \frac{U + (M-1)U' + (M-1)(U-3J))}{(2M-1)}, \tag{5.3}$$

where M is the number of orbitals in the low-energy model. In the present case $M=2$, as we restrict ourselves to the Mn e_g orbitals, and $U' = U - 2J$ due to (approximate) cubic symmetry of the perovskite unit cell, resulting in an averaged interaction $\tilde{U} = U - \frac{5}{3}J$ which takes into account the mutual screening of the e_g orbitals.

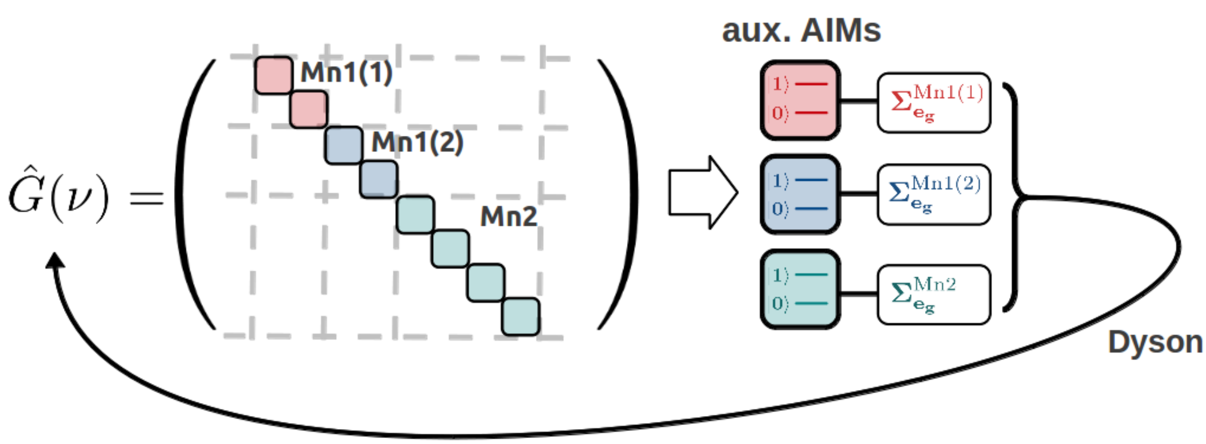

Figure 5.3: Approximate scheme employed to treat the inequivalent Mn atoms within the LCMO unit cell. Each type of locally inequivalent Mn atoms, i.e., Mn$1(1)$, Mn$1(2)$, and Mn2, is mapped onto an auxiliary two-orbital AIM, labeled $|0\rangle$ and $|1\rangle$ and representing the NMTO downfolded basis of the e_g orbitals. The solution of each auxiliary AIM yields a of local 2×2 (diagonal) self-energy matrices $\Sigma^i_{e_g}(\nu)$: collecting them and exploiting their symmetry relations yields a self-energy matrix for the whole unit cell, which is used to update the Green's function by means of the Dyson equation.

5.2.1 GGA+DMFT results: bulk & nano structure

The results presented in the following, concerning the size-control of the charge-orbital ordering of LCMO are based on the paper published in the APS Journals ''Physical Review Letters'': PRL **107**, 197202 (2011) [272].

In the following we show how we performed the *ab-initio* analysis of bulk and nanoscale LCMO, in order to compare the systems' crystal and electronic structure in a physically sensible context. The spin polarized calculations suggest the changes in the crystal structure, due to size reduction, to be held responsible for the destabilization of the CE phase in favor of a FM metallic one, already within DFT. Including electronic correlations within DMFT indicates a trend toward CO and OO even in the absence of long-range order. Finally, we show the structural and electronic changes, induced by the application of hydrostatic pressure, to lead to a different scenario compared to the one determined by the effects of size reduction.

Crystal structure *ab-initio* & comparison with experiments. In order to build the monoclinic unit cell of LCMO, we considered the experimentally measured structure [247], henceforth referred to as $\mathcal{S}_{\text{expt}}$, and we performed the structural optimization, yielding the structure referred to as $\mathcal{S}_{\text{bulk}}$, in order to compare with parameters of $\mathcal{S}_{\text{model}}$ (see below) on the same footing. The performed DFT calculations showed the CE insulating phase to be stable by 18 meV/f.u. over the FM metallic solution. The calculated electronic structure in terms of density of states and magnetic moments are found to be in good agreement with those reported previously in literature [270].

In order to study the problem of nanoscale LCMO, we first created a large supercell in the monoclinic structure, from which a cluster of diameter $2-3$ nm having approximate spherical shape was cut out (cf. Table 5.1). In the construction of the clusters, care has been taken to maintain the stoichiometry as closely as possible. For this structure, referred to as $\mathcal{S}_{\text{nano}}$, we carried out a full structural optimization: the positions of the atoms were relaxed towards equilibrium, using the conjugate gradient technique until the Hellmann-Feynman forces [271] became less than 0.001 eV/Å. Following this procedure, the 2 nm cluster contains a total of 370 atoms and the 3 nm cluster contains a total of 700 atoms, pushing it to the limit of our DFT structural optimization. In order to perform the DFT calculation on the cluster, a simple cubic supercell with periodic boundary conditions was used, where two neighboring clusters were kept separated by 10 Å, which essentially makes the interaction between cluster images negligible.

The considered DFT cluster sizes are smaller than the experimental realizations [256] of sizes 15 nm. Hence only the inner region of the above constructed clusters of $2-3$ nm size is expected to mimic the prototypical behavior of the experimentally studied clusters. In order to understand the consequences of the size-controlled structural changes for such relatively larger clusters, we hence constructed a model bulk system, which we refer to as $\mathcal{S}_{\text{model}}$. It is built out of the structural units belonging to the innermost core and the next to the core layer of the optimized LCMO in the nanoscale geometry $\mathcal{S}_{\text{nano}}$ and subsequently imposing the symmetry considerations, as shown in detail in Table 5.1. The construction of $\mathcal{S}_{\text{model}}$ leads to consideration of the local oxygen environments around Mn atoms as well as the tilt and rotation connecting two MnO_6 octahedra, the same as that in the core region of $\mathcal{S}_{\text{nano}}$.

The **lattice parameters** and the Mn-O bond lengths of $\mathcal{S}_{\text{model}}$ are compared to the bulk structure $\mathcal{S}_{\text{bulk}}$ in Table 5.2. The detailed structural information can be obtained in the supplemental material (SM) of Ref. [272]. We find that the lattice parameters of $\mathcal{S}_{\text{model}}$. show substantial reduction compared to those of $\mathcal{S}_{\text{bulk}}$. The change in the a parameter appears to be the largest with a change of about 0.19 Å, with moderate changes in the b and c parameters, of 0.09 Å. Qualitatively, this trend of reduction in lattice parameters and also the nature of reduction agree very well with the crystal structure data extracted from x-ray diffraction of nanoclusters of LCMO of 15 nm size (cf. Fig. 4 in Ref. [256]). We note that the reduction in lattice parameters in the model structure gave rise to about 6% reduction in the volume compared to that of the bulk system; the first experiments [256] report a 2% reduction. In this respect, let us notice that the 6% reduction was obtained for $\mathcal{S}_{\text{model}}$ constructed out of $\mathcal{S}_{\text{nano}}$ of 3 nm, while a similar procedure for $\mathcal{S}_{\text{nano}}$ of 2 nm gave rise to larger volume reduction (8%): this indicates that the volume reduction increases upon decreasing cluster size, justifying the difference between the obtained volume reduction on the $2-3$ nm cluster and the experimentally observed volume reduction on the 15 nm cluster. One of the important structural quantities is the **orthorhombic strain**:

$$\text{OS}_{\parallel} = 2\frac{(c-a)}{(c+a)}, \qquad \text{OS}_{\perp} = 2\frac{(a+c-\sqrt{2}b)}{(a+c+\sqrt{2}b)}, \tag{5.4}$$

where $\text{OS}_{\parallel}$ gives the strain in the ac plane, while $\text{OS}_{\perp}$ is that along the b axis. For $\mathcal{S}_{\text{bulk}}$, the orthorhombic strain is highly anisotropic with a negligible value of $\text{OS}_{\perp} \approx 0.002$ and a high value of $\text{OS}_{\parallel} \approx 0.021$. For $\mathcal{S}_{\text{model}}$, we find instead the orthorhombic strains to be comparable: $\text{OS}_{\perp} \approx 0.02$ and $\text{OS}_{\parallel} \approx 0.01$. This trend is also in very good agreement with experimental results by Sarkar *et al.* [256], where the where the lattice parameters have been inferred by powder X-ray diffraction (XRD) measurements.

However, the experimental scenario is not lacking ambiguity: while the suppression of the CO state upon size reduction it is a well established phenomenon, its origin is not yet clear. Independent experimental investigations [274, 275, 276] reported that the lattice parameters and unit cell volume are slightly larger than in the bulk counterparts, and that the room temperature $Pbnm$ perovskite structure, lattice distortion, Mn-O distances, and octahedral tilt are practically unaffected by the particle size. The inconsistency of the experimental data point to the difficulties connected to the experimental synthesis of manganite clusters, e.g., impure phases, grain boundaries, and non-stoichiometry. It is indeed known that variation from perfect stoichiometry may strongly affect the magnetic properties of both bulk and nano samples, see e.g., Ref. [276] and references therein.

However, the present theoretical calculation is devoid of these difficulties and unbiased toward any experimental structure, as we perform a complete geometrical optimization of a perfectly stoichiometric nanocluster. The theoretical optimization, carried out at zero temperature, shows structural changes involving (i) a reduction in volume and (ii) a change in orthorhom-

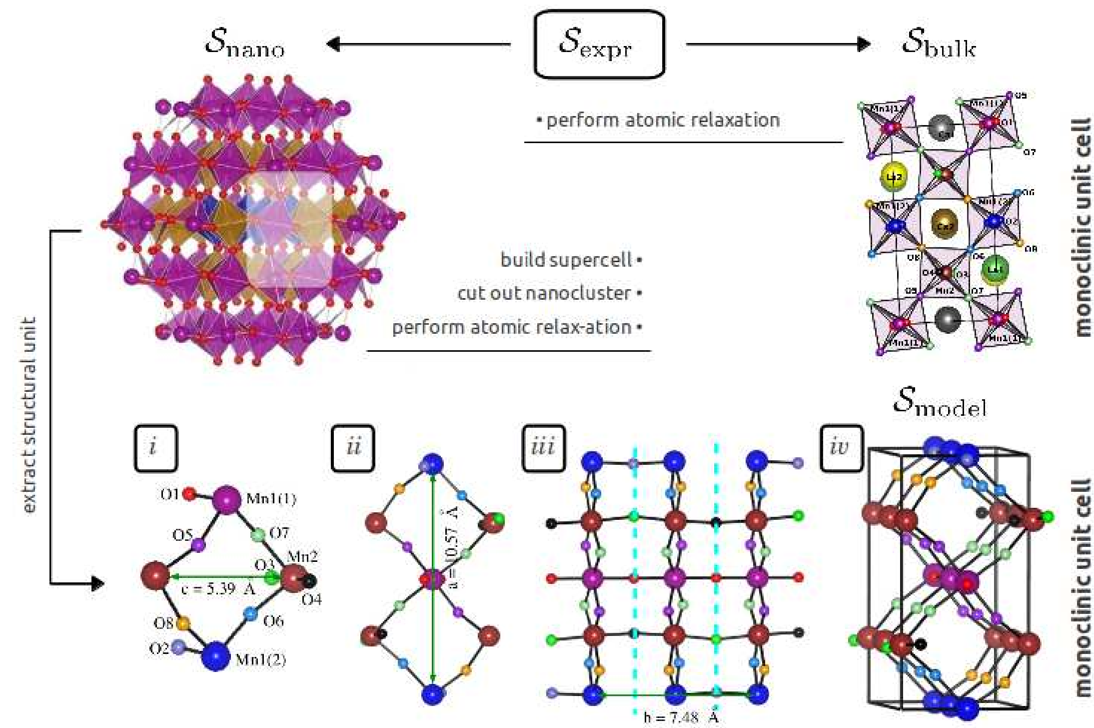

Table 5.1: Construction of the model structures analyzed within DFT. As a starting point the experimentally measured LCMO structure $\mathcal{S}_{\rm expr}$ was considered. A structural optimization was performed to obtain the lattice parameters for the bulk monoclinic LCMO structure $\mathcal{S}_{\rm bulk}$; the different inequivalent La, Ca, Mn and O atoms are labeled accordingly. Definition $\mathcal{S}_{\rm nano}$: an approximately spherical LCMO cluster of $2-3$ nm size was cut out of a $\mathcal{S}_{\rm expr}$ supercell, and a structural optimization was performed; the MnO_6 octahedra belonging to the outermost surface layer, next to the surface, and core region, are shown in magenta, brown and blue, respectively. As only the core region of the $2-3$ nm size nanostructure can be considered representative of the experimental 15 nm cluster, a structural unit was extracted from the shaded region of $\mathcal{S}_{\rm nano}$ and used to build $\mathcal{S}_{\rm model}$: (i) structural unit chosen from S_{nano} already defines the lattice parameter, c; (ii) applying inversion about Mn1(1) atom, the lattice parameter a is defined; (iii) applying mirror reflections passing through apical oxygens (marked as dashed lines) the lattice parameter b is defined; (iv) the fully constructed unit cell of $\mathcal{S}_{model}$. La/Ca atoms are not shown for clarity. Adapted after Ref. [272].

Table 5.2: Lattice parameters and Mn-O bond lengths (in Å) of $\mathcal{S}_{\rm model}$ in comparison to $\mathcal{S}_{\rm bulk}$. The entries for the Mn-O bond length from left to right correspond to that along the FM chain, between the FM chains, along the b-direction, and the average. In the case of Mn2-O the average distance with the inequivalent O atoms along each given direction is taken [272].

	$\mathcal{S}_{\rm bulk}$				$\mathcal{S}_{\rm model}$			
Lattice parameters	$a=5.47$, $b=7.58$, $c=5.48$				$a=5.28$, $b=7.49$, $c=5.39$			
Mn1(1)-O	2.18	1.93	1.94	2.02	1.97	1.92	1.91	1.93
Mn1(2)-O	2.09	1.92	1.94	1.98	1.97	1.92	1.91	1.93
Mn2-O	1.92	1.92	1.94	1.93	1.92	1.88	1.92	1.91

bic strain from an highly anisotropic one in bulk to a nearly isotropic one on the nanoscale. Those structural changes are indeed is in qualitative agreement with the experimental findings in Ref. [274] in which the low-temperature structural data, which are the relevant ones for the CO phase, differ significantly between the bulk and the nanoclusters. It confirms that our constructed model structure captures the essential structural changes in the nanoscale surprisingly well, and proves that the role of surface beyond what is already taken into account in construction of the model structure is small.

Destabilization of CO order. Next, we calculated the electronic structure for $\mathcal{S}_{\text{model}}$ and compared it with that of $\mathcal{S}_{\text{bulk}}$. In order to understand the following results, it is useful to recall that the main result from the analysis of the crystal structure is the reduced difference between the average Mn1-O and Mn2-O bond lengths in $\mathcal{S}_{\text{model}}$ than in $\mathcal{S}_{\text{bulk}}$. Hence, one expects that the charge disproportionation (CD) between Mn1 and Mn2 sites to decrease in $\mathcal{S}_{\text{model}}$. Furthermore, we note that for $\mathcal{S}_{\text{bulk}}$ the difference between the longest and the shortest Mn-O bond-lengths is large for Mn1 and tiny for Mn2. This gives rise to the crystal field splitting Δ between the two Mn e_g states, Mn $3z^2$-r^2 and Mn x^2-y^2, as large as 0.63 eV for Mn1 sites and less than 0.02 eV for the Mn2 sites. In contrast for $\mathcal{S}_{\text{model}}$, the bond length differences are much more similar for both types of Mn sites. This is reflected in similar Δ's for the nanomodel, i.e., 0.15 eV for Mn1 sites and 0.10 eV for Mn2 sites. Together these two effects weaken CO as well as OO in $\mathcal{S}_{\text{model}}$. This ordering is important to stabilize the AF structure found in the bulk. Indeed, with charge and orbital ordering weakened, we find FM to be stable by 20 meV in $\mathcal{S}_{\text{model}}$, in accordance with the experimental observations [256, 257].

The microscopic origin of the size-controlled transition from AF to FM, therefore, can be traced back to the size-induced structural changes. The corresponding **density of states** (DOS) of $\mathcal{S}_{\text{bulk}}$ with AF ordering of Mn spins, in comparison to that of $\mathcal{S}_{\text{model}}$ with FM ordering, are shown in Fig. 5.4. Considering the DOS for $\mathcal{S}_{\text{bulk}}$, the crystal field splitting due to the Jahn-Teller distortions between Mn $3z^2$-r^2 and Mn x^2-y^2 is clearly seen. In the majority spin channel, Mn $3z^2$-r^2 states at the Mn1 site are more occupied than the Mn $3z^2$-r^2 states at the Mn2 site, giving rise to CD between Mn1 and Mn2. We also find OO at the Mn1 sites with a preferential occupation of Mn $3z^2$-r^2 over Mn x^2-y^2. The CO, although incomplete, together with the AFM spin ordering gives rise to an insulating solution with a small but finite gap at E_F already at the DFT level. Considering the DOS of $\mathcal{S}_{\text{model}}$, we find that the splitting between Mn $3z^2$-r^2 and Mn x^2-y^2 is less pronounced and the Mn1 d and Mn2 d states to be similar. The reduced Δ together with the increased bandwidth, compared to the bulk structure, drives $\mathcal{S}_{\text{model}}$ to a metallic phase with a finite density of states at the Fermi energy E_F. The increased bandwidth is caused by the reduction in volume as well as by the FM ordering which allows hopping processes within a double exchange mechanism [244, 245].

Role of electronic correlations. So far we have discussed the effect of the changes of the crystal structure, in particular in terms of the distortions of the oxygen environment, due to size reduction. Those effect have a direct influence on the electronic structure of the system

and seem to play a determinant role in the destabilization of the charge, orbital and magnetic order observed in the bulk. However, as the electronic configuration of the Mn atoms involve an open $3d$ shell, strong correlation effects are naturally expected, and their relevance, e.g., in determining the nature of the pressure-induced MIT or pure $LaMnO_3$ [262] or in CMR spectra in doped compounds [263] has been recently shown.
While at the nanoscale spatial confinement, and possibly the lack of a proper metallic screening of the Coulomb interactions, may enhance correlation effects, the interplay between electronic correaltions and the lattice distortions is highly non-trivial. Hence, it is reasonable to investigate the role of electronic correlation in the absence of long-range magnetic order, i.e., considering a paramagnetic ground state. The analysis of the broken symmetry phase is more complicated: besides requiring the implementation of *ad hoc* self-consistent DMFT equations [98], in the present case one has also to be careful to properly take into account the presence of the inequivalent kinds Mn sites within the unit cell, and is therefore postponed to future works.

In order to take into account the **influence of the missing electronic correlations** in GGA, we performed (paramagnetic) DMFT calculations for both $\mathcal{S}_{\text{bulk}}$ and $\mathcal{S}_{\text{model}}$ structures. We considered the low-energy Mn e_g-only Hubbard Hamiltonian (5.2), obtained by menas of the NMTO downfolding technique from a apramagnetic GGA calculation.

Let us consider $\mathcal{S}_{\text{bulk}}$. The **orbital occupations** of the three types of inequivalent Mn sites, listed in Table 5.3: already at the DFT level (in brackets) the two types of inequivalent Mn1 sites are more occupied than the Mn2 sites. In this respect, calculations performed for the half-doped manganite $Pr_{0.5}Ca_{0.5}MnO_3$ by Anisimov *et at.* [273] showed negligible CD. The CD

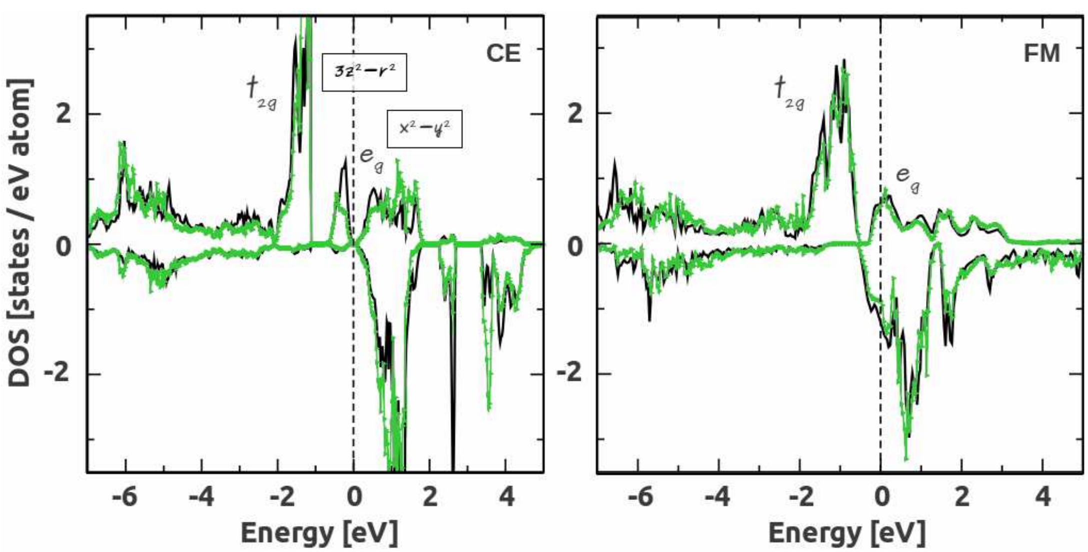

Figure 5.4: GGA spin-polarized DOS, projected onto Mn1 d (black solid line) and Mn2 d (green solid line) states calculated for the CE insulating phase of $\mathcal{S}_{\text{bulk}}$ (left panel) and the FM metallic phase of $\mathcal{S}_{\text{model}}$ (right panel). The positive and negative values corresponds to the majority and minority spins, respectively. The zero of energy is set at E_F. Adapted after Ref. [272].

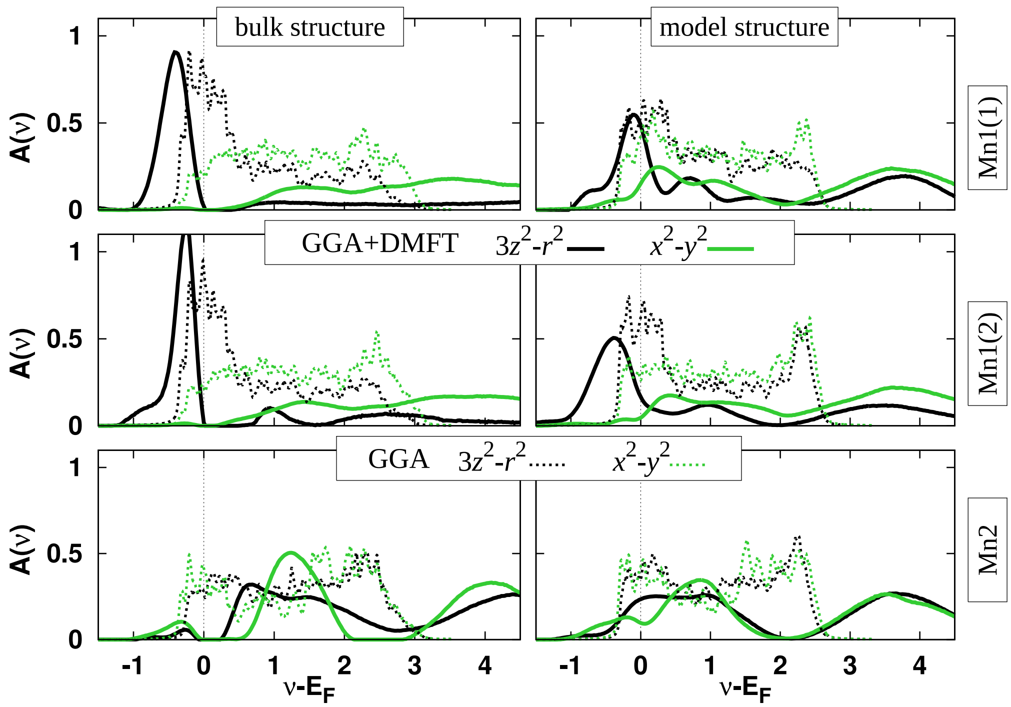

Figure 5.5: GGA+DMFT spectral function $A(\nu)$ (solid lines) for the e_g states of three inequivalent classes of Mn atoms, for the $\mathcal{S}_{\text{bulk}}$ and $\mathcal{S}_{\text{model}}$ structures, compared to the corresponding GGA paramagnetic DOS (dashed lines). The black and green lines correspond to the $3z^2 - r^2$ and $x^2 - y^2$ states, respectively. Adapted after Ref. [272].

obtained in the present case is presumably driven by the significant Jahn-Teller effect at the Mn1 site. In addition to the CD, within DFT the system also displays orbital order. Electronic correlations enhance both kinds of ordering dramatically, making CO and OO nearly complete. This establishes the correlation-driven stability of CO and OO with almost complete CD in the paramagnetic phase.

Furthermore, we compute the DFT+DMFT **spectral function** for both $\mathcal{S}_{\text{bulk}}$ and $\mathcal{S}_{\text{model}}$, obtained via the analytic continuation of the QMC data by means of MEM. In the presence of electronic correlations, spectral weight is transferred to high frequencies in the form of Hubbard bands:

Table 5.3: Orbital occupations $\langle n \rangle = \langle n_\uparrow + n_\downarrow \rangle$ for Mn $3z^2 - r^2$ (first entry) and $x^2 - y^2$ (second entry) states, calculated within GGA+DMFT for the different inequivalent types of Mn atoms in the unit cell of $\mathcal{S}_{\text{bulk}}$ and $\mathcal{S}_{\text{model}}$. In brackets the corresponding GGA occupancions are given [272].

	$\mathcal{S}_{\text{bulk}}$		$\mathcal{S}_{\text{model}}$	
	$3z^2-r^2$	x^2-y^2	$3z^2-r^2$	x^2-y^2
Mn1(1)	0.87 (0.50)	0.01 (0.11)	0.52 (0.31)	0.09 (0.20)
Mn1(2)	0.85 (0.47)	0.01 (0.12)	0.72 (0.38)	0.04 (0.19)
Mn2	0.04 (0.15)	0.09 (0.25)	0.16 (0.21)	0.16 (0.25)

the almost complete CD and enhanced orbital polarization (OP) at the Mn1 sites determines the opening of a gap at the chemical potential of the the DFT+DMFT spectral function for the bulk structure even without long-range spin ordering, as shown in the left panel of Fig. 5.5. Note the opening of the charge gap is stabilized by long-range Coulomb interactions which, being neglected in DMFT, in the present calculation reduce to their Hartree contribution, taken into account on the GGA level. However, in the DFT paramagnetic DOS the charge disproportionation is incomplete and the insulating solution is obtained only by assuming the long-range AF spin ordering.

Turning to $\mathcal{S}_{\text{model}}$, the DFT occupancies show Mn^{3+}-like and Mn^{4+}-like sites to be similar with only a weak CD. The inclusion of the correlation effects through DMFT enhances CD to some extent following the trend seem for $\mathcal{S}_{\text{bulk}}$. However, CD remains incomplete with an average occupation of Mn^{3+}-like and Mn^{4+}-like sites of $\langle n \rangle \approx 0.6-0.7$ and $\langle n \rangle \approx 0.3$, respectively, in comparison to the values $\langle n \rangle \approx 0.9$ and $\langle n \rangle \approx 0.1$, respectively, obtained for $\mathcal{S}_{\text{bulk}}$. At the same time, this leads to a metallic DFT+DMFT spectral function for $\mathcal{S}_{\text{model}}$, with finite weight at the chemical potential, as shown in the right panel of Fig. 5.5.

The above analysis conclusively establishes that size reduction leads to the weakening of charge disproportionation. Note that, although $\mathcal{S}_{\text{nano}}$ does not maintain strict stoichiometry, the constructed $\mathcal{S}_{\text{model}}$ is strictly stoichiometric, pointing to the fact that destabilization of CO is driven by the structural changes due to size confinement, rather than due to deviation from half-doping.

Comparison with the system under pressure. As one of the major structural changes upon size reduction is the volume compression, it is worthwhile to compare the structural and electronic changes induced by size reduction to those occurring under hydrostatic pressure. To this end, we carried out calculations of LCMO, with uniformly reduced lattice parameters with 6% reduced volume, the atomic positions being optimized in DFT, referred to as structure $\mathcal{S}_{\text{press}}$. The details of the optimized structure are given in the SM of Ref. [272]. Following the self-consistent DFT calculations on $\mathcal{S}_{\text{press}}$, the Mn e_g only low-energy Hamiltonian was constructed and the corresponding Hubbard Hamiltonian was solved using DMFT. Compared to $\mathcal{S}_{\text{model}}$, we find that at the DFT level CD and orbital polarization are much weaker, even though the volume is the same. In this less polarized configuration, where all Mn sites are filled with $\langle n \rangle \approx 0.5$ electrons (i.e., $1/8$ filling) and electronic correlations are less relevant. The DMFT orbital and site occupations remain very similar to the DFT values with $\langle n \rangle \approx 0.4-0.6$ electrons per site, and the system is far away from a metal-insulator transition (MIT). This leads us to conclude that the nanoscopic system is much closer to a MIT than bulk $La_{0.5}Ca_{0.5}MnO_3$ under hydrostatic pressure. Although compression of volume and Mn-O bonds happens both in nanoscale and on the application of pressure, the larger $OS_{\|}$ in the case of nanoscale compared to that under pressure makes the Mn e_g bandwidth smaller for the former, through reduction in Mn-O-Mn bond angle. The size reduction and application of hydrostatic pressure, therefore, should be considered as two very different routes.

In conclusion, we have studied the effect of size reduction on charge-orbital order in half-doped LCMO manganites. within DFT+DMFT. Our analysis indicates that the size reduction leads to a substantial reduction in volume as well as a change in the nature of the orthorhombic strain. The structural changes under size reduction are responsible for a weakening of both charge and orbital ordering, making the ferromagnetic metallic state energetically favorable compared to the CE-type AF insulating state, which is the ground state of the bulk structure. While such effect has been observed, the experimental situation is faced with difficulties, like the possible presence of impure phases, the grain boundaries, and non-stoichiometry. The theoretical calculations were carried out considering a perfect nanocluster in isolation, and, therefore, devoid of such complications. Through construction of the model structure, the issue of non-stoichiometry was also avoided. Furthermore, we predict the nanoscopic system to be closer to the MIT in comparison to the system under pressure with the same amount of volume reduction, suggesting that the structural changes induced by size reduction an by the application of hydrostatic pressure to be of different nature.

In this picture, the role of electronic correlations is to enhance a preexisting CO order, which is entwined with the amplitude of the crystallographic distortions. Hence, electronic correlation can either result in dramatic effect, as in the bulk, where strong tendencies toward CO ordering are predicted also in the absence of long-range order, or be weaker, as in the nanocluster (or in the system under pressure), leading to an incomplete CD.
Beside static Jahn-Teller distortions, one may also consider the lattice dynamics by introducing an electron-phonon coupling. The interplay between strong correlations and lattice distortion allows to explain the insulating nature of the paramagnetic state, in which electrons are easily trapped as Jahn-Teller polarons [263]. In the present framework, the electron-phonon coupling could also play a role: it can either favor or contribute to the destabilization of the CO order, depending whether it enhances the differences between the Mn1 and Mn2 octahedra. However, due to the non-trivial interplay between the Coulomb repulsion and the electron-phonon coupling, a prediction in this sense may be hazardous.

5.2.2 nano-DMFT results for finite-size nanocluster

The results presented in this section are still unpublished.

The theoretical DFT+DMFT results discussed above are remarkably consistent with the experimental observations, and also suggest the possibility of a size-driven MIT. As we have already mentioned, the relatively high magnetic field ($H \gtrsim 1$ T) necessary to trigger a CMR effect in the manganites, compared the one of artificial multilayer systems, represents the major drawback of those compounds and prevent their employment for possible technological applications. Obviously, a system close to a phase transition is instead highly susceptible to the application of external perturbation, including electric or magnetic field, hydrostatic or chemical pressure, and mechanical stress. Hence, size-engeneered LCMO clusters at the verge of the MIT constitute a promising possibility for a tunable device. In this respect, a systematic analysis of the properties of manganites as a function of size would be indeed highly desirable.
In order to investigate a LCMO nanocluster within DFT+DMFT, we need to define a suitable lattice model, characterized by the lattice parameters obtained by a DFT structural optimization. As discussed, the results obtained suggest the lattice distortions to be responsible for the destabilization of the AF insulating phase, hence pointing out the key role of the structural optimization. Unfortunately, the numerical workload associated to this process is already challenging in the case of a $2-3$ nm size nanocluster (to be compared to the 15 nm cluster realized in the experiments), and the *ab-initio* realization of larger clusters is not feasible. Therefore, we need to find an alternative method to study the size dependence of the electronic structure, and eventually of the magnetoresistance of LCMO nanoclusters.

Interfacing DFT & nano-DMFT. In this respect, the flexibility of the nanoscopic extension of DMFT may be a suitable alternative, if supplied with a realistic input extracted from DFT. Hence, we build a finite-size structure of Mn atoms, henceforth referred to as $\mathcal{S}_{\text{finite}}$. This is done extracting a crystal unit from the core region of $\mathcal{S}_{\text{finite}}$, replicating it in all directions and then cutting out a cluster having approximate spherical shape. Note that the hopping parameter used for $\mathcal{S}_{\text{finite}}$ are extracted from the core region of $\mathcal{S}_{\text{nano}}$, and hence are determined by the lattice parameters and distortions obtained by means of the atomic relaxation of $\mathcal{S}_{\text{nano}}$.

In order to understand what kind of result nano-DMFT would yield, in the following we consider a $\mathcal{S}_{\text{finite}}^{[46]}$ structure, i.e., a nanocluster made of $N = 46$ Mn atoms overall, corresponding to $N_{\text{ineq}} = 23$ inequivalent atoms due to inversion symmetry. The system is described by the low-energy Hamiltonian (5.2) where the sums over the Mn indexes is now limited by the finite size of the nanocluster, i.e., $i = 1, ..., N$. The on-site energy of both e_g orbitals of each Mn atoms, as well as the hopping amplitudes between nearest neighbor Mn atoms are extracted from the NMTO downfolded real-space one-particle Hamiltonian $h_{imjm'}$, while the interaction parameters are those discussed in Sec. 5.2 and considered in the previous analysis. It is important to notice that, in order to obtain a highly symmetric nanocluster, which is important to lower the number of inequivalent atoms, such a procedure may yields a system which deviates from perfect stoichiometry. For instance, in the present realization of the LCMO nanocluster there is an unbalance of Mn1(1), Mn1(2) and Mn2 atoms which slightly deviates from the ration $1:1:2$, as indeed it contains $12:12:22$ Mn atoms, respectively (see also 5.3). This would most likely have an effect on the physics of the system.

Another issue to consider in the interface between DFT and nano-DMFT concerns the double counting corrections, which is highly non-trivial, as already discussed in the context of the standard DFT+DMFT. Here, we correct the on-site energy of each Mn atom with an Hartree-like term $\tilde{U}\ n_{im}$, where we take for $\tilde{U}$ the averaged Coulomb potential (5.3) and for n_{im} the GGA density of each type of Mn atoms in the monoclinic unit cell of $\mathcal{S}_{\text{model}}$.

Once all the elements of the multi-impurity Anderson Hamiltonian have been defined, one can proceed to the numerical solution of the system, by means of nano-DMFT. Employing the nano-approximation, each locally inequivalent Mn atom is mapped onto an auxiliary two-orbital AIM, describing the correlated Mn e_g orbitals interacting with a classical t_{2g} spin. The solution of each auxiliary AIM yields a local 2×2 (diagonal) self-energy matrix $\Sigma^i_{e_g}(\nu)$. According to the symmetry relations defining the equivalent sites, a self-energy matrix for the whole nanocluster is build, and it is used to update the Green's function by means of the Dyson equation. The process is iterated until self-consistency.

Before turning to the results, let us notice that the number of strictly locally inequivalent atoms is sensibly higher than all the previously presented applications of nano-DMFT. Besides the

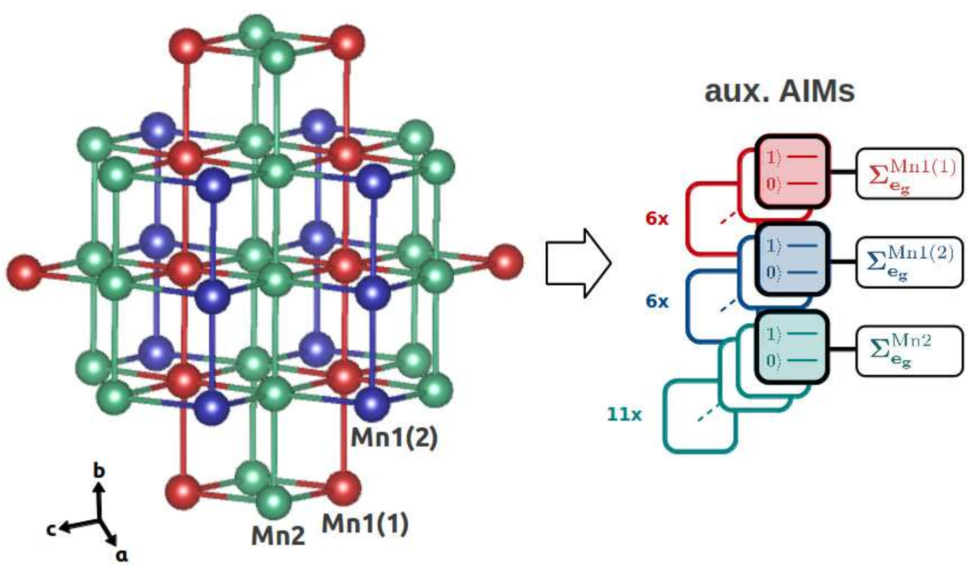

Figure 5.6: Schematic representation of the chosen $\mathcal{S}^{[46]}_{\text{finite}}$ structure: red, blue, and green color correspond to the inequivalent types of Mn atoms, labeled Mn1(1), Mn1(2), and Mn2 atoms, respectively. Within nano-DMFT, for each locally inequivalent atom one can define an auxiliary AIM: six for each type of Mn1 atoms and eleven for the Mn2 atoms overall. The solution of each auxiliary AIM yields a local 2×2 (diagonal) self-energy matrix $\Sigma^i_{e_g}(\nu)$.

intrinsic differences between Mn1 and Mn2 atoms, one would expect the main differences (among atoms belonging to the same Mn class) to arise between atoms of the inner region (henceforth ‘‘bulk’’ atoms) and atoms on the surface of the nanocluster (henceforth ‘‘surface’’ atoms). Although a sharp separation between the two kinds of atoms cannot be done, a naïve, yet intuitive, way to discriminate bulk and surface atoms would be to consider each atom’s connectivity within the present realization of the $\mathcal{S}^{[46]}_{\text{finite}}$ structure. Hence, one can label as surface atoms the Mn atoms with $z = 2, 3$ nearest neighbors, and as bulk atoms the ones with $z = 4, 5, 6$ nearest neighbors.

Electronic structure. In the following, we present preliminary results of nano-DMFT paramagnetic calculations for the $\mathcal{S}^{[46]}_{\text{finite}}$ cluster. According to the nominal valence of the Mn^{3+} and Mn^{4+} atoms in the nanocluster, an average occupancy of (almost, due to off-stoichiometry) half an electron per atom is required to achieve charge neutrality, as for bulk $La_{0.5}Ca_{0.5}MnO_3$. At this density one does not expect strong correlation effects. However, as already discussed, a nanoscopic system can be contacted to macroscopic charge reservoirs, so that the amount of electric charge within the cluster would depend on the equilibrium chemical potential of the junction, and can also be controlled by means of a gate voltage V_G. In the weak-hybridization regime $\Gamma \ll U, T$ (let us recall here, that $\Gamma = 2\pi\rho V^2$ is the scattering amplitude to the reservoir DOS ρ for an hybridization strength V), the effect of the reservoir on the local spectrum of the nanocluster would be negligible. Hence, one can consider the isolated nanocluster and perform a systematic study as a function of V_G.

In Fig. 5.7 the results for the **spectral weight at the Fermi energy** $A(E_F)$ are compared to the **orbitally-resolved occupations** per selected sites $\langle n_{im}\rangle = \langle n_{im\uparrow} + n_{im\downarrow}\rangle$ and averaged on the whole cluster $\langle n\rangle_{\text{cluster}} = \frac{1}{N}\sum_{i=1}^{N}\frac{1}{2}\sum_{m=1}^{2}\langle n_{im}\rangle$, as a function of eV_G, where e is the electric charge, for the $N = 46$ sites cluster,

At $eV_G = 0$ all Mn atoms in $\mathcal{S}^{[46]}_{\text{finite}}$ are half-filled, with on average one electron per e_g orbital, and display a charge gap at the Fermi energy. A divergent imaginary part of the nano-DMFT self-energy in Matsubara representation in both e_g orbitals suggests that the system is a Mott insulator. The Mott phase persists until $eV_G \approx 1$ eV, when the occupation of the low-lying e_g level (the $x^2 - y^2$ in the case of Mn1 and the $3z^2 - r^2$ in the case of Mn2) is driven out of half-filling and undergoes a transition to a metallic state, while the other e_g level remains insulating. This is confirmed by the corresponding imaginary part of the self-energy displaying a typical FL behavior for the former, and diverging for the latter. In this regime all kind of Mn atoms display orbital polarization, but only a weak CD between Mn1 and Mn2 atoms is observed.
The *orbital selective* Mott phase is destabilized at higher voltage values: at $eV_G \approx 2$ eV both orbitals of Mn2 atoms exhibit metallic character, while Mn1 $3z^2 - r^2$ are still blocked into the Mott insulating phase till $eV_G \gtrsim 2.5$ eV. This suggests that the crystal field splitting Δ between the Mn e_g orbitals is similar for the Mn1 atoms and larger than in the Mn2 ones. Above a voltage threshold the transition to the metallic phase is complete, and further increasing V_G rapidly weaken correlations effects, as the average cluster occupation $\langle n\rangle_{\text{cluster}}$ decreases.

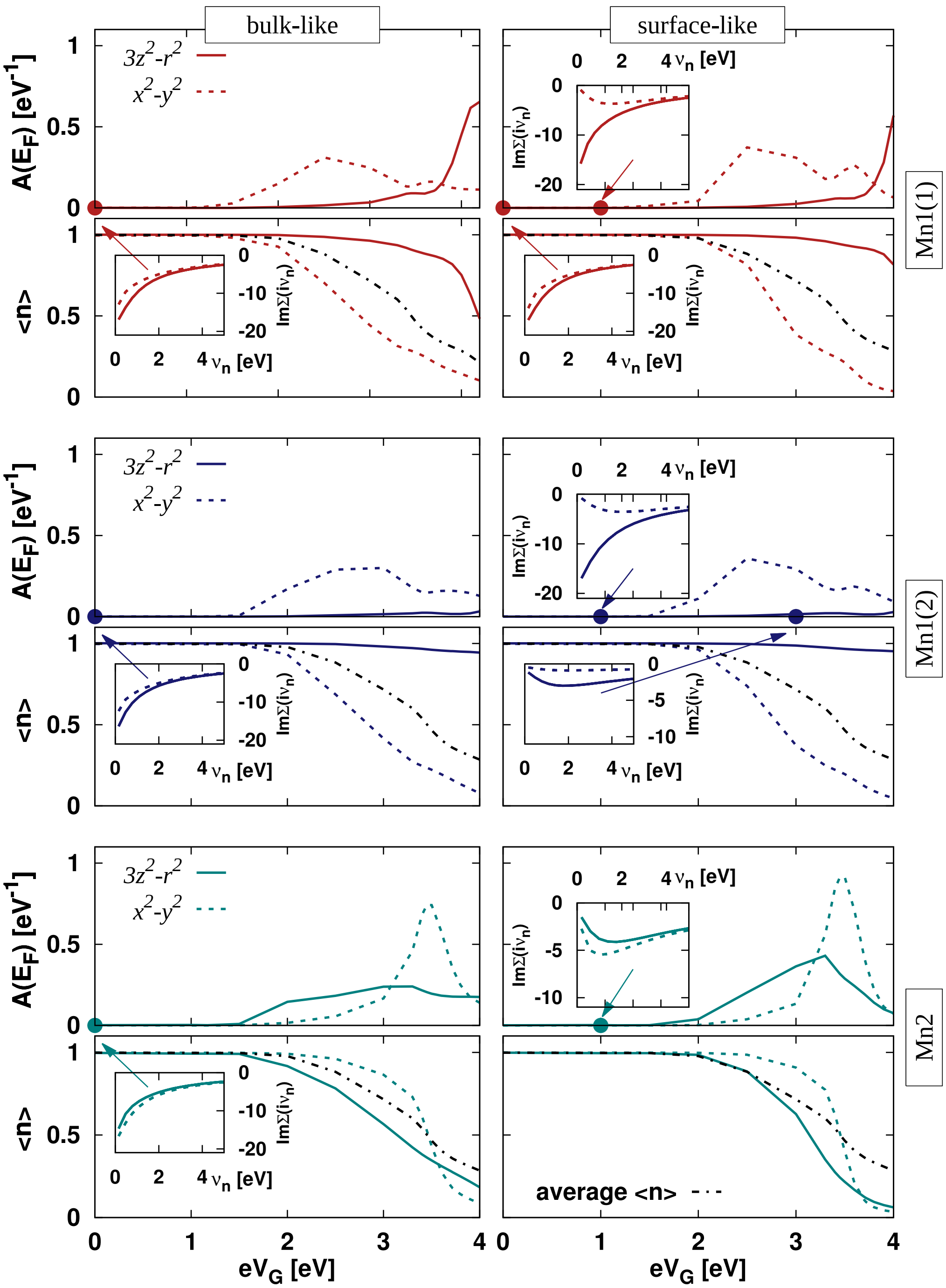

Figure 5.7: Evolution as a function of the gate voltage V_G of the spectral weight at the Fermi energy $A(E_F)$ and orbitally-resolved occupations $\langle n_{im}\rangle$ for representative bulk (left panels) and surface (right panels) Mn atoms of the $\mathcal{S}^{[46]}_{\text{finite}}$ structure. Solid and dashed lines correspond to the $3z^2 - r^2$ and $x^2 - y^2$ states, respectively, while the dot-dashed line denotes the cluster average $\langle n\rangle_{\text{cluster}} = \frac{1}{N}\sum_{i=1}^{N}\frac{1}{2}\sum_{m=1}^{2}\langle n_{im}\rangle$. The insets show the imaginary part of the local self-energy $\Sigma(\imath\nu_n)$ in Matsubara representation for selected values of eV_G.

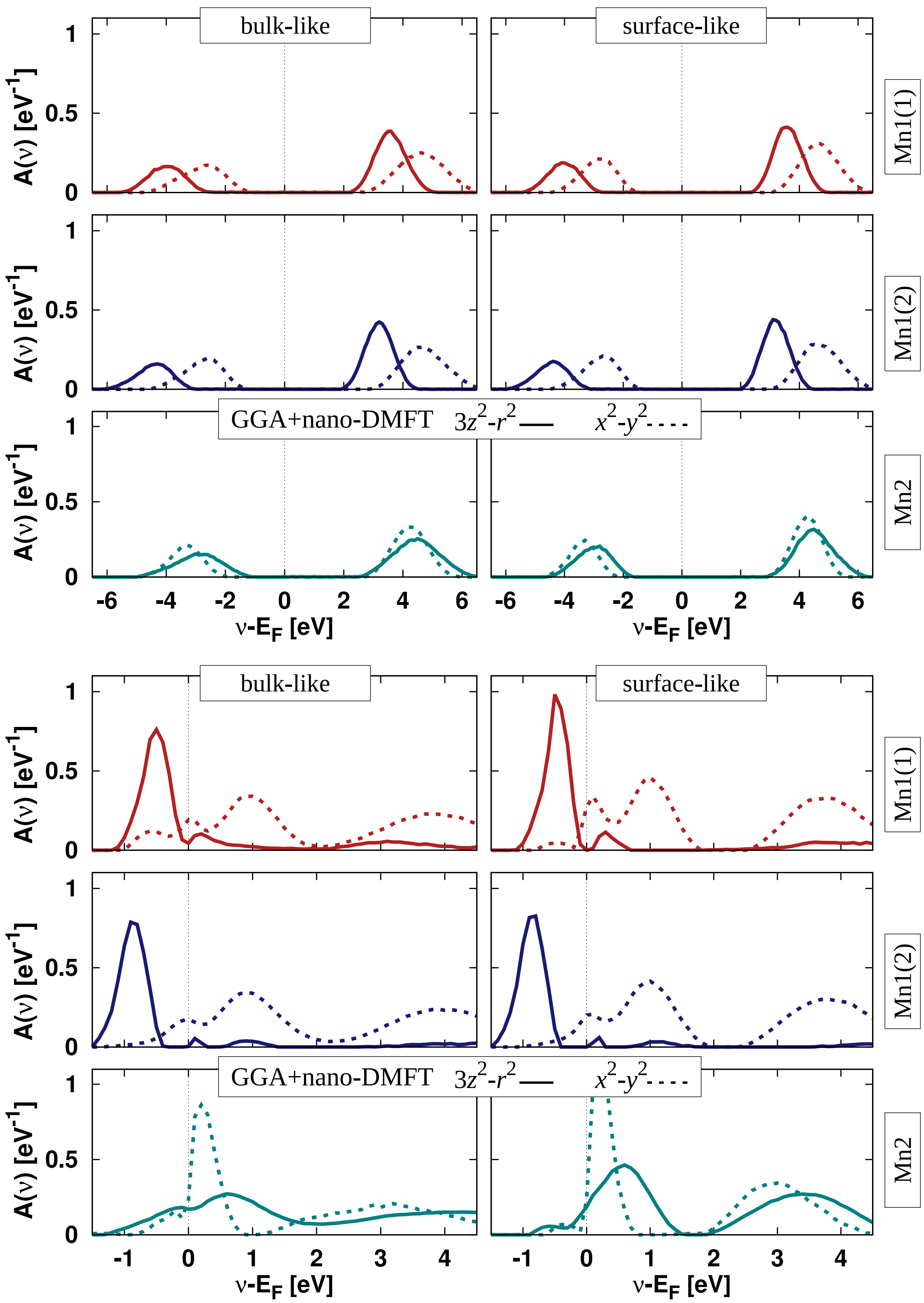

Figure 5.8: Representative nano-DMFT spectral function $A(\nu)$ of three inequivalent classes of Mn atoms, located in the bulk (left panles) at the surface (right panels) of the the $\mathcal{S}^{[46]}_{\text{finite}}$ structure, for $eV_G = 0$ (upper panels) and $eV_G = 3.7$ eV (lower panels). Solid and dashed lines correspond to the $3z^2 - r^2$ and $x^2 - y^2$ states, respectively.

In order to further shed light on the nature of the Mott phases electronic phases suggested by the previous analysis, it is useful to consider the nano-DMFT **spectral function** of representative atoms of the $\mathcal{S}^{[46]}_{\text{finite}}$ structure, which are obtained via the analytic continuation of the QMC data by means of the MEM. The resulting spectral function, shown in Fig. 5.8 for some representative bulk and surface atoms of the $\mathcal{S}^{[46]}_{\text{finite}}$, confirm the orbital selective character of the Mott phase, as a function of the gate voltage V_G.
At $eV_G = 0$ (upper panels) all spectra display a charge gap of order U at the chemical potential. Concerning the Mn1 atoms, the energy shift between the $3r^2 - z^2$ and $x^2 - y^2$ states, reminiscent of the crystal field splitting due to the static Jahn-teller distortions, is clearly visible in both the lower and the upper Hubbard bands. This determines, in the lower Hubbard band, the states with $x^2 - y^2$ character to lie closer to the Fermi energy E_F than the $3r^2 - z^2$ ones. While the evolution of the spectral function upon increasing V_G is non-trivial, the splitting is probably responsible for the $x^2 - y^2$ states to cross E_F before the $3r^2 - z^2$ ones, as can be observed in the upper panels of Fig. 5.7 related to the Mn1 atoms. In the Mn2 atoms instead, the spectral function of $x^2 - y^2$ and $3r^2 - z^2$ states look quite similar.
At large eV_G, i.e., $eV_G = 3.7$ eV, as shown in the lower panels of Fig. 5.7, both orbitals of all the atoms considered display a finite spectral weight at E_F (the value depending both on the orbital and on the kind of Mn atom). In general, we observe that there is no substantial qualitative difference between the bulk and surface atoms (of the same Mn kind). The reason for this is probably the size of the system considered, and more pronounced differences are expected upon increasing it.

In conclusion, we have investigated a finite-size LCMO nanocluster $\mathcal{S}^{[46]}_{\text{finite}}$, which we have build replicating the unit cell of the core region of $\mathcal{S}_{\text{nano}}$. Depending on the filling, which can be controlled by means of a gate voltage, we observe different electronic phases. At half-filling strong electronic correlations dominate and each Mn atom is in a Mott-like insulating phase. Driving the system away from half-filling, we observe a wide range of voltages in which the system displays a site-dependent orbital selective Mott phase, which is probably determined by the Jahn-Teller splitting between the e_g states in the Mn^{3+}-like atoms. Further lowering the filling weakens electronic correlations and drives the nanocluster to a paramagnetic metallic phase.

5.3 Outlook

Concerning the theoretical analysis of bulk and nanoscale half-doped manganite LCMO, we have shown that, by means of DFT+DMFT, one is able to provide an independent confirmation of the recent experimental scenario [256, 257, 258, 259], suggesting the destabilization of the CO order to be determined by the structural changes of the orthorhombic distortions and Jahn-Teller splittings, upon size reduction.

We also considered a finite structure, with the aim to investigate clusters of different size, expanded in all three dimensions around their center of symmetry. This is certainly possible from the point of view of the numerical workload, within nano-DMFT. However, issues may rise to obtain the proper hopping parameters, due to the lack of a proper atomic relaxation of larger finite clusters. An *ab-initio* calculation beyond the 3 nm cluster is not feasible. However, we expect further atomic relaxation to be important in the evolution of the nanocluster physical properties toward a bulk behavior.

Moreover, while the Coulomb interaction certainly plays an important role in determining the electronic properties of the manganites, one should also consider the **effects of the electron-phonon interaction** and its interplay with the Coulomb repulsion. How may the coupling between the electronic and lattice degrees of freedom modify the present theoretical picture?
Another interesting point also concerns the analysis of the system in the (spontaneously) broken symmetry phases. Alternatively one can break the symmetry by means of the application of an external magnetic field H, and compute the resistance $R(H)$, e.g., from the static optical conductivity $\sigma(\Omega=0)$ [263], and estimate the CMR.

Conclusions

In the field of strongly correlated electronic systems, the overwhelming amount of experiments which can be realized in modern research laboratories leads frequently to the discovery of novel physical phenomena. However, for many of those phenomena, a comprehensive understanding of their microscopic origin remains elusive. This is often due to the theoretical difficulties to deal with many-body effects entailed by electronic interactions. In particular, in the case of nanoscopic systems, the confinement of electrons into narrow, low-dimensional regions as well as the lack of a proper metallic screening are expected to enhance their mutual interactions. As a result, at the nanoscale, the physics is often dominated by electronic correlations.

This work aims towards a better understanding of correlation effects, in nanoscopic systems, where very little is known beyond the framework of impurity models. To this end we developed a novel tool, based on existing many-body techniques, whose flexibility allows us to access electronic and transport properties of complex nanostructures, involving many degrees of freedom and inhomogeneities, in the presence of strong electronic correlations. Supported by the results obtained on a variety of systems, we believe that the proposed scheme may have the potential to establish itself as a breakthrough for numerical simulation in this field.

In this respect, chapter 1 is meant to give an overview on the world of nanoscopic systems, both from the experimental and theoretical point of view. The first part describes the systems of interest and the experimental techniques which are relevant in the context of this work. In the second part we discuss the interplay between the different energy scales in the framework of standard models, such as the Anderson impurity model (AIM), which is an important tool for the description of electronic correlations. In this context, we show the fingerprints of strong electronic correlations at the nanoscale, e.g., the Coulomb blockade and the Kondo effect, which heavily affect electronic and transport properties of the system. The latter are mainly investigated by means of transport spectroscopy, which represents the main contact between theory and experiments. Hence, in the last part of this chapter we discuss the formalism of quantum transport in nanoscopic systems, and the connection to the theoretical evaluation of the electrical conductance.

The aim of chapter 2 is to introduce the many-body theory employed in the rest of this work. A natural starting point is the dynamical mean-field theory (DMFT) and its justification

as the local approximation for the self-energy of infinite-dimensional fermionic lattice models. In particular, we derive the well-known self-consistent equations of the mapping on the AIM, and discuss some details of the impurity solvers employed in chapter 3, 4 & 5. We illustrate the density functional theory (DFT) and its interface with DMFT, which was necessary to obtain a realistic description of manganites systems (see chapter 5).
In nanoscopic systems, also correlation effects beyond mean-field are expected to be of importance, and require to consider extensions of DMFT. A brief overview on the available techniques can convince that, among those, the most suitable to be applied to nanoscopic systems is probably the dynamical vertex approximation (DΓA). In this respect, we introduce the two-particle and parquet formalism at the basis of DΓA. The last part of this chapter is devoted to the description of the novel method we developed to apply DMFT and DΓA to correlated nanostructures (see chapters 3 & 4).

In chapter 3 we test the nano-DMFT and nano-DΓA methods on models of quasi one-dimensional π-conjugated ring molecules. The availability of a numerically exact benchmark, due to the few degrees of freedom involved, make those systems an ideal reference system to explore the effects of electronic correlations. Hence, it allows us to understand the reliability of the approximation employed. Scanning the parameters space we identify the regions where local and/or nonlocal electronic correlations are relevant. In particular, both a high-connectivity within the nanostructure and the hybridization to non-interacting metallic leads rapidly suppress non-local spatial correlations, so in a wide range of parameters and structures the nano-DMFT is a reliable approximation. In the opposite limit, non-local spatial correlations may heavily influence the physics of the ring, generally driving the system toward an insulating phase. This can be directly observed in the suppression of both the spatially-resolved one-particle electronic spectral function and the intrinsically non-local transport properties, i.e., the conductance through the nanostructure.
In specific cases, we include non-local correlations beyond mean-field by means of nano-DΓA, which generally leads to an improvement over nano-DMFT [those results are not yet published]. The analysis in the direction of molecular systems, however, is far from being exhaustive and calls for further systematic investigations. Possible research lines include the investigation of interference effect in ring nanostructure in the presence of a magnetic field (Aharonov-Bohn effect) as well as transport properties through nanostructures bridging magnetic or superconducting leads. On the other hand, the evaluation of two-particle vertex functions represents a challenging numerical task and requires further development of numerical tools in order to improve both the efficiency and the applicability of the method.

In chapter 4 we exploit the versatility of nano-DMFT to build model structures for to simulate mechanically controlled break junctions, where a vacuum gap bridges two facing contacts made of several correlated atoms, resulting in a tunneling barrier. In the presence of electronic correlations, we predict deviations from the exponential dependence of the conductance on the width of the barrier, expected in the case of tunneling in a point-contact geometry. A spatially-

resolved analysis of the electronic structure of the junction indicates a strong tendency towards a metal-to insulator transition (or rather a crossover) involving the atom sitting at the sharp edge of each of the contacts. In contrast the rest of the system is weakly affected by the size of the tunneling gap. The calculations carried out for several realizations of quantum junctions, suggests the phenomenon to be a general feature, which may even be observed experimentally, e.g., detecting the conductance anomaly in transport measurements.
In the above analysis, the crystal structure of the junction is kept fixed. While on one hand this allows to disentangle the effects of electronic and lattice rearrangements, on the other hand it may be not a realistic description of the experimental conditions. Structural effect could be, nevertheless, taken into account resorting to the combination of the present approach with *ab-initio* techniques.

In the last chapter, we discuss an important contribution that we made to clarify the controversial experimental scenario on the effect of size reduction on the half-doped manganite $La_{0.5}Ca_{0.5}MnO_3$. The destabilization upon size reduction of the complex charge-orbital (CO) and antiferromagnetic ordering is an uncontested experimental evidence. However, its interpretation is somehow unclear due to possible issues regarding the quality of the sample. Hence, we study a defect-free and stoichiometric cluster through the combination of *ab-initio* DFT(GGA) & DMFT methods, to be able to compare the results to the case of the bulk on equal footing. This allows us to identify the changes of the lattice parameters due to size reduction, and the resulting crystal field, as the microscopic origin of the destabilization of the ordered phase. While DFT alone already provides a remarkably qualitative agreement with the experiments, DMFT also suggest that electronic correlations favor the realization of a CO ordering even in the absence of a long-range magnetic order.
The above results are obtained neglecting dynamic lattice distorsions (phonons). However, it is well known that the coupling between the electronic and lattice degrees of freedom, and its interplay with the Coulomb interaction and the Hund's exchange, play a relevant role in bulk manganites, Hence, a reasonable question arise: how does the above scenario for the manganite nanocluster change in the presence of electron-phonon coupling?
As a final remark, we notice that the above method, due to its computational complexity, is limited to clusters of a few nm. Hence, a thoughtful analysis as a function of size of the experimentally realized clusters size, ranging from 15 nm to a few μm (the latter displaying bulk properties), although highly desirable, is hardly feasible. In this respect, we presented some preliminary results suggesting that cluster of different size could be investigated with nano-DMFT.

Appendix A

Linear Response conductance

In the following we provide the details of the derivation of the linear response conductance through an extended interacting system.

Decomposition of $K_{\mathbf{RL}}(\imath\Omega_l)$. Below, we derive the decomposition (1.71) of the current-current correlation function into a bubble term and the vertex corrections. For the sake of clearness, we recall the definitions (1.67) of the correlation function

$$K_{\alpha\alpha'}(\imath\Omega_l) = \int_0^\beta d\tau \, \Big\langle T_\tau J_\alpha(\tau) J_{\alpha'}(0) \Big\rangle \mathrm{e}^{\imath\Omega_l \tau}, \tag{A.1}$$

where $\alpha, \alpha' = L, R$, and the expression (1.68) of the current flowing in and out the scattering region (compare also with Fig. 1.8, which indicates the verse of the positive current) reads

$$J_L = \imath \sum_\sigma V_{\mathrm{L}} (c^\dagger_{1\sigma} c_{\ell\sigma} - c^\dagger_{\ell\sigma} c_{1\sigma}), \tag{A.2a}$$

$$J_R = \imath \sum_\sigma V_{\mathrm{R}} (c^\dagger_{r\sigma} c_{N\sigma} - c^\dagger_{N\sigma} c_{r\sigma}). \tag{A.2b}$$

Explicitly substituting the expression of the current (A.2) in the correlation function (A.1) yields

$$\begin{aligned} K_{\mathrm{RL}}(\imath\Omega_l) =& (\imath V_{\mathrm{R}})(\imath V_{\mathrm{L}}) \sum_\sigma \int_0^\beta d\tau \; \mathrm{e}^{\imath\Omega_l\tau} \\ & \times \Big\langle T_\tau \Big\{ c^\dagger_{r\sigma}(\tau) c_{N\sigma}(\tau) c^\dagger_{1\sigma}(0) c_{\ell\sigma}(0) - c^\dagger_{r\sigma}(\tau) c_{N\sigma}(\tau) c^\dagger_{\ell\sigma}(0) c_{1\sigma}(0) \\ & - c^\dagger_{N\sigma}(\tau) c_{r\sigma}(\tau) c^\dagger_{1\sigma}(0) c_{\ell\sigma}(0) + c^\dagger_{N\sigma}(\tau) c_{r\sigma}(\tau) c^\dagger_{\ell\sigma}(0) c_{1\sigma}(0) \Big\} \Big\rangle . \end{aligned} \tag{A.3}$$

As each term within the time-ordered product is formally a non-local two-particle Green's function (or generalized susceptibility) which can be written in terms of its Fourier representation

$$\chi^{\sigma\sigma'}_{ik\ell m}(\tau_1, \tau_2, \tau_3) = \frac{1}{\beta^3} \sum_{\nu\nu'} \sum_\omega \chi^{\sigma\sigma'}_{ik\ell m}(\nu, \nu', \omega) \; \mathrm{e}^{i\nu\tau_1} \mathrm{e}^{-i(\nu+\omega)\tau_2} \mathrm{e}^{i(\nu'+\omega)\tau_3}. \tag{A.4}$$

The above relation can be used to evaluate the imaginary time integral as

$$\int_0^\beta d\tau\ \chi^{\sigma\sigma'}_{ik\ell m}(\tau,\tau,0)\ \mathrm{e}^{\imath\Omega\tau} = \frac{1}{\beta^2}\sum_{\nu\nu'}\chi^{\sigma\sigma'}_{ik\ell m}(\nu,\nu',\Omega), \tag{A.5}$$

which defines the physical susceptibility $\chi^{\sigma\sigma'}_{ik\ell m}(\Omega)$. The generalized susceptibility itself can naturally be decomposed into a bubble term, describing the independent propagation of two particles, and the vertex corrections, as

$$\begin{aligned}\chi^{\sigma\sigma'}_{ik\ell m}(\nu,\nu',\Omega) &= -\beta G_{k\ell\sigma}(\nu+\Omega)G_{mi\sigma}(\nu)\delta_{\nu\nu'}\delta_{\sigma\sigma'} \\ &\quad - \sum_{\{j\}\in\mathrm{S}} G_{j_1\ell\sigma}(\nu+\Omega)G_{mj_4\sigma}(\nu')F^{\sigma\sigma'}_{j_1j_2;j_3j_4}(\nu,\nu',\Omega)G_{kj_2\sigma'}(\nu'+\Omega)G_{j_3i\sigma'}(\nu').\end{aligned} \tag{A.6}$$

Replacing the integral of each time-ordered product with the susceptibility (A.4) and hence with the expression (A.5) and its decomposition (A.6) with the proper index structure, the correlation function (A.3) can be recast as

$$\begin{aligned}K^{\text{bubble}}_{\text{RL}}(\imath\Omega_l) = &-(\imath V_{\text{R}})(\imath V_{\text{L}})\frac{1}{\beta}\sum_n\sum_\sigma \\ &\times\big[G_{N1\sigma}(\imath\nu_n+\imath\Omega_l)G_{\ell r\sigma}(\imath\nu_n) - G_{N\ell\sigma}(\imath\nu_n+\imath\Omega_l)G_{1r\sigma}(\imath\nu_n) \\ &\quad - G_{r1\sigma}(\imath\nu_n+\imath\Omega_l)G_{\ell N\sigma}(\imath\nu_n) + G_{r\ell\sigma}(\imath\nu_n+\imath\Omega_l)G_{1N\sigma}(\imath\nu_n)\big]\end{aligned} \tag{A.7a}$$

$$\begin{aligned}K^{\text{vertex}}_{\text{RL}}(\imath\Omega_l) = &-(\imath V_{\text{R}})(\imath V_{\text{L}})\frac{1}{\beta^2}\sum_{nn'}\sum_{\sigma\sigma'}\sum_{\{j\}\in\mathrm{S}} \\ &\times\big[G_{j_11\sigma}(\imath\nu_n+\imath\Omega_l)G_{\ell j_4\sigma}(\imath\nu_n) - G_{j_1\ell\sigma}(\imath\nu_n+\imath\Omega_l)G_{1j_4\sigma}(\imath\nu_n)\big] \\ &\times\ F^{\sigma\sigma'}_{j_1j_2;j_3j_4}(\imath\nu_n,\imath\nu'_n,\imath\Omega_l) \\ &\times\big[G_{Nj_2\sigma'}(\imath\nu'_n+\imath\Omega_l)G_{j_3r\sigma'}(\imath\nu'_n) - G_{rj_3\sigma'}(\imath\nu'_n+\imath\Omega_l)G_{j_4N\sigma'}(\imath\nu'_n)\big],\end{aligned} \tag{A.7b}$$

yielding the form (1.71) in terms of the bubble and vertex corrections contributions.

Analytic continuation of the correlation function. For the sake of simplicity, let us consider the bubble contributions and the vertex corrections separately.

In order to perform the analytic continuation of the **bubble contribution** to the correlation function $K^{\text{bubble}}_{\text{RL}}$ rely on the analytical properties of the bare current vertex $\lambda_\alpha(\imath\nu_n,\imath\nu_n+\Omega_l)$ in the complex plane. Introducing the complex variables z and ω in place of the fermionic and bosonic Matsubara frequency, respectively, the bare vertex is defined as

$$\lambda_\alpha(z,z+\omega) = (1-2\delta_{\alpha L})\ \imath V_\alpha^2[g_\alpha(z+\omega)-g_\alpha(z)], \tag{A.8}$$

where the prefactor just takes into account the proper sign, i.e., $\mp$ for $\alpha\!=\!L,R$ respectively. As the bare current vertex (A.8) is defined in terms of the non-interacting Green's function of the

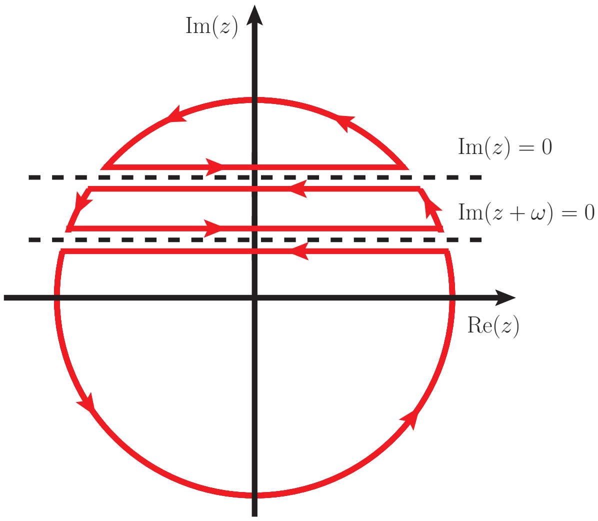

Figure A.1: Contour integral (red solid line) in the complex plane, chosen in order to perform the analytic continuation of the bubble contribution to the current-current correlation function $K_{\rm RL}(\imath\omega)$. The poles of the bare vertex function $\lambda_\alpha(z, z+\omega)$ are located along the (dashed) lines $\mathrm{Im}(z) = 0$ and $\mathrm{Im}(z+\omega) = 0$ of the complex plane, dividing it into three regions, labeled by $k = 1, 2, 3$. Within each region, the corresponding bare vertex, defined in terms of the leads' non-interacting Green's function, is analytic.

leads at the interface sites, its poles are located along the lines $\mathrm{Im}(z) = 0$ and $\mathrm{Im}(z+\omega) = 0$. Those lines divide the complex plane into three regions, which are labeled by the additional index $k = 1, 2, 3$ and where $\lambda_\alpha^{[k]}(z, z+\omega)$ is analytical in both of its arguments.

In order to perform the analytic continuation of the bare vertex in each of those regions, one has to make the appropriate choice to shift in the complex plane the position of the poles of both $g_\alpha(z)$ and $g_\alpha(z+\omega)$ case by case, i.e., introducing the substitutions $z \to \epsilon \pm \imath 0^+$ and $\omega \to \Omega \pm \imath 0^+$. In practice, this is done using the standard technique [90] to replace the sum over the Matsubara frequency with an energy integral over the a proper contour in the complex plane, as shown in Fig. A.1, in each of the regions.

The bare vertex $\lambda^{[k]}$, analytically continued to the real axis, assumes the following form

$$\lambda_\alpha^{[1]} = (1 - 2\delta_\alpha)\, \imath V_\alpha^2 [g_\alpha^r(\epsilon+\Omega) - g_\alpha^r(\epsilon)], \tag{A.9a}$$

$$\lambda_\alpha^{[2]} = (1 - 2\delta_{\alpha L})\, \imath V_\alpha^2 [g_\alpha^r(\epsilon+\Omega) - g_\alpha^a(\epsilon)], \tag{A.9b}$$

$$\lambda_\alpha^{[3]} = (1 - 2\delta_{\alpha L})\, \imath V_\alpha^2 [g_\alpha^a(\epsilon+\Omega) - g_\alpha^a(\epsilon)], \tag{A.9c}$$

where $g^{r,a}(\epsilon)$ are the corresponding retarded and advanced analytic continuation of the Green's function of the leads.
As for $\Omega \to 0$ both $\lambda_\alpha^{[1]}$ and $\lambda_\alpha^{[3]}$ will eventually vanish, the only term eventually contributing to the linear conductance is the one proportional to $\lambda_\alpha^{[2]}$, so that the bubble contribution to the retarded correlation function $K_{\rm RL}^r$ (dropping the irrelevant terms) reads

$$\begin{aligned} K_{\rm RL}^r(\Omega) = -\sum_\sigma \int_{-\infty}^{\infty} \frac{d\epsilon}{2\pi\imath}\, & [f(\epsilon+\Omega) - f(\epsilon)] \\ & \times \lambda_{\rm L}^{[2]}(\epsilon, \epsilon+\Omega) G_{N1\sigma}^a(\epsilon) \lambda_{\rm R}^{[2]}(\epsilon, \epsilon+\Omega) G_{1N\sigma}^r(\epsilon+\Omega), \end{aligned} \tag{A.10}$$

where $f(\epsilon) = (\mathrm{e}^{\beta\epsilon} + 1)^{-1}$ is the Fermi distribution of the electrons in the scattering region, and ϵ is the energy measured with respect to the Fermi level. If one performs carefully the limit

$\Omega \to 0$, the bare vertex reduces to

$$\lambda_\alpha^{[2]} = (1 - 2\delta_{\alpha L}) 2\pi\imath V_\alpha^2 \rho_\alpha^r(\epsilon), \tag{A.11}$$

where $\rho^r_{\mathrm{L,R}}(\epsilon)$ is the DOS of the L or R lead, given by the imaginary part of the retarded Green's function $g^r_{\mathrm{L,R}}(\epsilon)$. Defining

$$\Gamma_\alpha = 2\pi V_\alpha^2 \rho_\alpha^r(\epsilon), \tag{A.12}$$

and rearranging all the prefactors, the limit (1.65) yields eventually the expression for the conductance (1.77) that we report below, for the sake of clearness

$$G = 2\frac{e^2}{h}\int_{-\infty}^{\infty} d\epsilon \left(- \frac{\partial f(\epsilon)}{\partial \epsilon}\right)\mathcal{T}(\epsilon), \tag{A.13}$$

where the (spin-independent) transmission coefficient (1.78) reads

$$\mathcal{T}(\epsilon) = \Gamma_{\mathrm{L}}(\epsilon) G^a_{1N}(\epsilon) \Gamma_{\mathrm{R}}(\epsilon) G^r_{N1}(\epsilon). \tag{A.14}$$

On the other hand, the analytic continuation of the **vertex correction** term of the current-current correlation function, i.e., $K^{\text{vertex}}_{\mathrm{RL}}$, is quite complex and a complete derivation is beyond the scope of this work. Therefore, we just provide the result and a brief discussion of its derivation.

Following Oguri [89], the analytic continuation can be done according the Eliashberg theory of the analytic properties of the vertex part [91]. As a function of three complex variables, $F(z,z,\omega)$ has poles along the horizontal lines $\mathrm{Im}(z) = 0$ and $\mathrm{Im}(z+\omega) = 0$, along the vertical lines $\mathrm{Im}(z') = 0$ and $\mathrm{Im}(z'+\omega) = 0$, and along the diagonals $\mathrm{Im}(z-z') = 0$ and $\mathrm{Im}(z+z'+\omega) = 0$. The latter divide the complex plane into 16 regions, in each of which $F(z,z,\omega)$ is analytical in all of its arguments. Analogously to the bubble term, the integral performed along the proper contour in each region of the complex plane yields the corresponding analytic continuation. However, one can show that most of those contributions actually vanish as the analytically continued frequency $\Omega \to 0$, either because $\lambda_\alpha^{[k]} \to 0$, in this limit, if $k = 1, 3$ (according to the properties of the bare current vertex $\lambda_\alpha^{[k]}$, as discussed above), or due to the Fermi distribution function arising from the contour integral [89]. Hence, the only non vanishing contribution to the linear conductance has the form

$$\Lambda^{[2]}_{\mathrm{R};j_4 j_1}(\epsilon,\epsilon) = \lambda^{[2]}_{\mathrm{R}}(\epsilon,\epsilon)\delta_{j_1 N}\delta_{N j_4} + P^{[2]}_{\mathrm{R};j_4 j_1}(\epsilon,\epsilon), \tag{A.15}$$

where $P^{[2]}_{\mathrm{R};j_4 j_1}(\epsilon,\epsilon)$ has a complicated expression in terms of $F(\epsilon,\epsilon,0)$ and accounts for the vertex corrections. Hence, the scattering rates change accordingly as

$$\begin{aligned} \Gamma_{\mathrm{L}} &= 2\pi\rho_{\mathrm{L}} V_{\mathrm{L}}^2, \\ \Gamma_{\mathrm{R};j_4 j_1} &= 2\pi\rho_{\mathrm{R}} V_{\mathrm{R}}^2 \delta_{j_1 N}\delta_{N j_4} + P^{[2]}_{\mathrm{R};j_4 j_1}(\epsilon,\epsilon). \end{aligned} \tag{A.16}$$

The above results modify the (spin-independent) transmission coefficient (A.14) as

$$\mathcal{T}(\epsilon) = \sum_{j_1, j_4 \in S} \Gamma_{\mathrm{L}}(\epsilon) G^a_{1 j_4}(\epsilon) \Gamma_{\mathrm{R};j_4 j_1}(\epsilon,\epsilon) G^r_{j_1 1}(\epsilon), \tag{A.17}$$

yielding the final expression (1.80), which includes vertex corrections.

Appendix B

About the asymptotic behavior of correlation functions

In the HF-QMC method, widely employed within DMFT (and its extensions) as a solver for the impurity problem [93, 103, 113], one has to switch back and forth between the frequency and the time representations by means of a Fourier Transform (FT). The intrinsic limitation, imposed by the numerics, to a finite grid in any of the Fourier-conjugated domains deeply influences the accuracy of the FT, in particular concerning the asymptotic behavior of the Matsubara correlation functions (e.g., Green's functions and two-particle susceptibilities). An improper treatment of the asymptotic behavior may lead to inaccurate, possibly unphysical, results. Hence, the FT has to be performed with care.

In the following we discuss the usual method employed to improve the quality of the FT within HF-QMC, relying on an expansion in terms of its *spectral moments*. We focus mainly on the asymptotic behavior of the one-particle Green's function, while we also briefly discuss a possible strategy to be applied to the susceptibility. In particular we provide the details necessary to apply the method in the framework of the nanoscopic extension of DMFT. For the sake of clearness, below we recall the relevant multi-impurity Anderson Hamiltonian

$$\begin{aligned} H = &- \sum_{ij} \sum_{\sigma} t_{ij} c^{\dagger}_{i\sigma} c_{j\sigma} - \mu \sum_{i} \sum_{\sigma} c^{\dagger}_{i\sigma} c_{i\sigma} + U \sum_{i} c^{\dagger}_{i\uparrow} c_{i\uparrow} c^{\dagger}_{i\downarrow} c_{i\downarrow} \\ &+ \sum_{i\eta k} \sum_{\sigma} (V_{i\eta k} c^{\dagger}_{i\sigma} l_{\eta k\sigma} + V^{*}_{i\eta k} l^{\dagger}_{\eta k\sigma} c_{i\sigma}) + \sum_{\eta k} \sum_{\sigma} \epsilon_{\eta k\sigma} l^{\dagger}_{\eta k\sigma} l_{\eta k}, \end{aligned} \tag{B.1}$$

and the generic element of the inverse Matsubara one-particle Green's function

$$\left\{\hat{G}^{-1}\right\}_{ij}(\imath\nu_n) = \imath\nu_n \delta_{ij} + t_{ij} - \sum_{\eta k} \frac{V_{i\eta k} V^{*}_{j\eta k}}{\imath\nu_n - \epsilon_{\eta k}} - \Sigma_{ij}, \tag{B.2}$$

where we recall that i, j are the real-space indexes labeling the position of the sites of the nanostructure, while η labels the non-interacting environment with the dispersion relation $\epsilon_{\eta k}$.

Asymptotic behavior and FT within the HF-QMC. Within the nanoscopic extension of DMFT, one deals with electronic correlations by mapping the original system into a set of auxiliary AIMs. Each of the local AIM is defined by a Weiss field $\mathcal{G}_0(\imath\nu_n)$, and (within the present implementation) its numerical solution is obtained with a HF-QMC solver. However, in order to perform the QMC sampling, one needs to switch to the imaginary time domain, defining the FT of the Weiss field

$$\mathcal{G}_0(\tau) = \frac{1}{\beta}\sum_n \mathcal{G}_0(\imath\nu_n)\,\mathrm{e}^{\imath\nu_n\tau}. \tag{B.3}$$

In the HF-QMC, the sampling is performed on auxiliary fluctuating Ising fields, living on a discrete imaginary time grid in the interval $[0,\beta)$ [103]. The sampled data $G(\tau)$ can be projected back, by means of another FT, to the frequency domain

$$G(\imath\nu_n) = \int_0^\beta d\tau\, G(\tau)\,\mathrm{e}^{-\imath\nu_n\tau}, \tag{B.4}$$

where the Dyson equation is most conveniently evaluated, in order to extract the (local) self-energy. Due to the discrete sampling procedure, the number of *time slices* L spanning the time domain defines the Nyquist frequency $\pi L/\beta$ as the maximum frequency of the Fourier component that can be obtained without aliasing error. However, the accuracy of a discrete FT is poor already below the Nyquist frequency. The importance of obtaining a reliable FT in the whole frequency domain can be understood if one considers that many physical quantities are directly evaluated from the Green's function, e.g., the density $\langle n\rangle = 1 - G(\tau = 0^-)$, also related to the sum over the Matsubara frequencies of the Green's function.

In order to improve the asymptotic behavior of the one-particle Green's function, one relies on a high-frequency expansion in terms of the **spectral moments** $M_{ij}^{(k)}$, which are determined only by the Hamiltonian. The knowledge of few low-order spectral moments allows to determine the coefficient of a suitable polynomial **model function** $g(\imath\nu_n)$ for which (i) the asymptotic behavior is the same as the one of the original Green's function, and (ii) the corresponding FT $g(\tau)$ is known *analytically*. While the model function recovers the asymptotic behavior of the Green's function in the high-frequency regime, it presumably provides a poor description of the low-energy physic of the system, enclosed in the Green's function. Hence, provided the output of the QMC sampling, one can define

$$\Delta g(\tau) := G(\tau) - g(\tau), \tag{B.5}$$

so that the FT (B.4) can be written as

$$G(\imath\nu_n) = g(\imath\nu_n) + \int_0^\beta d\tau\, \Delta g(\tau)\,\mathrm{e}^{-\imath\nu_n\tau} = g(\imath\nu_n) + \Delta g(\imath\nu_n), \tag{B.6}$$

where the FT of the difference function $\Delta g(\tau)$ has to be performed numerically. However $\Delta g(\imath\nu_n)$, which encloses all the information about the low-energy physics, is *by construction* asymptotically vanishing for $\nu \to \infty$ and its numerical evaluation does not introduce any errors in the asymptotic behavior of the Green's function.

While the above construction allows for an analytical treatment of the asymptotic behavior, the numerical FT $\tau \to \nu$ is still unstable, as the range in which $\Delta g(\imath\nu_n)$ is required, usually extends far above the Nyquist frequency $\pi L/\beta$. In order to overcome this problem, one usually employs a *spline interpolation* of $\Delta g(\tau)$ which yields the difference function on a finer grid: $L \to \tilde{L} \gg L$, corresponding to a lareger Nyquist frequency. A possible implementation of the spline, including physical boundary conditions for the interpolation, is also discussed in this appendix.

An analogous procedure is required to evaluate the FT (B.3) involving the Weiss field (although this usually requires no additional interpolation). In particular, a careful treatment of the asymptotic behavior of both the one-particle Green's function and the Weiss field is relevant for the evaluation of the self-energy, obtained by the Dyson equation

$$\Sigma(\imath\nu_n) = \mathcal{G}_0{}^{-1}(\imath\nu_n) - G^{-1}(\imath\nu_n), \tag{B.7}$$

which tends to be unstable in the high-frequency regime due to the matrix inversions. Within DMFT (and its extensions) the whole FT procedure discussed above, and represented schematically in Fig. B.1, has to be performed at each step of the self-consistency loop.

Spectral moments of the one-particle Green's function. The expansion of the Green's function in terms of the spectral moments can be obtained considering its Lehmann representation

$$G_{ij}(\imath\nu_n) = \frac{1}{\mathcal{Z}} \sum_{\ell m} \left[\frac{\mathrm{e}^{-\beta\epsilon_\ell} + \mathrm{e}^{-\beta\epsilon_m}}{\imath\nu_n + \epsilon_\ell - \epsilon_m} \right] \langle \ell | c_i | m \rangle \langle m | c_j^\dagger | \ell \rangle. \tag{B.8}$$

Exploiting the identity

$$(\imath\nu_n + \epsilon_\ell - \epsilon_m)^{-1} = \frac{1/\imath\nu_n}{1 - \dfrac{\epsilon_m - \epsilon_\ell}{\imath\nu_n}} = \frac{1}{\imath\nu_n} \sum_{k=0}^{\infty} \left(\frac{\epsilon_m - \epsilon_\ell}{\imath\nu_n} \right)^k, \tag{B.9}$$

some algebra, and the cyclic property of the trace, yield

$$G_{ij}(\imath\nu_n) = \sum_{k=0}^{\infty} \left(\frac{1}{\imath\nu_n} \right)^{k+1} M_{ij}^{(k)} := \sum_{k=0}^{\infty} \left(\frac{1}{\imath\nu_n} \right)^{k+1} \langle \{ L^k c_i, c_j^\dagger \} \rangle \tag{B.10}$$

where $L^k c_i = \big[\dots \big[[c_i, \mathcal{H}], \mathcal{H} \big], \dots, \mathcal{H} \big]$, i.e., the commutator of the annihilation operator with the Hamiltonian, iterated k times, and $\langle \mathcal{O} \rangle$ denotes the thermal average of the operator $\mathcal{O}$.

If we consider Hamiltonian (B.1), where for convenience the chemical potential μ is included into the definition of the local elements of t_{ij}, then the lowest order spectral moments appearing

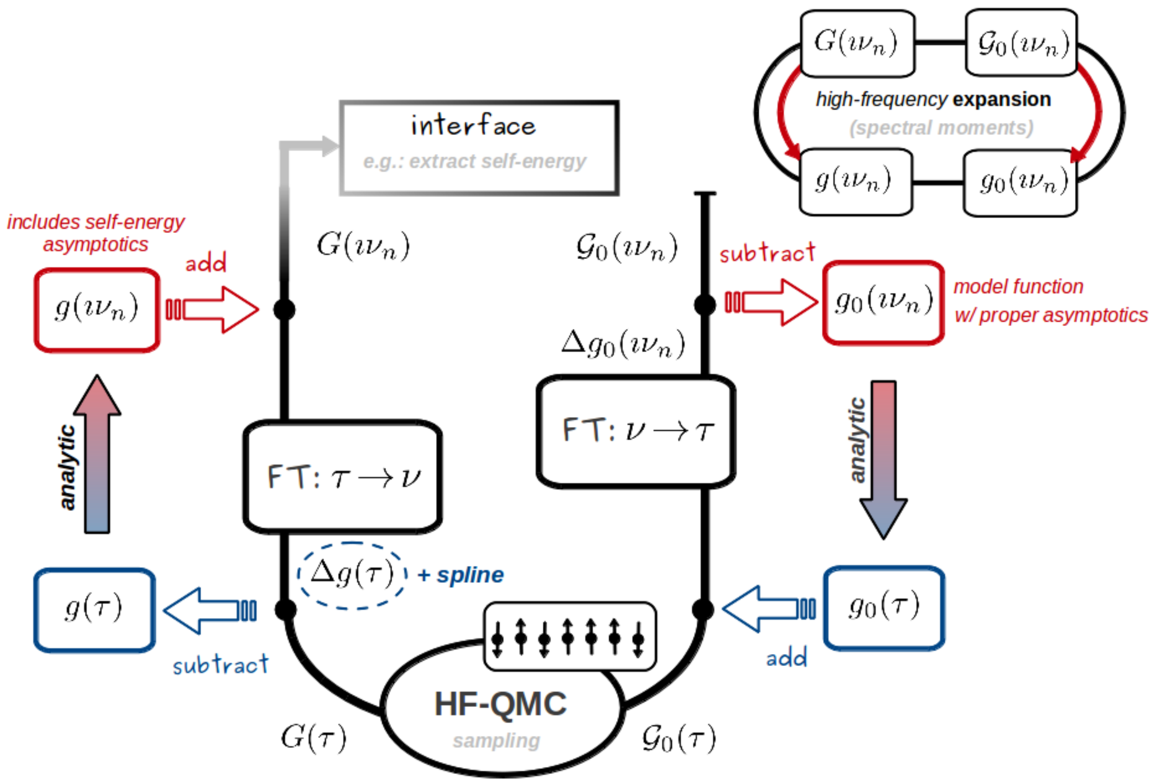

Figure B.1: Advanced FT scheme to properly treat the asymptotic behavior of the one-particle Green's function and of the Weiss field within HF-QMC,

in the expansion (B.10) are given by

$$M^{(k)}_{ij\sigma} = \begin{cases} \delta_{ij} & k=0 \\ -t_{ij} + U\langle n_{i-\sigma}\rangle\delta_{ij} & k=1 \\ \sum_{\ell} t_{i\ell}t_{\ell j} - Ut_{ij}(\langle n_{i-\sigma}\rangle + \langle n_{j-\sigma}\rangle) + U^2\langle n_{i-\sigma}\rangle\delta_{ij} + \sum_{\eta k} V_{i\eta k}V^*_{j\eta k} & k=2, \end{cases} \tag{B.11}$$

where the spin index σ has been restored to highlight the cross dependence of $M^{(k)}_{\sigma}$ on $\langle n_{-\sigma}\rangle$.

Spectral moments of the self-energy. The expression for the spectral moment expansion of the self-energy can be obtained in the following way. We consider the real-space Dyson equation (B.2) retrieving only the lowest orders in $\imath\nu_n$ in the expansion of the hybridization function, and introducind the expansion of the self-energy, as

$$\{G^{-1}\}_{ij}(\imath\nu_n) \approx \imath\nu_n\delta_{ij} + t_{ij} - \frac{1}{\imath\nu_n}\sum_{\eta k} V_{i\eta k}V^*_{j\eta k}\left[1 + \frac{\epsilon_k}{\imath\nu_n} + \dots\right] - \Sigma^{(0)}_{ij} - \Sigma^{(1)}_{ij}/\imath\nu_n, \tag{B.12}$$

while a general expansion for the the Green's function $G_{ij}(\imath\nu)$ reads

$$G_{ij}(\imath\nu_n) \approx \left(\frac{1}{\imath\nu_n}\right)c^{(0)}_{ij} + \left(\frac{1}{\imath\nu_n}\right)^2 c^{(1)}_{ij} + \left(\frac{1}{\imath\nu_n}\right)^3 c^{(2)}_{ij}. \tag{B.13}$$

The aim is to obtain an expression for the coefficients $c^{(k)}$ in terms of the unknown spectral moments of the self-energy $\Sigma^{(k)}$, so that the latter can be extracted from the comparison between the expansions (B.10) and (B.13) of the Green's function. Being careful about its matrix nature, the Green's function (B.12) can be inverted and expanded, yielding the coefficients

$$c_{ij}^{(k)} = \begin{cases} \delta_{ij} & k=0 \\ -t_{ij} + \Sigma_{ij}^{(0)} & k=1 \\ \sum_{\eta k} V_{i\eta k} V_{j\eta k}^{*} + \Sigma_{ij}^{(1)} + \sum_{\ell} \big(t_{i\ell} + \Sigma_{i\ell}^{(0)}\big)\big(t_{\ell j} + \Sigma_{\ell j}^{(0)}\big) & k=2. \end{cases} \tag{B.14}$$

Imposing $c_{ij}^{(k)} \overset{!}{=} M_{ij}^{(k)}$ yields eventually the spectral moments of the self-energy

$$\Sigma_{ij\sigma}^{(k)} = \begin{cases} U\langle n_{i-\sigma}\rangle \delta_{ij} & k=0 \\ U^2 \langle n_{i-\sigma}\rangle \big(1 - \langle n_{i-\sigma}\rangle\big)\delta_{ij} & k=1. \end{cases} \tag{B.15}$$

Let us notice, that the $k=0$ and $k=1$ spectral moments $\Sigma^{(k)}$ of the self-energy are purely local due to a non-trivial cancellation between the moments $M^{(k)}$, which holds in general for any Hubbard-like Hamiltonian, see e.g. Refs. [277, 278].

Spectral moments of the Weiss field. In the following we show that the Weiss field $\mathcal{G}_0$ of the auxiliary AIMs, defined as

$$\mathcal{G}_{0i}{}^{-1}(\imath\nu_n) = \big\{G_{ii}\big\}^{-1}(\imath\nu_n) + \Sigma_{ii}(\imath\nu_n), \tag{B.16}$$

has the same spectral moments of the local element of the non-interacting Green's function of the whole nanostructure. The latter property holds generally for any Weiss field corresponding to a subset of degrees of freedom of the system; in particular it holds in the case of $d{+}p$ models for strongly correlated materials, where electronic correlation are treated within DMFT (and hence the auxiliary AIM is defined) only in the subset of the d orbitals.

In order to be proven, the above statement requires the evaluation of the high-frequency expansion of $\big\{G_{ii}\big\}^{-1}(\imath\nu_n)$, together with the spectral moments (B.15) of the self-energy, to be plugged in the Dyson equation (B.16). The former can be obtained considering the expansion of the inverse of the local element of (B.13), which reads

$$\big\{G_{ii}\big\}^{-1}(\imath\nu_n) \approx \imath\nu_n \bigg\{ c_{ii}^{(0)} - \frac{1}{\imath\nu_n} c_{ii}^{(1)} + \Big(\frac{1}{\imath\nu_n}\Big)^2 \Big[\big(c_{ii}^{(1)}\big)^2 - c_{ii}^{(2)}\Big]\bigg\}. \tag{B.17}$$

Adding the high-energy expansion for the $\Sigma_{ii}(\imath\nu_n)$ and substituting the explicit form (B.14) for the local coefficients $c_{ii}^{(k)}$, the moments of the self-energy cancel out, eventually yielding

$$\big\{\mathcal{G}_{0i}\big\}^{-1}(\imath\nu_n) \approx \imath\nu_n + t_{ii} - \sum_{\eta k} V_{i\eta k} V_{i\eta k}^{*} - \sum_{\ell \neq i} t_{i\ell} t_{\ell i}. \tag{B.18}$$

The latter result is obtained evaluating carefully the expression $\left(c_{ii}^{(1)}\right)^2 - c_{ii}^{(2)}$ for all ℓ, as

$$\left(c_{ii}^{(1)}\right)^2 - c_{ii}^{(2)} = \Big(-t_{ii} + \Sigma_{ii}^{(0)}\Big)^2 - \sum_{\ell}\left(t_{i\ell} + \Sigma_{i\ell}^{(0)}\right)\left(t_{\ell i} + \Sigma_{\ell i}^{(0)}\right) - \sum_{\eta k} V_{i\eta k} V_{i\eta k}^{*} - \Sigma_{ii}^{(1)}$$

$$\text{implying} \quad \left(c_{ii}^{(1)}\right)^2 - c_{ii}^{(2)} = \begin{cases} -\sum_{\eta k} V_{i\eta k} V_{i\eta k}^{*} - \Sigma_{ii}^{(1)} & l = i \\ -\sum_{\eta k} V_{i\eta k} V_{i\eta k}^{*} - \Sigma_{ii}^{(1)} - \sum_{\ell \neq i} t_{i\ell} t_{\ell i} & l \neq i \end{cases} . \tag{B.19}$$

Finally the expansion of the inverse Weiss field (B.18) reads

$$\mathcal{G}_{0i}(\imath\nu_n) \approx \Big(\frac{1}{\imath\nu_n}\Big) d_{ij}^{(0)} + \Big(\frac{1}{\imath\nu_n}\Big)^2 d_{ij}^{(1)} + \Big(\frac{1}{\imath\nu_n}\Big)^3 d_{ij}^{(2)}. \tag{B.20}$$

where the coefficients

$$\begin{aligned} d_{ij}^{(0)} &= 1 \\ d_{ij}^{(1)} &= -t_{ii} \\ d_{ij}^{(2)} &= \sum_{\eta k} V_{i\eta k} V_{i\eta k}^{*} + \sum_{\ell} t_{i\ell} t_{\ell i}, \end{aligned} \tag{B.21}$$

coincide with the expansion coefficients $c_{ii}^{(k)}$ of the Green's function, given in (B.14), in the absence of the self-energy.

High-frequency models for the one-particle Green's function. Finally, it is necessary to define two independent model, for the *diagonal* (i.e., in the case $i = j$) and the *off-diagonal* ($i \neq j$) elements of the Green's function. For convenience, hereafter we adopt the notation $\imath\nu_n = z$, substituing the Matsubara frequency with the complex variable z.
An appropriate **diagonal model** reads

$$g_{\text{dia}}(z) = \frac{1}{z - a - b/(z-c)} \overset{c=0}{\simeq} \frac{1}{z} + a\frac{1}{z^2} + (b + a^2)\frac{1}{z^3}, \tag{B.22}$$

where $c \neq 0$ would including higher order contributions in the series above. By the comparison of the high-frequency expansions of the model (B.22) and of the system Green's function (B.10), one can easily extract the coefficients of the model

$$\begin{cases} a = M_{ii}^{(1)} \\ b = M_{ii}^{(2)} - \left(M_{ii}^{(1)}\right)^2, \end{cases} \tag{B.23}$$

and its FT can be obtained performing the Matsubara sum in the complex z plane, as

$$T\sum_{n} \frac{\mathrm{e}^{-\imath\nu_n\tau}}{\imath\nu_n - z_0} = \frac{1}{2\pi\imath}\oint f(z)\frac{\mathrm{e}^{-z\tau}}{z - z_0} dz = f(z_0)\mathrm{e}^{-z_0\tau} \quad \tau < 0, \tag{B.24}$$

where $f(z)$ is the Fermi function. The expression of the FT for positive imaginary time $\tau > 0$ is recovered exploiting antiperiodic property of the fermionic imaginary time Green's function

$$G(\tau > 0) = -G(\tau - \beta). \tag{B.25}$$

In order to perform the Matsubara sum (B.24) it is necessary to reduce the model function to simple fractions, as

$$g_{\text{dia}}(z) = \frac{1}{z_+ - z_-}\left(\frac{z_+}{z - z_+} + \frac{z_-}{z - z_-}\right) \tag{B.26}$$

where z_+ and z_- are the roots of $g_{\text{dia}}^{-1}(z) = 0$. Relations (B.24) and (B.25) yield the FT of the local model

$$g_{\text{dia}}(\tau > 0) = \frac{1}{z_+ - z_-}\left[(-1)(z_+)\frac{\mathrm{e}^{-z_+(\tau-\beta)}}{\mathrm{e}^{z_+\beta} + 1} + (z_-)\frac{\mathrm{e}^{-z_-(\tau-\beta)}}{\mathrm{e}^{z_-\beta} + 1}\right]. \tag{B.27}$$

Analogously, an appropriate **off-diagonal model** reads

$$g_{\text{off}}(z) = \frac{a}{z^2 - bz - c} \stackrel{c=0}{=} \frac{a}{z^2(1 - b/z)} \simeq \frac{a}{z^2} + \frac{ab}{z^3}, \tag{B.28}$$

yielding the coefficients

$$\begin{cases} a = M_{ij}^{(1)} \\ b = M_{ij}^{(2)}/M_{ij}^{(1)}, \end{cases} \tag{B.29}$$

with the additional condition that $g_{\text{off}} = 0$ trivially, if the corresponding $t_{ij} = 0$. Reducing the non-local model to simple fractions form yields

$$g_{\text{off}}(z) = \frac{a}{z(z-b)} = \frac{a}{b}\left(\frac{1}{z-b} - \frac{1}{z}\right) \tag{B.30}$$

and to the corresponding FT

$$g_{\text{off}}(\tau > 0) = \frac{a}{b}\left[\frac{1}{2} - \frac{\mathrm{e}^{-b(\tau-\beta)}}{\mathrm{e}^{b\beta} + 1}\right]. \tag{B.31}$$

In the particular case in which $g^{-1}(z)$ (either diagonal or off-diagonal) has a **double pole** the model is reduced to the form

$$g_{\text{double}}(z) = \frac{d}{(z - z_0)^2}, \tag{B.32}$$

with the coefficients being $d = 1$ and $z_0 = a/2$ in the former and $d = a$ and $z_0 = 0$ in the latter case. Hence, the corresponding FTs are given by

$$g_{\text{double}}(\tau > 0) = \frac{\mathrm{e}^{-z_0(\tau-\beta)}}{\mathrm{e}^{z_0\beta} + 1}\left[\frac{\mathrm{e}^{z_0\beta}}{\mathrm{e}^{z_0\beta} + 1}\beta + (\tau - \beta)\right]. \tag{B.33}$$

Once the approximating functions are known in both domains, one only needs to perform the numerical FT of the difference between the Green's function and the corresponding model.

Interpolation: cubic spline. As already discussed, in addition to the expansion and to the definition of the approximating models by means of the moments of the Green's function, we need a spline interpolation of the QMC Green's function (more precisely, of the difference with its model) in the imaginary time domain $[0, \beta)$. A brief derivation and the numerical implementation of the standard scheme is provided, e.g., in Ref. [279]. In the following we recall the basic steps in order to stress the important choice of the *boundary conditions*. A spline interpolation is necessary to get a $G(\tau)$ with as many points as needed in order to get a reasonably accurate FT.

In general, given a tabulated function $y_i = y(x_i)$ with $i = 1, \ldots, N$ and given also the second derivatives of the function at these points, it is possible to interpolate the function and compute its value in any given point within the whole interval $[x_1, x_N]$. While the spline is, *by definition*, a polynomial constrained to pass through all the points of the tabulated function $y(x_i)$, in order to obtain a spline which is *smooth* in the first derivative, and *continuous* in the second derivative, one needs to employ a cubic polynomial , defined by

$$y = Ay_i + By_{i+1} + \frac{1}{6}\Big(A^3 - A\Big)\big(x_{j+1} - x\big)^2 y_i'' + \frac{1}{6}\Big(B^3 - B\Big)\big(x_{j+1} - x\big)^2 y_{i+1}''. \tag{B.34}$$

It is easy to verify that this form grants that $y_i'' = y''(x_i)$, and it is trivial to obtain the second derivative of the polynomial,

$$y'' = Ay_i'' + By_{i+1}''. \tag{B.35}$$

At this point, the math assures that one is able to obtain the interpolating function in any point within the interval $[x_1, x_N]$. A set of $N-2$ equations can indeed be obtained requiring the first derivatives to be continuous across boundaries between two intervals (obviously one cannot require this condition for both the extreme points of the interval). The condition reads, hence, for each value of the index j

$$\left.\frac{dy}{dx}\right|_{x=x_{j+1}}^{(j)} \stackrel{!}{=} \left.\frac{dy}{dx}\right|_{x=x_j}^{(j+1)}, \tag{B.36}$$

resulting in a set of equations for $j = 2, \ldots N-1$, which reads

$$\frac{y_{j+1} - y_j}{x_{j+1} - x_j} - \frac{y_j - y_{j-1}}{x_j - x_{j-1}} = \frac{1}{6}\big(x_{j+1} - x_j\big)y_{j+1}'' + \frac{1}{3}\big(x_{j+1} - x_{j-1}\big)y_j'' + \frac{1}{6}\big(x_j - x_{j-1}\big)y_{j-1}''. \tag{B.37}$$

If one consider , for the sake of simplicity, the case of a homogeneous mesh, i.e., $h \equiv x_{j+1} - x_j$ for each $j = 2, \ldots, N-1$, the system can be easily written in the compact matrix form

$$\begin{pmatrix} 1 & 4 & 1 & 0 & 0 & \ldots & 0 & 0 \\ 0 & 1 & 4 & 1 & 0 & \ldots & 0 & 0 \\ 0 & 0 & 1 & 4 & 1 & \ldots & 0 & 0 \\ \vdots & & & \ddots & \ddots & \ddots & & \vdots \\ 0 & 0 & \ldots & 0 & 1 & 4 & 1 & 0 \\ 0 & 0 & \ldots & 0 & 0 & 1 & 4 & 1 \end{pmatrix} \begin{pmatrix} y_1'' \\ y_2'' \\ \vdots \\ \vdots \\ y_N'' \end{pmatrix} = \frac{6}{h^2} \begin{pmatrix} y_1 - 2y_2 + y_3 \\ y_2 - 2y_3 + y_4 \\ \vdots \\ \vdots \\ y_{N-2} - 2y_{N-1} + y_N \end{pmatrix}.$$

However, the set contains N unknowns, i.e., the set of derivatives $\{y''_i\}$, but only $N-2$ linear equations, and is therefore not solvable until the two remaining conditions are imposed. The simplest **boundary conditions** would require the second derivative at the extreme points of the interval to be vanishing: this method is currently known as *natural* spline, and yields a tridiagonal system (which can be solved in $O(N)$ operations) in terms of the unknowns y''_i for $i=2,\dots,N-1$. However, the latter condition is *not* consistent with the physical (and mathematical) properties of the imaginary time Green's function, and may yield unstable results (see, e.g., Ref. [112] and references therein). More physically sensible conditions can be imposed considering that the function to interpolate interpolate, $\Delta g_{ij}(\tau) = G_{ij}(\tau) - g_{ij}(\tau)$, verify the following conditions

$$\frac{dy}{dx}\bigg|_{x=x_1}^{(j=1)} + \frac{dy}{dx}\bigg|_{x=x_N}^{(j=N-1)} \stackrel{!}{=} 0 \tag{B.38a}$$

$$y''_1 + y''_N \stackrel{!}{=} 0, \tag{B.38b}$$

which follow from the presence of a (physical) discontinuity of the Green's function at $\tau=0$, determined by the *sum rule*

$$G(0^+) + G(\beta) = 1. \tag{B.39}$$

Imposing the equations (B.38a) and (B.38b), we modify the equations for $j=2$ and $j=N-1$, which depend on y''_1 and y''_N, while the others $N-4$ equations remain unchanged. Condition (B.38a) is indeed

$$\frac{y_2-y_1}{h} - \frac{1}{3}hy''_1 - \frac{1}{6}hy''_2 + \frac{y_N-y_{N-1}}{h} + \frac{1}{6}hy''_{N-1} + \frac{1}{3}hy''_N = 0. \tag{B.40}$$

Using relation (B.38b), i.e. replacing y''_N with $-y''_1$ and solving for the latter, leads finally to

$$y''_1 = \frac{1}{4}\left\{\frac{6}{h^2}\Big(y_N - y_{N-1} + y_2 - y_1\Big) - y''_2 + y''_{N-1}\right\}. \tag{B.41}$$

Substituting this expression in equations $j=2$ and $j=N-1$ and using relation (B.38b) in the latter again, one eventually obtain the following equations: for $j=2$

$$\frac{6}{h^2}\Big(\frac{5}{4}y_1 - \frac{9}{4}y_2 + y_3 + \frac{1}{4}y_{N-1} - \frac{1}{4}y_N\Big) = \frac{15}{4}y''_2 + y''_3 + \frac{1}{4}y''_{N-1} \tag{B.42}$$

while for $j=N-1$

$$\frac{6}{h^2}\Big(-\frac{1}{4}y_1 + \frac{1}{4}y_2 + y_{N-2} - \frac{9}{4}y_{N-1} + \frac{5}{4}y_N\Big) = \frac{1}{4}y''_2 + y''_{N-2} + \frac{15}{4}y''_{N-1}. \tag{B.43}$$

The system in matricial form is therefore

$$\begin{pmatrix} \frac{15}{4} & 1 & 0 & 0 & \dots & \frac{1}{4} \\ 1 & 4 & 1 & 0 & \dots & 0 \\ 0 & 1 & 4 & 1 & \dots & 0 \\ \vdots & & \ddots & \ddots & \ddots & \vdots \\ 0 & 0 & \dots & 1 & 4 & 1 \\ \frac{1}{4} & 0 & \dots & 0 & 1 & \frac{15}{4} \end{pmatrix} \begin{pmatrix} y''_2 \\ y''_3 \\ \vdots \\ \vdots \\ y''_{N-1} \end{pmatrix} = \frac{6}{h^2} \begin{pmatrix} \frac{5}{4}y_1 - \frac{9}{4}y_2 + y_{N-2} + \frac{1}{4}y_{N-1} - \frac{1}{4}y_N \\ y_2 - 2y_3 + y_4 \\ \vdots \\ \vdots \\ -\frac{1}{4}y_1 + \frac{1}{4}y_2 + y_{N-2} - \frac{9}{4}y_{N-1} + \frac{5}{4}y_N \end{pmatrix}$$

The system is now solvable, but no more tridiagonal due to more complex boundary conditions. The knowledge of the second derivatives of the tabulated function allows to interpolate it in any point within the interval $[x_1, x_N]$.

Representative results. In order to illustrate the accuracy of the method, in Fig. B.2 are shown representative results, obtained for the exact QMC solution of a benzene ring in the *NN t* hopping configuration, for the standard parameters $U = 2t$, $V = 0$ and $T = 0.05t$ (compare with the extensive discussion in Sec. 3.2 and the corresponding subsections). In the upper left panel we compare the result of a naïve discrete FT against the one obtained by means of the spectral moment expansion and a spline interpolation: the former shows oscillatory behavior with zeros (or poles, in the general case) at multiples of the Nyquist frequency instead of displaying an $1/\nu_n$

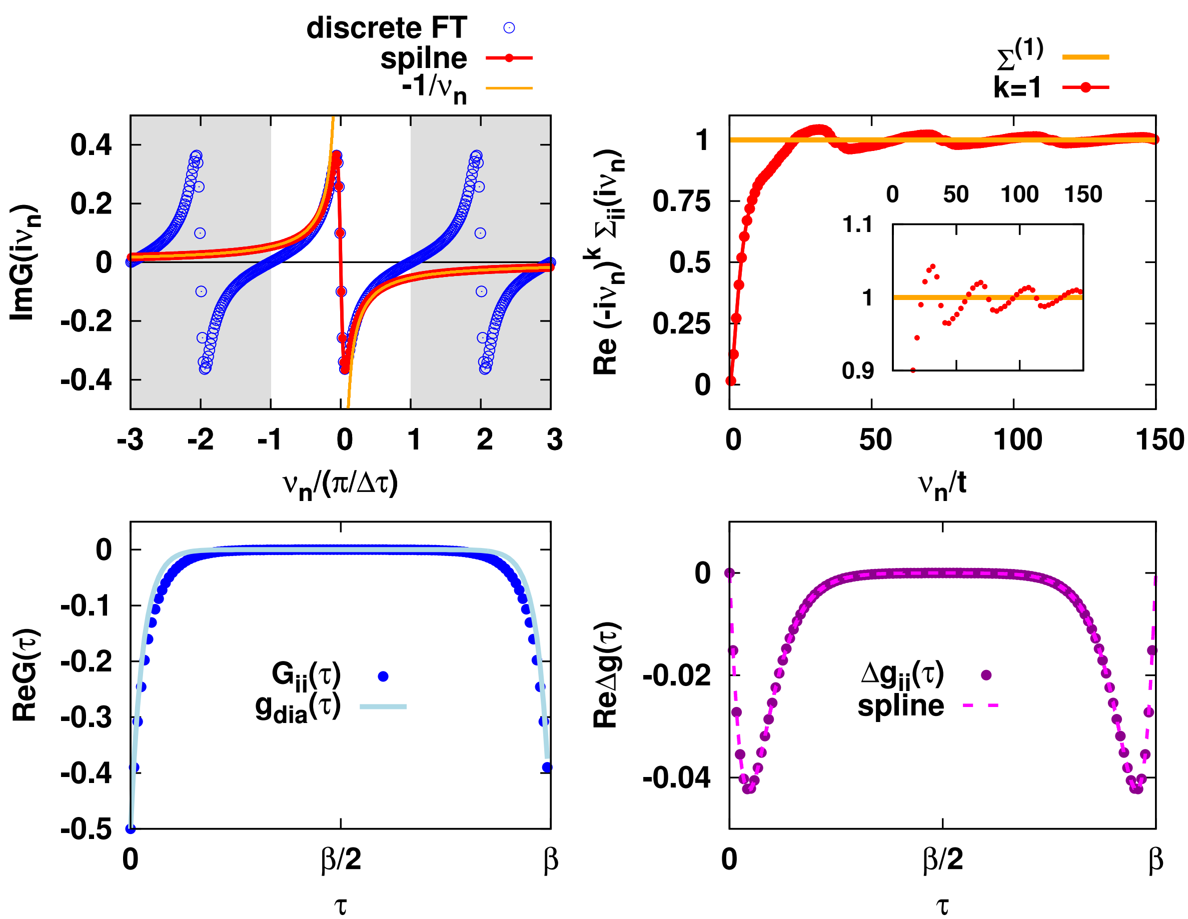

Figure B.2: Upper panel: comparison of a naïve FT (open cirles) and an advance spline (red filled symbols) based on the spectral moment (orange) expansion of the Green's function (left panels); asymptotic behavior of the local self-energy, given by $\Sigma^{(1)} = U^2\langle n\rangle\big(1-\langle n\rangle\big)$ (right panel). Lower panels: local Green's function $G_{ii}(\tau)$ against the corresponding model $g_{\text{dia}}(\tau)$ (left panel); difference function $\Delta g_{ii}(\tau)$ and its spline interpolation (right panel).

asymptotic behavior at high-frequency. In general, the low-energy physics cannot be described correctly by a $1/\imath\nu_n$ term, in particular in the present case, where the system is insulating. In the upper right panel the asymptotic behavior of the local self-energy is shown: the latter decays to its spectral moment $\Sigma^{(1)} = U^2\langle n\rangle\big(1-\langle n\rangle\big)$ in the high-frequency regime. Note that, due to the numerical implementation of the QMC, the results presented here (and in the rest of this work) are consistent with $\Sigma^{(0)} = 0$, as the Hartree shift $U\langle n\rangle$, which determines the frequency-independent contribution of the self-energy is already taken into account in a shift of the chemical potential. Finally, the lower panels show the local Green's function $G_{ii}(\tau)$ against the corresponding model $g_{\text{dia}}(\tau)$ (left panel) and the difference function $\Delta g_{ii}(\tau) = G_{ii}(\tau)–g_{\text{dia}}(\tau)$ with its *sum rule* spline interpolation (right panel).

Asymptotic behavior of correlation functions. The whole scheme is not limited to the one-particle Green's function, but can also be extended to susceptibilities, yet not without supplementary difficulties. Within this work, in order to obtain a reliable asymptotic behavior for the generalized susceptibility, we employed an ED impurity solver which relies on its Lehmann representation and requires, hence, no FT at all. However, QMC still represents the most natural choice for for complex systems, e.g, clusters with many atoms or including orbital degrees freedom. Hence, for the sake of completeness, in the following we briefly discuss how a proper FT of the susceptibility can be achieved within the HF-QMC, and remand to Ref. [112] and references therein for a deeper reading.

While the one-particle Green's function $G(\tau)$ is a smooth function of τ, with a single discontinuity at $\tau = 0$, the two-particle Greens function depends on three independent imaginary time variables, e.g., see the definition of the generalized susceptibility (in the *ph* notation) introduced in the context of the AIM, and reported below for the sake of clarity

$$\begin{aligned}\chi^{\nu\nu'\omega}_{ph,\sigma\sigma'} &:= \chi\big(\underbrace{\nu\sigma,(\nu+\omega)\sigma}_{\text{outgoing electrons}};\underbrace{\nu'\sigma',(\nu'+\omega)\sigma'}_{\text{incoming electrons}}\big) = \\ &= \int_0^\beta d\tau_1 d\tau_2 d\tau_3\, \chi_{\sigma\sigma'}(\tau_1,\tau_2,\tau_3)\mathrm{e}^{-i\nu\tau_1}\mathrm{e}^{i(\nu+\omega)\tau_2}\mathrm{e}^{-i(\nu'+\omega)\tau_3},\end{aligned} \tag{B.44}$$

with

$$\chi_{\sigma\sigma'}(\tau_1,\tau_2,\tau_3) = \Big\langle T_\tau c^\dagger_\sigma(\tau_1)c_\sigma(\tau_2)c^\dagger_{\sigma'}(\tau_3)c_{\sigma'}(0)\Big\rangle. \tag{B.45}$$

In the case of DCA or cellular-DMFT [134], the correlation function would also depend on the the three vectors k, k', q of the Brillouin zone of the cluster. It is evident that a direct FT, and the corresponding spline process, is extremely expensive and intrinsically inaccurate. The main reason for it, is the complex structure of discontinuity lines and planes in the tridimensional τ space, but also to the non-trivial task of performing a multi-dimensional spline.

Hence, the correlation function (B.44) can be obtained in the frequency and reciprocal space by contracting the fermionic operators pairwise and evaluating the corresponding FT for each configuration of the auxiliary fields in the HF-QMC. Note that this is only possible as for a given configuration the Wick's theorem [67] holds, as the Hubbard-Stratonovich transformation of the interaction term maps the many-body Hamiltonian into an ensemble of decoupled auxiliary fields [103]. Hence, the evaluation of the correlation function requires the FT (for a very large number of configuration) of a functions $g(\tau_i, \tau_j)$ which displays singularities. However, it is possible to split up $g(\tau_i, \tau_j)$ as

$$g(\tau_i, \tau_j) = g^{(0)}(\tau_i - \tau_j) + \delta g(\tau_i, \tau_j). \tag{B.46}$$

where

$$g^{(0)}(\tau_i) = \frac{1}{L} \sum_{j=i}^{L} g(\tau_{i+j-1}, \tau_j), \tag{B.47}$$

doe *not* indicate a non-interacting Green's function, but rather the time translationally invariant part of $g(\tau_i, \tau_j)$ and depends on one τ variable. One can show that $g^{(0)}(\tau_i)$ contains the singularity, but as it only depends on the difference $\tau_i - \tau_j$, it can be easily FT using a spline, in the same spirit as discussed above. The rest $\delta g(\tau_i, \tau_j)$ is a smooth function, and can be accurately FT by fitting it with a two-dimensional polynomial. Overall, this decomposition allows to achieve reliable results even if $g(\tau_i, \tau_j)$ is only known on a rather sparse mesh [112].

It is worth mentioning at least an alternative method to obtain a reliable asymptotic behavior or two-particle correlation functions within DMFT, which has been recently proposed by Kuneŝ [219]. While it has been implemented for a HF-QMC, it is nevertheless, general, and do not rely on any assumption on the impurity solver.

In this scheme, the two-particle correlation functions (B.44) is split into a low- and high-frequency regions. The complication, with respect to the case of the one-particle Green's function or the self-energy, is that the low- and high-frequency regions are coupled, as it can be easily seen recasting the correlation function (in a given channel r) as

$$\chi^{\nu\nu'\omega} = \chi_0^{\nu\nu_1\omega} - \chi_0^{\nu\nu_1\omega} \Gamma_r^{\nu_1\nu_2\omega} \chi^{\nu_2\nu'\omega}, \tag{B.48}$$

where $\chi_0^{\nu\nu'\omega} = -\beta G(\nu) G(\nu+\omega) \delta_{\nu\nu'}$ is the particle-hole bubble, and $\Gamma_r^{\nu\nu'\omega}$ is the vertex function irreducible n channel the corresponding channel. This easily shown considering the definition of the susceptibility if terms of the full vertex $F^{\nu\nu'\omega}$ and the Bethe-Salpeter equation relating it to the irreducible vertex $\Gamma_r^{\nu\nu'\omega}$ (cf. also with Sec. 2.3.2 for a detailed discussion of the diagrammatic formalism): plugging the latter into the former eventually yields relation (B.48).
It is possible to show [219] that the asymptotic behavior of the two-particle correlation function is essentially determined by particle-hole bubbles, and hence by the one-particle Green's function, which is more easily accessible in a wide frequency domain.

Albeit the original method [219] was developed in the special case of a susceptibility corresponding to the response to a *static* perturbation, i.e., for a correlation function $\chi^{\nu\nu'\omega=0}$, an extension to finite ω has been recently carried out implemented within an ED impurity solver [166], in which the knowledge and the understanding of the key features in the frequency dependence of the local two-particle vertex functions [158] are exploited in order to identify the region where the vertex function display a non-perturbative behavior.

Bibliography

[1] R. P. Feynman, *There's plenty of room at the bottom*, Engeneeering and Science **43**, 22 (1960).

[2] M. W. Browne, *2 Researchers Spell 'I.B.M.', Atom by Atom*, New York Times (1990).

[3] K. E. Drexler, *Engines of Creation: The Coming Era of Nanotechnology*, Anchor Books, New York, (1986).

[4] Ph.D. comics, *buzzwords*, http://www.phdcomics.com/comics/archive.php?comicid=1252 (2009).

[5] G. Binnig, H. Rohrer, Ch. Gerber, and E. Weibel, *Surface Studies by Scanning Tunneling Microscopy* Phys. Rev. Lett. **49**, 57 (1982).

[6] G. Binnig and H. Rohrer, *Scanning tunneling microscopy from birth to adolescence*, Rev. Mod. Phys. **59**, 615 (1987).

[7] G. Binnig and H. Rohrer, *In touch with atoms*, Rev. Mod. Phys. **71**, 324 (1999).

[8] A. M. Smith, S. Dave, S. Nie, L. True, and X. Gao, *Multicolor quantum dots for molecular diagnostics of cancer*, Expert Rev. Mol. Diagn. **6**, 231 (2006).

[9] L. D. True and X. Gao, *Quantum dots for molecular pathology: their time has arrived*, J. Mol. Diagn. **9**, 7 (2007).

[10] M. A. Reed, J. N. Randall, R. J. Aggarwal, R. J. Matyi, T. M. Moore, and A. E. Wetsel, *Observation of Discrete Electronic States in a Zero-Dimensional Semiconductor Nanostructure*, Phys. Rev. Lett. **60**, 535 (1988).

[11] U Banin, Y. W. Cao, D. Katz, and O. Millo, *Identification of atomic-like electronic states in indium arsenide nanocrystal quantum dots*, Nature **400**, 542 (1999).

[12] V. N. Soloviev, A. Eichhöfer, D. Fenske, and U. Banin, *Molecular Limit of a Bulk Semiconductor: Size Dependence of the ''Band Gap'' in CdSe Cluster Molecules*, J. m. Chem. Soc. **122**, 2573 (2000).

[13] V. L. Colvin, M. C. Schlamp, and A. P. Alivisatos, *Light-Emitting-Diodes Made from Cadmium Selenide Nanocrystals and a Semiconducting Polymer*, Nature **370**, 354 (1994).

[14] P. K. Santra and P. V. Kamat, *Mn-Doped Quantum Dot Sensitized Solar Cells: A Strategy to Boost Efficiency over 5%*, J. Am. Chem. Soc. **134**, 2508 (2012).

[15] L. A. Ponomarenko, F. Schedin, M. I. Katsnelson, R. Yang, E. W. Hill, K. S. Novoselov, A. K. Geim, *Chaotic Dirac Billiard in Graphene Quantum Dots*, Science **320**, 356 (2008).

[16] R. M. Westervelt, *Graphene Nanoelectronics*, Science **320**, 324 (2008).

[17] M. A. Kastner, *The single-electron transistor*, Rev. Mod. Phys. **64**, 849 (1992).

[18] G. M. Jones, B. H. Hu, C. H. Yanga, M. J. Yang, R. Hajdaj, and G. Hehein, *Enhancement-mode metal-oxide-semiconductor single-electron transistor on pure silicon*, App. Phys. Lett. **89**, 073106 (2006).

[19] A. Morello, J. J. Pla, F. A. Zwanenburg, K. W. Chan, K. Y. Tan, H. Huebl, M. Möttönen, C. D. Nugroho, C. Yang, J. A. van Donkelaar, A. D. C.Alves, D. N. Jamieson, C. C. Escott, L. C. L. Hollenberg, R. G. Clark, and A. S. Dzurak. *Single-shot readout of an electron spin in silicon*, Nature **467**, 687 (2010).

[20] J. Kondo, *Resistance Minimum in Dilute Magnetic Alloys*, Prog. Theor. Phys. **32**, 37 (1964).

[21] A. C. Hewson, *The Kondo Problem to Heavy Fermions*, Cambridge University Press (1997).

[22] L. I. Glazman and M. E. Raikh, *Resonant Kondo transparency of a barrier with quasilocal impurity*, JETP Lett. **47**, 452 (1988).

[23] T. K. Ng and P. A. Lee, *On-site Coulomb repulsion and resonant tunneling*, Phys. Rev. Lett. **61**, 1768 (1988).

[24] D. Goldhaber-Gordon, H. Shtrikman, D. Mahalu, D. Abusch-Magder, U. Meirav, and M. A. Kastner, *Kondo effect in a single-electron transistor*, Nature **391**, 156 (1998).

[25] S. M. Cronenwett, T. H. Oosterkamp, and L. P. Kouwenhoven, *A Tunable Kondo Effect in Quantum Dots*, Science **281**, 540 (1998).

[26] W. G. van der Wiel, S. De Franceschi, T. Fujisawa, J. M. Elzerman, S. Tarucha, and L. P. Kouwenhoven, *The Kondo Effect in the Unitary Limit*, Science **289**, 2105 (2000).

[27] University of Basel, http://www.nanoelectronics.ch/research/molecular.php

[28] Royal Society of Chemistry, *Experimental Nanoscience for Undergraduates*.

[29] N. Agraït, A. Levy-Yeyati, J. M. van Ruitenbeek, *Quantum properties of atomic-sized conductors*, Phys. Reps. **377**, 81 (2003).

[30] B. J. van Wees, H. van Houten, C. W. J. Beenakker, J. G. Williamson, L. P. Kouwenhoven, D. van der Marel, and C. T. Foxon, *Quantized Conductance of Point Contacts in a Two-Dimensional Electron Gas*, Phys. Rev. Lett. **60**, 848 (1988).

[31] C. J. Muller, J. M. Krans, T. N. Todorov, and M. A. Reed, *Quantization effects in the conductance of metallic contacts at room temperature*, Phys. Rev. B **53**, 1022 (1996).

[32] J. M. Luttinger, *An Exactly Soluble Model of a Many-Fermion System*, J. Math. Phys. **4** 1154 (1963).

[33] S. Andergassen, V. Meden, H. Schoeller, J. Splettstösser, and M. R. Wegewijs, *Charge transport through single molecules, quantum dots and quantum wires*, Nanotechnology **21**, 272001 (2010).

[34] L. Venkataraman, J. E. Klare, C. Nuckolls, M. S. Hybertsen, and M. L. Steigerwald, *Dependence of single-molecule junction conductance on molecular conformation*, Nature **442**, 904 (2006).

[35] M. Reed, C. Zhou, C. J. Muller, T. P. Burgin, and J. M. Tour *onductance of a Molecular Junction*, Science **278**, 252 (1997).

[36] H. Park, A. K. L. Lim, A. Alivisatos, J. Park, and P. L. McEuen, *Fabrication of metallic electrodes with nanometer separation by electromigration*, Appl. Phys. Lett. **75**, 301 (1999).

[37] A. R. Champagne, A. N. Pasupathy, and D. C. Ralph, *Mechanically Adjustable and Electrically Gated Single-Molecule Transistors*, Nano Lett. **5**, 305 (2005).

[38] X. Xiao, B. Xu, and N. J. Tao, *Measurement of Single Molecule Conductance: Benzenedithiol and Benzenedimethanethiol*, Nano Lett. **4**, 267 (2004).

[39] M. Tsutsui, Y. Teramae, S. Kurokawa, and A. Sakai, *High-conductance states of single benzenedithiol molecules*, Appl. Phys. Lett. **89**, 163111 (2006).

[40] L. Olesen, E. Laegsgaard, I. Stensgaard, F. Besenbacher, J. Schiøtz, P. Stoltze, K. W. Jacobsen, and J. K. Nørskov, *Quantized conductance in an atom-sized point contact*, Phys. Rev. Lett. **72**, 2251 (1994); J. M. Krans, C. J. Muller, N. van der Post, F. R. Postma, A. P. Sutton, T. N. Todorov, and J. M. van Ruitenbeek, Phys. Rev. Lett. 74, 2146 (1995); Olesen *et al.*, Phys. Rev. Lett. **74**, 2147 (1995).

[41] J. M. Krans, J. M. van Ruitenbeek, V. V. Fisun, I. K. Yanson, and L. J. De Jongh, *The signature of conductance quantization in metallic point contacts*, Nature **375**, 767 (1995).

[42] E. Scheer, P. Joyez, D. Esteve, C. Urbina, and M. H. Devoret, *Conduction Channel Transmissions of Atomic-Size Aluminum Contacts*, Phys. Rev. Lett. **78**, 3535 (1997).

[43] J. C. Cuevas1, A. Levy-Yeyati, A. Martín-Rodero, G. Rubio Bollinger, C. Untiedt, and N. Agraït, *Evolution of Conducting Channels in Metallic Atomic Contacts under Elastic Deformation*, Phys. Rev. Lett. **81**, 2990 (1998).

[44] J. C. Cuevas, E. Scheer, *Molecular electronics: An Introduction to Theory and Experiments*, World Scientific Publishing (2010).

[45] M. Kiguchi, O. Tal, S. Wohlthat, F. Pauly, M. Krieger, D. Djukic, J. C. Cuevas, and J. M. van Ruitenbeek, *Highly Conductive Molecular Junctions Based on Direct Binding of Benzene to Platinum Electrodes*, Phys. Rev. Lett. **101**, 046801 (2008).

[46] A. A. Aligia, K. Hallberg, B. Normand, and A. P. Kampf, *Detection of Topological Transitions by Transport Through Molecules and Nanodevices*, Phys. Rev. Lett. **93**, 076801 (2004).

[47] N. Néel, J. Kröger, L. Limot, T. Frederiksen, M. Brandbyge, and R. Berndt, *Controlled Contact to a* C_60 *Molecule*, Phys. Rev. Lett. **98**, 065502 (2007).

[48] J. J. Parks, A. R. Champagne, G. R. Hutchison, S. Flores-Torres, H. D. Abruna, and D. C. Ralph, *Tuning the Kondo Effect with a Mechanically Controllable Break Junction*, Phys. Rev. Lett. **99**, 026601 (2007).

[49] N. Roch, S. Florens, V. Bouchiat, W. Wernsdorfer, and F. Balestro, *Quantum phase transition in a single-molecule quantum dot*, Nature **453**, 633 (2008).

[50] J. J. Parks, A. R. Champagne, T. A. Costi, W. W. Shum, A. N. Pasupathy, E. Neuscamman, S. Flores-Torres, P. S. Cornaglia, A. A. Aligia, C. A. Balseiro, G. K.-L. Chan, H. D. Abruña, D. C. Ralph, *Mechanical Control of Spin States in Spin*-1 *Molecules and the Underscreened Kondo Effect*, Science **328**, 1370 (2010).

[51] M. Karolak, D. Jacob, and A. I. Lichtenstein, *Orbital Kondo Effect in Cobalt-Benzene Sandwich Molecules*, Phys. Rev. Lett. **107**, 146604 (2011).

[52] J. Li, W.-D. Schneider, R. Berndt, and B. Delley, *Kondo Scattering Observed at a Single Magnetic Impurity*, Phys. Rev. Lett. **80**, 2893 (1998).

[53] V. Madhavan, W. Chen, T. Jamneala, M. F. Crommie, N. S. Wingreen, *Tunneling into a Single Magnetic Atom: Spectroscopic Evidence of the Kondo Resonance*, Science **280**, 567 (1998).

[54] M. Ternes, A. J. Heinrich, and W.-D. Schneider, *Spectroscopic manifestations of the Kondo effect on single adatoms*, J. Phys.: Condens. Matter **21**, 053001 (2009).

[55] N. Néel, J. Kröger, R. Berndt, T. O. Wehling, A. I. Lichtenstein, and M. I. Katsnelson, *Controlling the Kondo Effect in CoCu$_n$ Clusters Atom by Atom*, Phys. Rev. Lett. **101**, 266803 (2008).

[56] T. O. Wehling, A. V. Balatsky, M. I. Katsnelson, A. I. Lichtenstein, and A. Rosch, *Orbitally controlled Kondo effect of Co adatoms on graphene*, Phys. Rev. B **81**, 115427 (2010).

[57] S. J. Chorley, M. R. Galpin, F. W. Jayatilaka, C. G. Smith, D. E. Logan, and M. R. Buitelaar, *Tunable Kondo Physics in a Carbon Nanotube Double Quantum Dot*, Phys. Rev. Lett. **109**, 156804 (2012).

[58] E. A. Osorio, T. Bjørnholm, J.-M. Lehn, M. Ruben, and H. S. J. van der Zant, *Single-molecule transport in three-terminal devices*, J. Phys.: Condens. Matter **20**, 374121 (2008).

[59] R. Hanson, L. P. Kouwenhoven, J. R. Petta, S. Tarucha, L. M. K. Vandersypen, *Spins in few-electron quantum dots*, Rev. Mod. Phys. **79**, 1217 (2007).

[60] L. P. Kouwenhoven, D. G. Austing, and S. Tarucha, *Few-electron Quantum Dots*, Rep. Prog. Phys. **64**, 701 (2001)

[61] N. F. Mott, *The Basis of the Electron Theory of Metals, with Special Reference to the Transition Metals*, Proc. Phys. Soc. **62**, 416 (1949).

[62] N. F. Mott, *Metal-Insulator Transition*, Rev. Mod. Phys. **40**, 677 (1968).

[63] J. Friedel, *The distribution of electrons round impurities in monovalent metals*, Philosophical Magazine **43**, 153 (1952).

[64] P. W. Anderson, *Localized Magnetic States in Metals*, Phys. Rev. **124**, 41 (1961).

[65] B. T. Matthias, M. Peter, H. J. Williams, A. M. Clogston, E. Corenzwit, and R. C. Sherwood, *Magnetic Moment of Transition Metal Atoms in Dilute Solution and Their Effect on Superconducting Transition Temperature*, Phys. Rev. Lett. **5**, 542 (1960).

[66] P. Coleman, *Introduction to Many Body Physics*, Cambridge University Press (2012).

[67] G. D. Mahan, *Many-particle physics*, Plenum Publishers (1981).

[68] J. R. Schrieffer and P. A. Wolff, *Relation between the Anderson and Kondo Hamiltonians*, Phys. Rev. **149**, 491 (1966).

[69] A. A. Abrikosov, *Electron scattering on magnetic impurities in metals and anomalous resistivity effects*, Physics **2**, 5 (1965).

[70] H. Suhl, *Dispersion Theory of the Kondo Effect*, Phys. Rev. **138**, 515 (1965).

[71] P. Nozières, *A fermi-liquid description of the Kondo problem at low temperatures*, J. Low Temp. Phys. **17**, 31 (1974).

[72] P. W. Anderson, *A poor man's derivation of scaling laws for the Kondo problem*, J. Phys. C: Solid State Phys. **3**, 2436 (1970).

[73] K. G. Wilson, *The renormalization group: Critical phenomena and the Kondo problem*, Rev. Mod. Phys. **47**, 773 (1975).

[74] Y. Kanai, R. S. Deacon, S. Takahashi, A. Oiwa, K. Yoshida, K. Shibata, K. Hirakawa, Y. Tokura, and S. Tarucha, *Electrically tuned spin-orbit interaction in an InAs self-assembled quantum dot*, Nature Nanotechnology **6**, 511 (2011).

[75] S. Grap, V. Meden, and S. Andergassen, *Interplay of Coulomb interaction and spin-orbit effects in multilevel quantum dots*, Phys. Rev. B **86**, 035143 (2012).

[76] K. Grove-Rasmussen, S. Grap, J. Paaske, K. Flensberg, S. Andergassen, V. Meden, H. I. Jørgensen, *Magnetic-Field Dependence of Tunnel Couplings in Carbon Nanotube Quantum Dots*, Phys. Rev. Lett. **108**, 176802 (2012).

[77] M. A. Ruderman and C. Kittel, *Indirect Exchange Coupling of Nuclear Magnetic Moments by Conduction Electrons*, Phys. Rev. **96**, 99 (1954).

[78] T. Kasuya, *A Theory of Metallic Ferro- and Antiferromagnetism on Zener's Model*, Prog. Theor. Phys. **16**, 45 (1956).

[79] K. Yosida, *Magnetic Properties of Cu-Mn Alloys*, Phys. Rev. **106**, 893 (1957).

[80] R. Landauer, *Spatial variation of currents and fields due to localized scatterers in metallic conduction*, IBM J. Res. Dev. **1**, 223 (1957).

[81] M. Büttiker, *Four-Terminal Phase-Coherent Conductance*, Phys. Rev. Lett. **57**, 1761 (1986).

[82] D. Jacob, Ph.D. thesis, Universidad de Alicante (2007).

[83] H. Bruus and K. Flensberg, *Many-Body Quantum Theory in Condensed Matter Physics: An Introduction*, Oxford University Press (2004).

[84] M. Brandbyge, J. Schiøtz, M. R. Sørensen, P. Stoltze, K. W. Jacobsen, and J. K. Nørskov, L. Olesen, E. Laegsgaard, I. Stensgaard, and F. Besenbacher, *Quantized conductance in atom-sized wires between two metals*, Phys. Rev. B **52**, 8499 (1995).

[85] A. Szafer and A. D. Stone, *Theory of Quantum Conduction through a Constriction*, Phys. Rev. Lett. **62**, 300 (1989).

[86] R. Peierls, *Zur Theorie des Diamagnetismus von Leitungselektronen*, Z. Phys. A **80**, 763 (1933).

[87] Y. Meir and N. S. Wingreen, *Landauer formula for the current through an interacting electron region*, Phys. Rev. Lett. **68**, 2512 (1992).

[88] L. V. Keldysh, *Diagram Technique for Nonequilibrium Processes*, Sov. Phys. JETP, **20**, 1018 (1965).

[89] A. Oguri, *Transmission Probability for Interacting Electrons Connected to Reservoirs*, J. Phys. Soc. Jpn. **70**, 2666 (2001).

[90] A. A. Abrikosov, L. P. Gorkov, and I. A. Dzatloshinskii, *Methods of Quantum Field Theory in Statistical Physics*, Dover (1975).

[91] G. M. Eliashberg, *Transport equation for a degenerate system of fermi particles*, Sov. Phys. JETP **14**, 866 (1962).

[92] C. Caroli, R. Comberscot, P. Nozieres, and D. Saint-James, *Direct calculation of the tunneling current*, Phys. C **4**, (1971).

[93] E. Gull, A. J. Millis, A. I. Lichtenstein, A. N. Rubtsov, M. Troyer, and P. Werner, *Continuous-time Monte Carlo methods for quantum impurity models*, Rev. Mod. Phys. **83**, 349 (2011).

[94] I. Syôzi, Prog. Theor. Phys., **6**, 3 (1951).

[95] J. Hubbard, *Electron Correlations in Narrow Energy Bands*, Proc. Roy. Soc. A **276**, 238 (1963).

[96] W. Metzner and D. Vollhardt, *Correlated Lattice Fermions in $d = \infty$ Dimensions*, Phys. Rev. Lett. **62**, 324 (1989).

[97] A. Georges and G. Kotliar, *Hubbard model in infinite dimensions*, Phys. Rev. B **45**, 6479 (1992).

[98] A. Georges, G. Kotliar, W. Krauth and M. Rozenberg, *Dynamical mean-field theory of strongly correlated fermion systems and the limit of infinite dimensions*, Rev. Mod. Phys. **68**, 13 (1996).

[99] E. Müller-Hartmann, *Correlated fermions on a lattice in high dimensions*, Z. Physik B **74**, 507 (1989).

[100] J. W. Negele and H. Orland, *Quantum Many-Particle Systems*, Addison-Wesley, New York (1987).

[101] M. Jarrell, and J. E. Gubernatis, *Bayesian Inference and the Analytic Continuation of Imaginary-Time Quantum Monte Carlo Data*, Physics Reports Vol. **269**, 133 (1996).

[102] H. Kajueter and G. Kotliar, *New Iterative Perturbation Scheme for Lattice Models with Arbitrary Filling*, Phys. Rev. Lett. **77**, 131 (1996).

[103] J. E. Hirsch and R. M. Fye, *Monte Carlo Method for Magnetic Impurities in Metals*, Phys. Rev. Lett. **56**, 2321 (1986).

[104] N. Rubtsov, V. V. Savkin, and A. I. Lichtenstein, *Continuous-time quantum Monte Carlo method for fermions*, Phys. Rev. B **72**, 035122 (2005).

[105] P. Werner, A. Comanac, L. de' Medici, M. Troyer, and A. J. Millis, *Continuous-Time Solver for Quantum Impurity Models*, Phys. Rev. Lett. **97**, 076405 (2006).

[106] M. Caffarel and W. Krauth, *Exact diagonalization approach to correlated fermions in infinite dimensions: Mott transition and superconductivity*, Phys. Rev. Lett. **72**, 1545 (1994).

[107] C. Lanczos, *An Iteration Method for the Solution of the Eigenvalue Problem of Linear Differential and Integral Operators*, J. Res. Nat. Bur. Stand. **45**, 255 (1950).

[108] K. G. Wilson, *The renormalization group: Critical phenomena and the Kondo problem*, Rev. Mod. Phys. **47**, 773 (1975).

[109] N. E. Bickers, *Review of techniques in the large-N expansion for dilute magnetic alloys*, Rev. Mod. Phys. **59**, 845 (1987).

[110] Th. Pruschke and N. Grewe, *The Anderson model with finite Coulomb repulsion*, Z. Phys. B: Condens. Matter **74**, 439 (1989).

[111] K. Haule, S. Kirchner, J. Kroha, and P. Wölfle, *Anderson impurity model at finite Coulomb interaction U: Generalized noncrossing approximation*, Phys. Rev. B **64**, 155111 (2001).

[112] O. Gunnarsson, G. Sangiovanni, A. Valli, and M. W. Haverkort, *Fourier transformation and response functions*, Phys. Rev. B **82**, 233104 (2010).

[113] N. Blümer, *Efficiency of quantum Monte Carlo impurity solvers for the dynamical mean-field theory*, Phys. Rev. B **76**, 205120 (2007).

[114] M. Imada, A. Fujimori, Y. Tokura, *Metal-insulator transitions*, Rev. Mod. Phys. **70**, 1039 (1998).

[115] J. J. Binney, N. J. Dowrick, A. J. Fisher, and M. E. J. Newman, *The Theory of Critical Phenomena*, Oxford University Press (1992).

[116] L. S. Ornstein and F. Zernike, *Accidental deviations of density and opalescence at the critical point of a single substance*, Proc. Acad. Sci. Amsterdam **17**, 793 (1914).

[117] P. W. Anderson, *Absence of Diffusion in Certain Random Lattices*, Phys. Rev. **109**, 1492 (1958).

[118] M. Born and R. Oppenheimer, *Zur Quantentheorie der Molekeln*, Ann. Phys. **84**, 457 (1927).

[119] R. Arita, *Methods for electronic structure calculations with dynamical mean field theory: An overview and recent developments*, ISSP International Workshop, Kashiwa (2007).

[120] P. Hohenberg and W. Kohn, *Inhomogeneous Electron Gas*, Phys. Rev. **136**, B864 (1964).

[121] K. Held, *Electronic structure calculations using dynamical mean field theory*, Adv. Phys. **56**, 829 (2007).

[122] M. Levy, *Universal variational functionals of electron densities, first-order density matrices, and natural spin-orbitals and solution of the v-representability problem*, Proc. Natl. Acad. Sci. USA **76**, 6062 (1979).

[123] R. O. Jones and O. Gunnarsson, *The density functional formalism, its applications and prospects*, Rev. Mod. Phys. **61**, 689 (1989).

[124] W. Kohn and L. J. Sham, *Self-Consistent Equations Including Exchange and Correlation Effects*, Phys. Rev. **140**, A1133 (1965).

[125] J. P. Perdew, K. Burke, M. Ernzerhof, *Generalized Gradient Approximation Made Simple*, Phys. Rev. Lett. **77**, 3865 (1996); J. P. Perdew, K. Burke, M. Ernzerhof, *Erratum: Generalized Gradient Approximation Made Simple*, Phys. Rev. Lett. **78**, 1396 (1997).

[126] G. H. Wannier, *The Structure of Electronic Excitation Levels in Insulating Crystals*, Phys. Rev. **52**, 191 (1937).

[127] O. K. Andersen, *Linear methods in band theory*, Phys. Rev. B **12**, 3060 (1975).

[128] O. K. Andersen and T. Saha-Dasgupta, *Muffin-tin orbitals of arbitrary order*, Phys. Rev. B **62**, R16219 (2000).

[129] V. I. Anisimov, J. Zaanen, and O. K. Andersen, *Band theory and Mott insulators: Hubbard U instead of Stoner I*, Phys. Rev. B **44**, 943 (1991).

[130] M. T. Czyżyk and G. A. Sawatzky, *Local-density functional and on-site correlations: The electronic structure of La_2CuO_4 and $LaCuO_3$*, Phys. Rev. B **49**, 14211 (1994).

[131] N. D. Mermin and H. Wagner, *Absence of Ferromagnetism or Antiferromagnetism in One- or Two-Dimensional Isotropic Heisenberg Models*, Phys. Rev. Lett. **17**, 1133 (1966).

[132] A. Schiller and K. Ingersent, *Systematic $1/d$ Corrections to the Infinite-Dimensional Limit of Correlated Lattice Electron Models*, Phys. Rev. Lett. **75**, 113 (1995).

[133] G. Kotliar, S. Y. Savrasov, G. Pálsson and G. Biroli, *Cellular Dynamical Mean Field Approach to Strongly Correlated Systems*, Phys. Rev. Lett. **87**, 186401 (2001).

[134] Th. Maier, M. Jarrell, Th. Pruschke and M. H. Hettler, *Quantum cluster theories*, Rev. Mod. Phys. **77**, 1027 (2005).

[135] M. H. Hettler, A. N. Tahvildar-Zadeh and M. Jarrell, *Nonlocal dynamical correlations of strongly interacting electron systems*, Phys. Rev. B **58**, 7475 (R) (1998).

[136] M. H. Hettler, M. Mukherjee, M. Jarrell, H. R. Krishnamurthy, *Dynamical cluster approximation: Nonlocal dynamics of correlated electron systems*, Phys. Rev. B **61**, 12739 (2000).

[137] Th. Maier, M. Jarrell, Th. Pruschke, and J. Keller, *d-Wave Superconductivity in the Hubbard Model*, Phys. Rev. Lett. **85**, 1524 (2000).

[138] M. Jarrell, Th. Maier, M. H. Hettler, and A. N. Tahvildarzadeh, *Phase Diagram of the Hubbard Model: Beyond the Dynamical Mean Field*, Europhys. Lett. **56**, 563 (2001).

[139] C. Huscroft, M. Jarrell, Th. Maier, S. Moukouri, and A. N. Tahvildarzadeh, *Pseudogaps in the 2D Hubbard Model*, Phys. Rev. Lett. **86**, 139 (2001).

[140] A. Fuhrmann, D. Heilmann, and H. Monien, *From Mott insulator to band insulator: A dynamical mean-field theory study*, Phys. Rev. B **73**, 245118 (2006).

[141] S. Biermann, A. Poteryaev, I. Lichtenstein, and A. Georges, *Dynamical Singlets and Correlation-Assisted Peierls Transition in VO_2*, Phys. Rev. Lett. **94**, 026404 (2005).

[142] J. M. Tomczak, F. Aryasetiawan, and S. Biermann, *Effective bandstructure in the insulating phase versus strong dynamical correlations in metallic VO_2*, Phys. Rev. B **78**, 115103 (2008).

[143] G. Baym and L. P. Kadanoff, *Conservation Laws and Correlation Functions*, Phys. Rev. **124**, 287 (1961).

[144] G. Baym, *Self-Consistent Approximations in Many-Body Systems*, Phys. Rev. **127**, 1391 (1962).

[145] A. Toschi, A. A. Katanin, and K. Held, *Dynamical vertex approximation: A step beyond dynamical mean-field theory*, Phys. Rev. B **75**, 045118 (2007).

[146] K. Held, A. A. Katanin, and A. Toschi, *Dynamical vertex approximation - an introduction*, Prog. Theor. Phys. Suppl. **176**, 117 (2008).

[147] A. A. Katanin, A. Toschi, and K. Held, *Comparing pertinent effects of antiferromagnetic fluctuations in the two- and three-dimensional Hubbard model*, Phys. Rev. B **80**, 075104 (2009).

[148] A. N. Rubtsov, M. I. Katsnelson, and A. I. Lichtenstein, Ann. Phys. **327**, 1320 (2012).

[149] A. N. Rubtsov, M. I. Katsnelson, and A. I. Lichtenstein, *Dual boson approach to collective excitations in correlated fermionic systems*, Phys. Rev. B **77**, 033101 (2008).

[150] A. Rubtsov, M. I. Katsnelson, A. I. Lichtenstein, and A. Georges, *Dual fermion approach to the two-dimensional Hubbard model: Antiferromagnetic fluctuations and Fermi arcs*, Phys. Rev. B **79**, 045133 (2009).

[151] S. Brener, H. Hafermann, A. N. Rubtsov, M. I. Katsnelson, and A. I. Lichtenstein, *Dual fermion approach to susceptibility of correlated lattice fermions*, Phys. Rev. B **77**, 195105 (2008).

[152] A. A. Katanin, *The effect of six-point one-particle reducible local interactions in the dual fermion approach*, J. Phys. A: Math. Theor. **46**, 045002 (2013).

[153] S.-X. Yang, H. Fotso, H. Hafermann, K.-M. Tam, J. Moreno, Th. Pruschke, and M. Jarrell, *Dual fermion dynamical cluster approach for strongly correlated systems*, Phys. Rev. B **84**, 155106 (2011).

[154] C. Slezak, M. Jarrell, Th. Maier and J. Deisz, *Multi-scale Extensions to Quantum Cluster Methods for Strongly Correlated Electron Systems*, J. Phys.: Condens. Matter **21**, 435604 (2009).

[155] A. Toschi, Habilitationsschrift, Technische Universität Wien (2011).

[156] T. A. Maier, M. Jarrell, and D. J. Scalapino, *Structure of the Pairing Interaction in the Two-Dimensional Hubbard Model*, Phys. Rev. Lett. **96**, 047005 (2006).

[157] A. Toschi, G. Rohringer, A. A. Katanin, and K. Held, *Ab initio calculations with the dynamical vertex approximation*, Ann. Phys. **523**, 698 (2011).

[158] G. Rohringer, A. Valli, and A. Toschi, *Local electronic correlations at the two-particle level*, Phys. Rev. B **86**, 125114 (2012).

[159] D. Sénéchal, A.-M. Tremblay, C. Bourbonnais, *Theoretical Methods for Strongly Correlated Electrons*, Springer, Berlin (2003).

[160] D. B. McWhan, A. Menth, J. P. Remeika, W. F. Brinkman, and T. M. Rice, *Metal-Insulator Transitions in Pure and Doped V_2O_3*, Phys. Rev. B **7**, 1920 (1973).

[161] N. E. Bickers, *Self-consistent many-body theory for condensed matter systems*, Addison Wesley, New York (1998).

[162] L. Boehnke, H. Hafermann, M. Ferrero, F. Lechermann, and O- Parcollet, *Orthogonal polynomial representation of imaginary-time GreenâĂŹs functions*, Phys. Rev. B **84**, 075145 (2011).

[163] H. Hafermann, K. R. Patton, and P. Werner, *Improved estimators for the self-energy and vertex function in hybridization-expansion continuous-time quantum Monte Carlo simulations*, Phys. Rev. B **85**, 205106 (2012).

[164] S. X. Yang, H. Fotso, J. Liu, T. A. Maier, K. Tomko, E. F. D'Azevedo, R. T. Scalettar, Th. Pruschke, and M. Jarrell, *Parquet approximation for the 4×4 Hubbard cluster*, Phys. Rev. E **80**, 046706 (2009).

[165] K.-M. Tam, H. Fotso, S.-X. Yang, Tae-Woo Lee, J. Moreno, J. Ramanujam, and M. Jarrell, *Solving the Parquet Equations for the Hubbard Model beyond Weak Coupling*, arXiv:1108.4926 (2011).

[166] S. Hummel, Diplomarbeit, Technische Universität Wien (2013).

[167] T. Schäfer, G. Rohringer, O. Gunnarsson, S. Ciuchi, G. Sangiovanni, A. Toschi, *Divergent Precursors of the Mott-Hubbard Transition at the Two-Particle Level*, arXiv:1303.0246 (2013).

[168] G. Rohringer, A. Toschi, A. Katanin, and K. Held, *Critical Properties of the Half-Filled Hubbard Model in Three Dimensions*, Phys. Rev. Lett. **107**, 256402 (2011).

[169] J. K. Freericks and V. Zlatić, *Exact dynamical mean-field theory of the Falicov-Kimball model*, Rev. Mod. Phys. **75**, 1333 (2003).

[170] N. Furukawa, *Transport Properties of the Kondo Lattice Model in the Limit $S=\infty$ and $D=\infty$*, J. Phys. Soc. Jpn. **63**, 3214 (1994).

[171] S. Florens, *Nanoscale Dynamical Mean-Field Theory for Molecules and Mesoscopic Devices in the Strong-Correlation Regime*, Phys. Rev. Lett. **99**, 046402 (2007).

[172] J. Kuneŝ, R. Arita, P. Wissgott, A. Toschi, H. Ikeda, and K. Held, *Wien2wannier: From linearized augmented plane waves to maximally localized Wannier functions*, Comp. Phys. Commun. **181**, 1888 (2010).

[173] M. Potthoff and W. Nolting, *Metallic surface of a Mott insulator-Mott insulating surface of a metal*, Phys. Rev. B **60**, 7834 (1999).

[174] S. Biermann, A. Georges, A. Lichtenstein, and T. Giamarchi, *Deconfinement Transition and Luttinger to Fermi Liquid Crossover in Quasi-One-Dimensional Systems*, Phys. Rev. Lett. **87**, 276405 (2001).

[175] M. Snoek, I. Titvinidze, C. Tőke, K. Byczuk, and W. Hofstetter, *Antiferromagnetic order of strongly interacting fermions in a trap: real-space dynamical mean-field analysis*, New J. Phys. **10**, 093008 (2008).

[176] A. Schwabe, D. Gütersloh, and M. Potthoff, *Competition between Kondo Screening and Indirect Magnetic Exchange in a Quantum Box*, Phys. Rev. Lett. **109**, 257202 (2012).

[177] I. Titvinidze, A. Schwabe, N. Rother, and M. Potthoff, *Dynamical mean-field theory of indirect magnetic exchange*, Phys. Rev. B **86**, 075141 (2012).

[178] D. Jacob, K. Haule, and G. Kotliar, *Kondo Effect and Conductance of Nanocontacts with Magnetic Impurities*, Phys. Rev. Lett. **103**, 016803 (2009).

[179] D. Jacob, K. Haule, and G. Kotliar, *Dynamical mean-field theory for molecular electronics: Electronic structure and transport properties*, Phys. Rev. B **82**, 195115 (2010).

[180] B. Surer, M. Troyer, P. Werner, T. O. Wehling, A. M. Läuchli, A. Wilhelm, and A. I. Lichtenstein, *Multiorbital Kondo physics of Co in Cu hosts*, Phys. Rev. B **85**, 085114 (2012).

[181] G. C. Solomon, D. Q. Andrews, T. Hansen, R. H. .Goldsmith, M. R. Wasielewski, R. P. Van Duyne, and M. R. Ratner, *Understanding quantum interference in coherent molecular conduction*, J. Chem. Phys. **129**, 541701 (2008).

[182] T. Markussen, R. Stadler, and K. S. Thygesen, *The Relation between Structure and Quantum Interference in Single Molecule Junctions*, Nano Lett. **10**, 4260 (2010).

[183] Y. Aharonov and D. Bohn, *Significance of Electromagnetic Potentials in the Quantum Theory*, Phys. Rev. **115**, 485 (1959).

[184] Y. Aharonov and D. Bohn, *Further ConsitIerations on Electromagnetic Potentials in the Quantum Theory*, Phys. Rev. **123**, 1511 (1961).

[185] J. P. Bergfield, G. C. Solomon, C. A. Stafford, and M. A. Ratner, *Novel Quantum Interference Effects in Transport through Molecular Radicals*, Nano Lett. **11**, 2759 (2011).

[186] H. Song, Y. Kim, Y. H. Jang, H. Jeong, M. A. Reed, and T. Lee, *Observation of molecular orbital gating*, Nature **462**, 1039-1043 (2009).

[187] A. A. Kocherzhenko, L. D. A. Siebbeles, and F. C. Grozema, *Chemically Gated Quantum-Interference-Based Molecular Transistor*, J. Phys. Chem. Lett. **2**, 1753 (2011).

[188] S.-H. Ke, W. Yang, and H. U. Baranger, *Quantum Interference Controlled Molecular Electronics*, Nano Lett. **8**, 3257 (2008).

[189] M. Marchi, S. Azadi, S. Sorella, *Fate of the Resonating Valence Bond in Graphene*, Phys. Rev. Lett. **107**, 086807 (2011).

[190] F. A. Kekulé, *Sur la constitution des substances aromatiques*, Bulletin de la Societe Chimique de Paris **3**, 98 (1865).

[191] F. A. Kekulé, *Untersuchungen über aromatische Verbindungen*, Liebigs Annalen der Chemie und Pharmacie **137**, 129, (1866).

[192] K. P. C. Vollhardt and N. E. Schore, *Organic Chemistry: Structure and Function*, 6th edition, W. H. Freeman & Co Ltd, New York (2010).

[193] W. L. Jolly, *Modern Inorganic Chemistry*, McGraw-Hill (1984).

[194] E. Hückel, *Quantentheoretische beiträge zum benzolproblem*, Zeit. Physik **70**, 204 (1931).

[195] E. Hückel, *Quanstentheoretische beiträge zum benzolproblem*, Zeit. Physik **72**, 310 (1931).

[196] E. Hückel, *Quantentheoretische beiträge zum problem der aromatischen und ungesättigten verbindungen*, Zeit. Physik **76**, 628 (1932).

[197] E. Hückel, *Die freien radikale der organischen chemie*, Zeit. Physik **83**, 632 (1933).

[198] R. Hoffmann and R. B. Woodward, *Selection Rules for Concerted Cycloaddition Reactions*, J. Am. Chem. Soc. **87**, 395 (1965).

[199] M. H. Hettler, W. Wenzel, M. R. Wegewijs, and H. Schoeller, *Current Collapse in Tunneling Transport through Benzene*, Phys. Rev. Lett. **90**, 076805 (2003).

[200] J. D. Barr, J. P. Bergfield, C. A. Stafford, *Effective field theory of interacting π electrons*, Phys. Rev. B **86**, 115403 (2012).

[201] E. Ising, *Beitrag zur Theorie des Ferromagnetismus*, Z. Phys. **31** 253 (1925).

[202] K. Huang, *Statistical mechanics*, Wiley (1987).

[203] C. Itzykson, J.-M. Drouffe, *Statistical field theory, Volume 1: From Brownian motion to renormalization and lattice gauge theory*, Cambridge University Press (1989).

[204] M. Julliere, *Tunneling between ferromagnetic films*, Phys. Lett. A **54** 225 (1975).

[205] M. Johnson, R. H. Silsbee, *Interfacial charge-spin coupling: Injection and detection of spin magnetization in metals*, Phys. Rev. Lett. **55** 1790 (1985).

[206] A. Valli, G. Sangiovanni, O. Gunnarsson, A. Toschi, and K. Held, *Dynamical Vertex Approximation for Nanoscopic Systems*, Phys. Rev. Lett. **104**, 246402 (2010).

[207] A. Valli, G. Sangiovanni, A. Toschi, and K. Held, *Correlation effects in transport properties of interacting nanostructures*, Phys. Rev. B **86**, 115418 (2012).

[208] J. Rincón, K. Hallberg, A. A. Aligia, and S. Ramasesha, *Quantum Interference in Coherent Molecular Conductance*, Phys. Rev. Lett. **103**, 266807 (2009).

[209] J. P. Bergfield and C. A. Stafford, *Many-body theory of electronic transport in single-molecule heterojunctions*, Phys. Rev. B, **79**, 245125 (2009).

[210] J. P. Bergfield, and C. A. Stafford, *Thermoelectric Signatures of Coherent Transport in Single-Molecule Heterojunctions*, Nano Lett. **11**, 3072 (2009).

[211] D. Bohr and P. Schmitteckert, *The dark side of benzene: Interference vs. interaction*, Ann. Phys., **524**, 199-204 (2012).

[212] L. Tosi, P. Roura-Bas, and A. A. Aligia, *Nonequilibrium conductance through a benzene molecule in the Kondo regime*, J. Phys.: Condens. Matter **24**, 365301 (2012).

[213] P. Roura-Bas, L. Tosi, A. A. Aligia, and K. Hallberg, *Interplay between quantum interference and Kondo effects in nonequilibrium transport through nanoscopic systems*, Phys. Rev. B **84**, 073406 (2011).

[214] M. R. Calvo, J. Fernández-Rossier, J. J. Palacios, D. Jacob, D. Natelson, and C. Untiedt, *The Kondo effect in ferromagnetic atomic contacts*, Nature. **458**, 1150 (2009).

[215] P. Lucignano, R. Mazzarello, A. Smogunov, M. Fabrizio, and E. Tosatti, *Kondo conductance in an atomic nanocontact from first principles*, Nat. Mater. **8**, 563 (2009).

[216] C. Karrasch, V. Meden, and K. Schönhammer, *Finite-temperature linear conductance from the Matsubara GreenâĂŹs function without analytic continuation to the real axis*, Phys. Rev. B **82**, 125114 (2010).

[217] M. R. Galpin, F. W. Jayatilaka, D. E. Logan, and F. B. Anders, *Interplay between Kondo physics and spin-orbit coupling in carbon nanotube quantum dots*, Phys. Rev. B **81**, 075437 (2010).

[218] N. Parragh, A. Toschi, K. Held, and G. Sangiovanni, *Conserved quantities of $SU(2)$-invariant interactions for correlated fermions and the advantages for quantum Monte Carlo simulations*, Phys. Rev. B **86**, 155158 (2012).

[219] J. Kuneŝ, *Efficient treatment of two-particle vertices in dynamical mean-field theory*, Phys. Rev. B **83**, 085102 (2011).

[220] C. Karrasch, R. hedden, R. Peters, Th. Pruschke, K. Schönhammer, and V. Meden, *A finite-frequency functional renormalization group approach to the single impurity Anderson model*, J. Phys.: Condens. Matter **20**, 345205 (2008).

[221] V. Janiš and V. Pokorný, *Vertex corrections to the electrical conductivity in models with elastically scattered electrons*, Phys. Rev. B **81**, 165103 (2010).

[222] S. T. F. Hale and J. K. Freericks, *Effect of vertex corrections on longitudinal transport through multilayered nanostructures: Dynamical mean-field theory approach applied to the inhomogeneous Falicov-Kimball model*, Phys. Rev. B **83**, 035102 (2011).

[223] C. Berthod and T. Giamarchi, *Tunneling conductance and local density of states in tight-binding junctions*, Phys. Rev. B **84**, 155414 (2011).

[224] K. Palotás, Werner A. Hofer, and L. Szunyogh, *Theoretical study of the role of the tip in enhancing the sensitivity of differential conductance tunneling spectroscopy on magnetic surfaces*, Phys. Rev. B **83**, 214410 (2011).

[225] K. Palotás, Werner A. Hofer, and L. Szunyogh, *Simulation of spin-polarized scanning tunneling microscopy on complex magnetic surfaces: Case of a Cr monolayer on Ag(111)*, Phys. Rev. B **84**, 174428 (2011).

[226] A. Pecchia and A. Di Carlo, *Atomistic theory of transport in organic and inorganic nanostructures*, Rep. Prog. Phys. **67**, 1497 (2004).

[227] M. Strange, I. S. Kristensen, K. S. Thygesen, and K. W. Jacobsen, *Benchmark density functional theory calculations for nanoscale conductance*, J. Chem. Phys. **128**, 114714 (2008).

[228] P. Delaney and J. C. Greer, *Correlated Electron Transport in Molecular Electronics*, Phys. Rev. Lett. **93**, 036805 (2004).

[229] J. Kröger, N. Néel, and L. Limot, *Contact to single atoms and molecules with the tip of a scanning tunneling microscope* J. Phys.: Condens. Matter **20**, 223001 (2008).

[230] L. C. Venema, J. W. G. Wildöer, C. Dekker, G. A. Rinzler, R. E. Smalley, *STM atomic resolution images of single-wall carbon nanotubes*, Appl. Phys. A **66**, S153 (1998).

[231] J. M. Blanco, F. Flores, and R. Perez, *STM-theory: Image potential, chemistry and surface relaxation*, Prog Surf. Sci. **81**, 403 (2006).

[232] S. Jin, T. H. Tiefel, M. McCormack, R. A. Fastnacht, R. Ramesh, L. H. Chen, *Thousandfold Change in Resistivity in Magnetoresistive La-Ca-Mn-O Films*, Science **264**, 413 (1994).

[233] R. M. Kusters, J. Singleton, D. A. Keen, R. McGreevy, and W. Hayes, *Magnetoresistance measurements on the magnetic semiconductor* $Nd_{0.5}Pb_{0.5}MnO_3$, Physica B **155**, 362 (1989).

[234] R. von Helmolt, J. Wecker, B. Holzapfel, L. Schultz, and K. Samwer, *Giant negative magnetoresistance in perovskitelike* $La_{2/3}Ba_{1/3}MnO_x$ *ferromagnetic films*, Phys. Rev. Lett. **71**, 2331 (1993).

[235] H. Y. Hwang, T. T. M. Palstra, S.-W. Cheong, B. Batlogg, *Pressure effects on the magnetoresistance in doped manganese perovskites*, Phys. Rev. B **52**, 15046 (1995).

[236] G. M. Jonker, J. H. van Santen, *Ferromagnetic compounds of manganese with perovskite structure*, Physica **16**, 337 (1950).

[237] G. Papavassiliou, M. Fardis, M. Belesi, M. Pissas, I. Panagiotopoulos, G. Kallias, and D. Niarchos, *Polarons and phase separation in lanthanum-based manganese perovskites: A ^{139}La and ^{55}Mn NMR study*, Phys. Rev. B **59**, 6390 (1999).

[238] E. Dagotto, T. Hotta, and A. Morfeo, *Colossal Magnetoresistant Materials: The Key Role of Phase Separation*, Physics Reports **344**, 1 (2001).

[239] A. J. Millis, P. B. Littlewood, and B. I. Shraiman, *Double Exchange Alone Does Not Explain the Resistivity of $La_{1-x}Sr_xMnO_3$*, Phys. Rev. Lett. **74**, 5144 (1995).

[240] H. Röder, J. Zang, and A. R. Bishop, *Lattice Effects in the Colossal-Magnetoresistance Manganites* , Phys. Rev. Lett. **76**, 1356 (1996).

[241] A. J. Millis, B. I. Shraiman, and R. Mueller, *Dynamic Jahn-Teller Effect and Colossal Magnetoresistance in $La_{1-x}Sr_xMnO_3$*, Phys. Rev. Lett. **77**, 175 (1996).

[242] P. E. Kornilovitch, *Band Structure of the Jahn-Teller Polaron from Quantum Monte Carlo*, Phys. Rev. Lett. **84**, 1551 (2000).

[243] M. B. Salamon and M. Jaime, *The physics of manganites: Structure and transport,* Rev. Mod. Phys. **73**, 583 (2001).

[244] C. Zener, *Interaction between the d-Shells in the Transition Metals. II. Ferromagnetic Compounds of Manganese with Perovskite Structure*, Phys. Rev. **82**, 403 (1951).

[245] P. W. Anderson and H. Hasegawa, *Considerations on Double Exchange*, Phys. Rev. **100**, 675 (1955).

[246] P. Schiffer, A. P. Ramirez, W. Bao, and S.-W. Cheong, *Low Temperature Magnetoresistance and the Magnetic Phase Diagram of $La_{1-x}Ca_xMnO_3$*, Phys. Rev. Lett. **75**, 3336 (1995).

[247] P. G. Radaelli, D. E. Cox, M. Marezio, and S-W. Cheong, *Charge, orbital, and magnetic ordering in $La_{0.5}Ca_{0.5}MnO_3$s*, Phys. Rev. B **55** 3015 (1997).

[248] M. Tokunaga, N. Miura, Y. Tomioka, and Y. Tokura, *High-magnetic-field study of the phase transitions of $R_{1-x}Ca_xMnO_3$ (R=Pr, Nd)*, Phys. Rev. B **57**, 5259 (1998).

[249] M. M. Savosta, V. A. Borodin, M. Maryško, Z. Jirák, J. Hejtmánek, and P. Novák, *Ferromagnetic-antiferromagnetic transition in $Pr_{0.51}Sr_{0.49}MnO_3$ manganite*, Phys. Rev. B **65**, 224418 (2002).

[250] J. P. Joshi, R. Gupta, A. K. Sood, S. V. Bhat, A. R. Raju, and C. N. R. Rao, *Temperature-dependent electron paramagnetic resonance studies of charge-ordered $Nd_{0.5}Ca_{0.5}MnO_3$*, Phys. Rev. B **65**, 024410 (2001).

[251] J. P. Joshi, A. K. Sood, S. V. Bhat, S. Parashar, A. R. Raju, and C. N. R. Rao, *An electron paramagnetic resonance study of phase segregation in $Nd_{0.5}Sr_{0.5}MnO_3$*, J. Magn. Magn. Mater. **279**, 961 (1995).

[252] E. O. Wollan and W. C. Koehler, *Neutron Diffraction Study of the Magnetic Properties of the Series of Perovskite-Type Compounds $[(1-x)La, xCa]MnO_3$*, Phys. Rev. **100**, 545 (1955).

[253] H. Kuwahara, Y. Tomioka, A. Asamitsu, Y. Moritomo, and Y. Tokura, *A First-Order Phase Transition Induced by a Magnetic Field*, Science **270**, 961 (1995).

[254] D. P. Kozlenko, I. N. Goncharenko, B. N. Savenko and V. I. Voronin, *High Pressure Effects on the Crystal and Magnetic Structure of $La_{0.7}Sr_{0.3}MnO_3$*, J. Phys.: Condensed Matter **16**, 6755 (2004).

[255] A. Asamitsu, Y. Tomioka, H. Kuwahara and Y. Tokura, *Current switching of resistive states in magnetoresistive manganites*, Nature **388**, 50 (1997).

[256] T. Sarkar, B. Ghosh, A. K. Raychaudhuri, and T. Chatterji, *Crystal structure and physical properties of half-doped manganite nanocrystals of less than 100-nm size*, Phys. Rev. B **77**, 235112 (2008).

[257] S. S. Rao, K. N. Anuradha, S. Sarangi, and S. V. Bhat, *Weakening of charge order and antiferromagnetic to ferromagnetic switch over in $Pr_{0.5}Ca_{0.5}MnO_3$ nanowires*, Appl. Phys. Lett. **87**, 182503 (2005).

[258] E. Rozenberg, G. Jung, M. Auslender, G. Gorodetsky, I. Felner, E. Sominski, A. Gedanken, and Y . M. Mukovskii, *Magnetic properties of crystalline $La_{0.9}Ca_{0.1}MnO_3$: Comparison of bulk and nanometer-sized samples*, J. Appl. Phys. **99**, 08Q305 (2006).

[259] T. Sarkar, P. K. Mukhopadhyay, A. K. Raychaudhuri, and S. Banerjee, *Structural, magnetic, and transport properties of nanoparticles of the manganite $Pr_{0.5}Ca_{0.5}MnO_3$*, J. Appl. Phys. **101**, 124307 (2007).

[260] P. Grünberg, R. Schreiber, Y. Pang, M. B. Brodsky, and H. Sowers, *Layered Magnetic Structures: Evidence for Antiferromagnetic Coupling of Fe Layers across Cr Interlayers*, Phys. Rev. Lett. **57**, 2442 (1986).

[261] *The 2007 Nobel Prize in Physics - Press Release* The Royal Swedish Academy of Science, Nobelprize.org.

[262] A. Yamasaki, M. Feldbacher, Y.-F. Yang, O. K. Andersen, and K. Held, *Pressure-Induced Metal-Insulator Transition in $LaMnO_3$ Is Not of Mott-Hubbard Type*, Phys. Rev. Lett. **96**, 166401 (2006).

[263] Y.-F. Yang and K. Held, *Localization of strongly correlated electrons as Jahn-Teller polarons in manganites*, Phys. Rev. B **77**, 212401 (2007).

[264] Y.-F. Yang and K. Held, *Dynamical mean field theory for manganites*, Phys. Rev. B **82**, 195109 (2010).

[265] G. Kresse and J. Hafner, *Ab initio molecular dynamics for liquid metals*, Phys. Rev. B **47**, 558 (1993).

[266] G. Kresse and J. Hafner, *Ab initio molecular-dynamics simulation of the liquid-metal-amorphous-semiconductor transition in germanium*, Phys. Rev. B **49**, 14251 (1994).

[267] G. Kresse and J. Furthmüller, *Efficiency of ab-initio total energy calculations for metals and semiconductors using a plane-wave basis set*, Comput. Mat. Sci. **6**, 15 (1996).

[268] G. Kresse and J. Furthmüller, *Efficient iterative schemes for ab initio total-energy calculations using a plane-wave basis set*, Phys. Rev. B **54**, 11169 (1996).

[269] J.-H. Park, C. T. Chen, S-W. Cheong, W. Bao, G. Meigs, V. Chakarian, and Y. U. Idzerd, *Electronic Aspects of the Ferromagnetic Transition in Manganese Perovskites*, Phys. Rev. Lett. **76**, 4215 (1996).

[270] P. K. de Boer, H. van Leuken, R. A. de Groat, T. Rojo, and G. E. Barberis, *Electronic structure of $La_{0.5}Ca_{0.5}MnO_3$*, Solid State Communications **102**, 621 (1997).

[271] R. P. Feynman, *Forces in Molecules*, Phys. Rev. **56**, 340 (1939).

[272] H. Das, G. Sangiovanni, A. Valli, K. Held, and T. Saha-Dasgupta, *Size Control of Charge-Orbital Order in half-Doped Manganite $La_{0.5}Ca_{0.5}MnO_3$*, Phys. Rev. Lett. **107**, 197202 (2010).

[273] V. I. Anisimov, I. S. Elfimov, and M. A. Korotin, *Orbital and charge ordering in $Pr_{1-x}Ca_xMnO_3$ ($x = 0$ and 0.5) from the ab initio calculations*, Phys. Rev. B **55**, 15494 (1997).

[274] Z. Jirák, E. Hadová, O. Kaman, K. Knížek, M. Maryško, E. Pollert, M. Dlouhá, and S. Vratislav, *Ferromagnetism versus charge ordering in the $Pr_{0.5}Ca_{0.5}MnO_3$ and $La_{0.5}Ca_{0.5}MnO_3$ nanocrystals*, Phys. Rev. B **81**, 024403 (2010).

[275] M. Auslender, A. I. Shames, E. Rozenberg, E. Sominski, A. Gedanken, and Ya. M. Mukovskii, *Electron paramagnetic resonance study of size and nonstoichiometry effects on magnetic ordering in half-doped $La_{0.5}Ca_{0.5}MnO_3$ manganite*, J. Appl. Phys. **107**, 09D702 (2010).

[276] E. Rozenberg, M. I. Tsindlekht, I. Felner, E. Sominski, A. Gedanken, Ya. M. Mukovskii, and C. E. Lee, *Size and Nonstoichiometry Effects on Magnetic Properties of* $La_{0.5}Ca_{0.5}MnO_3$ *Manganite*, IEEE Trans. Magn. **45**, 2576 (2009).

[277] J. J. Deisz, D. W. Hess, and J. W. Serene, *Vertex symmetry and the asymptotic frequency dependence of the self-energy*, Phys. Rev. B **55**, 2089 (1997).

[278] J. K. Freericks and V. Turkowski, *Inhomogeneous spectral moment sum rules for the retarded Green function and self-energy of strongly correlated electrons or ultracold fermionic atoms in optical lattices*, Phys. Rev. B **80**, 115119 (2009).

[279] W. H. Press, S. A. Teukolsky, W. T. Vetterling, and B. P. Flannery, *Numerical Recipes: The Art of Scientific Computing*, Cambridge University Press (2007).

Acknowledgments

I would like to thank my advisor, Karsten Held, for giving me the possibility to join his group. An outstanding scientist, always able to get the physical picture, and a skillful group leader: all his effort through the years, together with an amazing net of guests and collaborators, contributed to create a friendly and productive environment, for which I will always be grateful.

I consider myself particularly privileged, as throughout my stay in Vienna I could avail myself of the ‘‘scientific care’’ of both Giorgio Sangiovanni and Alessandro Toschi. With them I felt immediately at ease: I owe them way more than I could express in these acknowledgments. The former has guided me since my early steps into research, and besides introducing me to the *fancy art* of shell scripting, spent an insane amount of time working side to side with me... no matter if day, night or weekends. When he was awarded the professorship and moved to Würzburg, I came to the (not painless) decision to stay here, but I know I can still refer to him whenever I need help. However, this gave me the possibility to intensify my scientific relations with the latter, and allowed me to learn a lot: his deep scientific understanding (which goes well beyond physics) and his pedagogical skills are rare, and the way he devotes himself to each project and each student (no matter how many are there) is unbelievable.

I certainly also owe much to Massimo Capone, who I consider my earliest *mentor*. His wisdom, foresight, and common sense (which is rare nowadays) have always impressed me: indeed his support and approval had an important role in my decision to move here.

I would like to thank all the valuable collaborators of the project presented in this thesis. Olle Gunnarsson, for providing the cluster QMC solver, which played an important role in many stages of the research discussed within this thesis. Sabine Andergassen for her kindness and the valuable discussions, which allowed me to focus on the relevant aspects of the problem when my path was leading astray. Hena Das and Tanusri Saha-Dasgupta, who performed the nasty DFT calculation within the manganites project: we also appeared in the press! I also thank them for their kind hospitality during my stay in Kolkata.

I thank my (past and present) colleagues for contributing to the nice and relaxed atmosphere of the group, giving life to stimulating discussions, and for never denying any request for help. Philipp Hansmann, Nico Parragh (my office mate for almost three years) and Philipp Wissgott,

the original members of the group when it was born. Their farewell marked the end of an *era* and many things changed, but ‘‘*everything is* (still) *always exceptionally urgent*’’ (quot.).
Georg Rohringer (from whom I have learned quite a lot in the last year of close collaboration), Elias Assmann, Shiro Sakai, Thomas Schäfer (to whom I am indebted for the revision to my terrible *deutsche Kurzfassung*... looking forward to the dance lessons!), Ciro Taranto (to whom I am thankful for the most challenging squash matches ever, and for sharing with me the passion for sushi), Patrik Thunström, Anna Toth, Markus Wallerberger, and Zhicheng Zhong (a remarkable scientist, ski-lessons mate, and nearly unbeatable table tennis player).
I would also like to mention some of the students who were part of the group during these years: Anna Galler, Stefan Hummel (in particular for the stunning liquid Ni_2 ice cream experience), Andreas Kainz, and Christian Ecker (who had nice words of appreciation and the patience to talk with me *auf Deutsch*). I also owe a special mention to the students who I have (although unofficially) co-supervised: Viktoria Motsch, David Rotter, and Stefanie Wolf. By my side, the teaching experience was quite instructive and allowed me to get a deeper understanding of my own research projects. I hope they value the time we spent together as much as I do.

I also acknowledge the Austrian Science Fund (FWF) through the CMS college No. WK004, the SFB ViCom Project No. F4103-N13, and the Austria-Russia joint Project No. I610-N16, as well as the EU-Indian network MONAMI, for financing my research activity in Vienna.

Also concerning the non-scientific component, there are many other reasons why I never regret the decision to move to Vienna. My father and my family, who always supported me to follow my way, although the separation was not an easy one. My friends (and former colleagues) in Rome, although time and distance eventually tend to weaken the contacts. Fortunately, I have found wonderful people here, that became my *Viennese family*: Emanuela (who was also appointed the role of fashion designer, ice skate instructor, and main referent for almost anything) & Peter, Jole (who took me to eat the best *california maki* ever), Antonello (my personal *guru*, who also introduced me to squash, before hanging up his racket...) & Angela, and Irene. I would like to thank also my flatmates, and many other people I spent an amazing time with, and in particular *neo*-mum Elisa. I apologize if I do not mention all of them here.

The Viennese experience changed me and allowed me to widen my view about the world, while traveling for conferences gave me amazing experiences. However, the landscape of the bridges over the Danube in Budapest remains without doubt one of the most beautiful ones I have ever seen. Perhaps because I look at it with different eyes, with respect to all the others, as I have friends there and I do not feel a tourist anymore. I could never be thankful enough to Viktória, for being by my side, introducing me to the Hungarian language, culture ("*waiting for the watermelon to come*"), and food (*húsleves, lecsó, kakaós csiga*, and *pogácsa* overall). Both for the laughs and the tears, for the sauna and for the concerts (I cannot imagine a life without these anymore), but also for being able to deal with my insanity. *A királynőm Pesten van*.